Wind, Shelf-current and Density-Driven Circulation in Poverty Bay, New Zealand

A Thesis

submitted in fulfilment

of the requirements for the Degree

of

Doctor of Philosophy

in Earth Sciences

by

Scott Alexander Stephens

The University of Waikato

Te Whare Wānanga o Waikato

The University of Waikato

February 2001

Frontispiece: Upper – Eastern Poverty Bay with Tuaheni Point in the background. Gisborne City and Waikanae Beach are in the foreground. The Turanganui River enters the bay on the near side of the port breakwater enclosure and is noticeably discoloured compared with the adjacent water inside the port.

Lower – Poverty Bay looking seaward, south to Young Nicks Head in the background. The Waipaoa River plume is visible hugging the foreground coast.

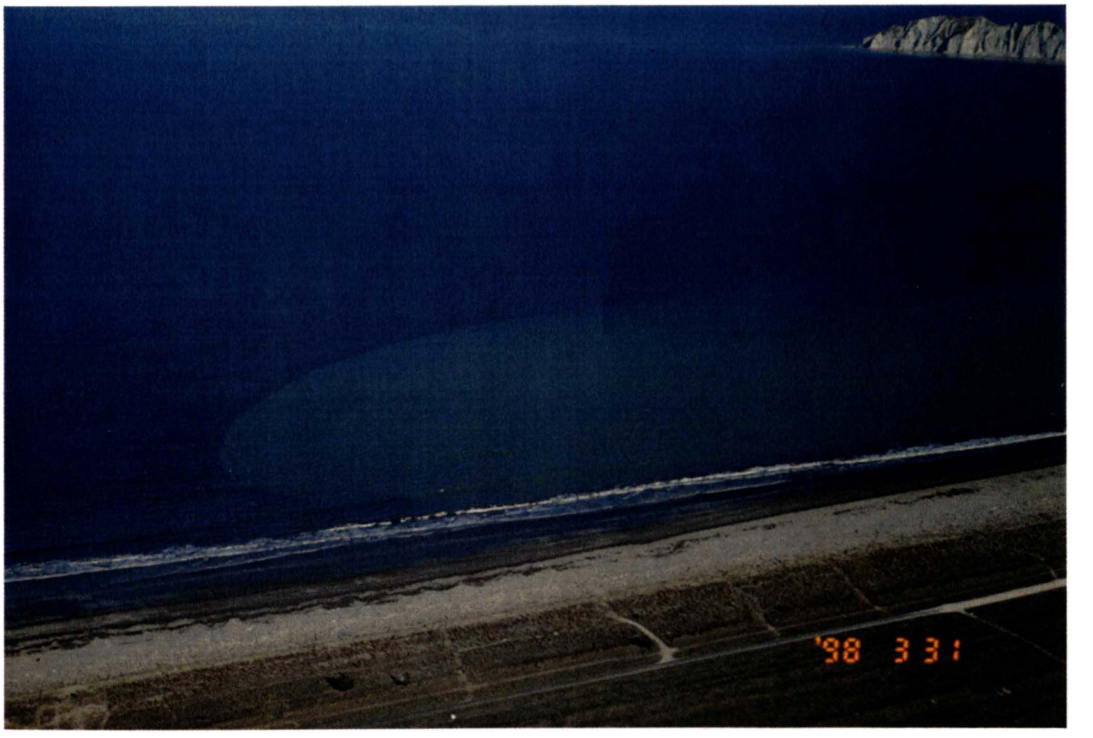

Abstract

This thesis describes the three-dimensional hydrodynamics of Poverty Bay in context of its bathymetry, forcing parameters and typical circulation patterns. The thesis provides a model of hydrodynamic processes in an exposed and stratified coastal embayment. Two field experiments were undertaken, with associated data analyses and interpretation, and numerical models were used to support and extend the data analyses.

Continental-shelf-currents exhibited a strong non-tidal component (mean 0.09 m s^{-1}, maximum 0.32 m s^{-1}) with relatively small tidal flows (mean 0.04 m s^{-1}, maximum 0.12 m s^{-1}). Wavelet analyses across the 8-512 hour cycle band showed that wind-forcing explained a large proportion of energy contained in the non-tidal shelf-current component. Coastal-trapped-waves with amplitudes of ≤ 0.1 m and velocity ≤ 0.2 m s^{-1} also contributed to non-tidal shelf-current motion. Correlation and regression analyses showed that CTWs generated by wind-driven water flux through Cook Strait, could account for up to 40% of variance in Gisborne shelf-currents, at timescales of 2-20 day period. Simulated sea-levels showed 88% energy attenuation occurred as CTWs exited Cook Strait, but only 3% attenuation occurred as CTWs travelled up-coast from Riversdale, therefore a barotropic CTW generated by a Cook Strait flux had approximately 9% its original energy on reaching Gisborne. Continental-shelf-currents formed occasional eddies of diameter ~4 km and velocity ~0.1 m s^{-1} in the lee of Tuaheni Point. Continental-shelf-currents contributed ~0.01 m s^{-1} to circulation in depths less than 18 m, small in comparison to those typically measured of 0.05-0.10 m s^{-1}.

Circulation was dominated by the combined influence of wind stress and river discharge, and since the prevailing wind created circulation patterns similar to the Waipaoa River discharge, both processes contributed to the prevailing anticyclonic horizontal circulation observed in Poverty Bay. River discharge was important for its role in stratifying the water column, typically producing an ~2m mixed surface layer with salinity < 34.5 psu compared with the marine background of 34.8-35.0 psu. This reduced vertical mixing, enhanced shear, and

facilitated faster horizontal velocities, thus creating higher sensitivity to wind-driven processes. Under most conditions, the wind was the most important contributor to circulation with a response time of 1 hour for the upper and lower layers and ~5 hours in the mid-water column. Simulations suggested that when Waipaoa River discharge exceeds 60 $m^3 s^{-1}$ it begins to dominate wind-induced circulation, but this occurs only ~11% of the time. The long-term wind-record suggested that offshore winds prevail 77% of the time, and these drive a time-averaged upwelling vertical circulation of 0.03-0.10 m s^{-1} and an anticyclonic mid-water gyre of ~0.04 m s^{-1}. The time-averaged vertical circulation is characterised by the offshore flow of buoyant surface water and onshore flow of dense marine water, while a time-averaged horizontal anticyclonic gyre exists in the mid-water column as water flows in past Tuaheni Point, circles the bay and flows out past Young Nicks Head. The time-averaged anticyclonic gyre primarily results from the interaction between the prevailing north-northwest winds and the bathymetry, since the prevailing wind pushes more surface water toward the southern side and out past Young Nicks Head (at ~0.10 m s^{-1}) than past Tuaheni Point (~0.03 m s^{-1}). Additionally, the bay is deeper in the northern entrance and this is the preferred channel for bottom-return-flows, having time-averaged shoreward flow of ~0.05 m s^{-1}. Variation from typical time-averaged circulation occurred approximately 23% of the time, when downwelling was induced during times of onshore wind stress.

Barotropic forcing by the Waipaoa River began to exert dominance over forcing by wind-stress when the discharges reached 0.5% of the bay volume per day, the plume growing to ~30% of total bay volume through entrainment and diffusion. Embayments with similar freshwater discharge to total volume ratios are expected to also show strong river-induced circulation.

Numerical simulations showed that the bathymetric features having largest influence on circulation were the cross-shore seabed gradient and the shape of the headlands. Correct depth representation was more important to circulation modelling in the inner bay, where headland effects were minor or non-existent, whereas the headlands influenced currents closer to the bay entrance, particularly in the lower water column. Abrupt headlands favoured eddy formation inside

embayments. The cross-shore seabed gradient guided up- and downwelling currents, and thus provided an important control on the response of the mid and lower water column to surface-driven flow. The enclosed geometry of an embayment creates recirculation-favourable pressure gradients in comparison to islands, reefs and headlands and consequently recirculation occurs earlier. An embayment eddy parameter E was developed to predict the presence of shelf-current-driven embayment eddies.

Acknowledgements

This thesis is a big achievement and something I am proud of. Its completion involved perseverance and single-mindedness, particularly in the latter stages, but I was fortunate that my enthusiasm grew with its progress. There have been many enjoyable experiences and many beneficial spin-offs, and I've met numerous persons who have contributed in some way. I have many people to thank.

Thanks to Professor Terry Healy who set up and supervised the project, put faith in my ability and provided the study opportunity along with the consulting, travel, and teaching experience. Terry has fathered many graduates and has worked many hours to provide opportunity for others and I am just one to share the benefits. I am enormously indebted to my chief supervisor Professor Kerry Black, whose experience and guidance was paramount to this thesis. Kerry's enthusiasm and genuine interest in research is contagious and there were many times I trudged down to visit under the PhD burden, only to skip back with the praise-inspired revelation that I was achieving great heights. Kerry is the busiest person I know, but always made time to help me out. Thanks also to Kerry for involving me in small contracts that provided financial support and travel opportunities. Thanks to my third supervisor, Dr. Rob Bell of NIWA, who was generous with his time and off whom I learned much about continental-shelf processes.

Thank you to Dirk Immenga and Brett Beamsley, with whom I shared many hours on a boat and quite a few underwater, the assistance in the field was invaluable. Dirk prepares thoroughly and is someone to trust in dangerous situations. Thanks to Tony Dolphin for companionship in the office and assistance with lots of things. Port Gisborne Ltd. and Mr. Ben Tahata (General Manager) are thanked for generous field logistical support and conference support. Gary and Jandy Morton provided accommodation during the main field experiment. Dr. Willem de Lange was always helpful to answer questions and supply code. Dr.s Richard Gorman and Karin Bryan provided assistance with Matlab and spectral analysis routines.

Thanks to the Department of Earth Sciences and Roger Briggs (chairperson) for financial and logistic support. Thanks to Sydney Wright, Elaine Norton, Mike Vennard and Steve Bergin for running the department and always being 'here to help'. I enjoyed the friendship of many other staff and graduate students within the Department of Earth Sciences during my PhD.

Finally, a big thank you to Sharon, for support in lots of ways. Specifically, help in the field was vital and proof reading much appreciated. It is far easier to focus on a project when other things are taken care of, and this thesis really accelerated with Sharon around.

Table of Contents

ABSTRACT **5**

ACKNOWLEDGEMENTS **9**

TABLE OF CONTENTS **11**

LIST OF FIGURES **17**

LIST OF TABLES **25**

1 - INTRODUCTION AND THESIS DEVELOPMENT **27**

1.1 INTRODUCTION 27

1.2 STUDY BACKGROUND 31

1.2.1 Bathymetry *32*

1.2.2 Circulation on the east coast of the North Island *32*

1.2.3 Poverty Bay inferred barotropic circulation *34*

1.2.4 Stratification *34*

1.2.5 Wind-water interaction *35*

1.2.6 Tides *37*

1.2.7 Waves *37*

1.2.8 Wave driven currents *39*

1.2.9 Port Gisborne AEE investigation *40*

1.2.10 Knowledge shortfall *41*

1.3 AIMS AND OBJECTIVES 42

1.4 THESIS STRUCTURE 43

1.4.1 Chapter 2 - Shelf-current driven recirculation in a coastal bay: a two-dimensional numerical study *45*

1.4.2 Chapter 3 – Circulation Patterns in Poverty Bay, New Zealand, measured by Boat-Mounted Global Positioning System Interfaced, Acoustic Doppler Current Profiler *46*

1.4.3 Chapter 4 - Complex Circulation in a Coastal Embayment: Shelf-current, Wind and Density-Driven circulation in Poverty Bay, New Zealand *46*

1.4.4 Chapter 5 – Coastal-trapped waves on the east coast of the North Island, New Zealand *47*

1.4.5 Chapter 6 – wavelet analysis *47*

1.4.6 Chapter 7 – Three-dimensional numerical modelling of Poverty Bay *48*

1.4.7 Chapter 8 – Discussion *48*

1.4.8 Chapter 9 – Conclusions *48*

2 - SHELF-CURRENT DRIVEN RECIRCULATION IN A COASTAL BAY: A TWO-DIMENSIONAL NUMERICAL STUDY 50

2.1 CONTEXT OF THE PAPER WITHIN THE THESIS 50

2.2 INTRODUCTION 52

2.3 NUMERICAL MODEL, BOUNDARY CONDITIONS AND METHODS 53

2.4 RESULTS AND DISCUSSION 59

2.4.1 Bluff-body bathymetry *59*

2.4.2 Geometric effects *60*

2.4.3 Embayment eddy parameter *62*

2.4.4 Smooth bathymetry *65*

2.4.5 Reef effects *67*

2.4.6 Depth alterations *69*

2.5 CONCLUSIONS 70

2.6 ACKNOWLEDGEMENTS 71

2.7 REFERENCES 72

2.8 TABLES 75

2.9 FIGURES 78

3 - CIRCULATION PATTERNS IN POVERTY BAY, NEW ZEALAND MEASURED BY BOAT-MOUNTED GLOBAL POSITIONING INTERFACED ACOUSTIC DOPPLER CURRENT PROFILER 88

3.1 CONTEXT OF THE PAPER WITHIN THE THESIS 88

3.2 SUMMARY 89

3.3 INTRODUCTION 89

3.4 METHODS 90

3.5 RESULTS 92

3.5.1 Current Circulation in Poverty Bay: 2 Feb 1997, 7:40-10:45 92
3.5.2 Current Circulation in Poverty Bay: 1 Feb 1997, 15:40-19:00 92
3.5.3 Conductivity, Temperature, Depth 93
3.6 DISCUSSION AND CONCLUSIONS 94
3.7 RECOMMENDATIONS FOR FUTURE WORK 95
3.8 ACKNOWLEDGEMENTS 95
3.9 REFERENCES 96
3.10 FIGURES 97

4 - COMPLEX CIRCULATION IN A COASTAL EMBAYMENT: SHELF-CURRENT, WIND AND DENSITY-DRIVEN CIRCULATION IN POVERTY BAY, NEW ZEALAND 102

4.1 CONTEXT OF THE PAPER WITHIN THE THESIS 102
4.2 ABSTRACT 103
4.3 INTRODUCTION 104
4.4 DATA ACQUISITION, PREPARATION AND PRELIMINARY OBSERVATIONS . 105
4.5 RESULTS 108
4.5.1 Continental-Shelf-currents 108
4.5.2 ADP and CTD Surveys 110
4.6 DISCUSSION 111
4.6.1 Shelf-currents 111
4.6.2 Plume-Driven Circulation 114
4.6.3 Wind-Driven Circulation 119
4.6.4 Transport Implications 122
4.7 CONCLUSIONS 123
4.8 ACKNOWLEDGEMENTS 125
4.9 LITERATURE CITED 126
4.10 TABLES 130
4.11 FIGURES 133

5 - COASTAL-TRAPPED WAVES ON THE EAST COAST OF THE NORTH ISLAND, NEW ZEALAND 144

5.1 CONTEXT OF THE PAPER WITHIN THE THESIS 144
5.2 INTRODUCTION 145
5.3 METHODS 147

5.4 RESULTS 152
5.4.1 Time-Domain Data Analyses: Cross-Correlation and Linear Regression 152
5.4.2 Numerical Simulations 153
5.5 DISCUSSION 154
5.6 CONCLUSIONS 156
5.7 RECOMMENDATIONS FOR FUTURE WORK 157
5.8 ACKNOWLEDGEMENTS 157
5.9 REFERENCES 158
5.10 TABLES 161
5.11 FIGURES 164

6 - WAVELET ANALYSIS OF THE WIND-CURRENT RELATIONSHIP 171

6.1 INTRODUCTION 171
6.2 METHODS 172
6.3 RESULTS AND DISCUSSION 174
6.4 CONCLUSIONS 178
6.5 ACKNOWLEDGEMENTS 178
6.6 FIGURES 179

7 - THREE-DIMENSIONAL SIMULATION OF POVERTY BAY 187

7.1 INTRODUCTION 187
7.2 METHODS 187
7.2.1 Model Bathymetry 188
7.2.2 Body-force 190
7.2.3 Ocean boundaries 194
7.2.4 River discharge 194
7.2.5 Wind input 197
7.2.6 Seabed friction 198
7.2.7 Stratification and model type 199
7.2.8 Model layers 203
7.2.9 Horizontal eddy viscosity 204
7.2.10 Vertical eddy viscosity 204
7.3 RESULTS AND DISCUSSION 206

7.3.1 *Model calibration* 206
7.3.2 *Body-force only* 225
7.3.3 *No shelf-current* 226
7.3.4 *River Only* 230
7.3.5 *Wind Only* 239
7.3.6 *Wind-induced circulation patterns* 244
7.3.7 *Floods* 253
7.3.8 *Wind-influence versus river-influence* 257
7.3.9 *Eddies* 260
7.3.10 *Bathymetric effects* 262
7.4 CONCLUSIONS 274
7.5 FUTURE WORK 275
7.6 ACKNOWLEDGEMENTS 276

8 - DISCUSSION 277

8.1 INTRODUCTION 277
8.2 CIRCULATION IN POVERTY BAY 277
8.3 IMPLICATIONS FOR OUTFALL EFFLUENT, LOBSTER RECRUITMENT AND AQUACULTURE DEVELOPMENTS 288
8.4 CONCLUSIONS 291
8.5 FIGURES 292

9 – CONCLUSIONS 297

9.1 INTRODUCTION 297
9.2 SPECIFIC THESIS AIMS 297
9.2.1 *Specific thesis aim 1 – the interplay between bathymetry and hydrodynamics* 297
9.2.2 *Specific thesis aim 2 – investigate continental-shelf-currents and their role in Poverty Bay* 298
9.2.3 *Specific thesis aim 3 – gather data of sufficient spatial coverage and quality to calibrate Model 3DD* 299
9.2.4 *Specific thesis aim 4 – investigate the balance between wind and river-induced hydrodynamics* 300
9.2.5 *Specific thesis aim 5- re-investigate the mechanisms responsible for the observed time-averaged anticyclonic horizontal gyre* 302

9.3 IMPLICATIONS FOR OTHER COASTAL EMBAYMENTS 302

BIBLIOGRAPHY.....305

APPENDIX 1 - CTD COUNTOURS 2 FEB 1997.....317

APPENDIX 2 - MODEL 3DD EQUATIONS AND CONSTANTS.....321

APPENDIX 3 - BODY-FORCE MATLAB SCRIPT.....327

List of Figures

Figure 1-1. Bathymetric map of Poverty Bay and the adjacent continental-shelf, with the location of Poverty Bay shown in inset. 30
Figure 1-2. Poverty Bay showing rivers, bathymetric contours, headlands and associated reefs, city and sewage outfall. 31
Figure 1-3. Oceanic circulation patterns around New Zealand, after National Institute of Water and Atmospheric Research (1997). Explanation of abbreviations referred to in text are: EAUC – East Auckland Current, ECC – East Cape Current, SC – Southland Current, DC – D'Urville Current. The Wairarapa Coastal Current is not marked but can be seen flowing northward inshore of the East Cape Current. 33
Figure 1-4. Gisborne airport wind rose from 86,046 hourly recordings, beginning 01:00, 1 January 1988 until 11:00, 8 August 1999. Data supplied by NIWA. Rick Liefting of NIWA wrote the wind-rose Matlab™ plotting routine. 36
Figure 1-5. The port area, showing Waikanae and Kaiti Beaches, Butlers Wall, the historical dredge disposal ground, and bathymetric contours. 39
Figure 2-1. Location map of Poverty Bay, New Zealand showing bathymetric contours and the S4 current-meter location (see Figure 2-4). 78
Figure 2-2. A) Circulation and salinity in Poverty Bay measured by vessel-mounted acoustic Doppler profiler and CTD probe: A) at 10 m depth on 17 September 1998, B) at 5 m depth on 19 September 1998. 78
Figure 2-3. Model grids used for simulations: (a) bluff-body; (b) smooth. 79
Figure 2-4. Measured tidal and residual current components at S4 (2) deployment site (Figure 2-1). The S4DW was deployed on the continental-shelf, approximately 24 m above the bed in 35 m water depth, six kilometres outside the Poverty Bay entrance. Shelf-current velocities range from 0.003-0.36 m s^{-1}. 79
Figure 2-5. Circulation over the bluff-body grid induced by a shelf-current with velocity described by $0.2\ cos[(2\pi/172800)\ t]$ m s^{-1}, positive to the east, time-averaged between 172800-518400 s (two cycles): (a) Full model grid, showing marked boundary for close up plots; (b) close up view of (a), revealing dominance of anticyclonic eddy when Coriolis is included; (c) close up view of bay showing equal-sized residual eddies when Coriolis is removed from the simulation. 80
Figure 2-6. Circulation in the bluff-body bay after 48 hours of steady 0.3 m s^{-1} shelf-current flow. Flow separation at the upstream headland has created a clearly defined wake, and weak (~0.01 m s^{-1}) recirculation is evident. L is the cross-shore embayment length scale, w is the embayment width. 80
Figure 2-7. Circulation in the bluff-body bay after 48 hours of steady 0.3 m s^{-1} shelf-current flow: (a) inertia carries the free-stream current past the upstream headland, causing flow separation and creating a wake, sea-level is set down in the wake adjacent to the free-stream due to horizontal shear entrainment; (b) on decreasing A_H to 0.001 $m^2 s^{-1}$, horizontal shear entrainment into the free-stream ceases and the set down disappears. In both simulations, sea-level set-down is induced at the downstream coast, by currents accelerating from the bay onto the continental-shelf (Bernoulli effect). Vectors indicate velocity and shading indicates sea-level in metres, as per the given scale. 81
Figure 2-8. Circulation in three bluff-body bathymetries after 48 hours of steady 0.3 m s^{-1} shelf-current flow, shown zoomed over the grid area I = 33:50, J = 33:58: (a) the existing bluff-body bay (Figure 2-3a) was modified to incorporate a flat seabed; (b) an embayment of twice the horizontal dimensions was created by extending the original grid from 50 to 70 cells in the J direction; (c) a step bathymetry was created with the same land-sea extent as the original bay but with no downstream coast; (d) sea-level measured over an alongshore transect through J = 36 for the three bathymetries. Vectors indicate velocity and shading indicates sea-level in metres, as per the given scale. 82
Figure 2-9. (a) Change in P (dP) versus embayment width, non-dimensionalised using L (w/L), for continental-shelf/embayment depths of 27 and 10 m; (b) $dP \times L^2/h^2$ versus w/L. Continental-shelf and embayment depth has been accounted for by multiplying dP by the dimensionless parameter L^2/h^2. 83
Figure 2-10. $dP \times L^2/h^2$ versus w/L, incorporating data using varying L. The fitted power curve relationship has an adjusted r^2 = 0.970. 83

Figure 2-11. Velocity field (vector) and bathymetry (shading in m) over the smooth bathymetry (Figure 2-3b), induced by 48 hours of steady 2 m s^{-1} shelf-current flow. No recirculation is evident. Note high frictional damping over the shallow inshore area.....84
Figure 2-12. Velocity field (vector) and sea-level (shading in m) induced by a shelf-current with velocity described by *0.2 cos[(2π/172800) t]* m s^{-1}, positive to the east: (a) at 66 hours during flow deceleration, pressure gradients oppose the initial free-stream current direction, and due to higher frictional influence, the shallow water currents are weak creating a cross-shore velocity gradient; (b) at 70 hours sea-level pressure gradients have overcome the slow inshore currents to form a phase eddy. 84
Figure 2-13. Flow field induced over smooth bathymetry (Figure 2-3b) by a shelf-current with velocity described by *0.2 cos[(2π/172800) t]* m s^{-1}, positive to the east: (a) velocity vector, time-averaged between 172800-518400 s (two cycles) and bathymetry (contour) with z_0 raised from 0.001-0.1 m over marked reef area (cells *I = 52:56, J = 30:42*); (b) velocity (vector) and pressure gradient (contour) during accelerating current at 54 hours; 85
Figure 2-14. Time-averaged velocity (vector) and bathymetry (contour) over the smooth grid with a 5 m high reef added, induced by a shelf-current with velocity described by *0.2 cos[(2π/172800) t]* m s^{-1}, positive to the east (time-averaged between 172800-518400 s, two cycles).....85
Figure 2-15. Time-averaged velocity (vector) and bathymetry (contour) over the smooth grid with A_H raised from 1-10 m^2 s^{-1} over marked reef area, induced by a shelf-current with velocity described by *0.2 cos[(2π/172800) t]* m s^{-1}, positive to the east (time-averaged between 172800-518400 s, two cycles).....86
Figure 2-16. Circulation over the smooth grid induced by a shelf-current with velocity described by *0.2 cos[(2π/172800) t]* m s^{-1}, positive to the east, time-averaged between 172800-518400 s (two cycles): (a) the eastern outer margin of the bay has been deepened by subtracting 4 m from grid cells *I = 46:52, J = 36:42*; (b) original smooth bathymetry (Figure 2-3b). 86
Figure 3-1. Coastline of Poverty Bay, New Zealand.....97
Figure 3-2. Currents measured by downward facing, boat mounted ADP, 1 February 1997, Poverty Bay, New Zealand. 98
Figure 3-3. Currents measured by downward facing, boat mounted ADP, 2 February 1997, Poverty Bay, New Zealand. 98
Figure 3-4. Salinity in Poverty Bay, 1 February 1997, 15:40-19:00. The scale on the upper right graph applies to all graphs. 99
Figure 3-5. Temperature in Poverty Bay, 1 February 1997, 15:40-19:00, showing evidence of thermal heating of surface waters throughout the day. The scale on the upper right graph applies to all graphs. 99
Figure 3-6. Temperature in Poverty Bay, 2 February 1997, 7:10-10:45. The scale on the upper right graph applies to all graphs.....100
Figure 3-7. Salinity in Poverty Bay, 2 February 1997, 7:10-10:45. The scale on the upper right graph applies to all graphs. 100
Figure 4-1. Poverty Bay location and bathymetry, showing sites of ADP (during Deployment-A) and S4 current-meters. 133
Figure 4-2. Gisborne airport wind rose from 86,046 hourly recordings, beginning 01:00, 1 January 1988 until 11:00, 8 August 1999. 134
Figure 4-3. Progressive vector plots for S4 current-meter deployments GT (mid-water-column) and GB (near-bed), 9 September to 23 October 1998. Tidal currents have little or no net transport. 135
Figure 4-4. Wind at Gisborne Airport (directions inverted to true vectors convention), and residual current velocity at current-meters GT and GB. Wind and currents have been bolded at times coinciding with ADP surveys. True north is in the vertical direction.....136
Figure 4-5. River discharge into Poverty Bay during the study period, 10 October – 23 September 1998. The Waimata River is the main tributary of the Turanganui River that discharges adjacent to Port Gisborne. An estimate of the Turanganui River discharge is shown based on Waimata River discharge, scaled to approximately one sixth of the Waipaoa River (Gorman et al., 1997). 136
Figure 4-6. Velocity and water density anomaly (-1000) measured by vessel-mounted real-time ADP and CTD, 8:54-15:21, 17 September 1998. Wind was northerly < 2 m s^{-1} (Figure 4-4). Depths are relative to lowest astronomical tide. CTD cast sites A, B and C (refer Figure 4-12) are marked on plots a and d.....137

Figure 4-7. Velocity and water density anomaly (-1000) measured by vessel-mounted real-time ADP and CTD, 13:50-15:54, 15 September 1998, under northerly wind of > 5 m s^{-1} (Figure 4-4). Depths are relative to lowest astronomical tide. 138
Figure 4-8. Velocity and water density anomaly (-1000) measured by bottom-mounted ADP and CTD, 7:25-11:52, 28 September 1998. Wind was southerly 3-4 m s^{-1} (Figure 4-4). Depths are relative to lowest astronomical tide. 139
Figure 4-9. Velocity and water density anomaly (-1000) measured by vessel-mounted real-time ADP and CTD, 7:59-15:21, 19 September 1998. The left-hand plots relate to the morning during an offshore breeze (< 3 m s^{-1}), while plots on the right relate to early afternoon during a southeast sea breeze of ~ 3 m s^{-1}. Densities relate to CTD casts spanning morning and afternoon, and are identical in both left and right-hand plots. Depths are relative to lowest astronomical tide. 140
Figure 4-10. Feather plots of hourly wind and current, over the duration of ADP bottom-mounted Deployment-A, 12:00, 28 September – 08:00, 29 September, 1998. Wind velocities have been inverted to true vectors convention. Speed magnitudes at 16 m elevation are overestimated due to acoustic interference with the water surface, but nonetheless are in close directional agreement with wind. True north is vertically up the page. 141
Figure 4-11. Rotary spectra of residual currents at GT (mid-water) and GB (near-bed). 142
Figure 4-12. Vertical density profiles A, B and C at distances 3000, 4300 and 7500 m respectively from the Waipaoa River, as measured from CTD casts taken at sites A, B and C (Figure 4-6a,d), on 17 September. The horizontal dashed line represents the approximate river plume depth. 142
Figure 5-1. Map of New Zealand, the model grid boundary (orientated 35°T), and the 200 m isobath representing the continental shelf. An ⊕ marks data collection station sites, refer to Table 5-1 for full meaning of abbreviations. 164
Figure 5-2. Band filtered (0.033 – 0.6 cpd) data. The vertical direction corresponds to the up-coast (north) direction for directional (wind and current) data, and to positive sea-level. Units for wind stress (W_B, W_C and W_G) are N m^{-2}, units for current (V_t and V_b) are cm s^{-1}, and units for sea-level (η_W, η_R and η_G) are mm. Refer to Table 5-1 for explanation of abbreviations. 165
Figure 5-3. Model grid used for simulation of wind generated CTWs (simulations SIM1, SIM2 and SIM3). Input sites for winds measured at W_B, W_C and W_G are marked by +, × and * respectively. Colour shading indicates bathymetry depth. 166
Figure 5-4. Raw time-series and cross-correlogram between low-pass-filtered real and simulated (SIM1) sea-level at Wellington Harbour (η_W). The correlation coefficient is 0.97 at lag 0, well above significance levels indicated by the horizontal dashed line. 167
Figure 5-5. Raw time-series and cross-correlogram between low-pass-filtered real and simulated (SIM1) sea-level at Riversdale (η_R). The correlation coefficient is 0.63 at lag 2, well above significance levels indicated by the horizontal dashed line. 168
Figure 5-6. a) Gisborne real and simulated (SIM1, SIM2 and SIM3) low-pass-filtered sea-level (simulated data are multiplied by 3 for clarity) and b) cross-correlogram between real and simulated data. The correlation coefficient and lags for simulations SIM1, SIM2 and SIM3 are 0.48, 0.46, 0.33 and 9-, 18-, 23-hour lags respectively. 169
Figure 6-1. A wavelet analysis example: A) cross-power contour map, B) power contour map of Signal 2, C) Signal 2 time-series, D) power contour map of Signal 1, E) Signal 1 time-series. Signal 1 = 0.1 $\sin(2\pi/64 \times t)$ and Signal 2 = (5 × Signal 1 + 10 $\sin(2\pi/128 \times t)$). 173
Figure 6-2. Wavelet analysis of the alongshore mid-water (GT) current component (time-series in plots E) and the alongshore wind component (time-series in plots C), for equivalent Fourier periods 2-512 hours, showing the cross-power in plots A. Plot 1 uses raw wind speed to compute the wavelet transform, while plot 2 uses wind stress calculated by the method of Wu (1982). 175
Figure 6-3. Auto-spectrum of Gisborne Airport wind along its principle axis 334/154°T. The spectrum contains 102036 hourly records from 1/1/88 – 22/8/99. Dashed lines show 95% confidence intervals. 177
Figure 6-4. Wavelet analysis of the alongshore mid-water (GT) current component (time-series in plot E) and the alongshore wind component (time-series in plot C), for equivalent Fourier periods 2-512 hours, showing the cross-power in plot A. 179
Figure 6-5. Wavelet analysis of the cross-shore mid-water (GT) current component (time-series in plot E) and the alongshore wind component (time-series in plot C), for equivalent Fourier periods 2-512 hours, showing the cross-power in plot A. 179

Figure 6-6. Wavelet analysis of the alongshore mid-water (GT) current component (time-series in plot E) and the cross-shore wind component (time-series in plot C), for equivalent Fourier periods 2-512 hours, showing the cross-power in plot A. 180
Figure 6-7. Wavelet analysis of the cross-shore mid-water (GT) current component (time-series in plot E) and the cross-shore wind component (time-series in plot C), for equivalent Fourier periods 2-512 hours, showing the cross-power in plot A. 180
Figure 6-8. Wavelet analysis of the alongshore near-bed (GB) current component (time-series in plot E) and the alongshore wind component (time-series in plot C), for equivalent Fourier periods 2-512 hours, showing the cross-power in plot A. 181
Figure 6-9. Wavelet analysis of the cross-shore near-bed (GB) current component (time-series in plot E) and the alongshore wind component (time-series in plot C), for equivalent Fourier periods 2-512 hours, showing the cross-power in plot A. 181
Figure 6-10. Wavelet analysis of the alongshore near-bed (GB) current component (time-series in plot E) and the cross-shore wind component (time-series in plot C), for equivalent Fourier periods 2-512 hours, showing the cross-power in plot A. 182
Figure 6-11. Wavelet analysis of the cross-shore near-bed (GB) current component (time-series in plot E) and the cross-shore wind component (time-series in plot C), for equivalent Fourier periods 2-512 hours, showing the cross-power in plot A. 182
Figure 6-12. Wavelet analysis of the alongshore mid-water (GT) current component (time-series in plot E) and the alongshore wind component (time-series in plot C), for equivalent Fourier periods 2-32 hours, showing the cross-power in plot A. 183
Figure 6-13. Wavelet analysis of the cross-shore mid-water (GT) current component (time-series in plot E) and the alongshore wind component (time-series in plot C), for equivalent Fourier periods 2-32 hours, showing the cross-power in plot A. 183
Figure 6-14. Wavelet analysis of the alongshore mid-water (GT) current component (time-series in plot E) and the cross-shore wind component (time-series in plot C), for equivalent Fourier periods 2-32 hours, showing the cross-power in plot A. 184
Figure 6-15. Wavelet analysis of the cross-shore mid-water (GT) current component (time-series in plot E) and the cross-shore wind component (time-series in plot C), for equivalent Fourier periods 2-32 hours, showing the cross-power in plot A. 184
Figure 6-16. Wavelet analysis of the alongshore near-bed (GB) current component (time-series in plot E) and the alongshore wind component (time-series in plot C), for equivalent Fourier periods 2-32 hours, showing the cross-power in plot A. 185
Figure 6-17. Wavelet analysis of the cross-shore near-bed (GB) current component (time-series in plot E) and the alongshore wind component (time-series in plot C), for equivalent Fourier periods 2-32 hours, showing the cross-power in plot A. 185
Figure 6-18. Wavelet analysis of the alongshore near-bed (GB) current component (time-series in plot E) and the cross-shore wind component (time-series in plot C), for equivalent Fourier periods 2-32 hours, showing the cross-power in plot A. 186
Figure 6-19. Wavelet analysis of the cross-shore near-bed (GB) current component (time-series in plot E) and the cross-shore wind component (time-series in plot C), for equivalent Fourier periods 2-32 hours, showing the cross-power in plot A. 186
Figure 7-1. Extent of the Poverty Bay hydrodynamic model grid, including the location of boundary data sources: the S4 current-meters, Gisborne Airport and rivers. 189
Figure 7-2. Poverty Bay 400 m bathymetry grid, used for hydrodynamic simulations, showing S4 deployment site (+). 190
Figure 7-3. Comparison between measured and simulated depth-averaged shelf-current, using just the body-force to drive the model. 194
Figure 7-4. The relationship between Waipaoa River discharge and velocity, from 587 gaugings undertaken since 1967: velocity = $0.3048 \times \text{discharge}^{0.2867}$. 195
Figure 7-5. River flow during the simulation period, dashed line is discharge measured at the up-river gauging station, light solid line is discharge delayed 15 hours and heavy solid line is discharge used in calibrated simulations (delayed 15 hours and multiplied by 1.5). 196
Figure 7-6. Wind recorded at Gisborne Aero during the simulation period, shown in true vectors convention and rotated +36° to match model grid orientation. 198
Figure 7-7. Temperature on the continental-shelf during the simulation period, at the current-meter locations GT (mid-water) and GB (near-bed). 200
Figure 7-8. Density, salinity and temperature at 1 m depth, 15 September 1998, showing the dominance of salinity on density distribution. 201
Figure 7-9. Density, salinity and temperature at 1 m depth, 19 September 1998. 202

Figure 7-10. Continental-shelf-currents rotated +36° to match model grid orientation. GT is mid-water, GB is near-bed and AV is the mean. 203
Figure 7-11. Measured data (left) compared with model output averaged over the time corresponding to the survey (right). Velocity vectors were measured using vessel-mounted ADP. Salinity and velocity patterns are generally well predicted but current magnitudes are under-predicted..... 213
Figure 7-12. Measured data on 15th September 1998, compared with model output from the calibration simulation averaged over the time corresponding to the survey. Velocity vectors were measured using vessel-mounted ADP. 215
Figure 7-13. Measured data on 17th September 1998, compared with model output from the calibration simulation averaged over the time corresponding to the survey. Velocity vectors were measured using vessel-mounted ADP. 217
Figure 7-14. Measured data on 19th September 1998, compared with model output from the calibration simulation averaged over the time corresponding to the survey. Velocity vectors were measured using vessel-mounted ADP, morning data shown in black (offshore wind), afternoon data shown in white (onshore wind)..... 219
Figure 7-15. Measured data on 26th September 1998, compared with model output from the calibration simulation averaged over the time corresponding to the survey. Velocity vectors were measured using bottom-mounted ADP; therefore data are only available within the instruments 15 m range from the seabed. 221
Figure 7-16. Measured data on 28th September 1998, compared with model output from the calibration simulation averaged over the time corresponding to the survey. Velocity vectors were measured using bottom-mounted ADP; therefore data are only available within the instruments 15 m range from the seabed. 223
Figure 7-17. Feather plots of hourly wind and current, over the duration of ADP bottom-mounted Deployment-A, 12:00, 28 September – 08:00, 29 September, 1998. Wind velocities have been inverted to true vectors convention. Speed values at 16 m elevation are unreliable due to acoustic interference with the water surface, but nonetheless are in close directional agreement with wind. 224
Figure 7-18. Model predicted currents at the ADP deployment A site 12:00, 28 September – 08:00, 29 September, 1998..... 224
Figure 7-19. Model output in layer 3 (4-6 m) at times coinciding with data surveys, using only the body-force as input. Since the body-force acceleration is applied uniformly to all vertical layers in the model, circulation in other layers is very close to that shown for layer 3..... 226
Figure 7-20. Model output coincident with the 17th September field survey, using wind and river discharge to force the model, and no body-force. 228
Figure 7-21. Comparison between measured data (top), the calibration simulation (middle) and simulation using only wind and river discharge as boundary conditions (bottom) at 6-9 m depth (left) and 9-12 m depth (right), 28th September 1998. 229
Figure 7-22. Model output using a shelf-current velocity boundary in place of the body-force. Plots on the left use measured shelf-current, while plots on the right use shelf-current multiplied by 5. Upper plots correspond to 59-hours and lower plots to 206-hours. Right-hand plots show that fast shelf-currents induce eddies..... 230
Figure 7-23. Model output coincident with the 17th September field survey, with Waipaoa and Turanganui River discharge the only boundary condition..... 235
Figure 7-24. Model output in layer k = 3 (4-6 m depth) at times coincident with field survey data, with Waipaoa and Turanganui River discharge the only boundary condition..... 236
Figure 7-25. Mean river-induced circulation over the simulation period..... 237
Figure 7-26. Mean river-induced circulation over the simulation period, with rotation effects not included. 238
Figure 7-27. Circulation in layer 1 (near-surface) coincident with the 28th September field survey: A) calibration simulation, B) model is forced by wind only. Note that surface velocities are reduced in B. 242
Figure 7-28. Mean wind-induced circulation in model layer 3 (4-6 m), the simulation includes wind stress as the only forcing mechanism (no stratification)..... 242
Figure 7-29. Mean wind-induced circulation over the simulation period, with rotation effects not included. 243
Figure 7-30. Poverty Bay model bathymetry showing the location of vertical cross-sections incorporated in Figure 7-32 and Figure 7-33..... 249
Figure 7-31. Velocity vector and sea-level contour coinciding with an onshore wind period at 52 hours in the calibration simulation. 249

Figure 7-32. Model output from the calibration simulation, coincident with 15th September field survey during offshore winds of > 5 m s^{-1}. Figure 7-30 gives *I* and *J* transect locations....250
Figure 7-33. Model output from the calibration simulation at 438 hours, following the 28th September field survey (428-431 hours) when winds had been onshore for 18 hours (Figure 7-6). 251
Figure 7-34. Time-averaged circulation and salinity in Poverty Bay during the calibration simulation. 252
Figure 7-35. Waipaoa River discharge: A) discharge history (contains gaps), B) flood discharge used for flood simulation (peak = 1079 m^3 s^{-1})....255
Figure 7-36. Flood simulation of the Waipaoa River 26/7/94 storm (Figure 7-35, B), shown at time coinciding with peak 1079 m^3 s^{-1} discharge. River discharge is the only forcing used in the simulation. 256
Figure 7-37. Simulation results showing: 1) the relationship between southerly wind speed and the time and discharge required to induce anticyclonic circulation, 2) the relationship between receding flood discharge and the southerly wind speed required to steer the entire discharging plume along the coast toward the port....259
Figure 7-38. Transient eddy formation adjacent to Tuaheni Point during the model calibration simulation. The steady-state eddy shown existed for over 11 hours, during onshore wind conditions. 261
Figure 7-39. Transient eddy formation adjacent to Young Nicks Head during the model calibration simulation. The phase eddy shown formed during a wind shift from on to offshore and existed for 2 hours. Note the general hydrodynamic variability. 262
Figure 7-40. Plan view of simple bluff-body bathymetry, depth contours shown by dotted lines. 267
Figure 7-41. Plan view of simple smooth bathymetry, depth contours shown by dotted lines. ...268
Figure 7-42. Plan view of simple bluff-body bathymetry: A) of constant 15 m depth, B) with sloping bay seabed and projecting east point....268
Figure 7-43. Model calibration simulation (left) compared with a similar simulation (right), but using a simple bluff-body bathymetry (Figure 7-40), at time coincident with the 17 September 1998 field survey during offshore winds. 269
Figure 7-44. Model calibration simulation (left) compared with a similar simulation (right), but using a simple bluff-body bathymetry (Figure 7-40), at time coincident with the 28 September 1998 field survey during offshore winds. 270
Figure 7-45. Model calibration simulation (left) compared with a similar simulation (right), but using a simple bluff-body bathymetry of constant 15 m depth (Figure 7-42), at time coincident with the 17 September 1998 field survey during offshore winds. 271
Figure 7-46. Time averaged cross-shore vertical sections through the water column: A) calibration simulation, B) bluff-body with sloping seabed, C) bluff-body with flat seabed....272
Figure 7-47. Model simulations at 50 hours using calibrated real forcing data, when continental-shelf-currents exhibit swift (~0.2 m s^{-1}) southwest flow past Tuaheni Point: A) calibration simulation, B) bluff-body bathymetry (experiment 1, Table 7-4), C) bluff-body bathymetry modified to include a projecting point (experiment 3, Table 7-4). 273
Figure 7-48. Circulation at 5 m depth in the simple smooth bathymetry (experiment 5, Table 7-4, Figure 7-41): A) during offshore winds on 17 September 1998, B) during onshore winds on 28 September 1998. 273
Figure 8-1. Three-dimensional shaded surface plot of Poverty Bay, showing typical circulation under *offshore* winds. Surface water migration is marked in red and bottom water migration in blue. River plumes are depicted in green....292
Figure 8-2. Three-dimensional shaded surface plot of Poverty Bay, showing typical circulation under *onshore* winds. Surface water migration is marked in red and bottom water migration in blue. River plumes are depicted in green....292
Figure 8-3. Three-dimensional shaded surface plot of Poverty Bay, showing typical circulation during high-discharge from the Waipaoa River. Surface water migration is marked in red and near-bed water migration in blue. The river plume is depicted in green....293
Figure 8-4. Three-dimensional shaded surface plot of a bluff-body embayment bathymetry (Figure 7-42a), depicting a steady-velocity continental-shelf-current turning into the embayment (blue arrows), embayment water entrained into the shelf-current from behind the upstream headland (small red arrows), sea surface elevation in the embayment showing set-up against the downstream coast and set-down in the upstream headland lee due to horizontal shear entrainment (green), and surface return-flow (large red arrow). 293
Figure 8-5. Three-dimensional shaded surface plot of a smooth embayment bathymetry (Figure 7-41), depicting an accelerating continental-shelf-current (blue arrows) sea surface elevation

at the coast (green) and surface water flow in the smooth embayment (red arrow). No eddy forms in this situation. 294
Figure 8-6. Three-dimensional shaded surface plot of a smooth embayment bathymetry (Figure 7-41), depicting a deccelerating continental-shelf-current (blue arrows) sea surface elevation at the coast (green) and surface water flow in the smooth embayment (red arrows). Eddy formation occurs due to favourable sea-surface pressure-gradients induced by the decelerating shelf-current. 295
Figure 8-7. Three-dimensional shaded surface plot of Poverty Bay, depicting a south-westerly continental-shelf-current forming an eddy adjacent to Tuaheni Point, and a north-easterly shelf-current flowing into Poverty Bay. 295
Figure A-9-1. Density (top), salinity (middle) and temperature (lower) at 1 m (left) and 2 m (right) depth in Poverty Bay, 2 February 1997. 317
Figure A-9-2. Density (top), salinity (middle) and temperature (lower) at 5 m (left) and 10 m (right) depth in Poverty Bay, 2 February 1997. 318
Figure A-9-3. Waipaoa River discharge leading up to the 2 February CTD survey. River discharges were less than 10 $m^3 s^{-1}$ for 12 days prior to the survey. 319

List of Tables

Table 2-1. List of numerical experiments described in text. Bluff bathymetries are based on Figure 2-3a while smooth bathymetries are based on Figure 2-3b. Parameters included in the table are: experiment identification number, embayment bathymetry type, additional simulation features, embayment width (w), embayment cross-shore extent (L), horizontal eddy viscosity (A_H), continental-shelf-current velocity (U), and flow regime – either steady or unsteady. Unless otherwise specified (eg. Table 2-2 & Table 2-3), all experiments included depth h = 27 m, roughness length z_0 = 0.001 m and unsteady flow regimes had a cycle period T = 48 hours. 75

Table 2-2. Quantification of the change in P (Equation 4) resulting from recirculation-favourable pressure gradients in the presence of a downstream coast (coastal embayment). Parameters included in the table are: description of bathymetry type, embayment width (w), embayment cross-shore extent (L), vertical eddy viscosity (A_Z), embayment width non-dimensionalised by cross-shore embayment extent (w/L), velocity of initial recirculation (U), island wake parameter P (calculated for both step and bay), equivalent embayment wake parameter (P_0), change in P (dP) and $dP \times L^2/h^2$ 76

Table 2-3. Quantification of the change in P (Equation 4) resulting from recirculation-favourable pressure gradients in the presence of a downstream coast (coastal embayment). Parameters included in the table are: description of bathymetry type, embayment width (w), embayment cross-shore extent (L), vertical eddy viscosity (A_Z), embayment width non-dimensionalised by cross-shore embayment extent (w/L), velocity of initial recirculation (U), island wake parameter P (calculated for both step and bay), equivalent embayment wake parameter (P_0), change in P (dP) and $dP \times L^2/h^2$ 77

Table 4-1. Mean wind speed and direction at Gisborne Airport, 1988-1998. 130

Table 4-2. Current speed statistics for S4DW current-meter, 24 m above seabed (GT) and S4 current-meter, 2 m above seabed (GB), deployed at latitude -38° 46.43', longitude 178° 03.87', 9 September to 23 October 1998. Measured refers to *in-situ* measurement, predicted refers to tidal currents "predicted" by harmonic analysis (Foreman, 1978) and residual refers to non-tidal component. 130

Table 4-3. Frequency, period, phase and time-shift of wind and current data coherent at the 95% significance level, in the range T = 2.5-24 hours. Positive phase and time-shift indicates that wind leads current, and *vice versa*. 131

Table 4-4. Frequency, period, phase and time-shift of *current* data coherent at the 95% significance level, in the range T = 2.5-24 hours. Positive phase and time-shift indicates that GT leads GB, and *vice versa*. 131

Table 4-5. Observed Poverty Bay circulation during ADP surveys, along with corresponding wind and shelf-current conditions. Up-coast and Down-coast refer to southwest and northeast flowing currents respectively. 132

Table 5-1. Recording station abbreviations for current, sea-level and wind data, including the chosen alongshore direction. 161

Table 5-2. Wind, current and sea-level, multi-linear regression analysis. $Y = aX_1 + bX_2 + c$, where Y = bolded variable, X_1 = A (alongshore component) and X_2 = C (cross-shore component). Prior to performing linear regression, data were aligned according to the shown lag. Lags were determined through cross-correlation in the time-domain, and refer to the lead of the bolded variable (Δt = 12-hours) 162

Table 5-3. Measured sea-level variance as a percentage of measured η_G variance. 163

Table 5-4. Cross-correlation results between real and simulated sea-levels. 163

Table 5-5. Predicted sea-level variance as a percentage of predicted $s\eta_W$ variance. 163

Table 7-1. Waipaoa River *discharge*, *velocity* and *time lag* from gauging station to bay, for the 486 hour model simulation window. 197

Table 7-2. Model vertical layer description 204

Table 7-3. Onshore wind periods and associated circulation patterns during the calibration simulation. 248

Table 7-4. Index of simple bathymetries used in simulations with calibration data 267

1 - Introduction and thesis development

1.1 INTRODUCTION

Poverty Bay is a coastal embayment located on the northeast coast of the North Island, New Zealand (Figure 1-1). Like numerous other coastal embayments worldwide, Poverty Bay is prized for its sheltered coastal environment. On the coast in the north of the bay is a small export port and the city of Gisborne (Figure 1-2) with its associated coastal environmental issues, such as the current practise of raw sewage discharge into the bay. Best practical management of such issues requires knowledge of circulation in the bay and the hydrodynamic driving processes. Scientific investigations associated with development of Port Gisborne have supplied much of the present hydrodynamic database (Williams, 1966; Miller, 1981; Bell, 1985; Kensington, 1990; Gorman et al., 1997; Black et al., 1997 and Stephens et al., 1997). These studies have shown that Poverty Bay possesses a complex hydrodynamic system. The wide entrance to Poverty Bay leaves it exposed to wave activity from the east and southeast, and provides opportunity for the bay to interact with shelf-currents and coastal-trapped-waves. River discharge creates stratification and supplies large volumes of sediment, and the bay is exposed to strong episodic winds from the southeast.

The proposed redevelopment of Port Gisborne to accommodate burgeoning East Cape forestry exports saw the commissioning of a large scientific investigation in 1996. The investigation was designed to assess the best options for port redevelopment and the likely environmental effects of that development, and to provide a scientific basis for the production of an Assessment of Environmental Effects (AEE) (Turnpenny et al., 1998). This involved investigations of the flora and fauna inhabiting the bay, port and nearby rocky reefs (Cole et al., 1997), sediment characteristics of the bay and port environs (Beamsley et al., 1997; Beamsley et al., 1998) and the hydrodynamics of Poverty Bay including wave refraction into the port area (Gorman et al., 1997; Black et al., 1997). The Coastal

Marine Group at The University of Waikato undertook the work, and the author of this thesis was employed as Project Manager. The investigation involved the deployment of 41 instruments and sediment traps at 24 mooring sites between 2 July and 28 September 1997, while episodic conductivity-temperature-depth (CTD) surveys were also undertaken (Gorman et al., 1997). Numerical three-dimensional hydrodynamic and wave refraction models were developed and used to predict circulation in Poverty Bay and sedimentation rates in the port and approach channels (Black et al., 1997).

Knowledge of circulation in Poverty Bay is not only useful for its effects on port development, which is primarily concerned with sediment transport, but is also relevant to the dispersal of raw sewage that is discharged into the bay. The daily average effluent discharge volume is 12684 m^3, and peak discharges reach 22400 m^3 per day (Pickett, 1999). Prior to applying for renewal of its discharge resource consent, the Gisborne District Council in 1998 commissioned a scientific investigation as part of an Assessment of Environmental Effects regarding the submarine sewer outfall. The author of this thesis was involved in the production of a field data collection report for the AEE investigation (Stephens and Black, 1998).

Nearshore oceanographic circulation not only controls the dispersal of human-induced pollutants, but also affects the behaviour of natural water-borne organisms, such as rock lobster larvae. The harvesting of rock lobster is an important industry in the Gisborne region, and the wharves of Port Gisborne provide an important recruitment habitat for water-borne juvenile rock lobster, known as *pueruli* (Andrew Jeffs, *pers. comm.*, December 1999). Uncertainty exists as to whether lobster larvae actively seek recruitment habitat or happen upon it by chance (Jeffs, 1999), but if the latter is true then circulation in the bay will be critical to their recruitment in the port area. Circulation will also impact influence the potential for aquaculture development inside the bay.

Knowledge of Poverty Bay hydrodynamics is therefore required to understand and aid the management of sedimentation in the port environs, dispersal of sewage in the bay, the recruitment of lobster larvae, and potential aquaculture developments.

Accordingly, the aim of this thesis is to investigate the hydrodynamics, or circulation, of Poverty Bay. The thesis builds on the hydrodynamic knowledge base provided by the Port Gisborne AEE investigation and the other studies that precede it (eg. Williams, 1966; Miller, 1981; Bell, 1985; Kensington, 1990). This introductory chapter examines the background database provided by previous studies, details the specific thesis objectives, and outlines the thesis structure.

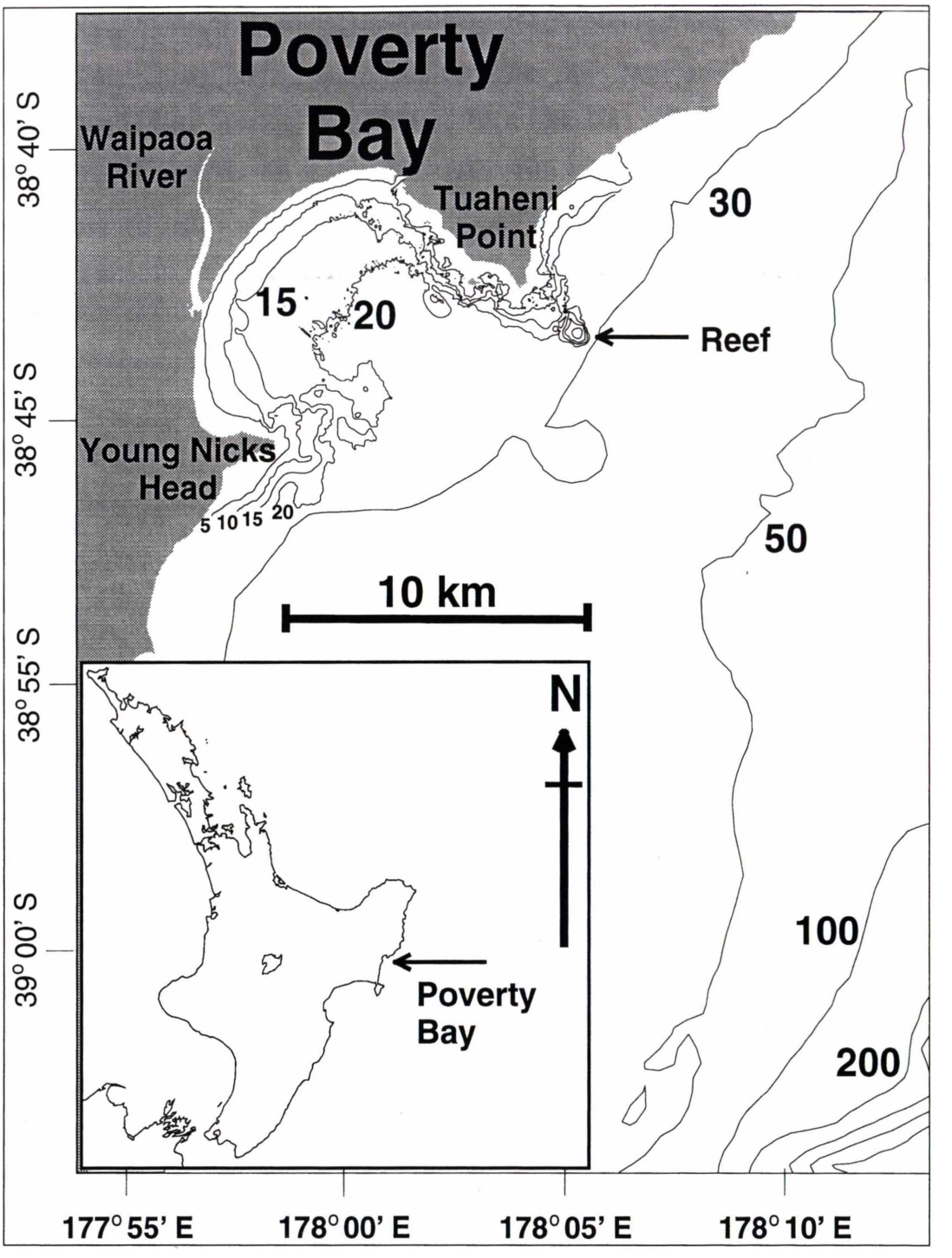

Figure 1-1. Bathymetric map of Poverty Bay and the adjacent continental-shelf, with the location of Poverty Bay shown in inset.

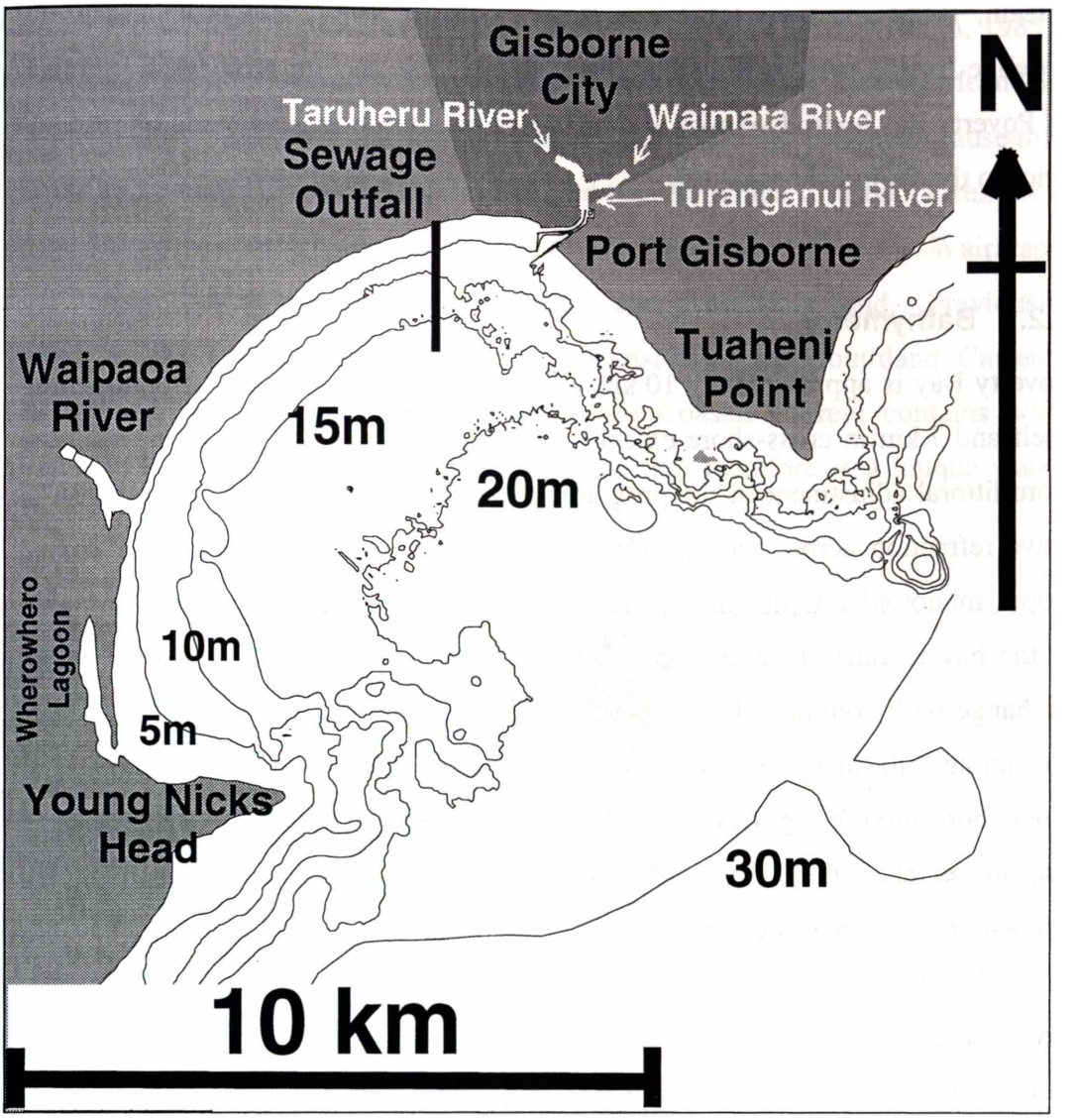

Figure 1-2. Poverty Bay showing rivers, bathymetric contours, headlands and associated reefs, city and sewage outfall.

1.2 STUDY BACKGROUND

Prior to the Port Gisborne AEE investigation, knowledge of Poverty Bay hydrodynamics was mostly limited to studies by Williams (1966), Miller (1981) and Kensington (1990). In particular Miller (1981) and Kensington (1990) have researched sediment textures, wave refraction patterns, tidal and wind driven currents using moored current meters, and undertaken limited sediment transport predictions. Other studies of Poverty Bay currents (Bell, 1985), wave conditions

(Heath, 1985) and tides (Gisborne Harbour Board, 1984) also provide a useful baseline for the present research. Accordingly, this section provides a summary of Poverty Bay hydrodynamics and related physical information based on research prior to the Port Gisborne AEE.

1.2.1 Bathymetry

Poverty Bay is approximately 10 km wide at its confluence with the continental-shelf and 7 km in cross-shore extent. The bay is rounded in planform, resulting from littoral adjustment of the prograding shoreline (Smith, 1988) in response to wave refraction across the bay (Miller, 1981; Kensington, 1990). The seabed slopes monotonically downward from its shoreline to approximately 25 m depth at the bay entrance (Figure 1-2). The wide and deep entrance allows for free exchange with continental-shelf water throughout the water column, unlike bays containing sills that often have high stratification due to limited exchange and cross-shore mixing, eg. Cockburn Sound (D'Adamo et al., 1997) and Shark Bay (Burling et al., 1999), Australia. Poverty Bay is nearly symmetrical about its cross-shore axis, but is deeper in the northern half near the bay entrance (Figure 1-2). The biggest asymmetrical feature occurs between the headlands flanking the bay entrance. Although not so obvious terrestrially, below the water surface the rocky reef associated with Young Nicks Head is comparatively rounded and unobtrusive, whereas the Tuaheni Point reef extends further onto the continental-shelf and is abruptly contoured (Figure 1-2). Morphologically, a closely similar bay reported in the literature is Jervis Bay, Australia, which possesses similar horizontal dimensions, depths, planform, and exposure to the continental-shelf (Holloway et al., 1992; Wang and Symonds, 1999).

1.2.2 Circulation on the east coast of the North Island

The main large-scale oceanic features along the North Island east coast are the East Auckland Current of warm saline water and the Canterbury Current (Southland Current) of cold saline sub-Antarctic water (Heath, 1985). The Canterbury current flows northward from Banks Peninsula (Figure 1-3). Conversely, the East Auckland current moves southward along the coast and splits at East Cape, one branch turning eastward and the other branch moving

clockwise, southward, past Poverty Bay, as the East Cape Current (Heath, 1985), (Figure 1-3). The observed current speed is ~18 cm s^{-1} (Heath, 1980). Meanders (Denhem et al., 1984) and changes in wind direction (Brodie, 1960) can cause this current to reverse. Chiswell (2000) identified the Wairarapa Coastal Current as a 40-50 km wide continental-shelf-current flowing northward past the Wairarapa coastline at least as far as Mahia Peninsula and possibly beyond. Previously known as the Canterbury Current or an extension of the Southland Current, Chiswell (2000) recognised that the Wairarapa Coastal Current contains both D'Urville Current and Southland Current water and therefore is a unique water body.

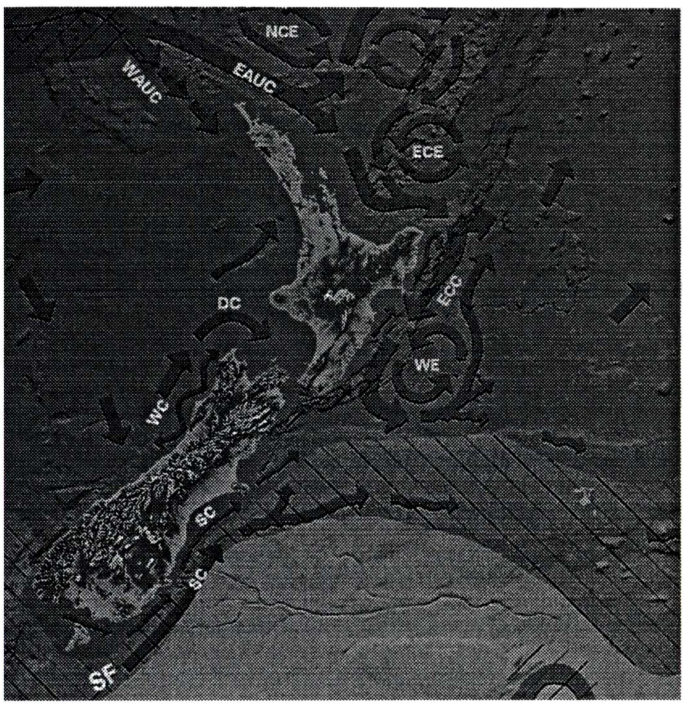

Figure 1-3. Oceanic circulation patterns around New Zealand, after National Institute of Water and Atmospheric Research (1997). Explanation of abbreviations referred to in text are: EAUC – East Auckland Current, ECC – East Cape Current, SC – Southland Current, DC – D'Urville Current. The Wairarapa Coastal Current is not marked but can be seen flowing northward inshore of the East Cape Current.

1.2.3 Poverty Bay inferred barotropic circulation

Based on previous studies using Aanderaa current meters (Bell, 1985), bottom drifters (Kensington, 1990) and Landsat imagery of suspended sediment (Miller, 1981), the time-averaged circulation in Poverty Bay has been characterised as an anticyclonic circulating gyre. Evidence from surface drifter measurements (Williams, 1966) suggested two large scale gyres: a large scale anticyclonic gyre and a small cyclonic gyre close to the harbour and Waikanae beach possibly driven by south-east winds. Records from 3 Aanderaa current meters deployed in Poverty Bay from 12th September to 1 November 1984 show a predominantly anticyclonic flow direction (Bell, 1985).

1.2.4 Stratification

Variations in density caused by freshwater input from rivers and local variations in temperature can drive a three dimensional circulation in coastal waters. The main cause of stratification in Poverty Bay is input of freshwater from the Waipaoa River and the Turanganui-Waimata-Taruheru River system, with the former contributing the larger volume. Average annual runoff for the Waipaoa catchment is recorded by Heath (1985) as 58 $m^3 s^{-1}$. Miller (1981) recorded a slight increase of temperature and salinity with depth in Poverty Bay, due to the overlying freshwater input from the rivers. Stratification will be enhanced during times of high rainfall, for example, between May and August (Miller, 1981) when the mean monthly rainfall is over 85 mm (New Zealand Meteorological Service, 1980) and during cyclones and extra tropical depressions that occur once or twice every year (Sinclair, 1993). For example, rainfalls of up to 900 mm occurred in 72 hours during Cyclone Bola (Singleton et al., 1989; Sinclair, 1993) causing a discharge of 5300 $m^3 s^{-1}$ from the Waipaoa River (Gisborne District Council, 1994).

Daily average and peak sewage discharge rates from the submarine outfall are 0.15 $m^3 s^{-1}$ and 0.26 $m^3 s^{-1}$ respectively (Pickett, 1999), and the buoyant sewage surfaces to form a plume similar to the rivers (Stephens and Black, 1998). These discharges are small compared with the mean Waipaoa River discharge, but may approach Turanganui volumes during times of low flow.

Seasonal variation in circulation can also be due to changes in the ambient seawater density relative to river water density. Summer and winter surface water temperature ranged between 19-20° C and 12.5-13.5° C respectively and this seasonal variation was greater in surface waters than deep water (Kensington, 1990). However, changes in density-driven circulation have not been observed or modelled. Foster and Carter (1997) discussed circulation changes resulting from sediment-load-induced density variation in Waipaoa River water. River water normally discharges on the surface. However decadal storms of >2000 $m^3 s^{-1}$ may cause large enough density changes in the river to cause bottom river discharge. Foster and Carter (1997) have no observations to confirm their hypothesis but large quantities of fluid mud on the seafloor following cyclone Bola provide some support (Kensington, 1990).

1.2.5 Wind-water interaction

The Raukumara range shelters Poverty Bay from the westerly wind that prevails over most of the North Island, producing warm dry winds from the west and north-west. Conversely the south to south-easterly winds, though often shorter in duration, may be far stronger (Smith, 1988). Along with the common regional westerly or north westerly wind situation, Hessell (1980) notes that katabatic drainage of cold air off the nearby Raukumara ranges at night helps to produce the observed predominance of north-westerly air flows in the morning, while the southeasterly sea breeze is often strong over the Gisborne region in the afternoon and evening. Hence the wind rose shows a strong cross-shore alignment at Gisborne (Figure 1-4).

Winds are capable of initiating currents both on the water surface and at depth. The process is initiated by wind shear stress acting on the water surface, the force inducing a current in the surface layer. Winds of sufficient strength are capable of generating surface currents strong enough to displace significant amounts of surface water. If the surface water is being pushed offshore from the coast, this in turn induces a return flow of water along the bottom to replace it, creating an upwelling situation close to shore. Conversely, onshore winds may push sufficient volumes of surface water inshore so that water begins to down-well at

the coast. Williams (1966) suggested that the anticyclonic surface circulation in Poverty Bay may reverse direction when strong south-easterly winds dominate. Kensington (1990) found bottom return flows to be induced in Poverty Bay when wind speeds exceeded 4-6 m s^{-1}. This range is higher than normally occurs in Poverty Bay; Miller (1981) reported lowest and highest mean monthly wind speeds of 3.75 m s^{-1} (March) and 4.94 m s^{-1} (November) respectively, while Hessell (1980) observed a 10-year mean of ~3.5 m s^{-1}.

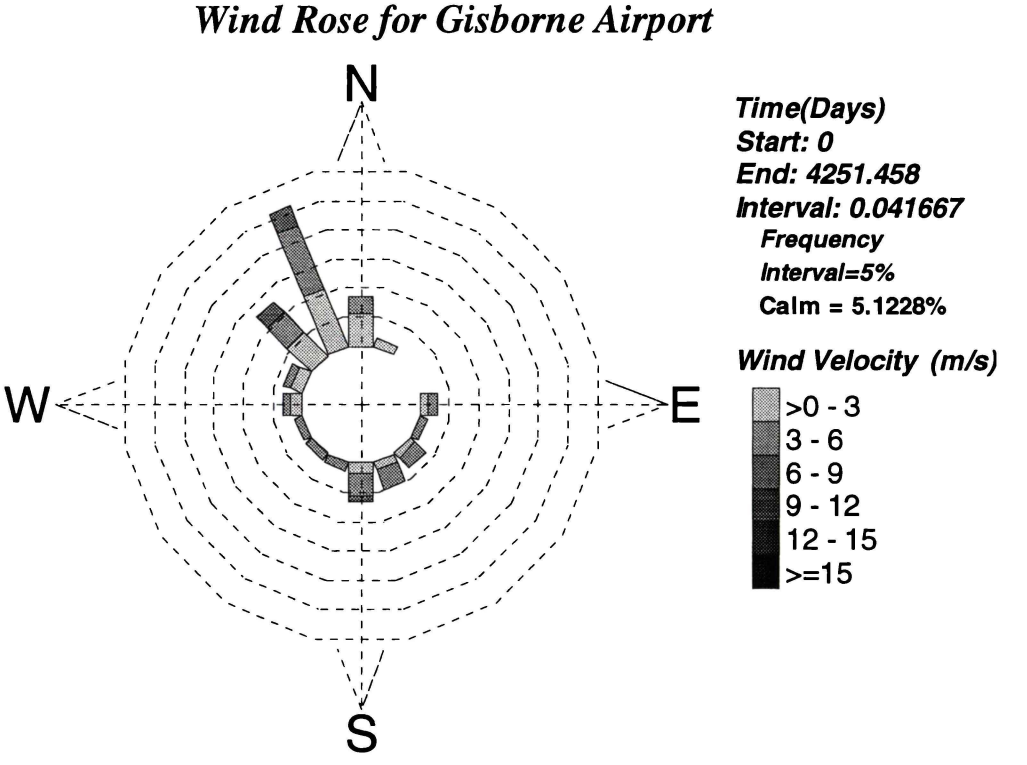

Figure 1-4. Gisborne airport wind rose from 86,046 hourly recordings, beginning 01:00, 1 January 1988 until 11:00, 8 August 1999. Data supplied by NIWA. Rick Liefting of NIWA wrote the wind-rose Matlab™ plotting routine.

However, episodic weather events certainly produce wind speeds well in excess of these values on occasions. Kensington (1990) noted a strong correlation between changes in wind speed and current speed at bottom mounted current meters near the harbour mouth, and the dredge-disposal grounds. This was also coincident with changes in salinity and temperature of bottom water. As would be expected, current directions opposed surface wind directions. Kensington (1990) hypothesised that shoreward, wind stress-induced surface currents would cause

water accumulation near the shore resulting in downwelling of less saline, warmer, surface water and a return flow seaward at the bottom, consistent with observation, and vice versa with the frequently-occurring katabatic north-west wind inducing bottom upwelling of ocean water.

1.2.6 Tides

The tidal range measured by the automatic tide gauge at the Port of Gisborne is micro-tidal (<2 m (Komar, 1998), 1.37 m at Spring tide and 1.22 m at neap tide (Gisborne Harbour Board, 1984). Kensington (1990) observed very little current variability relating to tidal rise or fall, suggesting that non-tidal forcing dominates in Poverty Bay. Kensington (1990) also noted the occurrence of a dual tidal peak ($T \approx 50$-60min), which is probably the signature of seiching within the harbour or of low frequency waves set up within the wider confines of Poverty Bay. Variations in temperature and salinity were observed to occur at tidal frequencies due to the advection of water that has a horizontal gradient in temperature and salinity (caused by the river water input), past the current meter sensor (Kensington, 1990).

1.2.7 Waves

Kensington (1990) explains the wave climate outside Poverty Bay as consisting of locally generated sea, generally from the north-east, and swell originating from the south or south-east. The orientation and size of the Bay entrance limit the approach direction of waves inside Poverty Bay to between 60 and 185° T. Smith (1988) reported average wave heights of 0.8-0.9 m and periods of 9-10 s and that the largest waves the bay experiences are from the south-west. Wave refraction inside Poverty Bay results in shoreline breaker angles of less than 5°, except at the extremities of the Bay (Miller, 1981). Most of the waves that reach the Port are from 150° T to 170° T.

The increase in storm occurrences in the winter causes identifiable seasonal variability in wave climate. In Poverty Bay, Miller (1981) observed a 0.4 m increase in the mean wave height in winter, while Smith (1975) reported longer period waves as more dominant during winter. Occasional extreme wave events

occur with waves up to 5.5 m recorded in Poverty Bay during storm events (Ministry of Works and Development, 1979). Moreover, tsunami waves, generated by tectonic or volcanic activity have been observed (Agnew and Smith, 1973; de Lange, 1983). For example, in 1960, the Chilean earthquake caused a 4m wave in Poverty Bay, with a 1m bore in Gisborne Harbour channel (de Lange, 1983; de Lange and Healy, 1986).

Wave refraction simulations using geometric optics theory show that the northernmost part of the bay and the Waikanae beach area are more energetic than the southern part of the bay, energy depending somewhat upon the angle of incident wave approach (Miller, 1981). The southern part of the bay is in the lee of Young Nick's Head, and experiences low energy, whereas Waikanae Beach has two zones of wave convergence. More detailed simulations by Kensington (1990) show four zones of wave focusing near the region where Port Gisborne Ltd is intending to expand (south-east of the Port entrance). Kensington (1990) characterised the distribution of wave energy within Poverty Bay on a coarse grid encompassing the whole harbour, and on a fine grid near the Port, assuming monochromatic deep-water waves with a Raleigh distribution and spring tide (Kensington, 1990). Significant wave heights were calculated using the JONSWAP 1976 fetch-limited wave spectrum equations for a typical storm developing in tropical latitudes (duration 12 hours, fetch 350 km and 500 km), and simulations were run for wave approach angles between 150° T and 185° T at 5° intervals. Results of the analysis show the area at the end of the existing breakwater will have the highest concentration of energy (6.9 m and 7.5 m maximum wave height for the two cases) with decreasing energy eastward toward the shore platforms on Kaiti beach (3 m maximum wave height for both cases).

Poverty Bay is approximately 10 km wide at its confluence with the continental-shelf and 7 km in cross-shore extent, and the relatively wide entrance leaves it exposed to wave action. The bay is rounded in planform, resulting from littoral adjustment of the prograding shoreline in response to wave refraction across the bay (Miller, 1981; Kensington, 1990). The strong wave refraction influence on shoreline form reflects the bays relatively small cross-shore fetch compared to its wide exposure to the open sea, similar to Yin-Yang Bay, Taiwan (Lin et al.,

1994). Other coastal bay examples with wide shelf exposure are Jervis Bay (Holloway et al., 1992; Wang and Symonds, 1999), Delaware Bay (Galperin and Mellor, 1990), Broken Bay (Kjerfve et al., 1992), Bristol Channel (Glorioso and Davies, 1995) and Nan Wan Bay (Lee et al., 1999a; Lee et al., 1999b). However these bays are generally larger than Poverty Bay and have uneven shoreline planform, probably reflecting a less wave-driven morphology. Other examples of coastal bays that have narrow entrances and are largely closed off from external wave activity are Port Phillip Bay (Black et al., 1993), Hudson Bay (Wang et al., 1994) and Indian River Lagoon (Liu et al., 1997).

1.2.8 Wave driven currents

Waves impinging on a beach generate secondary circulation patterns such as alongshore currents, shoreward drift patterns and seaward undertow. In Poverty Bay, Kensington (1990) concluded that waves breaking at an angle to the shoreline caused alongshore currents on Waikanae beach and along Butler's Wall. Mineralogical evidence suggests that alongshore currents flow north-eastward along Waikanae beach and along Butler's wall (Figure 1-5) and north-westward along Kaiti Beach, causing sediment movement and infilling of the main shipping approach channel (Miller, 1981).

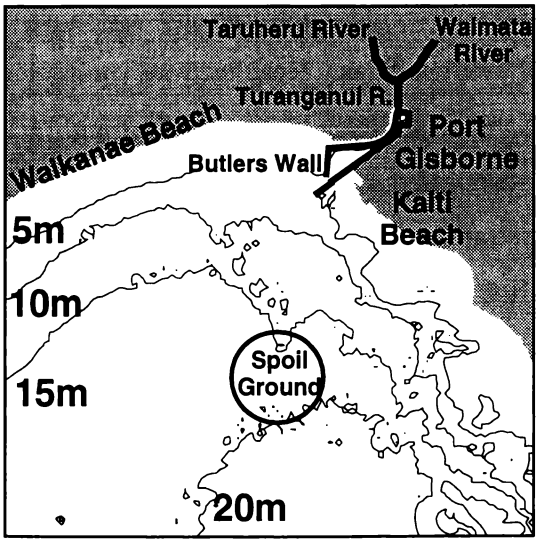

Figure 1-5. The port area, showing Waikanae and Kaiti Beaches, Butlers Wall, the historical dredge disposal ground, and bathymetric contours.

In addition to longshore currents, diabathic exchange from Waikanae beach has been hypothesised to account for chronic infilling of the port entrance (Miller, 1981). Strong seaward undertow induced by onshore storm surge and waves moves beach sediments offshore. The dredged channel traps these sediments, when normally they would move shoreward by wave drift in quieter periods (Miller, 1981).

1.2.9 Port Gisborne AEE investigation

The Port Gisborne AEE investigation involved one of the largest instrument deployments and numerical modelling studies performed in New Zealand at that time. Despite a focus on the port area, the investigation contributed substantially to the knowledge of flora and fauna, sedimentation and hydrodynamics throughout Poverty Bay. The additional findings of the study relevant to circulation in the bay are summarised below, incorporating data from Gorman et al. (1997) and Black et al. (1997).

For the data collected, residual (non-tidal) currents were generally less than 0.1 m s^{-1} in Poverty Bay, while tidal currents were less than 0.05 m s^{-1}, and more commonly 0.02-0.03 m s^{-1}. This indicates that a combination of non-tidal processes such as wind, density gradients and continental-shelf-currents are more important in driving circulation inside the bay than tides. Results from moored current-meters supported previous observations of anticyclonic circulation within the bay. Well-developed stratification was observed during all CTD surveys, with freshwater input from the rivers dominating stratification over temperature. Wind speeds capable of inducing bottom-return-flow currents (> 4 m s^{-1}, Kensington, (1990)) were present for 30% of the field data collection programme. Evidence for wind-driven upwelling occurred following a persistent offshore wind event of > 5 m s^{-1} on 22 August 1996. Surface water generally contained some freshwater content, but the identification of a saline marine water slug near the beach was suggestive of offshore-wind-driven upwelling following the offshore wind.

The three-dimensional hydrodynamic model 3DD (Black, 1995) depicted spatially complex and temporally variable surface dynamics within Poverty Bay. The

recurring patterns were (i) a tendency for the water to flow out of the bay along the transect linking Waipaoa River to Tuaheni Point, (ii) high salinity along the northern shore between the two river plumes, (iii) a strong influence of the inner shelf-currents and (iv) a dominant effect on surface circulation by the Waipaoa River plume. Patterns of flow and salinity within the bay remained highly variable (Black et al., 1997). The modelling showed that subsurface circulation was dominated by rotating eddies that responded to currents passing the entrance on the continental-shelf. The anticyclonic eddy was more pronounced, driving a net anticyclonic circulation in the bay. Temperature gradients were found to play a secondary role to salinity gradients, although thermoclines reduced vertical mixing and isolated the surface layer from the remainder of the water column (Black et al., 1997).

1.2.10 Knowledge shortfall

In addition to previous studies, the extensive AEE investigation provided new insights into the hydrodynamics of Poverty Bay. Nevertheless, several open questions remained.

Numerical modelling for the Port Gisborne AEE investigation showed that the bay is sensitive to shelf-currents, yet the failure of the primary deep-water tide gauge and lack of shelf current-meter deployments meant no meaningful shelf-current data was available. This was a serious deficiency since the correct representation of shelf-currents in the numerical model affects the balance between the three main non-tidal forcing parameters in Poverty Bay (wind, shelf-current and river discharge).

Kensington (1990) showed that wind-driven currents were responsible for three-dimensional circulation when in excess of 4 m s^{-1}, but the typical wind-induced circulation patterns and their variation with wind direction were unknown. Numerical modelling provided high spatial resolution, showing three-dimensional circulation under wind and plume-driven situations, yet high spatial resolution data was unavailable to confirm the model simulations.

Modelling by Black et al. (1997) showed wind and river discharge to influence three-dimensional circulation, with river discharge dominating surface water movement in Poverty Bay. The relative importance of these two processes to Poverty Bay hydrodynamics was not assessed, and flood simulations were not undertaken.

Black et al. (1997) suggested that the projection of Tuaheni Point onto the continental-shelf had an important influence on eddies, which modelling showed to dominate horizontal circulation in Poverty Bay. However, the effect on circulation of bathymetric features including the wide entrance, seaward slope, deep central section and disparate headland shapes was not fully investigated.

1.3 AIMS AND OBJECTIVES

The aim of this thesis is to describe the three-dimensional hydrodynamics of Poverty Bay in the context of its bathymetry, forcing parameters and typical circulation patterns. The goal is to provide a model of the processes driving circulation in an exposed and stratified coastal embayment that enhances the understanding of similar embayments worldwide.

The specific aims of the thesis follow from the study background and the knowledge shortfall outlined above. Specific aims are to:

1. examine the interplay between bathymetry and hydrodynamics in Poverty Bay to determine how bathymetric features affect time-averaged circulation and eddy formation;
2. investigate shelf-currents adjacent to Poverty Bay, and their role in forcing circulation inside the bay;
3. gather data of sufficient spatial coverage and quality to calibrate Model 3DD (Black, 1995) for the purpose of reproducing and analysing high resolution circulation in Poverty Bay;
4. investigate the balance between wind-stress and river-discharge induced hydrodynamic forcing in Poverty Bay, including normal and flood conditions;

5. re-investigate the mechanisms responsible for the observed time-averaged anticyclonic gyre in Poverty Bay.

1.4 THESIS STRUCTURE

This thesis partially incorporates information collected during the scientific investigation designed to provide the basis for an Assessment of Environmental Effects (AEE) for the proposed expansion of Port Gisborne Ltd. An intention of the authors' involvement as Project Manager in the AEE investigation was that that some of the author's production during the investigation would be included in the thesis and that the study should provide information for subsequent ongoing investigation into Poverty Bay hydrodynamic processes. These intentions are realised in the thesis, which refers on occasions to the information base contained in the AEE reports. The author researched and wrote the literature review included in Gorman et al. (1997), and relevant information has been transferred to the study background included in this chapter. That is the main inclusion of Port Gisborne AEE data in this thesis.

This thesis is presented as a blend of four papers aimed at the peer-reviewed literature, combined with five supporting chapters. Some of the papers have undergone peer review and been published, others have been submitted and are currently under review. The papers and chapters are presented sequentially, so that each builds in some way on those preceding. Chapters 1, 8 and 9 provide an introduction, discussion and conclusions respectively, while Chapters 6 & 7 follow the papers and continue to develop hydrodynamic knowledge of Poverty Bay.

In meeting the aims and objectives, this thesis has involved two field experiments, with associated data analyses and interpretation. Numerical models have also been used to support and extend the data analyses. The study background, thesis aims, and structure are presented in this introductory chapter. Since the thesis incorporates a series of papers aimed at the peer-reviewed literature, the necessity for each paper to stand alone dictates that the paper introductions contain some

repetition. For the same reason, these introductions do not place the papers in context of the thesis as a whole. Therefore the remainder of this chapter aims to outline the sequence of processes undertaken to meet the thesis aims, and explain the context of the papers and chapters within that sequence. The following paragraph introduces the sequence of events undertaken to address the thesis aims and objectives. A more detailed description of each chapter in context of the thesis as a whole is subsequently provided. Additionally, in each chapter containing a paper, a lead-in paragraph is included under the heading 'Context of the paper within the thesis'.

The first move toward meeting the thesis aims was a preliminary field experiment. This was undertaken to test instrumentation, and it supplied initial hydrodynamic observations and made recommendations for future fieldwork. This work is presented in Chapter 3 because it links with the second field experiment presented in Chapter 4. To address continental-shelf – bay interaction, a numerical experiment investigating embayment eddy formation was then undertaken (presented in Chapter 2) while preparing for the main thesis experiment. This was motivated by simulations depicting strong shelf-current driven eddies in Poverty Bay by Black et al. (1997), and by observations from the preliminary field experiment. The main thesis experiment was then undertaken and data analyses were used to infer forcing by tide, continental-shelf-currents, river discharge, and wind stress; indicating the dominant circulation forcing mechanisms and typical circulation patterns in the bay (Chapter 4). Investigation of coastal-trapped-waves was undertaken following identification of low-frequency motion on the continental-shelf in Chapter 4 (Chapter 5). Having found less coherence than expected in previous spectral analyses, wavelets were then used to re-investigate the wind-current relationship, finding significant coherence (Chapter 6). Typical circulation patterns and forcing processes in Poverty Bay were identified through the interpretation of field data in Chapters 4-6, but the specific thesis aims were not entirely achieved. Therefore numerical hydrodynamic modelling was undertaken to extend the data analyses (Chapter 7). These explained the relative magnitude of wind-stress- and river-discharge-forced circulation, the effect of floods, and the most prominent bathymetric controls on circulation. A discussion based on the preceding chapters, was then included to broadly summarise the

three-dimensional hydrodynamics of Poverty Bay in context of its bathymetry, forcing parameters and typical circulation patterns (Chapter 8). The thesis was then rounded off with conclusions to address the initial specific thesis aims (Chapter 9).

The preceding paragraph has briefly summarised the sequence of ideas developed during the thesis. Additionally, a more detailed description of each chapter and its relationship to those preceding is now presented.

1.4.1 Chapter 2 - Shelf-current driven recirculation in a coastal bay: a two-dimensional numerical study

During the period prior to fieldwork when the ADP was being upgraded to bottom-track (July 1997 - March 1998), two-dimensional numerical experiments were conducted to investigate the effect of continental-shelf-currents and topography on eddy formation in a coastal embayment (specific thesis aims 1 and 2). The investigation was motivated by previous simulations showing strong shelf-current driven eddies in Poverty Bay (Black et al., 1997), along with evidence for shelf-current intrusion into the bay, presented in the following paper (Chapter 3). Eddies are an important exchange mechanism between the continental-shelf and coastal embayments (Deleersnijder et al., 1992; Lin et al., 1994). Although there have been many numerical investigations of the parameters governing eddies around headlands, islands and reefs (Wolanski et al., 1984; Black and Gay, 1987; Black, 1989; Signell and Geyer, 1991 and Middleton et al., 1993), none have examined the parameters controlling recirculation in coastal embayments. The paper, based on hundreds of numerical simulations, identifies unique constraints on eddy formation due to the enclosed nature of an embayment, and develops a new parameter for prediction of embayment eddies.

The paper has been reviewed and resubmitted for publication in the Journal of Geophysical Research, Oceans.

1.4.2 Chapter 3 – Circulation Patterns in Poverty Bay, New Zealand, measured by Boat-Mounted Global Positioning System Interfaced, Acoustic Doppler Current Profiler

An important component of the field experiments was the use of a Sontek acoustic-Doppler-profiler (ADP) with real-time capability, used to gather high spatial resolution data. As the real-time capability of the Sontek ADP was prototype technology, a preliminary field experiment was performed with the instrument in combination with CTD. Chapter 3 is a paper based on the preliminary field experiment; it is mostly observational and makes several recommendations for future fieldwork. Observations include possible shelf-current intrusion into the bay at depth, a salinity stratified water column in the inner bay, complex currents near the port area, and substantial variation in overnight circulation. One of the recommendations was for improved horizontal resolution of the ADP, and the instrument was subsequently sent for an upgrade to bottom-track capability.

This paper was presented at Pacific Ports and Coasts '97, the 13th Australasian Coastal and Ocean Engineering Conference and 6th Australasian Port and Harbour Conference, Christchurch, New Zealand. The paper is published in the conference proceedings but did not undergo peer review.

1.4.3 Chapter 4 - Complex Circulation in a Coastal Embayment: Shelf-current, Wind and Density-Driven circulation in Poverty Bay, New Zealand

The paper in Chapter 4 describes the main thesis field experiment and presents the results. The data is used to infer forcing by tide, continental-shelf-currents, river discharge, and wind stress. The analysis of field data from all instruments gives the first indication of the relative importance of shelf-current, wind, and density-driven processes to Poverty Bay hydrodynamics, and the reason for persistent anticyclonic circulation in the bay (specific thesis aims 2, 4 and 5). The data analysis also provides a basis for later numerical model calibration (specific thesis aim 3).

This paper was presented at the Rotorua International Coastal Symposium 2000, underwent peer review, and has been accepted for publication in a Journal of Coastal Research Special Issue.

1.4.4 Chapter 5 – Coastal-trapped waves on the east coast of the North Island, New Zealand

Chapter 4 addressed continental-shelf-current forcing and an outcome of this was the identification of significant low-frequency motion in the shelf sea-level and current record, such as is often associated with coastal-trapped-waves (CTWs) (Csanady, 1997). Since CTWs can provide significant hydrodynamic forcing in coastal embayments (eg. Wright et al., 1987; Black et al., 1993) an investigation of CTW activity at Poverty Bay was therefore undertaken (Chapter 5). The paper employs wind and water level data obtained during the field study and from south of Poverty Bay including Cook Strait. Data analyses showed substantial evidence for CTW propagation between Cook Strait and Gisborne, and numerical simulations using Cook Strait inputs were able to partially reproduce low-frequency sea-level oscillations at Riversdale and Poverty Bay, showing that CTWs do propagate the Cook Strait region to Poverty Bay.

It is planned to submit this paper to the New Zealand Journal of Marine and Freshwater Research.

1.4.5 Chapter 6 – wavelet analysis

Despite evidence that CTWs propagate from Cook Strait to Poverty Bay, Chapter 5 showed there is considerable low-frequency energy at Poverty Bay that does not originate through propagating CTWs. CTWs are predominantly forced by alongshore wind stress (Buchwald and Adams, 1968) and a logical forcing mechanism for low-frequency energy near Poverty Bay is wind stress, particularly since 81% of current variance (energy) on the Poverty Bay continental-shelf was non-tidal (Chapter 4). Yet spectral analysis showed little relationship between wind and residual continental-shelf-currents adjacent to Poverty Bay (Chapter 4). Spectral analysis is designed for stationary time-series (Goring and Bell, 1999), but wavelet analysis is a comparatively new time-series analysis technique,

designed specifically to deal with non-stationary signals such as the wind-current relationship. This chapter presents the results of wavelet analyses between wind and shelf-currents, showing a strong and previously overlooked relationship.

1.4.6 Chapter 7 – Three-dimensional numerical modelling of Poverty Bay

Field surveys highlighted the variability of Poverty Bay hydrodynamics and showed that the forcing in the bay was dominated by the interaction of fluvial discharge and surface wind stress (Chapter 4). The shelf-current was demonstrated to have little effect on Poverty Bay circulation, contrary to previous simulations (Black et al., 1997). In light of this new knowledge, it was decided to re-run three-dimensional simulations of Poverty Bay, to calibrate the model using real shelf-currents. Furthermore, the ADP measurements provided a better spatial resolution for model calibration than moored current-meters used in the 1997 AEE investigation. The calibration of a Poverty Bay numerical model allows circulation to be broken down into its shelf-current, river discharge and wind stress driven constituents, providing insights that the field study could not. The model accounts for the relative magnitude of wind-stress- and river-discharge-forced circulation, the effect of floods, and the most prominent bathymetric controls on circulation. Thus the modelling chapter addresses specific thesis aims 1, 2, 4 and 5 in detail.

1.4.7 Chapter 8 – Discussion

The discussion chapter broadly summarises the three-dimensional hydrodynamics of Poverty Bay in context of its bathymetry, forcing parameters, typical circulation patterns and common variations. The chapter compares the results of this study with similar studies in other coastal embayments, to describe how circulation works in an exposed and stratified coastal embayment with small tidal flows.

1.4.8 Chapter 9 – Conclusions

This chapter provides a series of conclusions addressing the specific thesis aims.

2

2.1 CONTEXT OF THE PAPER WITHIN THE THESIS

Numerical simulations by Black et al. (1997) showed a strong shelf-current driven circulation in Poverty Bay: 'circulation in the bay below the surface in the mid-water column was dominated by rotating eddies that responded to currents passing the entrance on the continental-shelf'. Fieldwork presented in Chapter 3 provided further evidence that shelf-currents intruded into the bay near the seabed. Consequently this paper investigates the effect of continental-shelf-currents on circulation in a coastal embayment. The investigation utilises a two-dimensional numerical model to study the important eddy forming characteristics of the shelf-current and the bay topography. An embayment eddy parameter for predicting the onset of recirculation in coastal embayments is developed, and key bathymetric features are investigated including the alongshore to cross-shore bay dimension ratio, the depth to width ratio and the presence of a point reef. The paper meets the thesis objectives by establishing a link between continental-shelf-currents and circulation in an embayment (specific thesis aim 2), and by investigating the important bathymetric features of a coastal embayment that control recirculation (specific thesis aim 1). The paper was initiated when fieldwork was on hold due to the ADP upgrade, but was subsequently revised to include data from the 1998 field experiment.

Shelf-current driven recirculation in a coastal bay: a two-dimensional numerical study

Scott A. Stephens and Kerry P. Black[1]

Coastal Marine Group, Department of Earth Sciences, The University of Waikato, Private Bag 3105, Hamilton

and [1]ASR Ltd., P. O. Box 13048, Hamilton, New Zealand

Tel: +64-7-838-4024, Fax: +64-7-856-0115, Email: scotts@waikato.ac.nz, asrltd@clear.net.nz

Abstract. Eddy formation in a coastal embayment was investigated using two-dimensional simulations of simple bathymetries and shelf-currents, modelled on Poverty Bay, New Zealand. The enclosed geometry of an embayment creates recirculation-favourable pressure gradients in comparison to islands, reefs and headlands. Consequently, recirculation occurs earlier, and an embayment eddy parameter E was developed to predict embayment recirculation. Two conditions exist prior to eddy formation under both steady and unsteady flow conditions: (i) a velocity gradient (wake) exists, due either to abrupt flow separation, or in response to larger scale inertial and frictional forces, or some combination; (ii) a pressure gradient in the bay acts opposite to the free-stream flow, assisting the slower currents to reverse earlier than in the free-stream. Recirculation can begin wherever these two conditions are met, and this does not require prior flow separation. Flow separation, previously deemed prerequisite for eddy formation, simply provides an extreme velocity gradient. Simulations show that eddy formation need not involve advection of vorticity from a narrow boundary layer at the flow separation point, but are instead driven by a combination of velocity and pressure gradients. The Bernoulli effect found important in headland studies, may be absent in embayments, and horizontal shear is important in creating recirculation-favourable pressure gradients. In smooth coastal embayments where headland effects are minor, the presence of a point reef has a strong influence on recirculation, facilitating earlier development and stronger growth of phase eddies. This can occur due to both increased friction and associated turbulence increasing horizontal eddy viscosity over the reef.

2.2 INTRODUCTION

Eddies are important features near the coast, affecting water exchange between the continental-shelf and the coast and the distribution of water-borne particles. The separation of flow and the formation of eddies in a fluid flow (behind bluff bodies, in sharp bends and in sudden expansions) is of special importance in investigations concerned with the transport and dispersion of sediments and pollutants in rivers, estuaries and tidally-dominated coastlines [*Ferentinos and Collins*, 1980]. While there have been many numerical investigations of the parameters governing eddies around headlands, islands and reefs [*Wolanski et al.*, 1984; *Black and Gay,* 1987; *Black,* 1989; *Signell and Geyer,* 1991; *Middleton et al.*, 1993], few have examined the parameters controlling recirculation in coastal embayments. *Klinck [1996]* and *Perenne et al.* [1997] have modelled submarine shelf canyon flows and a recent numerical study by *Lee et al.* [1999a] reproduced tide-induced eddies in a coastal embayment. *Lee et al.* [1999a] used an analytic approach to find the fundamental bathymetric features controlling recirculation in a semi-enclosed basin. The bathymetry investigated was specific to Nan Wan Bay, and not general to other locations. This paper is motivated by an investigation of shelf-current influence on Poverty Bay, New Zealand (Figure 2-1), where persistent recirculation patterns have previously been measured (Figure 2-2). Poverty Bay is exposed to continental-shelf-currents by a wide entrance and previous three-dimensional numerical simulation of the bay hydrodynamics showed high sensitivity to shelf-currents, including the formation of eddies [*Stephens et al.*, 1999]. These simulations also showed circulation in Poverty Bay to be depth-dependent, owing to fresh-water induced stratification, and this created complex internal dynamics [*Stephens et al.*, 1999]. However, this paper is motivated by the apparent propensity for eddy formation due to shelf-current action. The paper neglects stratification and takes a more theoretical perspective, examining the depth-averaged effect of a passing shelf-current on an exposed coastal embayment. Although three-dimensional investigations have been undertaken more recently to investigate the vertical structure of coastal eddies [*Deleersnijder et al.*, 1992; *Wolanski et al.*, 1996; *Furukawa and Wolanski*, 1998; *Lee et al.*, 1999a; *Black et al.*, 2000], two-dimensional studies have been

very successful in simulating horizontal recirculation around simple bathymetries, both in the presence of steady currents and in the added complexity of unsteady flows [*Imasato,* 1983; *Wolanski et al.,* 1984; *Black and Gay,* 1987; *Ridderinkhof,* 1989; *Signell and Geyer,* 1991]. A two-dimensional model has the added advantage of reduced complexity and computational expense.

A coastal embayment contains unique geometric properties compared to the islands, reefs and headlands that have been previously studied. The sea surrounds islands, reefs and headlands, whereas an embayment has an enclosed coastline, with only one entrance. Furthermore, an embayment provides no direct obstruction to free-stream current flow. We investigate these features and their effect on recirculation using simple bathymetries. The use of simple bathymetries allows identification of fundamental eddy-forming parameters, so that results can be applied to similar embayments with wide exposure to continental-shelf-currents. *Signell and Geyer* [1991] concluded that eddies around headlands originate from vorticity generated in a narrow boundary layer along the headland, where the flow separates. The vorticity is then injected into the interior at the point of flow separation. This paper questions the need for vorticity injection in order for eddies to form, even though vorticity occurs in all eddies.

2.3 NUMERICAL MODEL, BOUNDARY CONDITIONS AND METHODS

The two-dimensional form of model 3DD is based on the two equations known as the momentum equation and the mass conservation equation. The momentum equation describes the acceleration/retardation of the water body when forces/friction are applied. The equation derives from Newton's 2nd law of motion i.e. the rate of change of motion (acceleration) of a body is directly proportional to the resultant force acting upon it and is in the direction of that force. The conservation equation keeps a check on the total mass entering/leaving small regions (model cells) and ensures that mass is conserved in these cells. An explicit finite difference (Eulerian) solution is used to solve the momentum and continuity equations for velocity and sea-level. The model provides for spatial

variation in roughness length (z_0) and horizontal eddy viscosity (A_H). Non-linear terms and Coriolis force can be included or neglected, while the land/sea boundaries can be set to free slip or no-slip. The two-dimensional form of model 3DD has been successfully applied and verified in a diverse range of situations [*Black*, 1987; *Black and Gay*, 1987; *Black et al.*, 1989; *Black and Gay*, 1991; *Black et al.*, 1993; *Young et al.*, 1994; *Middleton and Black*, 1994]. The model has been previously applied to investigate the parameters responsible for eddy formation behind islands and reefs [*Black and Gay*, 1987; *Black*, 1989].

The equations in 2-dimensions are:

Momentum

$$\frac{\partial u}{\partial t}^{(1)} + \frac{u\partial u}{\partial x} + \frac{v\partial u}{\partial y}^{(2)} - fv^{(3)} = -\frac{g\partial \zeta}{\partial x}^{(4)} - \frac{1\partial Patm}{\rho\partial x}^{(5)} + \frac{\rho a \gamma W_x |W|}{\rho(d+\zeta)}^{(6)}$$

$$-\frac{gu(u2+v2)1/2}{C2h}^{(7)} + A_H\left(\frac{\partial^2 u}{\partial x^2} + \frac{\partial^2 u}{\partial y^2}\right)^{(8)} \qquad (1)$$

$$\frac{\partial v}{\partial t}^{(1)} + \frac{u\partial v}{\partial x} + \frac{v\partial v}{\partial y}^{(2)} + fu^{(3)} = -\frac{g\partial \zeta}{\partial y}^{(4)} - \frac{1\partial Patm}{\rho\partial y}^{(5)} + \frac{\rho a \gamma W_y |W|}{\rho(d+\zeta)}^{(6)}$$

$$-\frac{gv(u2+v2)1/2}{C2h}^{(7)} + A_H\left(\frac{\partial^2 v}{\partial x^2} + \frac{\partial^2 v}{\partial y^2}\right)^{(8)} \qquad (2)$$

Mass conservation

$$\frac{\partial \zeta}{\partial t}+\frac{\partial}{\partial x}(d+\zeta)u+\frac{\partial}{\partial y}(d+\zeta)v=0 \qquad (3)$$

t is the time, u, v are vertically-averaged velocities in the x,y directions respectively, h the total water depth, d the depth below the sea-level datum, ζ the sea-level above the sea-level horizontal datum, g the gravitational acceleration, f the Coriolis parameter, P_{atm} the atmospheric pressure, A_H the horizontal eddy viscosity coefficient, C is Chezy's $C = 18\ log_{10}\ (0.37h/z_0)$.

The physical representations of each of the various terms in the momentum equation, as denoted by their superscript are: local acceleration[(1)]; inertia[(2)]; Coriolis[(3)]; pressure gradient due to sea-level variation[(4)]; pressure gradient due to atmospheric pressure[(5)]; wind stress[(6)]; bed friction[(7)]; horizontal eddy viscosity[(8)]. Atmospheric pressure[(5)] changes and wind stress[(6)] were not included in the simulations, therefore terms 5 and 6 in the momentum equation are negated. We now address the physical inputs to the model.

Numerical simulations are based on a simplified bathymetry that consists of a coastal embayment adjacent to a flat continental-shelf of 27 m depth. While the dimensions of the simulated bay and shelf are based on those of Poverty Bay, the simulations are designed to reproduce aspects of shelf-bay interaction, and not to model the exact hydrodynamics of Poverty Bay. Two simple bathymetries are used, the first a bluff-body bathymetry (Figure 2-3a) and the second a smooth bathymetry (Figure 2-3b) based on a cosine-squared formulation, taken from *Perenne et al.* [1997]. Both bathymetries are built into a rectangular grid of dimensions $I = 1{:}90, \times J = 1{:}50$, with cell spacing of 500 m. Total grid dimensions are therefore 45×25 km in the x and y directions respectively. The embayments have two key length scales that influence recirculation and are referred to often in this paper. The first is the embayment width w (the distance across the bay entrance), and the second is the embayment cross-shore extent L (the distance from the shore to the mouth of the bay), (Figure 2-3a). Both bathymetries consist of a flat continental-shelf, 17.5 km wide, 45 km long and 27 m deep, while the bay has width w = 10 km and cross-shore extent L = 7 km.

Inside the bluff-body bay, a planar seabed slopes from 27 m at the shelf up to 0 m at the shore. Minor alterations to each bathymetry are made during the paper, to investigate hydrodynamic reaction to specific bathymetric effects, and these alterations are discussed on introduction.

Hydrodynamic forcing in all simulations occurs at the western continental-shelf boundary, using a perpendicular velocity boundary that enables precise control of shelf-current speed. This was the only forcing mechanism used in the simulations, therefore all currents observed within the bay are produced purely through the interaction of the continental-shelf-current with the shelf-bay bathymetry. At the southern boundary, a perpendicular velocity boundary clamped at 0 m s^{-1} was used, confining current propagation to the alongshore direction. The eastern shelf boundary comprised of a sea-level boundary clamped to zero, allowing currents to pass through but with no sea-level change. Continental-shelf boundaries were placed at sufficient distance not to influence the hydrodynamics, either in or adjacent to the bay. However, in order to clearly illustrate circulation in the zone of interest, plots have generally been zoomed to focus on the bay (Figure 2-5a).

Shelf-current speeds at the western boundary were chosen to represent natural shelf-current flows as measured on the continental-shelf outside the Poverty Bay entrance (S4, Figure 2-1). Investigation of shelf-current forcing is left for another paper, however the results of the current-meter deployment relevant to this paper are presented. Tidal analysis revealed that the combined tidal component of flow on the shelf is small (mean speed ~0.04 m s^{-1}) compared with the non-tidal current (mean speed ~0.09 m s^{-1}), eg. Figure 2-4. The ratio of squared standard deviations (variance), between non-tidal and measured currents, indicated that 81% of shelf-current energy was derived from non-tidal forcing, signifying that non-tidal shelf-currents have greater influence on nearby Poverty Bay. Since residual currents are primarily orientated in the alongshore direction of the continental-shelf, the simulations in this paper assume alongshore propagation of the continental-shelf-current. It is evident from the current-meter deployment that shelf-current velocities range from 0.003-0.36 m s^{-1} and simulations in this paper are based on this velocity range.

Black and Gay [1987] recognised the importance of flow unsteadiness to eddy formation. While exhibiting periods of near steady flow over time scales of ~48 hours (Figure 2-4), the shelf-current near Poverty Bay experiences significant changes in speed and direction. Changes in alongshore direction occur at periods of less than one day up to five days and these reversals are not cyclic. Autospectra of raw currents revealed that there was significant energy across the spectrum, highest at periods longer than 10 days, but lacking definitive peaks. Given the lack of a dominant energy period, we arbitrarily chose a sinusoidal shelf-current of period 48 hours, to simulate the effects of unsteady forcing on the smooth bay. This allows eddy formation to be examined under controlled deceleration.

Poverty Bay is located at latitude 38.7°S, giving a Coriolis parameter $f = -9.12\times10^{-5}$ s^{-1} [*Gill*, 1982]. Coriolis was found to be an important flow modifying parameter in the simulations. Since Coriolis acts to deflect currents left in the Southern Hemisphere [*Gill*, 1982], the primary effect of the Coriolis force was to encourage the formation of anticyclonic recirculation and discourage cyclonic recirculation, leading to time averaged circulation such as shown in Figure 2-5 (a,b). For simplicity, it was decided not to study rotation effects in this paper. By eliminating Coriolis from our simulations (Figure 2-5c), the effects of other parameters such as pressure gradient, horizontal eddy viscosity and frictional variations, can better be isolated and studied.

Representation of the bottom friction[7] in the model requires parameterisation of the bed roughness length. The seabed over much of Poverty Bay and the adjacent continental-shelf is covered in fine sand and silt, introduced primarily by the Waipaoa River (Figure 2-1), whose catchment drains highly erodable tertiary siltstone country [*Foster and Carter*, 1997]. To reproduce frictional characteristics over this seabed, we have used a roughness length parameter z_0 = 0.001 m, slightly finer than the typical roughness length for sandy sediment of z_0 = 0.002 m [*Black*, 1989], but similar to the estuarine mean of z_0 = 0.001 m [*Black et al.*, 1989]. The rocky promontories located at the margins of Poverty Bay will have much larger associated roughness lengths (Figure 2-1). Initial simulations

assume $z_0 = 0.001$ m over the entire grid but variations are made later to represent the frictional effect of the reefs.

The horizontal eddy viscosity coefficient A_H was set to 1 $m^2 s^{-1}$ for most simulations. This value was found to provide the best calibration of a three-dimensional (3DD) Poverty Bay model [*Stephens*, 2000]. While measurements of horizontal eddy viscosity are typically of order 0.001 $m^2 s^{-1}$, model grid spacings of order 500 m do not allow accurate representation of small scale natural viscous processes. Indeed, using the same model as for this study *Black* [1989] observed that on a 100 m grid, A_H requires a magnitude of about 1 $m^2 s^{-1}$ to have an appreciable influence in the model on eddy circulation. We found that reducing A_H to an order of magnitude less than 1 $m^2 s^{-1}$ essentially removes horizontal shear entrainment on the 500 m grid.

We chose to use a slip boundary at the land/sea interface, as used by *Black and Gay* [1987]. Although a slip boundary is not realistic at natural scales within the coastal boundary layer, in the context of the numerical model it gives more realistic results. This occurs because a typical coastal boundary layer in the horizontal due to slip at the edge, is much smaller than the 500 m model grid cell size. Using a no-slip boundary would have set the velocity to zero at the coast, and unrealistically damped velocities up to at least 2 cells from land (1000 m). Furthermore, in most situations, the main factor slowing currents down near the coast is bed friction in shallower water, and not the coastal boundary layer [*Black and Gay*, 1987].

In this paper, the term "wake" is used to define an area of quiet water adjacent to the free-stream current. We define flow separation to occur where inertia carries the free-stream current past slower currents in the lee of an obstruction, creating a pronounced horizontal shear layer. Where the transition from fast to slow currents is gradual, we show that a wake can exist without pronounced flow separation occurring, although often the two co-exist [*Wolanski, et al.,* 1984; *Signell and Geyer,* 1991; *Middleton et al.,* 1993].

2.4 RESULTS AND DISCUSSION

2.4.1 Bluff-body bathymetry

Numerous numerical investigations have been made as to the parameters governing recirculating flow around a bluff-body object. These studies have concentrated on flow around islands and headlands [*Wolanski, et al.,* 1984; *Black and Gay,* 1987; *Black,* 1989; *Signell and Geyer,* 1991; *Middleton et al.,* 1993]. In this study, recirculation in a bluff-body embayment (Figure 2-3a) was examined for comparison with these earlier island and headland studies (Exp. 1, Table 2-1). Simulations were initially based on steady (velocity constant in time) shelf-currents of speed U = 0.01, 0.05, 0.1, 0.2 and 0.3 m s^{-1}, over the bluff bathymetry (Figure 2-3a). Currents were accelerated to steady-state over 12 hours using a sinusoidal ramp function and the final flow field was found to be independent of the ramp function time-scale. For these simulations a 12 hour ramp function was used, and resulted in no recirculation prior to the shelf-current reaching steady velocity. Simulations were run for 48 hours, with shelf-currents reaching a steady flow solution by at least 30 hours. The results of these simulations are not presented, although an example is shown in Figure 2-6. However, we observe that the dimensionless island wake parameter P was approximately 70% smaller than the expected value of 1 [*Wolanski et al.*, 1984] on initiation of recirculation. The island wake parameter

$$P = Uh^2/A_Z L \tag{4}$$

where U is the free stream velocity (m s^{-1}), h is the water depth (m), A_Z is the vertical eddy diffusion coefficient (m^2 s^{-1}) and L a length scale characterising the horizontal dimensions of the island [*Wolanski et al.*, 1984]. In an embayment, L is the distance from the shore to the mouth of the bay as this provides a geographical constraint on both wake and eddy size (Figure 2-6). P describes the ratio of advection to bottom friction and has been shown to work well in the description of recirculation in two-dimensional flows around islands [*Wolanski et al.,* 1984; *Pattiaratchi et al.,* 1987; *Denniss and Middleton,* 1994]. For values of $P \ll 1$ friction dominates the flow leading to a quasi-potential flow; stable wakes exist at the flow separation point of bathymetric obstructions when $P \sim 1$; and for

$P >> 1$, flow instabilities develop downstream [*Wolanski et al.*, 1984]. Therefore, eddies are observed when $P \sim 1$.

2.4.2 Geometric effects

There are important differences in the effects of the bluff-body embayment geometry compared with a bluff-body headland or island, as shown by the under-prediction of embayment recirculation by P. The first of these relates to the absence of a bathymetric projection into the free-stream current, which negates the Bernoulli effect experienced by a projecting headland. *Signell and Geyer* [1991] observed that water level set-down occurred at a headland tip due to the Bernoulli effect (kinetic energy + potential energy = constant), the free-stream current being forced to accelerate past the obstruction created by the headland. The set-down at the headland tip provided a pressure gradient favourable to initiating recirculation, with weak currents in the island wake being drawn back toward the tip [*Signell and Geyer*, 1991]. The Bernoulli effect acts only along streamlines. At the point of flow separation, the bluff-body embayment provides no obstruction to the free-stream flow (Figure 2-7a), and since the free-stream current is not disrupted in any way, the Bernoulli effect cannot act. Sea-level set-down due to the Bernoulli effect does occur at the *downstream* side of the bay (Figure 2-7a), where currents must accelerate to pass out of the bay to the continental-shelf. However this is inconsequential in driving recirculation in the bay, which is dominated by processes occurring around the *upstream* wake. Despite absence of the Bernoulli effect, sea-level set-down is still observed in the upstream headland lee (Figure 2-7a), caused by horizontal shear entrainment from the wake into the free-stream flow. This is proved by decreasing A_H to 0.001 $m^2 s^{-1}$ (Exp. 2, Table 2-1), horizontal shear entrainment into the free-stream ceases and the set down disappears (Figure 2-7b). Horizontal shear entrainment clearly affects pressure gradients, which are known to influence eddy formation [*Black and Gay,* 1987; *Black,* 1989; *Signell and Geyer,* 1991]. No water is entrained from the bay at the point of flow separation, no set-down occurs, and this greatly changes the size of the wake, the pressure gradient distribution, and the eddy (Figure 2-7). Therefore, in coastal embayments lacking a significant projection into the free-stream, horizontal shear entrainment into the free-stream

will be a considerable contributor to recirculation, but the Bernoulli effect will not.

It has been shown that recirculation-favourable pressure gradients can occur in the lee of a headland tip, aided by the Bernoulli effect or horizontal shear entrainment, or a combination of both. The second important difference between the embayment geometry and a headland or island, is the enclosed coastline of the bay. The internal embayment dimensions become an important control on recirculation, because the enclosed coastline restricts sea-level adjustment and exaggerates pressure gradients compared with an open-coast headland or island.

To investigate this, flow was simulated around three new bathymetries, all with flat 27 m depth, to eliminate variations in flow that may arise from different seabed slopes. The existing bluff-body bay was modified to incorporate a flat seabed (Figure 2-8a, Exp. 3a, Table 2-1), an embayment of twice the horizontal dimensions was created by extending the original grid from 50 to 110 cells in the *J* direction (Figure 2-8b, Exp. 3b, Table 2-1), and a step bathymetry was created with the same land-sea (*I*) extent as the original bay but with no downstream coast (Figure 2-8c, Exp. 3c, Table 2-1). For comparison, all 3 plots in Figure 2-8 are shown zoomed over the same grid area, I = 33:50, J = 33:58. A steady 0.2 m s^{-1} shelf-current was used in each simulation, and since the geometry at the point of flow separation is identical (L identical), P is the same for all three situations. Examining the current vectors, a wake has formed in each simulation, in the lee of the upstream headland. A slow (~0.01 m s^{-1}) recirculating current has developed in the wake of the two embayments (Figure 2-8a,b), whereas no recirculation exists past the step simulation (Figure 2-8c). Examining the water levels (Figure 2-8d), the shelf-current pressure gradient has set-up water level against the inshore and downstream coasts, so that water level is highest in the small bay and lowest over the stepped headland. Importantly, from Figure 2-8d, the alongshore sea-level gradient (between the alongshore extremities) is highest in the small bay, and almost zero past the stepped headland. Figure 2-8 demonstrates that although the free-stream momentum and wake size is similar over all three bathymetries, stronger pressure gradients in the constricted embayments drive recirculation. It was also observed that recirculation began earlier in the small embayment, taking

longer to develop in the large bay. Pressure gradients are therefore an important influence on recirculation in a semi-enclosed coastal embayment, and these are not accounted for by the dimensionless parameter P.

2.4.3 Embayment eddy parameter

Since P by itself is an inadequate descriptor of the propensity for eddy formation in coastal embayments, we determined to quantify the change in P in the presence of a downstream coast (Exp. 4, Table 2-1). To account for this change, a dimensionless parameter P_0 was required. As for P in the presence of an island, P_0 in an embayment is expected to equal 1 when a stable wake is present. The change in P (dP) resulting from the downstream coast is then $dP = P_0 - P$.

Firstly, simulations were run in the absence of a downstream coast to calculate P. This was undertaken by modifying the flat seabed bathymetry (Figure 2-8a), removing the eastern land cells I = 56:90, J = 36:49 and replacing with 27 m depth continental-shelf, to create a step bathymetry. Using the step bathymetry, the steady shelf-current velocity at which recirculation was first observed was 0.15 m s^{-1}, which we define as U_0. Weaker currents produced no recirculation while faster currents produced stronger recirculation. Following *Wolanski et al.* [1984] (eddies form when $P \sim 1$), we assumed that $P = 1$ at velocity U_0. L was defined as equal to the bay cross-shore extent (the distance from the shore to the mouth). Therefore, L = 7000 m, U_0 = 0.15 m s^{-1}, h = 27 m, which from Equation 4 gives A_Z = 0.0156 m^2 s^{-1}. Simulations were then run using 27 m depth bluff-body embayments of widths w = 25, 20, 15 and 10 km in the along-shelf direction, while the cross-shore embayment extent (L) was held constant at 7 km. Since the depth and upstream headland dimensions (where flow separation occurs) remained constant, h, L and A_Z remained unchanged. U was varied to find the velocity of initial recirculation, from which P was calculated for each embayment width using Equation 4 (Table 2-2).

In keeping with the preceding results, Table 2-2 shows that in an embayment, the shelf-current velocity U required to produce recirculation decreases with embayment width w. Therefore, when P was calculated for embayments of decreasing width it became progressively smaller, as the velocity required to

produce a stable wake and to form an eddy simultaneously decreased (Table 2-2). Thus a stable wake and eddy can form at $P < 1$ if a downstream coast is present, and the $P \sim 1$ recirculation condition [*Wolanski et al.*, 1984] is invalidated. This necessitates the calculation of an equivalent *embayment* wake parameter P_0.

To associate increased propensity for eddies with increasing P values we defined the variable P_0 as $P_0 = 1 / P$. It is seen from Table 2-2 that P_0 increases as w decreases, so P_0 is a better indicator of the propensity for eddy formation in the *embayments* than P. The change in P (dP) caused by the presence of the downstream coast at velocity U_0 was then calculated as $dP = P_0 - P$ (Table 2-2).

Since bottom friction is expected to change the velocity required to initiate eddies, and thus affect P_0 and dP, an identical set of simulations was next undertaken using similar bathymetries but with a depth of 10 m (compared with 27 m initially used). The initial recirculation velocity over a 10 m depth step bathymetry (no downstream coast) was $U_0 = 0.7$ m s^{-1}, which using $L = 7000$ m and $h = 10$ m gave $A_Z = 0.1$ m^2 s^{-1}. As above, calculations of dP, were repeated for the 10 m deep bathymetry (Table 2-2).

In searching for a dimensionless relationship to account for dP in the presence of a downstream coast, it was found that by adjusting dP with the dimensionless parameter $\frac{L^2}{h^2}$, data from simulations of different depth could be closely aligned (Figure 2-9a & 9b show the differences with and without normalisation). Dividing dP by h^2 acted to align the two data sets by accounting for the frictional influence of depth on eddy formation. Multiplication by L^2 simply provided a scaling factor to keep the relationship dimensionless, but had no effect on the data alignment since L remained identical between data sets.

To account for variation in L, simulations were repeated using bathymetries with L changed from 7000 m to both 5000 m and 9000 m, and dP was re-calculated following the method outlined above (Table 2-3). Eddies were slightly less inclined to form when L was decreased (because wake size was reduced) and vice

versa when increased, but the effect of changing L was minor in comparison to changing w (Figure 2-10).

A power-curve relationship could then be fitted:

$$dP\frac{L^2}{h^2} = 504300(\frac{w}{L})^{-2.9022} \quad (5)$$

having an adjusted $r^2 = 0.970$ (Figure 2-10). We therefore propose an embayment eddy parameter E, for prediction of recirculation in coastal embayments under steady shelf-currents:

$$E = P + dP \quad (6)$$

$$\text{where } dP = 5.0\times10^5(\frac{w}{L})^{-2.9022} \times \frac{h^2}{L^2} \quad (7)$$

Recirculation is induced by a steady shelf-current when E is ~1 or greater. E is based on P, but includes a correction factor dP to allow for recirculation-favourable pressure gradients set up against the downstream coast of an embayment. These effects are least for wide embayments and greatest for narrow embayments (Figure 2-10). The 10×7 km embayment used in initial simulations of steady shelf-currents (section 3.3.1) has a dP value of ~3 (Table 2-2), explaining why P was initially observed to be under-predicting recirculation.

The power coefficient for non-dimensionalised embayment width (w/L) in Equations 5 and 7 is close to an inverse cubic. If the inverse cubic relationship is assumed, then Equation 7 can be re-arranged to:

$$dP = K\frac{L}{w}(\frac{h}{w})^2 \quad (8)$$

where K is an unknown constant. The change in propensity for eddy formation (dP) in a coastal embayment compared with that of an island can therefore be quantified in terms of two dimensionless length-scale ratios. The propensity for

eddy formation increases with the ratio $\frac{L}{w}$, since this provides a geometric control on the size of the wake in which eddies form (eg. Figure 2-6). The propensity for eddy formation is more sensitive to the second ratio $\frac{h}{w}$, which represents the degree of frictional eddy damping within the embayment. As $\frac{h}{w}$ increases, frictional damping decreases within the embayment and eddies are more likely to form.

Re-fitting Equation 8 to the data in Figure 2-10 gave $K = 514814$, with an adjusted r^2 fit of 0.971. Therefore

$$dP = 5.1\times10^5 \frac{L}{w}(\frac{h}{w})^2 \tag{9}$$

Since the results of *Black* [1989] show that A_H affects the propensity for eddy formation, the precise value of K is expected to vary if A_H is changed in the model. The numerical dependence of K on A_H is not fully known in the context of this paper and is left for future investigation. However, A_H used in this study was chosen to be representative of natural horizontal diffusion and therefore K should be close to that observed in natural embayments.

2.4.4 Smooth bathymetry

Simulations of flow around a bluff-body are useful for determining the parameters governing recirculation where flow separation occurs, but coastal embayments are seldom sheer-sided in nature. Except for the reef at its northern margin, Poverty Bay itself has generally smooth bathymetric contours (Figure 2-1), and accordingly we investigated flow over the smooth bathymetry (Figure 2-3b). Having no prominent bathymetric projections at which flow separation is likely to occur, there are important differences in the mechanisms driving recirculation.

Simulations of steady currents of up to 2 m s^{-1} (Exp. 5, Table 2-1) showed that although a wake was formed in the embayment, abrupt flow separation was absent

and no recirculation was observed in the smooth embayment (Figure 2-11). However, recirculation was induced on the introduction of flow unsteadiness (Exp. 6, Table 2-1), driven by the 'phase-eddy mechanism' of *Black and Gay* [1987]. On deceleration of the free-stream flow, the slow frictionally-damped shelf-current at the inner margins of the bay reverses, in response to a water level gradient created as the shelf-current decelerates. This is the principle mechanism by which phase eddies are formed under transient currents [*Black and Gay*, 1987], the faster the flow deceleration, the stronger the water level gradient encouraging flows to reverse. *Signell and Geyer* [1991] also recognised the importance of flow unsteadiness to recirculation, and used the Keulegan-Carpenter number K_c to account for the balance between advection of momentum and local acceleration created by unsteady flows. *Signell and Geyer* [1991] demonstrated four flow regimes characterised by a combination of K_c and an equivalent Reynolds number Re_f, that similarly to P, characterises the balance of advection to friction. The combination of Re_f and K_c can therefore be used to predict the expected nature of the flow field downstream from an obstruction. However, P and K_c are difficult to apply to the smooth embayment, because they require a characterising length scale for the obstruction, difficult in the smooth embayment.

Figure 2-12 demonstrates the process by which a phase eddy forms in the smooth embayment (Exp. 6, Table 2-1). As shown in Figure 2-11, inertia carries the free-stream current past the bay, while high frictional damping helps slow currents in the inner bay, creating a cross-shore velocity gradient. On flow deceleration the pressure gradients oppose the initial free-stream current direction (Figure 2-12a), and due to higher frictional influence, the slower shallow water currents succumb and reverse first, forming a phase eddy (Figure 2-12b). This happens without prior flow separation. Previous numerical studies of recirculating flow around bluff-body headlands and islands, have identified eddies that form where flow separation occurs [*Wolanski, et al.,* 1984; *Signell and Geyer,* 1991; *Middleton et al.,* 1993]. *Signell and Geyer* [1991] observed that when flow along a boundary encounters an adverse pressure gradient, the deceleration due to the combined effect of the pressure gradient and the frictional drag causes the flow very close to the boundary to reverse. Away from the boundary, however, where frictional effects are not as strong, there is adequate momentum to keep the flow from

reversing. This results in flow separation, as the flow reversal near the boundary pushes the boundary layer streamlines offshore. *Signell and Geyer* [1991] then concluded that eddies around headlands originate from vorticity generated in a narrow boundary layer along the headland, where the flow separates. The vorticity is then injected into the interior at the point of flow separation. In our simulations of flow over a smooth embayment, we have shown that recirculation is generated over a much broader area than a narrow boundary layer. In the embayment, only two things must exist in order for recirculation to occur. There must be (i) a velocity gradient – such as created by increased friction in shallow water and (ii) a pressure gradient acting opposite to the free-stream that is strong enough to overcome the slower currents (Figure 2-12). Recirculation will begin wherever these two conditions are met, and for unsteady flows this does not require flow separation. In other two-dimensional studies, flow separation has always occurred prior to eddy formation, and recirculation has been assumed to be dependent on flow separation [*Wolanski et al.,* 1984; *Signell and Geyer,* 1991]. The reason that eddy formation is much stronger when flow separation does occur, is because flow separation helps to create a clearly defined wake, therefore the free-stream/wake velocity gradient is more pronounced (eg. Figure 2-6). However, this is simply an extreme case of the velocity gradient required for recirculation.

These results are not limited to unsteady flows. Re-examining eddy formation under steady current conditions (Figure 2-8, Exp. 1, Table 2-1), it is seen that the same two conditions are met, (i) a velocity gradient exists between the free-stream and the wake, and (ii) recirculation-favourable pressure gradients exist. However, eddy formation under steady conditions does require prior flow separation, so as to create recirculation-favourable pressure gradients through either horizontal shear entrainment or the Bernoulli effect. Nevertheless, prerequisites (i) and (ii) must still exist for eddy formation.

2.4.5 Reef effects

Poverty Bay has a rocky reef that projects out onto the continental-shelf from Tuaheni Point at the northern headland (Figure 2-1). The coarse reef has a greater bed roughness than the surrounding sandy substrate, and this will exert a greater

frictional effect on the water column, as shown by the friction terms(7) in the momentum equation (1). Further to this, *Middleton et al.* [1993] showed that high bed roughness can create associated turbulence that will raise local eddy viscosities, thereby affecting recirculation. Accordingly, we investigated how a point reef may affect embayment recirculation, through raised bed roughness and horizontal eddy viscosity.

The effects of a reef with high bed roughness were investigated by increasing z_0 from 0.001 m to 0.1 m at the eastern bay margin in model cells $I = 52{:}56$, $J = 30{:}42$ (Figure 2-13a, Exp. 7, Table 2-1). In water depth 27 m, this reduces Chezy's C from 72 to 36. From the quadratic friction term(7), this raises frictional deceleration by an order of magnitude and slows the shelf-current over the reef. If the shelf-current is accelerating, this causes the pressure gradient to increase over the reef (Figure 2-13b), but if the shelf-current is decelerating then water takes longer to flow off the reef area, resulting in a pressure gradient low. The net result is that shelf-current velocities are considerably reduced downstream of the reef, and these slow nearshore currents reverse earlier in response to the phase-eddy mechanism. This increases recirculation both in the bay and on the shelf adjacent to the reef, leading to the residual circulation shown in Figure 2-13a. The process is analogous to a topographic high over the reef area (Figure 2-14, Exp. 9, Table 2-1).

Middleton et al. [1993] argued that horizontal eddy viscosity A_H is often raised at headlands due to the increased turbulence of flow over irregular bottom topography. They concluded that rough bathymetry at Bass Point, Australia, raised A_H and prevented the formation of a narrow shear layer near the obstruction tip. Despite the existence of strong shelf-currents, recirculation was thereby prohibited due to lack of flow separation. A simulation was run with A_H raised from 1.0 to 10 $m^2 s^{-1}$ over the reef area, and z_0 returned to its background level of 0.001 m (Figure 2-15, Exp. 8, Table 2-1). The reef with high A_H has a similar effect to the reef with high z_0, reducing the shelf-current velocity on its downstream side. The effect of increasing A_H is to smooth out current shear caused by differential friction over the shallow inshore, compared with the deeper offshore, seabed. The result is to transfer momentum from faster offshore

currents to the slow currents adjacent to the land boundary, resulting in faster currents directly adjacent to the land. This further increases frictional dissipation in the shallow area by the quadratic friction law, and the net effect is to slow currents over the reef area. In other words, increasing A_H effectively increases frictional dissipation, by transferring momentum from fast offshore currents to the dissipative inshore region. Since currents are reduced in strength downstream of the reef, the phase-eddy mechanism results in earlier recirculation.

This result is opposite to the conclusions of *Middleton et al.* [1993], in that a reef with increased A_H promotes eddy formation rather than disturbing it. While field data provided good support for the theory of *Middleton et al.* [1993], numerical simulations were preliminary and less convincing, although later simulations by *Denniss et at.* [1995] supported the result. Clearly this is not the case for our simulations and this may be related to the model coding whereby 3DD allows for direct enhancement of A_H at any point on the grid. *Middleton et al.* [1993] did not include a horizontal eddy viscosity term and simulated increased turbulence by increasing the complexity of the bottom topography (and thus turbulence). Also, since recirculation is being driven almost exclusively by the phase-eddy mechanism in our simulations, a horizontal shear layer associated with flow separation is not so important to eddy formation.

2.4.6 Depth alterations

The interior of Poverty Bay is slightly deeper over the northeast half, evident from the 20 m contour (Figure 2-1). Consequently, a simulation was run incorporating a smooth grid with the eastern outer margin of the bay deepened by 4 m, undertaken by subtracting 4 m from grid cells $I = 46{:}52$, $J = 36{:}42$ (Figure 2-16a, Exp. 10, Table 2-1). The residual circulation over the modified embayment (Figure 2-16a) shows little influence in comparison to the unchanged bay (Figure 2-16b), indicating that headland or reef effects at the bay margins will be far more influential. The result is a slightly stronger residual eddy over the deepened half of the bay. This occurs because the phase eddy grows stronger under a decelerating shelf-current flowing from east to west. Deepening the east section reduces frictional effects, allowing the eddy to grow stronger once recirculation is

established. This result indicates that in coastal embayments with considerable bathymetric asymmetry, if headland effects are not considered, then phase eddies should grow larger over the deeper section. This matches well with observations of flood-ebb disparity between tidally induced recirculation eddies in Nan Wan Bay [*Lee et al.*, 1999b]. Our result suggests that asymmetric frictional influences are likely to be a contributing factor to the flood-ebb eddy disparity, although *Lee et al.* [1999b] found other topographic features to dominate due to their steering effect on the tidal currents.

2.5 CONCLUSIONS

Simulations of steady flow past a bluff-body embayment showed eddies to be 'headland eddies', dominated by the wake dimensions and with stable wake conditions predicted by P. However, the embayment has important topographic variations that influence recirculation and are not provided by islands or headlands. Where there is no topographic projection into the free-stream flow-lines, the recirculation-favourable pressure minimum associated with the Bernoulli effect is absent. A recirculation-favourable pressure minimum is created by horizontal shear entrainment from the wake into the free-stream instead. The enclosed geometry of an embayment enhances recirculation-favourable pressure gradients in comparison to an open island or headland, as water sets up against the downstream coast. Results showed that the smaller the embayment, the stronger the recirculation-favourable pressure gradient across the mouth, and the earlier eddies will form under a given shelf-current regime. An embayment eddy parameter E was developed to account for the downcoast effect of an enclosed embayment. Based on P, this parameter allows prediction of recirculation in open-coast embayments under steady shelf-current conditions.

We have shown that two factors exist prior to eddy formation under both steady and unsteady flow conditions: (i) a velocity gradient (wake) exists, due either to abrupt flow separation, or in response to larger scale inertial and frictional forces, or some combination; (ii) a pressure gradient acts opposite to the free-stream flow, assisting the slower inshore currents to reverse earlier than in the free-stream. In

unsteady flow, pressure gradients are created by flow acceleration or deceleration, and we have shown that recirculation may begin in the absence of prior flow separation. In steady flow, pressure gradients are created through either horizontal shear entrainment or the Bernoulli effect, and flow separation must therefore occur prior to eddy formation. Flow separation provides an extreme velocity gradient, however the processes that result in flow separation (inertia and current shear) are separate to the velocity and pressure gradients that drive recirculation across a wake. Since flow separation results in a clearly defined wake, it provides conditions conducive to eddy formation, but our simulations of unsteady flow over a smooth bathymetry show that flow separation and eddy formation can be entirely separated, and should not be confused. Our simulations show that eddy formation need not involve advection of vorticity from a narrow boundary layer at the flow separation point, as shown to be important in some situations by *Signell and Geyer* [1991].

In smooth coastal embayments where headland effects are minor, the presence of a point reef has a strong influence on recirculation, facilitating earlier development and stronger growth of phase eddies. Simulations showed this can occur due to both increased friction over the reef and to associated turbulence increasing horizontal eddy viscosity. Both processes result in increased frictional dissipation over the reef, slowing the shelf-current and aiding the phase-eddy mechanism. Reef effects were found to be considerably stronger than minor bathymetric asymmetry in the embayment.

2.6 ACKNOWLEDGEMENTS

The authors wish to thank anonymous reviewers for their suggestions leading to many improvements to this manuscript.

2.7 REFERENCES

Black, K.P., A numerical sediment transport model for application to natural estuaries, harbours and rivers, in *Numerical modelling applications to marine systems*, edited by J. Noye, pp. 77-105, Elsevier, North Holland, 1987.

Black, K.P., Numerical Simulation of Steady and Unsteady Meso-scale Eddies, 9th Australasian Conference on Coastal and Ocean Engineering, Adelaide, pp. 204-208, 1989.

Black, K.P., R.G. Bell, J.W. Oldman, G.S. Carter, and T.M. Hume, Features of 3-dimensional barotropic and baroclinic circulation in the Hauraki Gulf, New Zealand, *New Zealand Journal of Marine and Freshwater Research*, *34*, 1-28, 2000.

Black, K.P., and S.L. Gay, Eddy Formation in Unsteady Flows, *Journal of Geophysical Research*, *92* (C9), 9514-9522, 1987.

Black, K.P., and S.L. Gay, Reef-scale numerical hydrodynamic modelling developed to investigate crown-of-thorns starfish outbreaks, in *Acanthaster and the Coral Reef: A Theoretical Perspective*, edited by R. Bradbury, pp. 120-150, Springer-Verlag, 1991.

Black, K.P., D. Hatton, and M. Rosenberg, Locally and externally-driven dynamics of a large semi-enclosed bay in southern Australia, *Journal of Coastal Research*, *9* (2), 509-538, 1993.

Black, K.P., T.R. Healy, and M. Hunter, Sediment dynamics in the lower section of a mixed sand and shell-lagged tidal estuary, *Journal of Coastal Research*, *5* (3), 503-521, 1989.

Deleersnijder, E., A. Norro, and E. Wolanski, A Three Dimensional model of the water circulation around an island in shallow water, *Continental-shelf Research*, *12* (7/8), 891-906, 1992.

Denniss, T., and J.H. Middleton, Effects of viscosity and bottom friction on recirculating flows, *Journal of Geophysical Research*, *99* (C5), 10183-10192, 1994.

Denniss, T., J.H. Middleton, and R. Manasseh, Recirculation in the lee of complicated headlands: A case study of Bass Point, *Journal of Geophysical Research*, *100* (C8), 16087-16101, 1995.

Ferentinos, G., and M. Collins, Effects of Shoreline Irregularities on a Rectilinear Tidal Current and their significance in sedimentation processes, *Journal of Sedimentary Petrology*, *50*, 1081-1094, 1980.

Foster, G., and L. Carter, Mud Sedimentation on the Continental-shelf at an accretionary margin - Poverty Bay, New Zealand, *New Zealand Journal of Geology and Geophysics*, *40*, 157-173, 1997.

Furukawa, K., and E. Wolanski, Shallow Water Frictional Effects in Island Wakes, *Estuarine, Coastal, and Shelf Science*, *31*, 231-253, 1998.

Gill, A.E., *Atmosphere-Ocean Dynamics*, 662 pp., Academic Press, San Diego, 1982.

Imasato, N., What is tide induced Residual Current?, *Journal of Physical Oceanography*, *13*, 1307-1317, 1983.

Klinck, J.M., Circulation Near Submarine Canyons: A Modelling Study, *Journal of Geophysical Research*, *101* (C1), 1211-1223, 1996.

Lee, H.J., S.Y. Chao, K.L. Fan, and T.Y. Kuo, Tide-induced eddies and upwelling in a semi-enclosed basin: Nan Wan, *Estuarine, Coastal and Shelf Science*, *49*, 775-787, 1999a.

Lee, H.-J., S.-Y. Chao, and K.-L. Fan, Flood-ebb disparity of tidally induced recirculation eddies in a semi-enclosed basin: Nan Wan Bay, *Continental-shelf Research*, *19* (7), 871-890, 1999b.

Middleton, J.F., and K.P. Black, The low frequency circulation in and around Bass Strait: a numerical study, *Continental-shelf Research*, *14* (13/14), 1495-1521, 1994.

Middleton, J.H., D.A. Griffin, and A.M. Moore, Oceanic Circulation and Turbulence in the Coastal Zone, *Continental-shelf Research*, *13* (2/3), 143-168, 1993.

Pattiaratchi, C., A. James, and M. Collins, Island Wakes: a comparison between remotely sensed data and laboratory experiments, *Journal of Geophysical Research*, *92* (C1), 783-794, 1987.

Perenne, N., J. Verron, D. Renouard, D.L. Boyer, and X. Zhang, Rectified Barotropic Flow over a Submarine Canyon, *Journal of Physical Oceanography*, *27*, 1868-1893, 1997.

Ridderinkhof, H., Tidal and Residual Flows in the Western Dutch Wadden Sea III: Vorticity Balances., *Netherlands Journal of Sea Research*, *24* (1), 9-26, 1989.

Signell, R.P., and W.R. Geyer, Transient Eddy Formation Around Headlands, *Journal of Geophysical Research*, *96* (C2), 2561-2575, 1991.

Stephens, S.A., Wind, Shelf-current and Density-Driven Circulation in Poverty Bay, New Zealand, Unpublished PhD thesis, The University of Waikato, Hamilton, 2000.

Stephens, S.A., K.P. Black, T.R. Healy, and B. Tahata, Circulation in Poverty Bay New Zealand: A verification of numerical modelling predictions, in *Coasts and Ports '99: Challenges and Directions for the New Century*, pp. 639-643, National Committee on Coastal and Ocean Engineering, Institution of Engineers, Australia, Perth, 1999.

Wolanski, E., T. Asaeda, A. Tanaka, and E. Deleersnijder, 3-Dimensional Island Wakes in the Field, Laboratory Experiments and Numerical Models, *Continental-shelf Research*, *16* (11), 1437-1452, 1996.

Wolanski, E., J. Imberger, and M.L. Heron, Island Wakes in Shallow Coastal Waters, *Journal of Geophysical Research*, *89* (C6), 10553-10569, 1984.

Young, I.R., K.P. Black, and M.L. Heron, Circulation in the Ribbon Reef region of the Great Barrier Reef, *Continental-shelf Research*, *14* (2/3), 117-142, 1994.

2.8 TABLES

Table 2-1. List of numerical experiments described in text. Bluff bathymetries are based on Figure 2-3a while smooth bathymetries are based on Figure 2-3b. Parameters included in the table are: experiment identification number, embayment bathymetry type, additional simulation features, embayment width (w), embayment cross-shore extent (L), horizontal eddy viscosity (A_H), continental-shelf-current velocity (U), and flow regime – either steady or unsteady. Unless otherwise specified (eg. Table 2-2 & Table 2-3), all experiments included depth h = 27 m, roughness length z_0 = 0.001 m and unsteady flow regimes had a cycle period T = 48 hours.

Exp. #	Embayment type	Additional features	W (m)	L (m)	A_H ($m^2 s^{-1}$)	U ($m s^{-1}$)	Flow regime
1	Bluff	Sloping seabed	10000	7000	1	0.3	Steady
2	Bluff	Sloping seabed	10000	7000	0.0001	0.3	Steady
3a	Bluff	Flat seabed	10000	7000	1	0.2	Steady
3b	Bluff	Flat seabed	20000	14000	1	0.2	Steady
3c	Bluff	Flat seabed – Step	∞	7000	1	0.2	Steady
4	Bluff	Step and embayment, 30 combinations, see Table 2-2 & Table 2-3					
5	Smooth	–	10000	–	1	< 2	Steady
6	Smooth	–	10000	–	1	0.2	Unsteady
7	Smooth	Included reef of z_0 = 0.1 m	10000	–	1	0.2	Unsteady
8	Smooth	Reef of A_H = 10 $m^2 s^{-1}$	10000	–	1	0.2	Unsteady
9	Smooth	Includes 5 m high reef	10000	–	1	0.2	Unsteady
10	Smooth	Eastern bay deepened 4 m	10000	–	1	0.2	Unsteady

Table 2-2. Quantification of the change in P (Equation 4) resulting from recirculation-favourable pressure gradients in the presence of a downstream coast (coastal embayment). Parameters included in the table are: description of bathymetry type, embayment width (w), embayment cross-shore extent (L), vertical eddy viscosity (A_Z), embayment width non-dimensionalised by cross-shore embayment extent (w/L), velocity of initial recirculation (U), island wake parameter P (calculated for both step and bay), equivalent embayment wake parameter (P_0), change in P (dP) and $dP \times L^2/h^2$.

Description	W (km)	L (km)	A_Z ($m^2 s^{-1}$)	w/L	U ($m s^{-1}$)	$1 \quad P$	P_0	dP	$dP \times L^2/h^2$
Continental-shelf and embayment depth = 27 m									
Step	∞	7	0.0156	∞	0.15	1	1	0	0
Bay	25	7	0.0156	3.5714	0.14	0.9333	1.07	0.07	4075
Bay	20	7	0.0156	2.8571	0.12	0.8	1.25	0.25	16804
Bay	15	7	0.0156	2.1429	0.09	0.6	1.6667	0.6667	44810
Bay	10	7	0.0156	1.4286	0.04	0.2667	3.75	2.75	184842
Continental-shelf and embayment depth = 10 m									
Step	∞	7	0.01	∞	0.7	1	1	0	0
Bay	25	7	0.01	3.5714	0.68	0.97	1.03	0.03	14700
Bay	20	7	0.01	2.8571	0.66	0.94	1.06	0.06	29400
Bay	15	7	0.01	2.1429	0.63	0.9	1.11	0.11	53900
Bay	10	7	0.01	1.4286	0.50	0.71	1.4	0.4	196000

Table 2-3. Quantification of the change in P (Equation 4) resulting from recirculation-favourable pressure gradients in the presence of a downstream coast (coastal embayment). Parameters included in the table are: description of bathymetry type, embayment width (w), embayment cross-shore extent (L), vertical eddy viscosity (A_Z), embayment width non-dimensionalised by cross-shore embayment extent (w/L), velocity of initial recirculation (U), island wake parameter P (calculated for both step and bay), equivalent embayment wake parameter (P_0), change in P (dP) and $dP \times L^2/h^2$.

Description	W (km)	L (km)	A_Z ($m^2 s^{-1}$)	w/L	U ($m s^{-1}$)	$2 \quad P$	P_0	dP	$dP \times L^2/h^2$
Continental-shelf and embayment depth = 27 m									
Step	∞	5	0.0233	∞	0.16	1	1	0	0
Bay	25	5	0.0233	5	0.15	0.94	1.07	0.07	2286
Bay	20	5	0.0233	4	0.13	0.81	1.23	0.23	7913
Bay	15	5	0.0233	3	0.10	0.63	1.6	0.6	20576
Bay	10	5	0.0233	2	0.05	0.31	3.2	2.2	75446
Step	∞	9	0.0113	∞	0.14	1	1	0	0
Bay	25	9	0.0113	2.7778	0.13	0.93	1.08	0.08	8889
Bay	20	9	0.0113	2.2222	0.11	0.79	1.27	0.27	30000
Bay	15	9	0.0113	1.6667	0.08	0.57	1.75	0.75	83333
Bay	10	9	0.0113	1.1111	0.03	0.21	4.7	3.7	407407
Continental-shelf and embayment depth = 10 m									
Step	∞	5	0.0144	∞	0.72	1	1	0	0
Bay	25	5	0.0144	5	0.70	0.97	1.03	0.03	7500
Bay	20	5	0.0144	4	0.68	0.94	1.06	0.06	15000
Bay	15	5	0.0144	3	0.64	0.9	1.13	0.13	31250
Bay	10	5	0.0144	2	0.51	0.71	1.41	0.41	102500
Step	∞	9	0.0077	∞	0.69	1	1	0	0
Bay	25	9	0.0077	2.7778	0.67	0.97	1.03	0.03	24300
Bay	20	9	0.0077	2.2222	0.64	0.93	1.08	0.08	64800
Bay	15	9	0.0077	1.6667	0.61	0.88	1.13	0.13	105300
Bay	10	9	0.0077	1.1111	0.49	0.71	1.41	0.41	332100

2.9 FIGURES

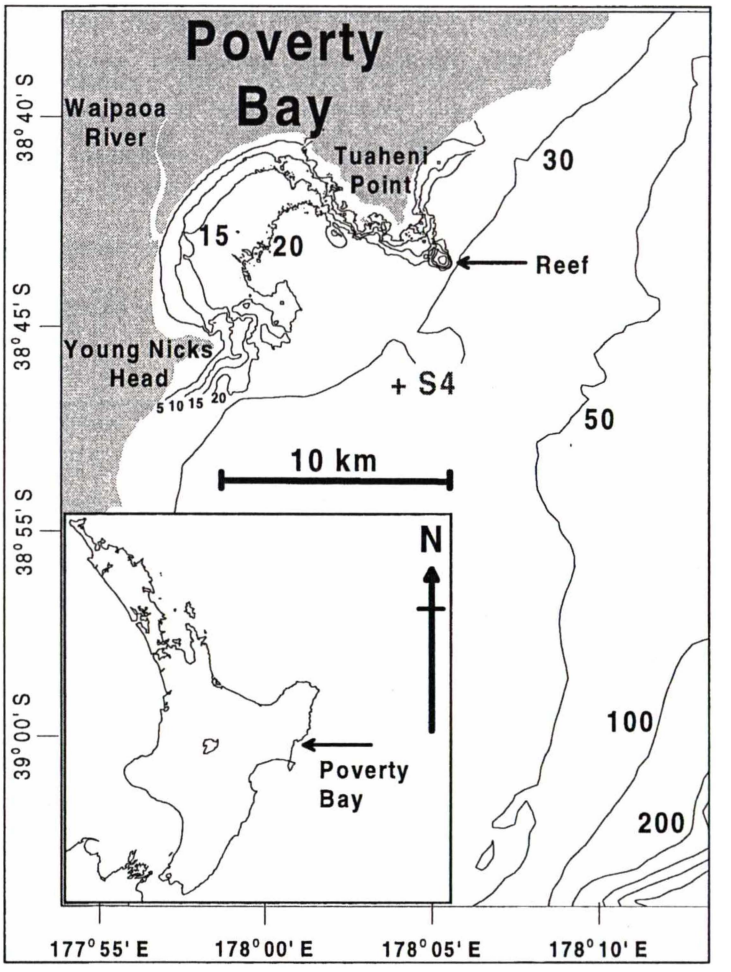

Figure 2-1. Location map of Poverty Bay, New Zealand showing bathymetric contours and the S4 current-meter location (see Figure 2-4).

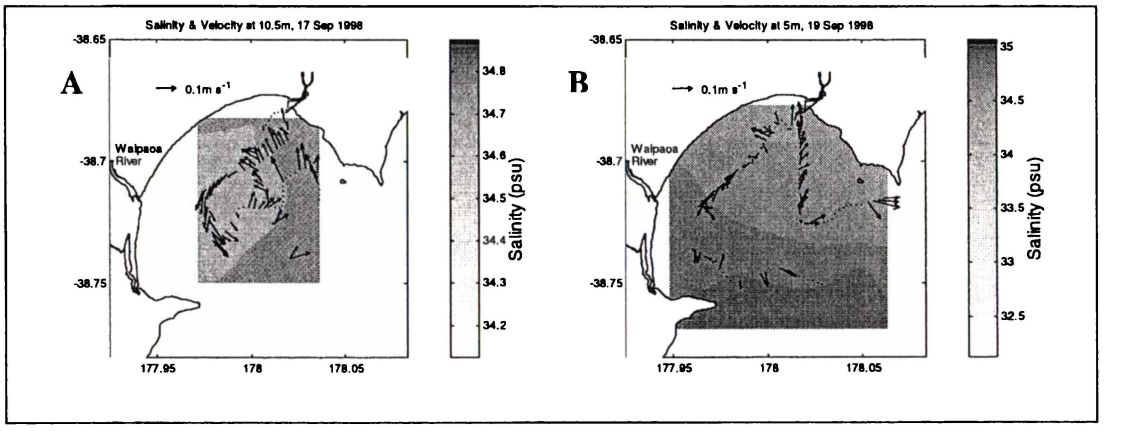

Figure 2-2. A) Circulation and salinity in Poverty Bay measured by vessel-mounted acoustic Doppler profiler and CTD probe: A) at 10 m depth on 17 September 1998, B) at 5 m depth on 19 September 1998.

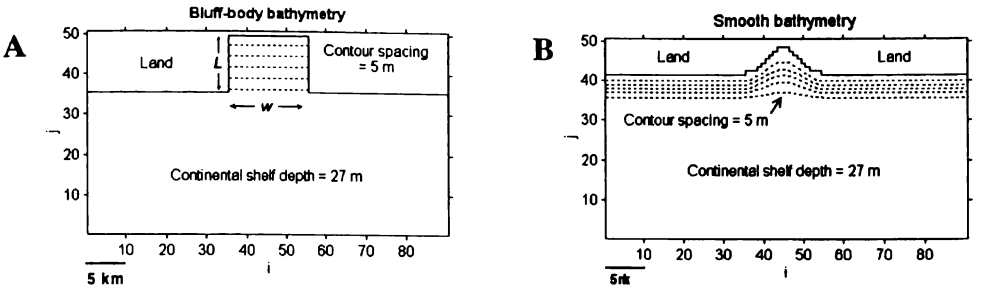

Figure 2-3. Model grids used for simulations: (a) bluff-body; (b) smooth.

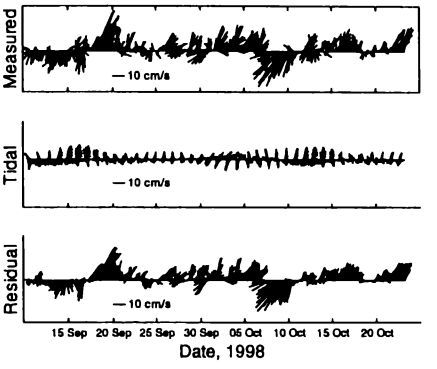

Figure 2-4. Measured tidal and residual current components at S4 (2) deployment site (Figure 2-1). The S4DW was deployed on the continental-shelf, approximately 24 m above the bed in 35 m water depth, six kilometres outside the Poverty Bay entrance. Shelf-current velocities range from 0.003-0.36 m s^{-1}.

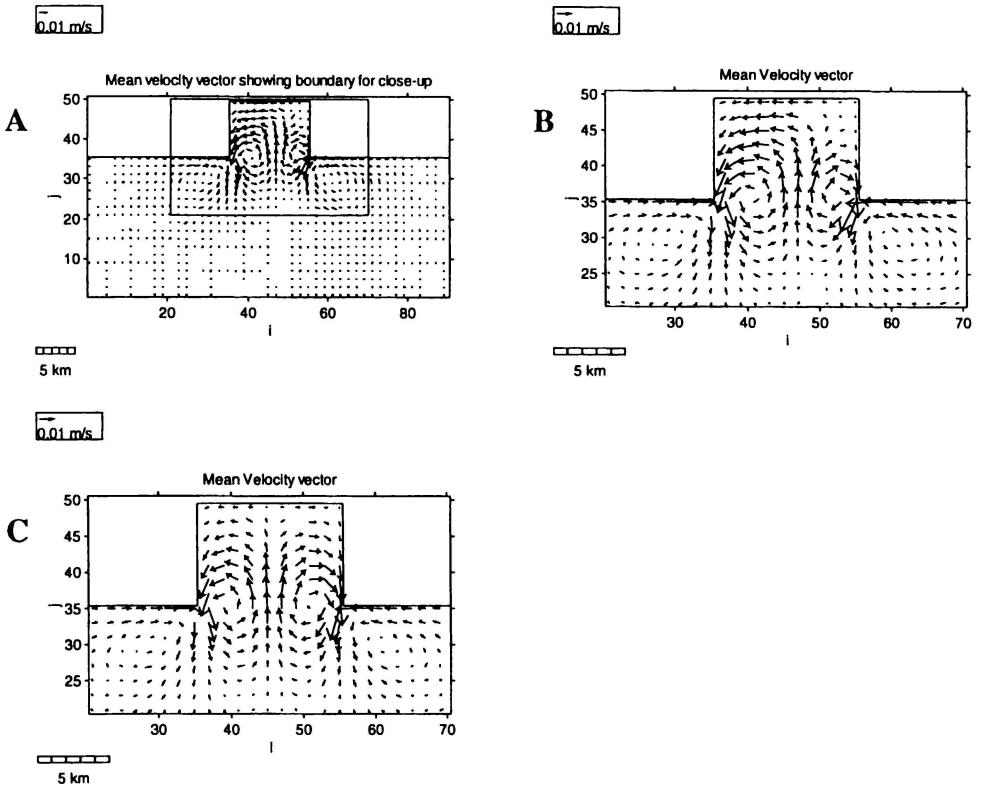

Figure 2-5. Circulation over the bluff-body grid induced by a shelf-current with velocity described by *0.2 cos[(2π/172800) t]* m s^{-1}, positive to the east, time-averaged between 172800-518400 s (two cycles): (a) Full model grid, showing marked boundary for close up plots; (b) close up view of (a), revealing dominance of anticyclonic eddy when Coriolis is included; (c) close up view of bay showing equal-sized residual eddies when Coriolis is removed from the simulation.

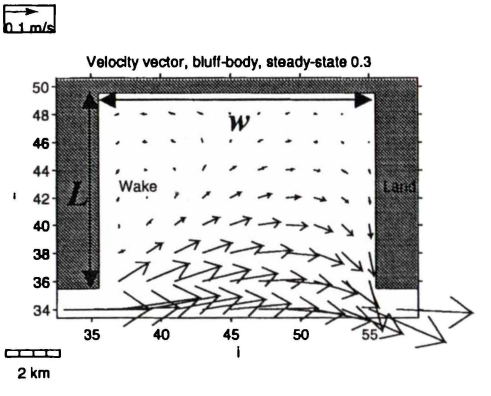

Figure 2-6. Circulation in the bluff-body bay after 48 hours of steady 0.3 m s^{-1} shelf-current flow. Flow separation at the upstream headland has created a clearly defined wake, and weak (~0.01 m s^{-1}) recirculation is evident. *L* is the cross-shore embayment length scale, *w* is the embayment width.

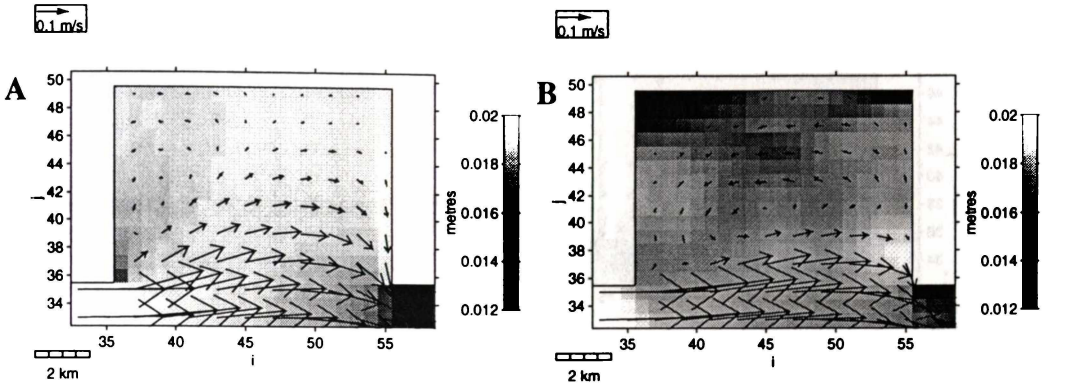

Figure 2-7. Circulation in the bluff-body bay after 48 hours of steady 0.3 m s^{-1} shelf-current flow: (a) inertia carries the free-stream current past the upstream headland, causing flow separation and creating a wake, sea-level is set down in the wake adjacent to the free-stream due to horizontal shear entrainment; (b) on decreasing A_H to 0.001 m^2 s^{-1}, horizontal shear entrainment into the free-stream ceases and the set down disappears. In both simulations, sea-level set-down is induced at the downstream coast, by currents accelerating from the bay onto the continental-shelf (Bernoulli effect). Vectors indicate velocity and shading indicates sea-level in metres, as per the given scale.

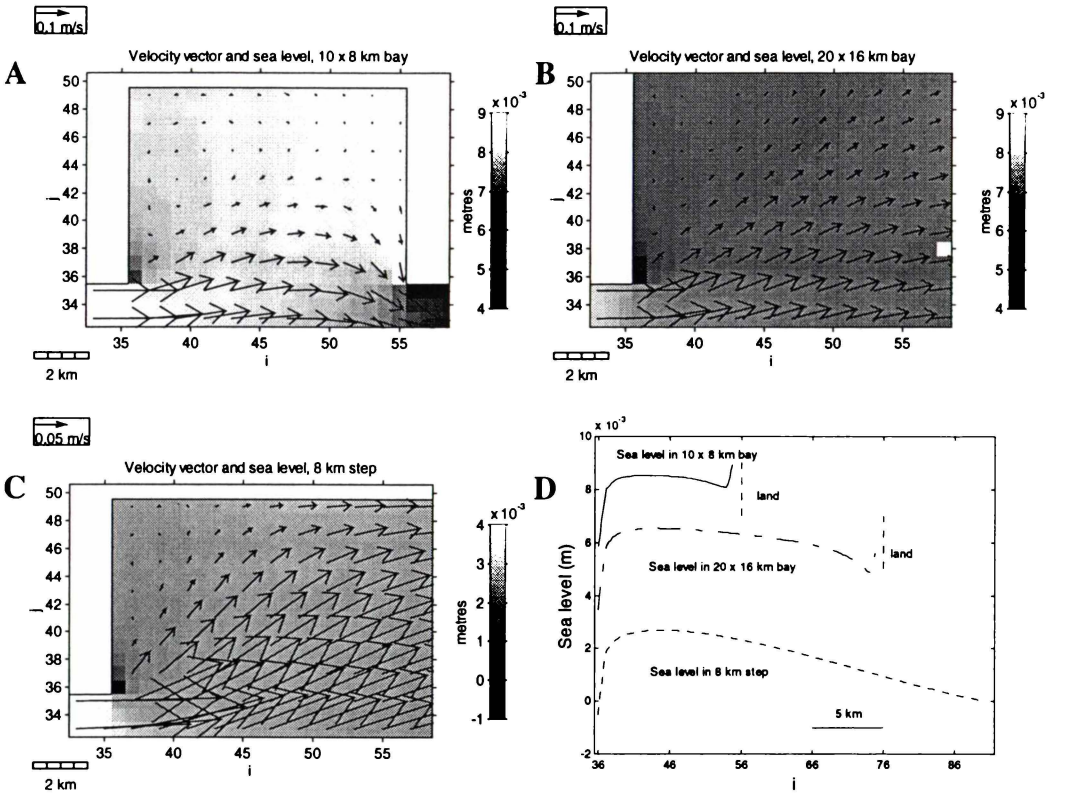

Figure 2-8. Circulation in three bluff-body bathymetries after 48 hours of steady 0.3 m s^{-1} shelf-current flow, shown zoomed over the grid area I = 33:50, J = 33:58: (a) the existing bluff-body bay (Figure 2-3a) was modified to incorporate a flat seabed; (b) an embayment of twice the horizontal dimensions was created by extending the original grid from 50 to 70 cells in the J direction; (c) a step bathymetry was created with the same land-sea extent as the original bay but with no downstream coast; (d) sea-level measured over an alongshore transect through J = *36* for the three bathymetries. Vectors indicate velocity and shading indicates sea-level in metres, as per the given scale.

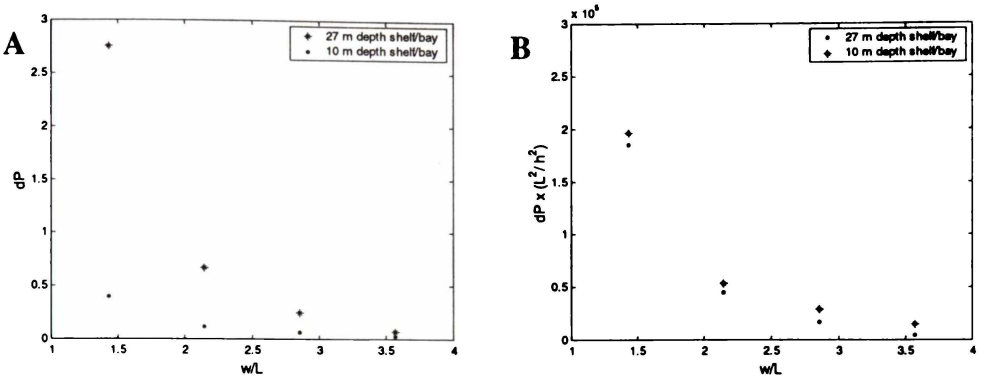

Figure 2-9. (a) Change in P (dP) versus embayment width, non-dimensionalised using L (w/L), for continental-shelf/embayment depths of 27 and 10 m; (b) $dP \times L^2/h^2$ versus w/L. Continental-shelf and embayment depth has been accounted for by multiplying dP by the dimensionless parameter L^2/h^2.

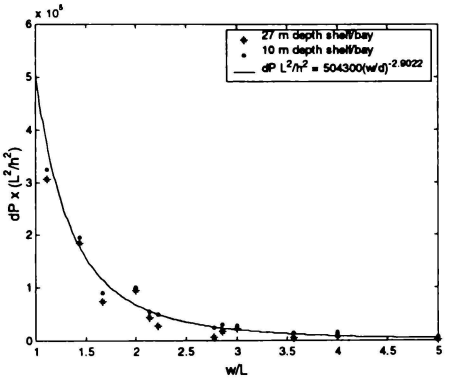

Figure 2-10. $dP \times L^2/h^2$ versus w/L, incorporating data using varying L. The fitted power curve relationship has an adjusted $r^2 = 0.970$.

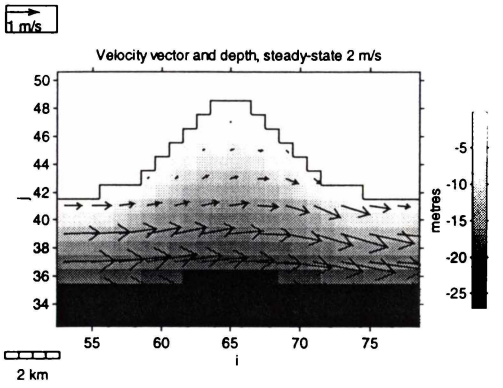

Figure 2-11. Velocity field (vector) and bathymetry (shading in m) over the smooth bathymetry (Figure 2-3b), induced by 48 hours of steady 2 m s^{-1} shelf-current flow. No recirculation is evident. Note high frictional damping over the shallow inshore area.

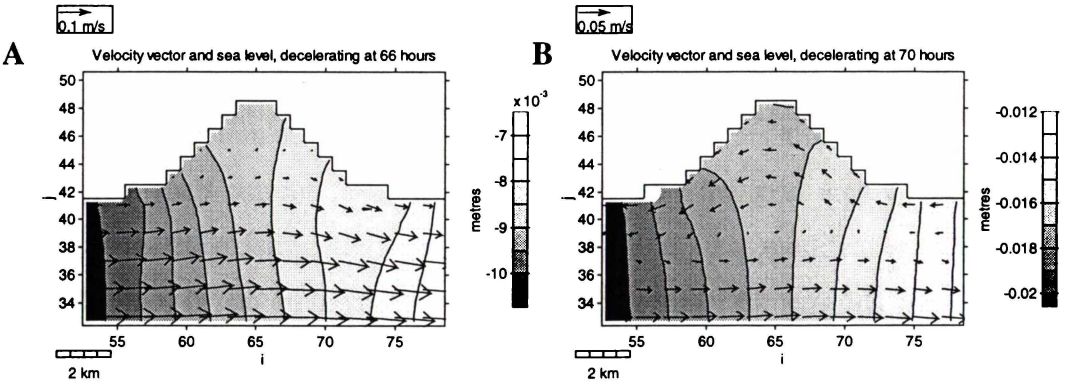

Figure 2-12. Velocity field (vector) and sea-level (shading in m) induced by a shelf-current with velocity described by $0.2\ cos[(2\pi/172800)\ t]$ m s^{-1}, positive to the east: (a) at 66 hours during flow deceleration, pressure gradients oppose the initial free-stream current direction, and due to higher frictional influence, the shallow water currents are weak creating a cross-shore velocity gradient; (b) at 70 hours sea-level pressure gradients have overcome the slow inshore currents to form a phase eddy.

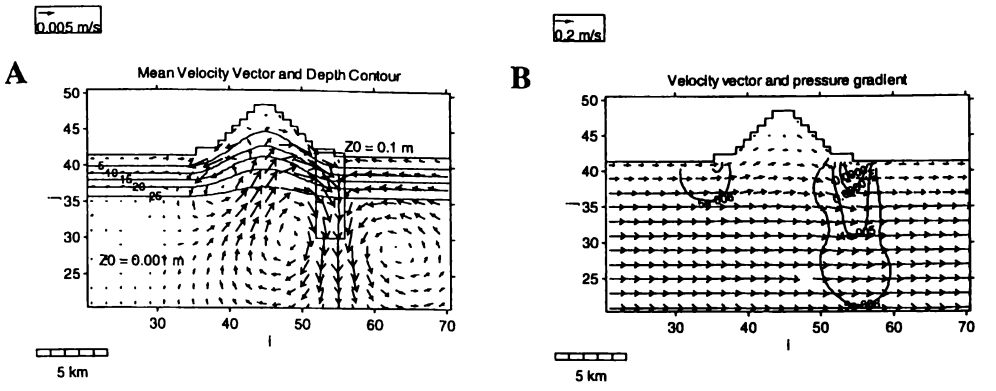

Figure 2-13. Flow field induced over smooth bathymetry (Figure 2-3b) by a shelf-current with velocity described by $0.2\ cos[(2\pi/172800)\ t]$ m s^{-1}, positive to the east: (a) velocity vector, time-averaged between 172800-518400 s (two cycles) and bathymetry (contour) with z_0 raised from 0.001-0.1 m over marked reef area (cells $I = 52{:}56$, $J = 30{:}42$); (b) velocity (vector) and pressure gradient (contour) during accelerating current at 54 hours;

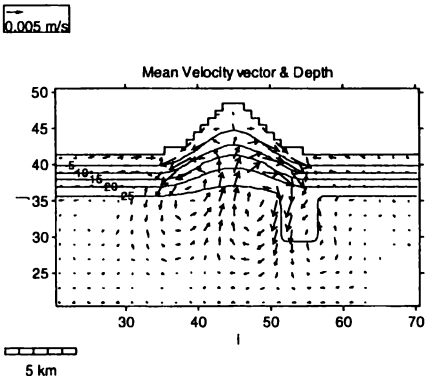

Figure 2-14. Time-averaged velocity (vector) and bathymetry (contour) over the smooth grid with a 5 m high reef added, induced by a shelf-current with velocity described by $0.2\ cos[(2\pi/172800)\ t]$ m s^{-1}, positive to the east (time-averaged between 172800-518400 s, two cycles).

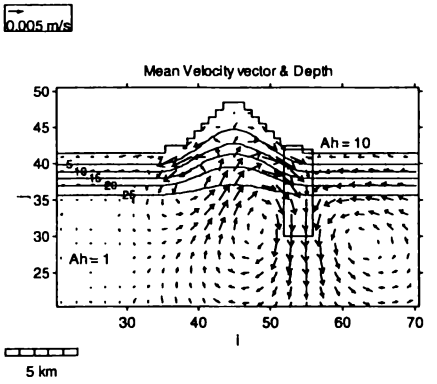

Figure 2-15. Time-averaged velocity (vector) and bathymetry (contour) over the smooth grid with A_H raised from 1-10 $m^2 s^{-1}$ over marked reef area, induced by a shelf-current with velocity described by *0.2 cos[(2π/172800) t]* $m s^{-1}$, positive to the east (time-averaged between 172800-518400 s, two cycles).

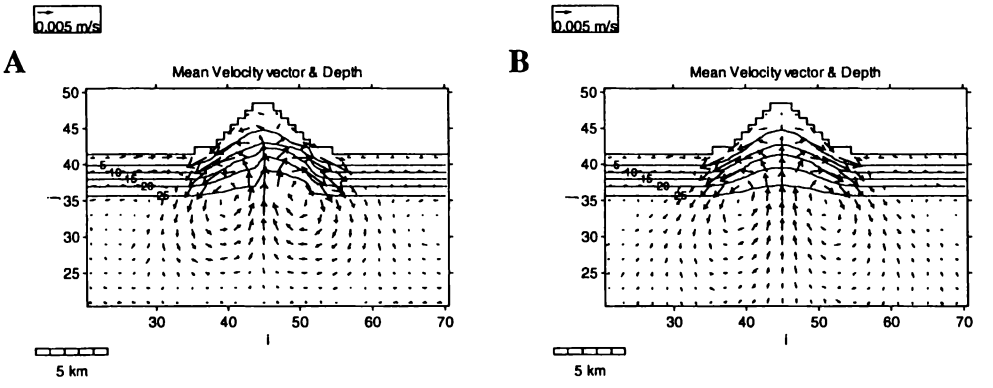

Figure 2-16. Circulation over the smooth grid induced by a shelf-current with velocity described by *0.2 cos[(2π/172800) t]* $m s^{-1}$, positive to the east, time-averaged between 172800-518400 s (two cycles): (a) the eastern outer margin of the bay has been deepened by subtracting 4 m from grid cells *I = 46:52*, *J = 36:42*; (b) original smooth bathymetry (Figure 2-3b).

3

3.1 CONTEXT OF THE PAPER WITHIN THE THESIS

An important component of the thesis field experiments was the use of a Sontek acoustic-Doppler-profiler (ADP) with real-time capability, used to gather high spatial resolution current data. This paper presents observations from a preliminary field experiment designed to test the ADP capability. Being early in the study the paper is mostly observational, presenting ADP results in combination with conductivity-temperature-depth (CTD) surveys. Observations include possible shelf-current intrusion into the bay at depth, a salinity stratified water column in the inner bay, complex currents near the port area, and substantial variation in overnight circulation. These observations set a basis for further work and the paper recommends future higher-density ADP surveys to calibrate a three-dimensional model. An outcome of this paper was the upgrade of the ADP to bottom-track capability. In the absence of a highly accurate (± 2 cm) GPS system this was required to achieve better horizontal spatial resolution in future.

Circulation Patterns in Poverty Bay, New Zealand, measured by Boat-Mounted Global Positioning System Interfaced, Acoustic Doppler Current Profiler

S.A. Stephens, K.P. Black, R.M. Gorman, T.R. Healy

Joint Centre of Excellence in Coastal Oceanography and Marine Geology, Coastal Marine Group, Department of Earth Sciences, The University of Waikato, and National Institute of Water and Atmospheric Research, Private Bag 3105, Hamilton, New Zealand

3.2 SUMMARY

A boat mounted acoustic Doppler current profiler in connection with new software by Sontek Inc. has been used to make real-time measurement of circulation in Poverty Bay, New Zealand. Results from Poverty Bay support an overall anticyclonic circulation pattern but with local variation along the northeast edge of the bay. Local variation is particularly noticeable offshore from the port indicating that variation in the general anticyclonic circulation pattern could be substantial at times. Acoustic Doppler current profiler measurements, in conjunction with conductivity, temperature, depth profiles provide evidence that intrusion of shelf waters into Poverty Bay may be helping to drive the circulation. Future work will use detailed acoustic Doppler current profiler measurements to calibrate a three-dimensional numerical hydrodynamic model of Poverty Bay, and substantiate the effect of shelf-currents on Poverty Bay circulation.

3.3 INTRODUCTION

Poverty Bay, New Zealand has high freshwater and suspended sediment inputs,

chiefly through the Waipaoa River, resulting in highly stratified water bodies within the bay. Average annual runoff for the total catchment is 58 $m^3 s^{-1}$ (Heath, 1985), but is subject to periodic surges, Cyclone Bola resulting in a discharge of 5300 $m^3 s^{-1}$ in the Waipaoa River (Gisborne District Council, 1994). High sediment input to the bay has been an ongoing concern for Port Gisborne Ltd. requiring constant maintenance dredging of their shipping channel. With planned expansion of the port, prediction of sediment movement and overall current circulation pattern within Poverty Bay is an important issue (Gorman et. al., (1997); Black et. al., (1997). Previous studies (Williams, (1966); Miller, (1981); Bell, (1985); Kensington, (1990) have identified a general anticyclonic circulation pattern within Poverty Bay. However with limited fixed current meter arrays, comprehensive measurement of circulation within the bay has never been achieved. The Acoustic Doppler Current Profiler (ADP) is a tool ideally suited to comprehensive measurement of current movement, measuring vertically downward through the water column from a moving vessel. This paper presents results of two surveys using the ADP and the circulation patterns associated with stratified water columns in Poverty Bay.

3.4 METHODS

ADP surveys were conducted from the University of Waikato 5.7 m plastic hulled "Mac-boat". The ADP, sampling at 1.5 MHz, was mounted upon an aluminium pole fastened to the side of the boat. Software written by Sontek Inc., specifically for collection of real-time current measurement from a vessel, was run on a Toshiba Pentium 100 portable PC interfaced with the ADP and global positioning system (GPS). A portable generator was used to power the computer and ADP.

Two surveys of current circulation in Poverty Bay were undertaken on 1st and 2nd February 1997. The survey on 2nd February is a more simple case than on the 1st and so is examined first in the results section below. The ADP was set up to sample in 2 m bin widths, with an averaging interval of 90 s, giving a theoretical precision of 0.32 cm s^{-1}. A mean velocity over each 90 s averaging interval was thus recorded every 2 m throughout the water column. As the blanking distance over which the 1.5 MHz ADP cannot measure was 0.4 m, and the instrument was

mounted 0.4 m under the still water level to ensure it was never removed from the water through boat roll, the first measurement available was at 2.8 m depth. The reason for choosing these parameters was primarily related to the desired accuracy of the measurements and the time constraints of the survey. A larger bin width results in greater precision, since the ADP acoustic pulse is longer so that current velocities are averaged through a larger sector of the water column. The longer the averaging interval, the greater the precision, since a greater number of velocity measurements are averaged. Although precision increases with these parameters, accuracy may decrease if the measuring bin overlaps the boundary of two currents flowing in the opposite direction, or should the ADP move over areas of changing current during an averaging interval. During the surveys there was a swell of approximately H = 1.5 m with a wind created "chop" up to 0.3 m in height that did result in some vertical movement in the ADP. A 2 m bin size was therefore chosen to ensure measurements were reliable despite the vertical movement of the ADP, since a 2 m bin uses a triangular weighting of measurements over 4 m (the measurements at the bin centre being more highly weighted). A 90 s averaging interval was chosen since it's combination with a 2 m bin width gave a good theoretical precision of 0.32 $cm\ s^{-1}$, and the boat was unlikely to drift over currents too different during this period. The boat was driven between sites, where it was allowed to drift under influence of wind and current while measurements were made. Differential GPS interfaced with the software allowed post-processing correction for boat movement. According to Sontek (1997), a stratified water column makes no difference to ADP readings, despite changes in sound velocity with temperature and salinity. The reason for this is that the refraction of the acoustic beam at the interface of two layers has a geometric effect equal and opposite to the effect of changes in sound speed, as illustrated by Snells law.

Conductivity, Temperature and Depth (CTD) profiles were taken during ADP averaging intervals using a Yeo-Kal CTD probe. Although allowing only fixed-point measurements, the instrument is very reliable. Measurements were made at 0, 1, 2, 5, 10, 15, 20 m and bottom. ADP and CTD measurements were made along 3 transects extending from inshore out to the mouth of Poverty Bay (Figure 3-4, 3, 4, 5). This sampling scheme was designed to give the greatest possible

coverage over the bay. Extra measurements were made offshore from the port area where a gyre in the general circulation pattern has been observed to form (Williams, (1966); Miller, (1981). Including driving time between sites and sampling time, it took approximately 3 hours to complete measurements at all 16 sites.

3.5 RESULTS

3.5.1 Current Circulation in Poverty Bay: 2 Feb 1997, 7:40-10:45

During this survey movement of water was uniform in direction throughout the water column (Figure 3-3). Except for immediately offshore from the Waipaoa River mouth there are no significant changes or reversals in flow direction between depths. The pattern of ADP readings shows the general circulation pattern is anticyclonic, water flowing in along the northeast side of Poverty Bay before turning towards the southwest. Unfortunately there were no measurements taken close to the southwest side of the bay, but the water body would be expected to flow outwards towards the ocean at this point. Current velocities flowing into Poverty Bay across its mouth can be seen to increase close to the bottom. A possible explanation for this is intrusion of a shelf-current into Poverty Bay, similar to Jervis Bay, Australia (Holloway et al., 1992), discussed further in the discussion section below.

3.5.2 Current Circulation in Poverty Bay: 1 Feb 1997, 15:40-19:00

Current circulation was complex over the period of this survey (Figure 3-2). A sea breeze from between 150°T and 120°T blew over the period and dropped from a speed of between 3.5 and 4 m s^{-1} over the previous 5 hours to 2 m s^{-1} by the end of the survey. As the Gisborne Airport weather station is inland approximately 2 km, in reality it is likely that the sea breeze was slightly stronger than that measured. Miller (1981) found that wind speeds were required to be above 4 m s^{-1} for associated wind driven upwelling processes to develop. Currents in the uppermost measured layer (2.8 m deep) flow in a different direction to those below, but do not appear to be related to the wind as measured at the airport.

Between 2.8 m and 6.8 m there is significant change in current direction along the outer northeast side of the bay with surface water moving towards the centre of Poverty Bay and underlying water moving inshore towards the port. This indicates a complex process occurring in this location, mirrored below 10.8 m depth where the current direction swings back towards central Poverty Bay. This may be part of a local gyre and could be a zone of up/down-welling water. Close to the port the current is influenced by the outflow from the Turanganui River. Offshore from the port there is evidence of a local anticyclonic gyre extending throughout the water column with water rotating away from the northeast side of the bay and flowing back out through the deeper section towards the centre. In central Poverty Bay extending in shore and along to the southwest by the Waipaoa River a general anticyclonic circulation pattern is evident, which extends throughout the water column and is similar to the survey on 2nd February. As for the 2nd February survey, currents flowing into Poverty Bay are stronger at depth.

3.5.3 Conductivity, Temperature, Depth

As a result of freshwater input from the Waipaoa and Turanganui Rivers, strong stratification in Poverty Bay is evident on 1st February, with the measurements showing a rapid salinity decline with depth in the upper 5 m and lower salinity surface water inshore (Figure 3-4). Below 10 m salinity is relatively uniform at about 33.7 psu. Surface waters along the northeast side of the bay are more saline than along the southwest side as would be expected with the anticyclonic circulation pattern shown by the ADP (Figure 3-2).

It is difficult to recognise the effects of a local gyre offshore from the port in the CTD readings, except that salinity in areas where current moves offshore is lower in the upper 5 m than where currents are moving onshore (Figure 3-4 and Figure 3-2). Temperature in survey 1 is warmer at the surface as a result of thermal heating of surface waters throughout the day (Figure 3-5).

In survey 2, 2nd February water temperatures exhibit as rapid drop below 15 m depth (Figure 3-6). This indicates possible intrusion of cold shelf water along the bottom, consistent with the current pattern across the mouth of Poverty Bay. This

is less evident on 1st February, however the CTD survey was undertaken late in the day when water temperatures may have been warmed, and currents entering Poverty Bay along the bottom were not as strong (Figure 3-2 and Figure 3-3). Surface temperatures close to the Waipaoa River show a significant decrease on 2nd February, indicating that cooler freshwater input from the river is overlying the surrounding bay water and has not yet had time to heat through the day (Figure 3-6 and Figure 3-7).

3.6 DISCUSSION AND CONCLUSIONS

The boat mounted ADP enabled a more comprehensive short term measurement of Poverty Bay circulation than has been achieved previously. Both surveys support the general anticyclonic circulation pattern in Poverty Bay that earlier research has shown to exist (Bell, (1985); Williams, (1966). However, the survey on 1st February identified local variation in this pattern, particularly on the northeast side of the bay close to the port, and near the surface. The variation between surveys overnight indicates that variation from the previously documented anticyclonic circulation pattern could be substantial at times, and this may be important in transporting sediment.

Observed in both surveys, increasing current velocities with depth at the bay entrance indicate that a shelf-current phenomenon intrudes into the bay close to the sea floor. This was also noticed at Jervis Bay, Australia by Holloway et al. (1992). Poverty Bay has many similarities to Jervis Bay including a nearby shelf-current, the East Cape current flowing past Poverty Bay. It is possible that eddies in the East Cape Current may help to drive circulation in Poverty Bay, and result in increasing velocities across the bay entrance. Water temperatures also exhibited a marked drop close to the bottom at the bay entrance, with a noticeable change in temperature gradient, particularly on 2nd February when bottom currents flowing into the bay were strongest.

The combination of the two is evidence that a separate water body to those in Poverty Bay is intruding. While the evidence is not conclusive, it does provide

significant impetus for further study to be carried out in Poverty Bay.

3.7 RECOMMENDATIONS FOR FUTURE WORK

Future work planned to be undertaken in poverty Bay involves a series of measurements by boat-mounted ADP and CTD in conjunction with shelf-current monitoring. This will aim to establish any link between shelf-current movement with Poverty Bay circulation. The trial results suggest that the ADP would be an excellent tool for the calibration of a three-dimensional numerical hydrodynamic model of Poverty Bay, as it allows comprehensive circulation measurement across a large part of the bay over a short time period. The surveys to date have shown that more dense sampling would be beneficial, perhaps by driving the boat at a steady speed across the bay, and that a smaller bin sampling range is needed in order to identify currents in the upper 2 m of the water column. It is recognised that in the 3 hours it took to complete a survey the circulation pattern may have altered. Any alteration would not be expected to be large, but measurements should be made as in as efficient a manner as possible, certainly sites close to each other should be sampled with as little delay as possible.

3.8 ACKNOWLEDGEMENTS

The Authors would like to thank Ben Tahata and Port Gisborne Ltd. for their generous support of field logistics. Thanks also to Brett Beamsley, John Radford and Dirk Immenga for their technical contribution.

3.9 REFERENCES

Bell, R. G. 1985: Coastal current data from Aanderaa current meter deployments 1982-1985. National Institute of Water and Atmospheric Research, Hamilton, New Zealand.

Black, K. P., Gorman, R. G., Stephens, S. A., Beamsley, B. J., Healy, T. R., Bell, R. G. and Oldman, J. W. 1997: Numerical Modelling for the Port Gisborne Expansion. The University of Waikato and National Institute of Water and Atmospheric Research, Hamilton, Pp. 303.

Gisborne District Council 1994: Waipaoa River at Kanakanaia - Monthly Suspended Sediment Yields. Gisborne District Council, Gisborne, Pp. 2.

Gorman, R. G., Stephens, S. A., Beamsley, B. J., Black, K. P., Bryan, K. and Healy, T. R. 1997: Field data collection programme for the Port Gisborne expansion. The University of Waikato and National Institute of Water and Atmospheric Research, Hamilton, Pp. 143.

Heath, R. A. 1985: A review of the physical oceanography of the seas around New Zealand-1982. *New Zealand Journal of Marine and Freshwater Research 19*:79-124.

Holloway, P. E., Symonds, G. and Nunes Vaz, R. 1992: Observations of circulation and exchange processes in Jervis Bay, New South Wales. *Australian Journal of Marine and Freshwater Research 43*:1487-1515.

Kensington, G. L. 1990: Port Developments and dredge spoil dispersion in Northern Poverty Bay. Unpublished MSc thesis, The University of Waikato, Hamilton. 235 p.

Miller, K. R. 1981: Surficial sediments and sediment transport in Poverty Bay. Unpublished MSc thesis, The University of Waikato, Hamilton. 179 p.

Sontek 1997: SonTek Acoustic Doppler Profiler (ADP) Principles of Operation: SonTek ADP Introductory Documentation, Software Version 4.4. Sontek Inc., San Diego.

Williams, H. C. 1966: The Gisborne submarine sewer outfall. *New Zealand Engineering 21*:110-120.

3.10 FIGURES

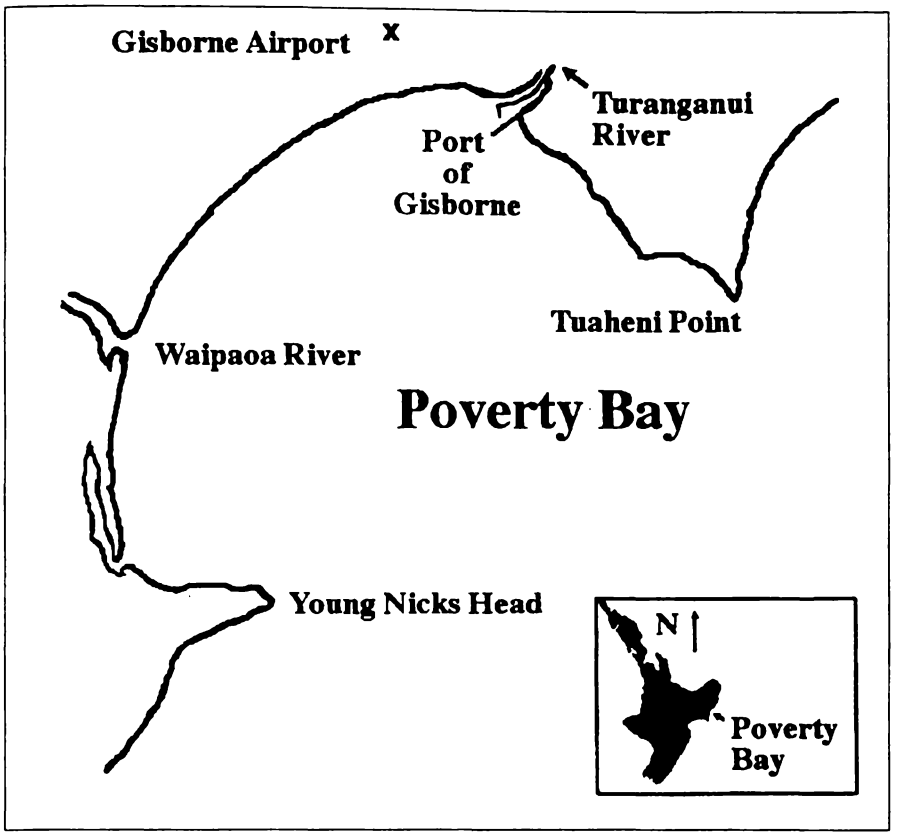

Figure 3-1. Coastline of Poverty Bay, New Zealand.

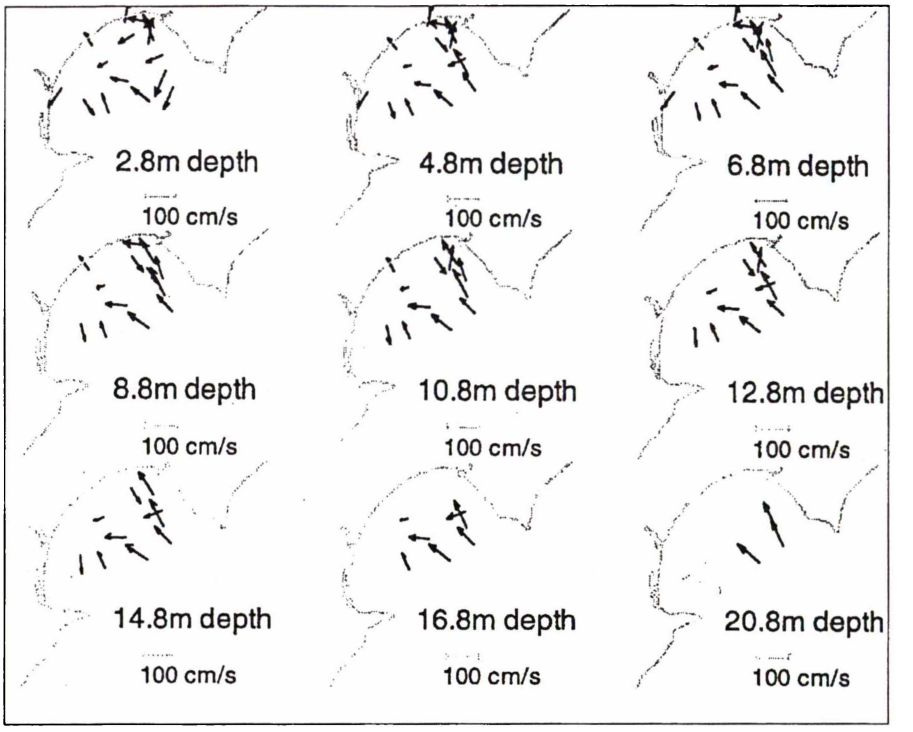

Figure 3-2. Currents measured by downward facing, boat mounted ADP, 1 February 1997, Poverty Bay, New Zealand.

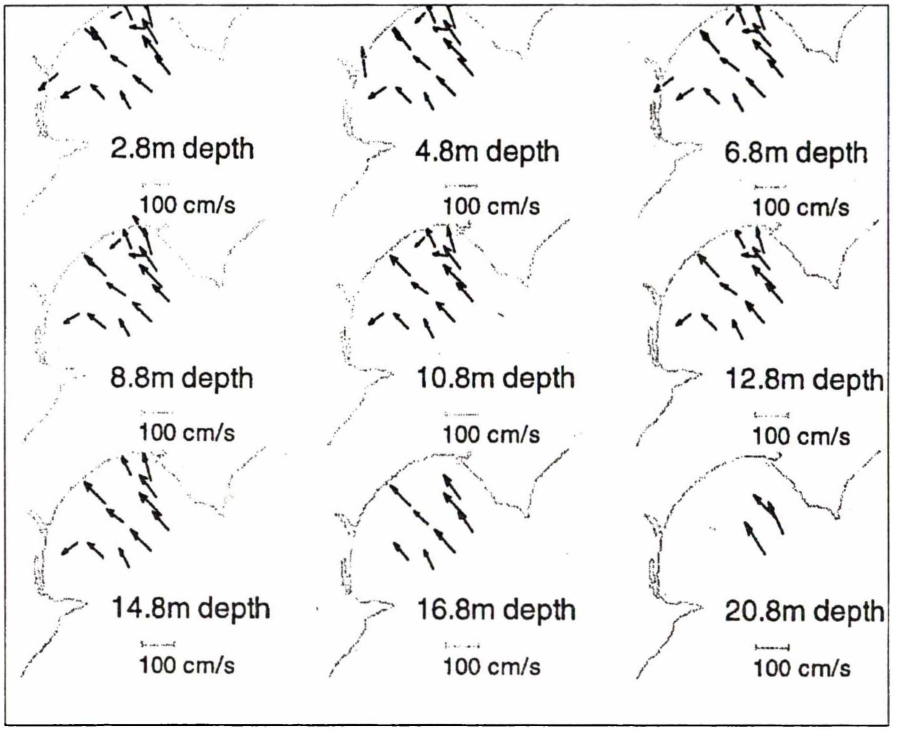

Figure 3-3. Currents measured by downward facing, boat mounted ADP, 2 February 1997, Poverty Bay, New Zealand.

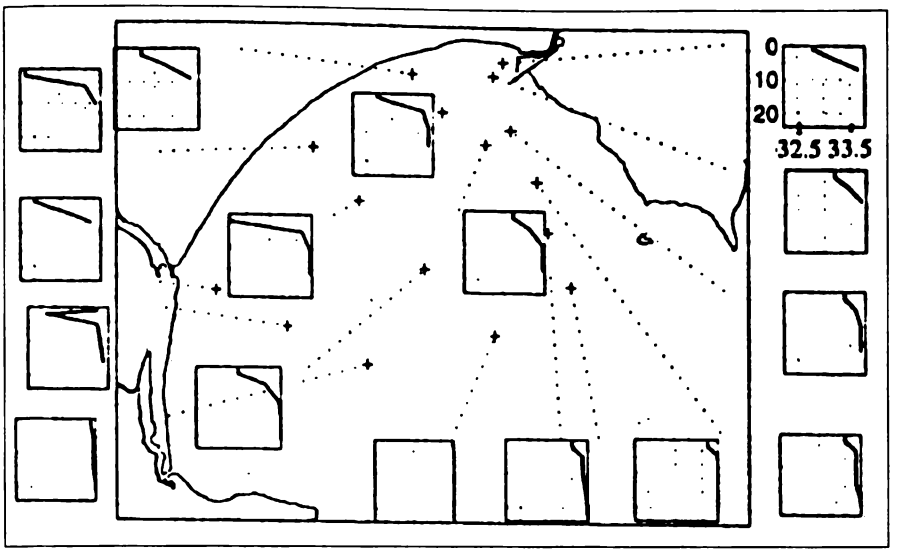

Figure 3-4. Salinity in Poverty Bay, 1 February 1997, 15:40-19:00. The scale on the upper right graph applies to all graphs.

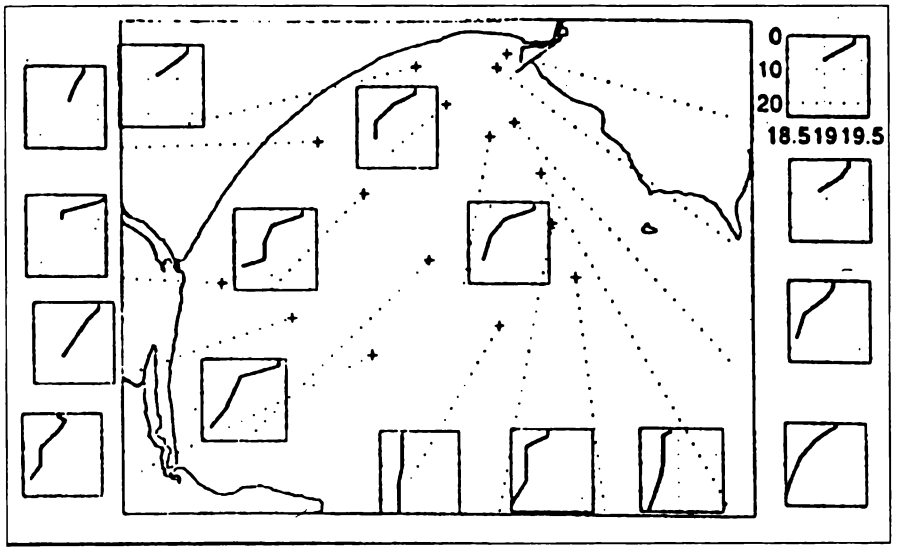

Figure 3-5. Temperature in Poverty Bay, 1 February 1997, 15:40-19:00, showing evidence of thermal heating of surface waters throughout the day. The scale on the upper right graph applies to all graphs.

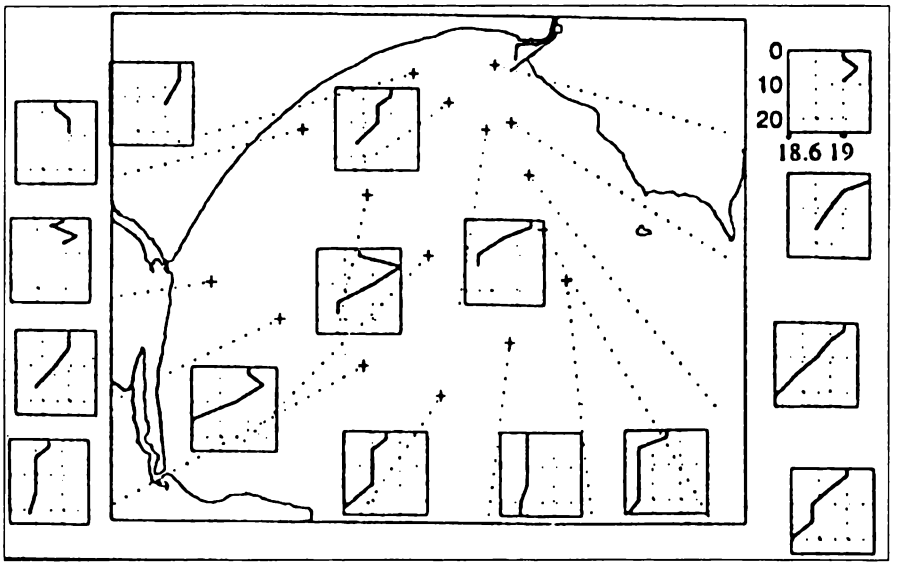

Figure 3-6. Temperature in Poverty Bay, 2 February 1997, 7:10-10:45. The scale on the upper right graph applies to all graphs.

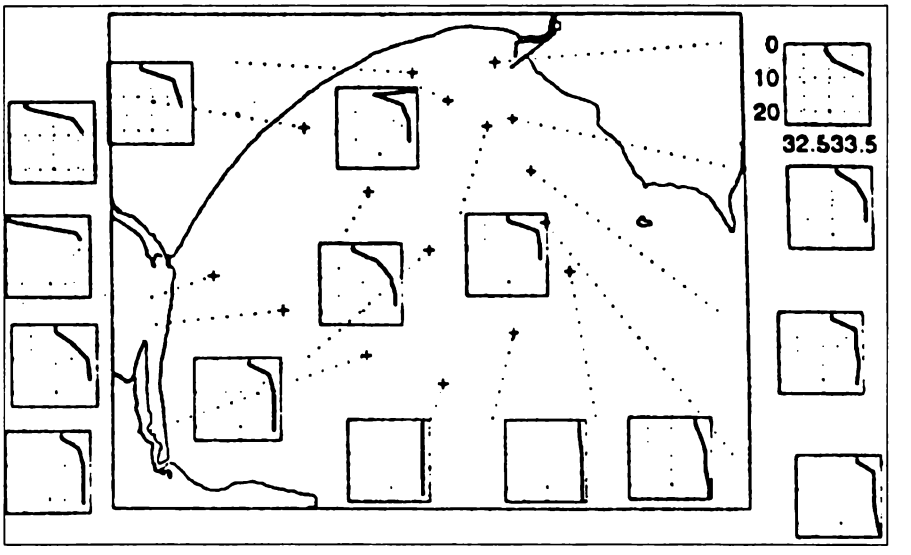

Figure 3-7. Salinity in Poverty Bay, 2 February 1997, 7:10-10:45. The scale on the upper right graph applies to all graphs.

4

4.1 CONTEXT OF THE PAPER WITHIN THE THESIS

The 1998 field experiment included fixed-current-meter deployments on the continental-shelf adjacent to Poverty Bay, along with episodic ADP and CTD surveys. The ADP and CTD were used to measure circulation inside the bay, while shelf-currents were simultaneously recorded. This allowed shelf-currents and their interaction with the bay to be investigated for the first time using real shelf-current data (specific thesis aim 2). This paper describes the field experiment and presents the results. The data is used to infer forcing by tide, continental-shelf-currents, river discharge, and wind stress. The analysis gives the first indication of the relative importance of shelf-current, wind, and density-driven processes to Poverty Bay hydrodynamics, and the reason for persistent anticyclonic circulation in the bay (specific thesis aims 2, 4 and 5). The data analysis also provides a basis for later numerical model calibration (specific thesis aim 3).

Complex Circulation in a Coastal Embayment: Shelf-current, Wind and Density-Driven circulation in Poverty Bay, New Zealand

Scott A. Stephens[1], Robert G. Bell[2] and Kerry P. Black[1]

Centre of Excellence in Coastal Oceanography and Marine Geology

[1]Coastal Marine Group, Department of Earth Sciences, The University of Waikato, Private Bag 3105

and

[2]National Institute of Water and Atmospheric Research Ltd., P. O. Box 11-115 Hamilton, New Zealand

4.2 ABSTRACT

Circulation in a coastal embayment was examined through real-time ADP and CTD surveys in combination with fixed current-meter deployment. The study addressed forcing by tide, continental-shelf-currents, river discharge and wind stress. The inner bay and adjacent shelf-currents exhibit a strong residual component with relatively small tidal flows, and although showing evidence of local wind forcing, the residual mid-water-column shelf-current appears dominated by regional-scale influences. Despite a wide entrance to the continental-shelf, circulation in the bay was found to be insensitive to shelf-currents. The Waipaoa River dominates freshwater discharge and stratification in Poverty Bay, and due to its location, the associated pressure and density gradients drive an anticyclonic gyre, the predominant circulation pattern. Above the critical wind speed of 4 m s^{-1}, the prevailing cross-shore aligned wind stresses drive upwelling and downwelling in the shallow embayment. Sensitivity to wind-driven effects is enhanced by surficial stratification due to freshwater inputs. The prevailing offshore wind results in offshore migration of surface water and induction of shelf water near the bed, supporting upwelling in the central bay due to river plume entrainment. The relative importance of river and wind driven forcing was unable to be established from the field study, although calculations

suggest river dominance under average conditions. This would be best addressed through future three-dimensional numerical modelling.

4.3 INTRODUCTION

Coastal embayments are prized for their sheltered access to the coastal environment, often containing port developments and towns or cities, with associated environmental issues. Poverty Bay, on the east coast of North Island New Zealand is such an embayment, with a small export port and city (Figure 4-1). An environmental issue facing Poverty Bay is the current practise of discharging sewage into the bay, from Gisborne city. Proper management of issues such as this, require a knowledge of circulation in the bay and the processes that drive it. Circulation not only controls the dispersal of man-made pollutants, but also affects the behaviour of natural water-borne organisms, such as rock lobster larvae. The harvesting of rock lobster is an important industry in the Gisborne region, and the wharves of Port Gisborne provide an important recruitment habitat for water-borne juvenile rock lobster, known as *pueruli* (Jeffs, 1999b). Accordingly, we examine circulation in Poverty Bay and the processes controlling it.

Similar studies have shown that in most embayments, circulation is influenced by a combination of external currents, tidal flows, wind and density currents interacting with the local bathymetry, eg. Ferentinos and Collins (1980), Galperin and Mellor (1990), Holloway *et al.* (1992), Wang et al. (1994), D'Adamo *et al.* (1997) and Black *et al.* (2000). Poverty Bay has a wide entrance exposing it to adjacent continental-shelf-currents (Figure 4-1), and the input of large volumes of freshwater (mean annual inflow approximately 70 $m^3 s^{-1}$), plus the predominance of cross-shore aligned wind stresses (Hessell, 1980), creates complex dynamics. An early investigation by Williams (1966) showed an anticyclonic circulation to predominate in much of the bay, and that winds of greater than 8 knots (4 $m s^{-1}$) had a pronounced influence on surface currents. Bell (1985) observed mid-water currents to generally flow inshore along the northern side of the bay, and northeast at the bay entrance, consistent with a net anticyclonic flow. Previous three-dimensional numerical modelling of Poverty Bay was undertaken by Black *et al.*

(1997), and identified the main processes and patterns of circulation. These included pronounced shelf-current driven gyres, highly variable surface currents due to river and wind-induced effects, and associated bottom-return flows. A large field study supplied calibration data for the modelling study (Gorman et al., 1997), but failed to provide either confirmation of shelf-current strengths, or high spatial resolution of currents in the bay. The work by Black *et al.* (1997) and Gorman *et al.* (1997), shows there are four main mechanisms that may drive circulation in Poverty Bay and these are wind, tides, river flow and continental-shelf-currents. The role of each process is here examined through the findings of a comprehensive short-term field study, involving fixed deployment current-meters, real-time Acoustic Doppler Profiler (ADP) and Conductivity, Temperature, Depth (CTD) surveys. Data gathering and manipulation is discussed, before presenting results from the various instruments. Results are then discussed in the context of the main forcing mechanisms, first tides, then the forcing of continental-shelf-currents and their influence on circulation are examined. The influence of river discharge is then addressed, and wind-driven circulation is discussed in combination with stratification. The goal of our work is to examine the complex interplay of freshwater discharge, wind field, and current field on circulation in the bay interior. The results can be used as a prelude to future numerical modelling, and as a guide to understanding the dynamics of similar coastal embayments.

4.4 DATA ACQUISITION, PREPARATION AND PRELIMINARY OBSERVATIONS

The 1998 field programme comprised measurements of the Poverty Bay current and density field, utilising vessel-mounted real-time ADP, S4 current-meters, and CTD. These measurements were supplemented by long-term wind and river-flow data. The field study was designed to overcome the shortcomings of previous field work (Gorman et al., 1997), by supplying accurate shelf-current data through S4 current-meter deployment, and high spatial resolution of the current field using real-time ADP.

Hourly wind data were obtained from the Gisborne Airport meteorological station (Figure 4-1), from Jan 1988 – Aug 1999. Table 4-1 shows that the 1998 year was in keeping with the general mean wind speed and direction, while the study period exhibited slightly stronger winds, which are typical for a spring season. Excepting a slightly higher mean wind speed, the study period was closely representative of mean conditions for the 11 year period. The yearly mean winds show little evidence of long-term variation due to El Nino effects (Table 4-1). The mean wind speed for the 11 year period was 3.5 m s^{-1} (irrespective of direction), therefore winds greater than 4 m s^{-1} are referred to in this paper as strong winds. Almost 55% of all winds blow from the north-northwest sector (Figure 4-2). Markedly fewer northwest winds and more southeast winds were observed in the afternoons, demonstrating the importance of afternoon sea-breeze effects in Poverty Bay. These results are similar to the long term observations at Gisborne Airport between 1962-1972 (Hessell, 1980). Along with the common regional westerly or north westerly wind situation, katabatic drainage of cold air off the nearby Raukumara ranges at night helps to produce the observed predominance of north-westerly air flows in the morning, while the southeasterly sea breeze is often strong over the Gisborne region in the afternoon and evening (Hessell, 1980). A wind rose for the present study period (not shown), similarly showed just greater than 60% of all wind to arrive from the north-northwest sector, with a pronounced sea breeze signature observed on comparison of morning and afternoon data. Thus the present study period is a fair representation of general wind conditions.

For the purposes of spectral analysis, gaps in the wind record of less than three hours were filled using linear interpolation, while gaps of greater than 2 hours were filled using the CLEAN algorithm of Baisch and Bokelmann (1999). This gave a complete hourly wind record from 0:00, 1 January 1988 to 11:00, 8 August 1999. Due to the prevailing northwest/southeast wind alignment, spectral analysis of cross-shore winds was performed along the principal data axis, that passed through 334°T. Dominant peaks in the spectra corresponded to 24 and 12 hour periods, showing a pronounced diurnal and semi-diurnal signature.

River discharge data was available for the Waipaoa and Waimata Rivers over the study period. The Waimata River is the main tributary of the Turanganui River (Figure 4-1), the Turanganui having approximately six times less flow volume than the Waipaoa River (Gorman et al., 1997). Average discharge of the Waipaoa River was $Q = 9.4$ m^3 s^{-1} (based on 5 gaugings), and the temperature $T = 13.8$ °C.

In order to relate shelf-currents to circulation in Poverty Bay, two InterOcean S4 electromagnetic current-meters were deployed between 10 September and 23 October 1998, six kilometres outside the Poverty Bay entrance, on the continental-shelf in 35 m water depth (Figure 4-1). An S4 mounted 2 m above the seabed recorded current speed and direction in three 20 s averages per minute every five minutes 18 October 1998. This current-meter is here-on referred to as GB. An S4DW, here-on referred to as GT, was deployed at approximately 24 m above the bed, to record current speed, direction and pressure in five 12 s averages per minute every five minutes. The S4DW was still recording when retrieved on 23 October 1998. Tidal analysis was performed by the least-squares harmonic method of Foreman (1978). The record duration of greater than 32 days allowed the main tidal current constituents to be resolved. Onset Tidbit temperature loggers were attached to each S4 (accuracy ± 0.15 °C).

Currents in Poverty Bay were measured using a Sontek Acoustic Doppler Profiler (ADP), operated with a depth bin of 1 m, and an averaging interval of 120 s, giving a precision of 0.54 cm s^{-1}. Apart from 2 surveys, the ADP was operated from a moving vessel, profiling vertically downward through the water column. The minimum measurement depth was 2.1 m below the water surface and, due to acoustic reflection off the bottom, no reliable measurements were obtained within approximately 1 m of the seabed. The maximum profiling range of the ADP, operating at 1500 kHz, was approximately 15 m, consequently no reliable data could be obtained at greater depths. Real-time vessel-mounted ADP surveys were undertaken on 13, 15, 17, 19, 21, 22 and 24 September 1998. The ADP does not operate well under conditions of large vertical movement, therefore reliable measurements were restricted to low swell and sea conditions, mainly during offshore winds. To obtain measurements in deeper water near the bay entrance, and in onshore winds, the ADP was deployed on a seabed frame to profile up

through the water column on 26 and 28 September 1998. The ADP was temporarily positioned on the seabed and left to measure for three consecutive 3-minute averaging intervals before being relocated, in this manner obtaining an indication of spatial change in currents around the bay in rough water. The ADP transducers were 0.73 m above the seabed, a 0.4 m blanking distance for the 1500kHz instrument plus 1 m depth bins meant that the shallowest measurement was made at 2.13 m depth (Sontek, 1997). Following several earlier relocations on 28 September, under onshore wind conditions rising to > 5 m s^{-1}, the ADP was deployed overnight (11:30, 28/9/98 to 08:50, 29/9/98) on the seabed (Figure 4-1) in ~16 m depth below lowest astronomical tide. This deployment is referred to as Deployment-A. Due to boundary interference effects at the water surface (Sontek, 1997), measurements made above 14 m were partially corrupted, therefore there is likely some unquantifiable error in near-surface measured velocities. For comparison with the hourly wind record, *U* and *V* velocities at each measurement cell depth were smoothed with a running mean, using an 11 point (33 minute) Hanning window, before decimating to hourly intervals.

Conductivity-temperature-depth (CTD) profiles were sampled during the ADP surveys, using an Applied Microsystems Ltd instrument, raised and lowered by hand. For contouring purposes, the data were gridded using a linear kriging method, Surfer© (Golden Software, 1996).

4.5 RESULTS

4.5.1 Continental-Shelf-currents

The dominant tidal height component around New Zealand is the semidiurnal M_2 lunar tide (Heath, 1985). Tidal analysis showed that on the continental-shelf adjacent to Gisborne, the tidal current with largest magnitude is the K_1 luni-solar diurnal, with a predicted major current ellipse semi-axis of 0.043 m s^{-1} compared with 0.025 m s^{-1} for M_2. The principal-lunar diurnal O_1 and larger-lunar-elliptic diurnal Q_1 tides, also have major ellipse amplitudes similar to the M_2 tide. Table 4-2 reveals that the combined tidal component of flow on the shelf is small (mean speed ~0.04 m s^{-1}) compared with the residual current (mean speed ~0.09 m s^{-1}), while progressive vector plots (Figure 4-3) show tidal currents at both current-

meters to flow parallel to the coast, with little or no net transport. Likewise, Gorman *et al.* (1997) found maximum tidal currents inside Poverty Bay to be less than 0.05 m s^{-1} and typically of order 0.02 m s^{-1}.

The ratio of squared standard deviations (variance), between residual and measured currents, indicates that 81% of shelf-current energy is derived from non-tidal mechanisms, signifying that residual shelf-currents will have greater influence on nearby Poverty Bay. On the continental-shelf, residual flows in the mid-water-column exhibited greater variance (energy) than near-bed currents, and reached higher maximum speeds (Table 4-2). Residual current at the mid-water-column current-meter (GT) is predominantly to the northeast (mean velocity 0.034 m s^{-1}), while the near-bed (GB) residual current is offshore to the southeast (mean velocity 0.059 m s^{-1}), (Figure 4-3).

The wind record was examined to find periods of consistently high speed or consistent wind direction, and these were visually compared with residual shelf-currents (Figure 4-4). There is no obvious relationship between wind and residual current records. Residual currents at GT and GB also show little obvious relationship, except when currents at GT are strong (18-20 September and 7-9 October), currents at GB appear to swing toward the same direction (Figure 4-4). The first strong current event at GT coincides with high river discharge, but the second event does not (Figure 4-5), precluding an explanation due to river-induced effects.

Given the strong diurnal and semi diurnal nature of the wind record at Gisborne Airport, cross-spectral analysis was undertaken to examine whether energy is transferred to the water column at these frequencies. For comparison in the frequency domain, GT, GB and wind data were aligned to common alongshore and cross-shore directions. Since the principal component axes of GT and GB were aligned at 33°T and 60°T, a longshore direction of 46°T was chosen as a best compromise between the two data sets, this being close to the natural longshore alignment of the coast (Figure 4-1). Currents at GT, GB and wind data were rotated 44° clockwise so that the longshore direction matched the x-axis. Wind directions were inverted to true vectors convention, so that velocities were

in the same sense as currents, and cross-spectral analysis was undertaken. Coherences significant at the 95% level indicated transfer of energy from wind to shelf-currents, at various periods between 2.5-18 hours (Table 4-3). Shelf-currents at GT and GB were coherent with each other, over this same period range (Table 4-4). No significant coherence between wind and currents was observed at periods of 12 or 24 hours. Significant coherence between wind and current was most commonly observed at cycles of approximately 18, 14.5 and 3 hours (Table 4-3), and at these periods GT and GB are approximately 180° out of phase with each other (Table 4-4). Phases of transfer between wind and current are inconsistent, however, at ~3 hour cycles the wind tends to lead the alongshore current response by less than 1 hour, but lags the cross-shore current.

4.5.2 ADP and CTD Surveys

Table 4-5 gives details of observed circulation during ADP surveys, along with corresponding wind and shelf-current conditions. Circulation in Poverty Bay was often observed to be anticyclonic, under a range of shelf-current and wind conditions. Real-time ADP and CTD survey results are presented in Figure 4-6 to Figure 4-9, and contain several features worthy of discussion. The key features of Figure 4-6 are the pronounced anticyclonic circulation in the bay, together with the obvious Waipaoa River discharge in the surface layer. This survey was undertaken at the time of highest discharge (74 $m^3 s^{-1}$) from the Waipaoa River (Figure 4-5) and winds were light (Table 4-5). A further feature is the presence of saline water (density anomaly greater than 26 kg m^{-3}) at the *surface* near the bay centre, constrained by the two buoyant river plumes. Another occurrence of surface water greater than 26 kg m^{-3} density anomaly was observed only during upwelling on 15 September (Figure 4-7). Figure 4-7 shows strong alongshore surface currents and associated onshore bottom currents. The density clearly shows that upwelling is occurring under strong offshore winds (Table 4-5). Figure 4-8 shows strong offshore currents in the vicinity of the Waipaoa River and a possible anticyclonic circulation in the upper water column. Currents at depth appear to flow in the opposite direction, inshore along the southern edge and out the northern end. The density reveals a downwelling slug of light water in the central bay, coinciding with the onshore wind (Table 4-5). Figure 4-9 shows a pronounced slug of buoyant surface water near the bay entrance. The current

vectors depict a change in circulation from morning to afternoon, that coincides with a shift from land to sea breeze (Table 4-5).

The results of Deployment-A are shown in Figure 4-10, revealing changing current trends with both time and depth. The feather plots of wind and current (Figure 4-10) clearly indicate the importance of near-surface wind-driven effects, with currents above 14 m (upper) closely mimicking wind directions. Between 7-13 m above the seabed (middle), the current was consistently offshore showing no wind influence. Below 6 m above the seabed (near-bed), currents flowed offshore at ~0.03 m s^{-1} during the initial 7 hour period of strong (> 4 m s^{-1}) onshore winds. An immediate change followed the decrease in wind speed to below 4 m s^{-1}, currents swinging progressively around toward the northwest (onshore) in bottom waters, at ~0.10 m s^{-1}.

4.6 DISCUSSION

4.6.1 Shelf-currents

The wide entrance to Poverty Bay allows for considerable exchange with shelf waters. Continental-shelf-currents at the entrance to Poverty Bay provide an obvious mechanism to drive circulation inside the bay, and numerical modelling by Black *et al.* (1997) showed pronounced shelf-current influence on the bay. Shelf-current velocities of ~0.5 m s^{-1} were simulated based on inferred water level gradients, the calibration data not including accurate shelf-currents. Data from the present field study, shows that mean currents on the continental-shelf are considerably less than those previously simulated by Black *et al.* (1997) (Table 4-2), therefore shelf-currents warrant further investigation.

An obvious source of residual current generation is local wind stress. Numerous investigations indicate that near a straight shoreline, the primary currents generated by local winds are directed within a few degrees parallel to the shoreline (Beer, 1983). The mean longshore wind stress during the shelf current-meter deployment period was 0.0834 N m^{-2} to the northeast. A rudimentary calculation of depth-averaged wind-driven flow velocity U_s can be made based on the assumption that steady-state wind stress is balanced by bottom friction:

$$U_s^2 = \frac{\tau C^2}{\rho_s g}$$

(Black and de Lange, 1995), where C is Chezy's C and τ is the mean wind stress (Gill, 1982). Assuming water depth $h = 35$ m and frictional roughness length of 0.002 m, then the mean longshore wind stress would produce a depth-averaged current of order 0.06 m s^{-1}. This is of the same order of magnitude as the observed mean residual mid-water-column current 0.032 m s^{-1}, and is suggestive of residual current forcing by the local wind. This is a rough estimate, since the equation assumes a steady state water body and steady wind, and these are far from satisfied during the study period (Figure 4-3).

Spectral analysis on the historic Gisborne Airport wind record showed energy peaks at cycles of period 12 and 24 hours, representing the topographically induced sea-breeze weather cycle. However cross-spectral analysis indicates that the local wind transfers energy to residual shelf-currents most commonly at cycles of period approximately 3, 14.5 and 18 hours (Table 4-3). Where significantly coherent (Table 4-4), the 180° phase shift between mid-water and near-bed currents shows a relationship that might typically be expected under wind-driven (Gill, 1982) or buoyancy-driven (McClimans, 1988) flows. The significant coherence between wind and current at these periods (Table 4-3), suggests that wind-driven effects are important, although significant coherence observed at periods of ~18 hours may be related to high energy in the current spectra, due to inertial motion (discussed further below). During the three ADP surveys in strong (> 4 m s^{-1}) offshore wind conditions (Table 4-5), both near-surface currents in the bay and those at GT were observed to flow offshore. Significantly, during two of these events, the near-bed shelf-current was observed to swing from offshore to a southerly direction, indicating a wind-driven influence on the shelf. Following these observations the wind record was further examined to find periods of consistently high speed or consistent wind direction, but these were not found to convincingly match times of current meander, as can be visualised from Figure 4-4. Examination of temperature records at the S4 sites provided little enlightenment. The upper thermistor showed greater variation in temperature

(12.8-13.8 °C) compared with the near-bed thermistor (12.9-13.6 °C), but the temperature variations did not appear to relate to specific wind or current events.

There is good evidence of occasional shelf-current forcing by local winds, but the net residual flow over the study period varies markedly between the mid-water and near-bed currents (Figure 4-3). Shelf-current variation is clearly also influenced by other oceanic or meteorological factors. One such factor is inertial rotational motion, motion that is dominated by rotation effects, arising from the Coriolis force (Gill, 1982). Since Coriolis acts to deflect currents to the left in the Southern Hemisphere, inertial rotational motions must be anticyclonic in nature (Gill, 1982). The theoretical period of inertial motion is around 19 hours at Poverty Bay, and a clear energy peak occurs in the autospectra of both residual current-meter records, at a period of 18 hours. The peak is not evident in the current-meter pressure record. Rotary spectral analysis resolves the combined U and V current components into two circular motions with opposite directions of rotation, and thus is an excellent method for recognising inertial currents, or circularly polarised waves in general (Gilmour, 1987). Figure 4-11 shows the spectra for the cyclonic and anticyclonic components of current at GT and GB. A peak occurs in the anticyclonic component of mid-water column current at period 18 hours, close to the theoretical period of inertial motion (19 hours), but is absent in the cyclonic component. Since the peak is absent in the cyclonic component, this is strongly suggestive of inertial rotational motion. Less pronounced evidence of inertial motion exists in the near-bed current also (Figure 4-11). Inertial currents relate to long waves or currents with a horizontal scale equal to or greater than the Rossby radius of deformation $r = c/f$, where $c = (gh)^{1/2}$ is the horizontal phase speed of the motion, g is gravitational acceleration, h is water depth, and f is the Coriolis frequency (Gill, 1982). Taking $g = 9.81\ m^2\ s^{-1}$, assuming $h \approx 50$ m on the continental-shelf, and $f = 9.116 \times 10^{-5}\ s^{-1}$ at Poverty Bay, gives $r = 2.43 \times 10^5$ m. Therefore, the inertial rotational motion identified in the current-meter record, has a length scale on the order of several hundred kilometres, and can be considered as a large scale regional effect on the shelf-current at Poverty Bay.

Another influence on the local shelf-current may be a northward flowing inner shelf-current, thought to exist on the east coast as an inshore counter-current of the southward directed East Cape current, further offshore (Chiswell and Roemmich, 1998). This is consistent with the observed north-eastward migration of the mid-water current during this study (Figure 4-3) and that observed by Bell (1985). Therefore shelf-currents adjacent to Poverty Bay are likely to be influenced primarily by larger scale regional currents with some modification by local wind. Another possible influence on coastal currents is that of coastal-trapped waves, shown to cause considerable water-level variation on the west coast of South Island New Zealand (Stanton, 1995). On comparison with down-coast wind and water-level records, Stephens *et al.* (in prep) found some evidence of coastal-trapped wave activity in the present current-meter data set. This was limited to periods 2.5-2.9 days and is unlikely to have a major contribution to the residual shelf-currents.

A northward directed mid-water shelf-current could drive a general anticyclonic circulation in the bay. Tuaheni Point at the northern entrance (Figure 4-1) projects further onto the shelf than Young Nicks Head at the south, providing an obstruction to shelf-current flow that may deflect current into the bay. Despite the logic for shelf-current forcing of the gyre in Poverty Bay, measurements during the field study did not directly confirm this. The near-bed shelf-current (GB) was offshore or to the south during all ADP surveys with no apparent affect on circulation in the bay, while the mid-water current (GT) showed some variation with apparently little relationship to bay circulation (Table 4-5). Anticyclonic circulation was observed at times of both up and down-coast shelf-current flow during light to moderate winds. It appears that baroclinic factors rather than barotropic shelf-currents may be more influential in dictating circulation within Poverty Bay.

4.6.2 Plume-Driven Circulation

ADP surveys during periods of low wind velocity showed near-surface current speeds to far exceed those predicted for wind-driven flow; currents obviously being forced by a mechanism other than local wind. In surveys undertaken when wind conditions were < 3 m s^{-1}, general circulation in the bay was observed to be

in the form of an anticyclonic gyre, encompassing the entire bay in both horizontal extent and throughout the water column. The measurements on 17 September (Figure 4-6) show an ideal example of this, with little local wind influence to disturb the bay-wide gyre. The ADP surveys showed the anticyclonic gyre to extend beyond calm days and, while modified by strong winds, a general anticyclonic circulation of order 0.1 m s^{-1} still exists under a variety of local wind conditions (Table 4-5). Previous observations by Williams (1966) and Bell (1985) concur with these findings, but offer no explanation as to the cause of the gyre. Black *et al.* (1997) show that river discharges have a pronounced effect on circulation in Poverty Bay, and accordingly this mechanism is investigated.

From 233,302 mean hourly values collected 1972-2000, the mean Waipaoa River discharge is 32.3 m^3 s^{-1}, with a standard deviation of 68.8 m^3 s^{-1}. The survey on 17 September coincides with the peak Waipaoa River discharge during the survey period of 74 m^3 s^{-1} (Figure 4-5), and the density plot (Figure 4-6) clearly shows the river plume near the water surface. River plumes are known to drive currents through a barotropic pressure gradient, due to the seaward sloping of the river plume, and through horizontal density gradients that drive a baroclinic return flow in the denser layer beneath the plume (Liu et al., 1997). The following discussion deals primarily with the Waipaoa River plume, since the Turanganui River and the ocean outfall (Figure 4-1) contribute significantly less freshwater to the bay, although the Turanganui River is important at times (Black et al., 1997). Garvine (1987) explains two length scales that strongly influence river plume structure and dynamics: the length scale set by the geomorphology, principally the river width at the mouth w, and the dynamical scale set by the baroclinic Rossby radius r_0. Their ratio forms the Kelvin number $K \equiv w/r_0$. The baroclinic Rossby radius is the horizontal length scale over which the pressure gradient force, due to the horizontal density gradient, and the Coriolis force obtain an equal order of magnitude (van Alphen et al., 1988). The Coriolis force, due to the earths rotation, will act to turn the buoyant plume to the left in the Southern Hemisphere. The baroclinic Rossby radius $r_0 \equiv c_0/f$ (Garvine, 1987), where c_0 is the reference phase speed of the buoyant outflow and f is Coriolis frequency, therefore provides an indication of plume spreading (van Alphen et al., 1988). The reference phase speed $c_0 = (g' h_0)^{1/2}$ (Garvine, 1987), where h_0 is the depth of

the upper layer in the reservoir upstream of the outlet channel where it originates, and g' is the reduced gravity $g(\rho_s - \rho_f)/\rho_f$, where ρ_s is the density of the ambient seawater and ρ_f is the density of the freshwater. Taking ρ_s = 1026.4 kg m^{-3} (Figure 4-6), ρ_f = 999 kg m^{-3} (salinity = 0 psu and temperature = 13.8°C), and h_0 = 1.48 m, gives reference phase speed c_0 = 0.37 m s^{-1}. Interestingly, the observed velocity of the plume to site C (Figure 4-6), between 5:00 (rising discharge began) and 11:00 (cast taken at site C), is ~0.34 m s^{-1}, which compares closely to the reference phase velocity c_0 = 0.37 m s^{-1} calculated in the river channel. In Poverty Bay, $f = 9.116 \times 10^{-5}$ s^{-1}, giving r_0 = 4024 m. From Waipaoa River flow gauging data, $w = A / h_0$ = 10.96 m, therefore K = 0.0027. Plumes with order-one Kelvin number may be expected to show strong Coriolis effects, while those with small Kelvin number should show weak effects (Garvine, 1987). Since $K << 0$, the river plume is expected to be non-rotational. Even in the event of a flood, when the river mouth width may increase to ~250 m, K remains small, indicating that the Waipaoa River plume will be almost always non-rotational. In harmony with this is the observation that, on the 17 September, the Waipaoa plume is limited to the southern half of the bay (Figure 4-6).

Garvine (1987) explains that hallmarks of non-rotational plume structure, are the strength of their discharge fronts. The front is defined as the region where the plume properties, such as density, vary on a horizontal scale much smaller than the plume as a whole. At a non-rotational plume front, attendant mass flux loss occurs due to entrainment, and the plume concentrates offshore toward the front, with the deepest pycnocline there along any cross-shore section (Garvine, 1987). The Waipaoa plume is again consistent with these constraints. Examination of CTD casts taken on 17 September show that the plume depth increases at progressively further distances from the Waipaoa River (Figure 4-12). The increasing plume width with distance from the river, occurs due to the entrainment of seawater through turbulent mixing (McClimans, 1988). Gaugings show that the river is ~1 m deep at its confluence, and that (from Figure 4-6) the plume is 4000 m wide and 7000 m long, then the volume of plume-mixed water is approximately 5.6×10^7 m^3. The mean discharge from 5:00 (rising discharge began) to 15:00 (survey finished) on 17 September was 66 m^3 s^{-1} (Figure 4-5). At this rate, the volume of water discharged by the Waipaoa River was

approximately 2.4×10^6 m^3. Therefore, the river plume has increased its volume by approximately 24 times, through entrainment of seawater, whereby the buoyant plume draws seawater water from underneath and from the sides (McClimans, 1988). Assuming Poverty Bay has horizontal dimensions of approximately 5900 $\times$ 9500 m and average depth of approximately 15 m, then the total volume of the bay is 8.4×10^8 m^3, and through entrainment, the river discharge has grown from $< 0.3\%$ to ~7% of the total bay volume. Clearly, this must influence circulation in the bay, and the pronounced anticyclonic circulation provides substantial evidence for plume-driven flow. The location of the Waipaoa River in southwestern Poverty Bay, and the non-rotational nature of the flow, mean that in the absence of wind-forcing, the plume is constricted to the southern half of the bay, and will favour anticyclonic circulation, presumably entraining water from the northern bay.

A dense surface wedge was observed between the rivers on 17 September (Figure 4-6) when discharges are high. The nature of the dense surface wedge suggests that it is upwelled oceanic water, and a distinct possibility is that under plume entrainment, water is being drawn from the central bay area, to be replaced by upwelling oceanic water. This process was first observed to occur during three-dimensional numerical simulations of the bay (Black et al., 1997). Field observations by Gorman *et al.* (1997) support the modelling results, also showing a high salinity patch between river plumes. The simulations of Black *et al.* (1997) showed the river plumes to have a strong influence on surface currents, creating offshore flow at the water surface and entraining seawater landward near the seabed. The present field study thus provides confirmation of this process, as simulated by Black *et al.* (1997). Upwelling has been shown to be a feature of topographically generated coastal recirculation (Deleersnijder et al., 1992), with upwelling near the eddy centre and downwelling at the extremities. In Poverty Bay, the anticyclonic gyre appears to be induced by the discharging Waipaoa river plume and comparison with Black *et al.* (1997) suggests that the upwelling is a feature of plume entrainment rather than of the gyre itself.

A measure of the relative contributions of density and wind driven shear in effecting lateral plume dispersion, is given by Visser (1996). The two effects become comparable when

$$\tau_w = \frac{\rho_a}{\rho_s} C_D W^2 = \frac{gN_z}{f\rho_s}\left(\frac{\rho_s - \rho_c}{y}\right)$$

where τ_w is wind stress, ρ_a is density of air = 1.29 kg m^{-3} (Tipler, 1982), W is wind velocity, ρ_c is water density at the coast, y is the cross-shore extent of the plume, C_D is the drag coefficient = 0.0012 (Large and Pond, 1981) and N_z is the bulk eddy viscosity (Visser, 1996). Using the reference phase speed c_0, assuming a roughness length of 0.002 m (Black et al., 1997) and average depth of the bay H = 15 m (Figure 4-1), an estimate of bulk eddy viscosity can be made by the method of Visser (1996), giving N_z = 0.012 m^2 s^{-1}. Taking the cross-shore density gradient from measured data at sites A and C (Figure 4-6 and Figure 4-12), gives ρ_s = 1025.63 kg m^{-3}, ρ_c = 1025.35 kg m^{-3} and y = 4500 m. Therefore, the wind speed required to drive horizontal plume spreading at a rate equivalent to the density-driven dispersion is 7.2 m s^{-1}. It is shown in the following section that winds of this magnitude drive significant surface currents and have a pronounced effect on circulation in the bay. It can be seen from this result, that the surface current driven by density gradients from the Waipaoa River plume, is equivalent to a relatively strong wind-driven current in Poverty Bay. This is during a discharge not far above the annual average, suggesting that density-driven flows are likely to be a dominant circulation forcing mechanism in Poverty Bay. In a study of river discharge into a coastal lagoon, Liu *et al.* (1997) found that the plume forced water motion through the barotropic pressure gradient, due to the seaward sloping of the river plume, and through horizontal density gradients that drive a baroclinic return flow in the denser layer beneath the plume. Liu *et al.* (1997) found the barotropic pressure gradient to be the dominant forcing in the lagoon, with the horizontal density gradients providing an important secondary forcing. Previous modelling by Black *et al*, (1997) did not specifically address this issue and it is unclear exactly which of these processes dominates in Poverty Bay, although the above calculations suggest that horizontal density gradients may be of paramount importance. Lacking sufficiently regular data to perform an

empirical orthogonal function analysis (Liu et al., 1997), future three-dimensional numerical modelling could be employed to address this issue.

4.6.3 Wind-Driven Circulation

Real-time and fixed deployment ADP surveys were obtained during strongly offshore, strongly onshore and variable wind conditions, and the circulation patterns observed under each of these situations are discussed below.

During the three ADP surveys in strong (> 4 m s^{-1}) *offshore* wind conditions, near-surface currents in the bay were observed to flow downwind (offshore) (Table 4-5). ADP surveys during times of highest wind speed (6 m s^{-1}) and apparent wind-driven near-surface flow on 15 September (Figure 4-7) and 21 September, showed that at the shallowest available measurement depth of 2.1 m (during vessel-mounted surveys), currents were ~0.10 m s^{-1}. For wind velocities of 6 m s^{-1}, the depth of frictional influence of wind (Ekman depth) extends to the seabed in Poverty Bay (Pond and Pickard, 1983). Assuming an approximate average depth in the bay of 15 m as the Ekman depth, then according to Ekman theory (Pond and Pickard, 1983) the calculated surface velocity based upon the measured current at 2.1 m depth is ~0.19 m s^{-1}, which is 3.1% of the wind speed. Magnitudes of wind-driven ocean currents at the water surface are typically ~3% of the wind speed (The Open University, 1989), but are often 1-2% in coastal situations due to bottom frictional effects (Prandle and Matthews, 1990). The calculations provide good evidence that the near-surface currents are driven by strong winds. During times of strong offshore wind, currents at depth inside the bay were observed to flow onshore, either as part of general circulation at depth or as part of a wind-driven bottom-return-flow. Clear evidence of a nearshore wind-driven upwelling event was observed on 15 September, with CTD showing dense saline water being drawn from offshore below 5 m depth, to upwell in the northwest corner of the bay (Figure 4-7). These observations agree with Williams (1966) observation of pronounced wind-driven surface flow when winds exceed 8 knots (4 m s^{-1}), but show that the wind-driven effects extend to the lower water column.

Wind-driven downwelling was also observed, under moderately strong *onshore* wind conditions on 28 September (Figure 4-8). CTD clearly shows that less dense surface water was forced by the wind against the shoreline in the central bay, where a localised downwelling slug was observed to 15 m depth. Further evidence of downwelling was shown during Deployment-A, initiated on 28 September following earlier shifts in ADP location. Feather plots of wind and current (Figure 4-10) clearly indicate the importance of near-surface wind-driven effects, with currents above 14 m (upper) closely matching wind directions. A counter up-wind flow is evident in the lower 5 m during the first 3 hours, when the wind speed was > 4 m s^{-1}. An immediate change in bottom currents followed decrease in onshore wind speed to below 4 m s^{-1}. The indication is that the initial near-bed flow was a wind-driven downwelling current, as confirmed by CTD (Figure 4-8). The ensuing near-bed current is consistent with an anticyclonic gyre in the bay, that may have established itself following subsidence of the onshore wind. Wind-driven downwelling was also observed by Kensington (1990) following a southerly (onshore) wind event involving a rapid change in wind speed from 0 m s^{-1} to a maximum of 7.3 m s^{-1}. Kensington (1990) observed a marked increase in current speed at a shallow (5 m) inshore site, from 0.03 m s^{-1} to 0.09 m s^{-1} due south, associated with a decrease in salinity and increase in temperature. Kensington (1990) concluded that in northern Poverty Bay, wind speeds > 6 m s^{-1} have a direct influence on current speed and direction, throughout the entire water column. Numerical simulation by Black *et al.* (1997) showed wind-driven currents to be of great importance in the surface layer, and wind-driven downwelling was simulated under onshore wind conditions of > 5 m s^{-1}.

While currents measured in the upper and lower water column during Deployment-A, can be related to wind stress and general anticyclonic circulation, the forcing in the mid-water-column is unclear. Currents measured during Deployment-A show no evidence of tidal influence, being consistent in the mid-water column over almost two semi-diurnal tidal cycles. Gorman *et al.* (1997) observed tidal currents in the inner bay to be less than 0.05 m s^{-1} and typically 0.02-0.03 m s^{-1}, considerably smaller than the currents measured in Deployment-A of order 0.10 m s^{-1}. River flows from the Turanganui River were less than 5 m^3 s^{-1} (Figure 4-5), and would not be expected to directly force an offshore mid-

water flow as observed, but cannot be discounted. Circulation in the vicinity of Deployment-A may be influenced by the nearby rocky reef (Figure 4-1). Real-time ADP surveys showed circulation to be most variable near the rocky reef, that separates deeper water bodies to each side and allows currents of opposing direction in close proximity, often onshore to the northeast and offshore to the southwest of the reef. In this way, the reef area creates a local scale effect where circulation is often different to that observed in the bay in general, and is also likely influenced by the proximity of the Turanganui River. Both Williams (1966) and Black *et al.* (1997) also observed variable flow patterns in this area.

Although CTD and Deployment-A show definite evidence of wind-driven downwelling on 28 September, circulation is more complex than a simple onshore surface and offshore bottom flow (Figure 4-8). While near-bottom currents flow out along the northern side of the bay, the upper water column exhibits an anticyclonic gyre. Flow near the Waipaoa River is strongly offshore, presumably at least partially due to the 13 $m^3 s^{-1}$ river outflow. Given the strong anticyclonic gyre induced on 17 September by a 74 $m^3 s^{-1}$ discharge (Figure 4-6), it appears possible that the weak surface gyre on 28 September may also be induced by river discharge.

Currents were also measured during a significant directional *wind swing* on 19 September (Figure 4-9), from off to onshore (Figure 4-4). A significant alteration in circulation was observed following the wind change, yet a similar wind swing on 13 September revealed no circulation change (Table 4-5). Although the circulation change on 19 September closely followed the wind reversal, near-surface currents of ~0.1 m s^{-1} are faster than would be expected of those driven by winds of ~3 m s^{-1} (Table 4-5). The reason for the different behaviour of the bay appears to be stratification, a significant discharge from the Waipaoa River on 17-18 September (Figure 4-5) deposited a large buoyant freshwater slug to the surface layer, evident on the 19 September (Figure 4-9). Below-surface densities are lower on the Turanganui River side of the bay, due to an active high discharge event from the Turanganui River (Figure 4-5). Conversely the survey on 13 September followed a period of low river discharge when stratification was weak. The presence of the buoyant slug capping the underlying dense marine water,

appears to increase the sensitivity to wind-driven near-surface flow (The Open University, 1989), that in turn effects a counter or return-flow in the lower water column. This facilitates a total reversal in circulation within 2 hours, driven by wind stress and heightened by a cap of buoyant surface water. The implication is that during times of high stratification, wind-driven processes are enhanced in the bay and may totally dominate circulation. This is supported by Keen and Glenn (1999). Through field studies supported by both two and three-dimensional numerical modelling, Keen and Glenn (1999) found that stratification was a critical component of hurricane-wind-driven upwelling and downwelling on the continental-shelf, that ceased to exist under barotropic conditions.

Higher stratification and susceptibility to wind-driven flow can generally be expected, compared with the present field study. The present field study encountered an uncharacteristically dry period in the region, during which time the average Waipaoa discharge was only 14.5 $m^3 s^{-1}$, compared with the average annual discharge of 33 $m^3 s^{-1}$. CTD surveys undertaken in 1996 by Gorman *et al.* (1997) showed frequent occurrence of buoyant freshwater slugs on the surface of Poverty Bay, with an average discharge from the Waipaoa River during the period of 51 $m^3 s^{-1}$. Although high stratification may enhance wind-driven effects, stratification in Poverty Bay is created by river discharge, that has been shown to induce pronounced circulation itself. The separation of these effects requires the plume to remain intact following discharge, as happened on 19 September, for at least 24 hours (Figure 4-9). The situation of concurrent active high discharge and strong winds was not surveyed, and the dominance of either forcing mechanism could not be directly quantified during the field study. Calculations in the preceding section indicate that under average conditions, Q = 33 $m^3 s^{-1}$, W = 3.5 m s^{-1}, river-induced effects should dominate. Three-dimensional numerical modelling could be utilised for future investigation of this issue.

4.6.4 Transport Implications

Circulation in Poverty Bay has important implications for lobster recruitment in the nursery area around Port Gisborne, and also the movement of the wastewater plume discharged from the city outfall (Figure 4-1). Uncertainty exists as to whether lobster larvae actively seek recruitment habitat or happen upon it by

chance (Jeffs, 1999a), but it is known that in the onshore moving *puerulus* phase they often swim actively at night and seek shelter during the day (Booth and Phillips, 1994). Night swimming *pueruli* have been observed at the surface but also lower in the water column (Booth and Phillips, 1994). The field study has shown that the prevailing offshore wind climate in the Gisborne region is contrary to the chances of settlement in the port area by surface swimming *pueruli*, but tends to induce shoreward flow in the lower water column. The commonly observed anticyclonic circulation (Table 4-5) is conducive to lobster settlement along the port side of the bay, and this circulation is favoured by high discharge from the Waipaoa River. This circulation may be disrupted in the surface layer adjacent to Port Gisborne, by the Turanganui River discharge.

The results of this study show that a buoyant wastewater plume discharged from the outfall under strong onshore wind conditions (usually in the afternoon) is likely to reach the nearshore zone under a downwelling current regime, and depending on dilution rates, may pose a risk to public health through water-contact recreation. Fortunately, the prevailing wind climate will act to distribute sewage offshore, to be to replenished by clean upwelled marine water. In situations dominated by river discharge, surface water in the vicinity of the ocean outfall is entrained into the river plumes, and replaced by upwelling oceanic water. In terms of public health risk to beach users adjacent to Gisborne city, the predominating circulation patterns are favourable.

4.7 CONCLUSIONS

An investigation of wind, density, shelf-current and tidal driven circulation in Poverty Bay was undertaken using real-time ADP, CTD and moored current-meter deployment. Currents within Poverty Bay and on the adjacent continental-shelf exhibit a strong residual component with relatively small tidal flows. Currents on the continental-shelf adjacent to Poverty Bay showed some evidence of local wind forcing, but receive much externally derived energy. The forcing of the mid-water column residual shelf-current can be linked in part to the local wind, an obvious inertial component is observed in the rotary spectra, and the overall flow direction is consistent with a north-flowing continental-shelf-current

(Chiswell and Roemmich, 1998). While a contribution from coastal-trapped-waves is possible, the residual mid-water-column current is likely dominated by regional-scale currents. Forcing of the near-bed residual shelf-current is more obscure. While the local wind has a definite influence, it does not significantly disturb the net offshore flow, and evidence for inertial currents is not as pronounced in the rotary spectra. The forcing of offshore near-bed residual flow could not be ascertained. Shelf-currents showed no consistent relationship with circulation in Poverty Bay, suggesting that other forcing mechanisms are more important.

Strong evidence has been presented that anticyclonic circulation is induced by the discharging Waipaoa River plume. At 74 $m^3 s^{-1}$, the peak discharge during the field study was only twice the annual mean, and since winter storms can often produce freshes of 200-500 $m^3 s^{-1}$ (Gorman et al., 1997) then the inertia of these discharges entering the bay are likely to dominate circulation. The Waipaoa River discharges along the southern extremity of the bay and supplies approximately six times the volume of the Turanganui River at the north. The dominance of the Waipaoa discharge means that circulation due to river-derived pressure and density gradients, is always likely to be in the anticlockwise direction. High salinity water observed between plumes, in the central bay, appears to be oceanic water upwelled under plume-induced circulation; comparison with Black *et al.* (1997) and Gorman *et al.* (1997) suggests this is a typical situation under plume-dominated flow.

A strong wind-driven influence was observed in the bay, above the critical wind speed of 4 m s^{-1}. Both wind-driven upwelling and downwelling were observed in the inner margins of the bay, and since the average wind speed is of order 4 m s^{-1}, this is likely to occur on a regular basis. The prevailing offshore wind climate suggests that upwelling will be particularly common, and is likely to combine with plume driven circulation to draw seawater inshore at depth along the northern side of the bay. Under stratified conditions, the wind can totally switch circulation in the bay inside two hours, and these conditions are likely to be more common compared with the present study period of limited rainfall.

This study has shown that in shallow coastal embayments, circulation can be dominated by external effects such as the wind field or freshwater discharges, rather than the interdependent shelf-current field. This is despite the wide bay entrance providing direct exposure to adjacent shelf-currents. A direct field comparison was unable to be made between the effects of high river discharge and those of strong winds, however calculations suggest that under average conditions of Waipaoa River discharge 33 $m^3 s^{-1}$ and wind speed 3.5 m s^{-1}, river-induced circulation should dominate. Day to day, this will depend on the relative magnitudes, and future three-dimensional numerical modelling is suggested to distinguish complexities of circulation created by these two processes in Poverty Bay.

4.8 ACKNOWLEDGEMENTS

The authors wish to thank Ben Tahata and Port Gisborne Ltd. for their generous logistic support during field work. Wind data was obtained from the Climate Database maintained by The National Institute of Water and Atmospheric Research Ltd. The Gisborne District Council generously supplied discharge data for the Waipaoa and Waimata Rivers. The authors wish to thank Dr. Andrew Jeffs of NIWA for his assistance regarding rock lobster behaviour.

4.9 LITERATURE CITED

Baisch, S. and Bokelmann, G. H. R. 1999: Spectral analysis with incomplete time series: an example from seismology. *Computers and Geosciences 25*:729-738.

Beer, T. 1983: Environmental Oceanography: an introduction to the behaviour of coastal waters, Pergamon Press, New York. 262 p.

Bell, R. G. 1985: Coastal current data from Aanderaa current meter deployments 1982-1985. National Institute of Water and Atmospheric Research, Hamilton, New Zealand.

Black, K. P., Bell, R. G., Oldman, J. W., Carter, G. S. and Hume, T. M. 2000: Features of 3-dimensional barotropic and baroclinic circulation in the Hauraki Gulf, New Zealand. *New Zealand Journal of Marine and Freshwater Research 34*:1-28.

Black, K. P. and de Lange, W. P. 1995: Numerical modelling of physical marine processes. Lecture notes: graduate course 0772.544. The University of Waikato, Hamilton, Pp. 74.

Black, K. P., Gorman, R. G., Stephens, S. A., Beamsley, B. J., Healy, T. R., Bell, R. G. and Oldman, J. W. 1997: Numerical Modelling for the Port Gisborne Expansion. The University of Waikato and National Institute of Water and Atmospheric Research, Hamilton, Pp. 303.

Booth, J. D. and Phillips, B. F. 1994: Early life history of spiny lobster. *Crustaceana 66(3)*: 271-291.

Chiswell, R. J. and Roemmich, D. 1998: The East Cape current and two eddies: a mechanism for larval retention. *New Zealand Journal of Marine and Freshwater Research 32(3)*: 385-397.

D'Adamo, N., Mills, D. A. and Wilkinson, D. L. 1997: Exchange processes in Cockburn Sound - a seasonally stratified embayment off southwest Australia. *In:* Pacific Ports and Coasts '97, Vol. 2. Centre for Advanced Engineering, Christchurch, Pp. 667-674.

Deleersnijder, E., Norro, A. and Wolanski, E. 1992: A Three Dimensional model of the water circulation around an island in shallow water. *Continental-shelf Research 12(7/8)*: 891-906.

Ferentinos, G. and Collins, M. 1980: Effects of Shoreline Irregularities on a Rectilinear Tidal Current and their significance in sedimentation processes. *Journal of Sedimentary Petrology 50*:1081-1094.

Foreman, M. G. G. 1978: Manual for tidal currents analysis and prediction. Institute of Ocean Sciences, Patricia Bay, Victoria, British Columbia, Canada, Pp. 70.

Galperin, B. and Mellor, G. L. 1990: A time dependant, three dimensional model of the Delaware Bay and river system. Part 1: Description of the model and Tidal analysis. *Estuarine, Coastal and Shelf Science 31*:1307-1317.

Garvine, R. W. 1987: Estuary plumes and fronts in shelf waters: A layer model. *Journal of Physical Oceanography 17(11)*: 1877-1896.

Gill, A. E. 1982: Atmosphere-Ocean Dynamics, Academic Press, San Diego. 662 p.

Gilmour, A., E. 1987: A preliminary rotary spectral analysis of inertial currents off the west coast of New Zealand. *New Zealand Journal of Marine and Freshwater Research 21(2)*: 353-357.

Golden Software 1996: Surfer. Golden Software Inc., Colorado.

Gorman, R. G., Stephens, S. A., Beamsley, B. J., Black, K. P., Bryan, K. and Healy, T. R. 1997: Field data collection programme for the Port Gisborne expansion. The University of Waikato and National Institute of Water and Atmospheric Research, Hamilton, Pp. 143.

Heath, R. A. 1985: A review of the physical oceanography of the seas around New Zealand-1982. *New Zealand Journal of Marine and Freshwater Research 19*:79-124.

Hessell, J. W. D. 1980: The Climate and Weather of the Gisborne Region. *New Zealand meteorological service miscellaneous publication 115(8)*: 29.

Holloway, P. E., Symonds, G. and Nunes Vaz, R. 1992: Observations of circulation and exchange processes in Jervis Bay, New South Wales. *Australian Journal of Marine and Freshwater Research 43*:1487-1515.

Jeffs, A. 1999a: Super-swimmers or lazy lobsters. *In:* New Zealand Marine Sciences Society Conference, Wellington.

Jeffs, A. 1999b: Vertical migration of lobster. December e-mail, National Institute of Water and Atmospheric Research, Auckland.

Keen, T. R. and Glenn, S. M. 1999: Shallow water currents during Hurricane Andrew. *Journal of Geophysical Research 104(C10)*: 23443-43458.

Kensington, G. L. 1990: Port Developments and dredge spoil dispersion in Northern Poverty Bay. Unpublished MSc thesis, The University of Waikato, Hamilton. 235 p.

Large, W. G. and Pond, S. 1981: Open ocean momentum flux measurements in moderate to strong winds. *Physical Oceanography 11*:324-337.

Liu, J. T., Zarillo, G. A. and Surak, C. R. 1997: The influence of river discharge on hydrodynamics and mixing in a subtropical lagoon. *Journal of Coastal Research 13(4)*: 1016-1034.

McClimans, T. A. 1988: Estuarine fronts and river plumes. *In:* Dronkers, J. and van Leussen, W. *ed.* Physical processes in estuaries, Springer-Verlag, Berlin, Heidelberg, pp. 55-69.

Pond, S. and Pickard, G. L. 1983: Introductory Dynamical Oceanography, Pergamon Press, New York. 329 p.

Prandle, D. and Matthews, J. 1990: The dynamics of nearshore surface currents generated by tides, wind and horizontal density gradients. *Continental-shelf Research 10(7)*: 665-681.

Sontek 1997: SonTek Acoustic Doppler Profiler (ADP) Principles of Operation: SonTek ADP Introductory Documentation, Software Version 4.4. Sontek Inc., San Diego.

Stanton, B. R. 1995: Sea-level Variability on the West Coast of New Zealand. *Journal of Physical Oceanography 25(6)*: 1265-1272.

Stephens, S. A., Black, K. P., Bell , R. G. and Healy, T. R. in prep: A search for coastal trapped waves on the east coast of the North Island.

The Open University 1989: Ocean Circulation, Pergamon Press, Oxford. 238 p.

Tipler, P. A. 1982: Physics, Worth, New York. 1062 p.

van Alphen, J. S. L. J., de Ruijter, W. P. M. and Borst, J. C. 1988: Outflow and Three-Dimensional Spreading of Rhine River Water in the Netherlands Coastal Zone. *In:* Dronkers, J. and van Leussen, W. *ed.* Physical processes in estuaries, Springer-Verlag, Berlin, Heidelberg, pp. 70-92.

Visser, A. W. 1996: Shear dispersion in a wind and density driven plume. *In:* Aubrey, D. G. and Friedrichs, C. T. *ed.* Buoyancy effects on coastal and

estuarine dynamics, American Geophysical Union, Washington DC, pp. 359.

Wang, J., Mysak, L. A. and Ingram, G. 1994: A Three-Dimensional Numerical Simulation of Hudson Bay Summer Ocean Circulation: Topographical Gyres, Separations, and Coastal Jets. *Journal of Physical Oceanography 24*:2496-2514.

Williams, H. C. 1966: The Gisborne submarine sewer outfall. *New Zealand Engineering 21*:110-120.

4.10 TABLES

Table 4-1. Mean wind speed and direction at Gisborne Airport, 1988-1998.

Year	Mean Speed ($m\ s^{-1}$)	Mean Direction (°T)	Mean Speed (irrespective of direction) ($m\ s^{-1}$)
1988	1.65	330	4.70
1989	0.71	320	4.53
1990	1.22	313	3.06
1991	1.28	314	3.19
1992	1.08	307	3.32
1993	0.92	300	3.09
1994	1.42	312	3.49
1995	1.33	315	3.26
1996	1.25	305	3.47
1997	1.16	314	3.28
1998	1.47	329	3.39
Study Period	2.92	330	4.23
1988 - 1998	1.2	315	3.5

Table 4-2. Current speed statistics for S4DW current-meter, 24 m above seabed (GT) and S4 current-meter, 2 m above seabed (GB), deployed at latitude -38° 46.43', longitude 178° 03.87', 9 September to 23 October 1998. Measured refers to *in-situ* measurement, predicted refers to tidal currents "predicted" by harmonic analysis (Foreman, 1978) and residual refers to non-tidal component.

	GT measured ($cm\ s^{-1}$)	GT predicted ($cm\ s^{-1}$)	GT residual ($cm\ s^{-1}$)	GB measured ($cm\ s^{-1}$)	GB predicted ($cm\ s^{-1}$)	GB residual ($cm\ s^{-1}$)
Minimum	0.0	0.2	0.2	0.8	0.1	0.8
Maximum	36.1	11.7	32.6	23.6	9.4	20.9
Mean	9.3	4.0	8.7	9.8	4.0	9.1
Standard deviation	6.2	2.1	5.6	4.4	1.9	3.5

Table 4-3. Frequency, period, phase and time-shift of wind and current data coherent at the 95% significance level, in the range $T = 2.5$-24 hours. Positive phase and time-shift indicates that wind leads current, and *vice versa*.

Cross-shore wind					
Period (hrs)	f (cycles / hour)	Phase °	Time Shift (hours)	Current data	Current axis
18.8	0.053	110	5.8	GB	Alongshore
18.8	0.053	-174	-9.1	GB	Cross-shore
14.5	0.069	-67	-2.7	GB	Cross-shore
11.2	0.089	-101	-3.2	GB	Cross-shore
8.8	0.113	-134	-3.3	GB	Cross-shore
6.0	0.168	21	0.3	GT	Cross-shore
3.6	0.279	66	0.7	GT	Alongshore
3.3	0.302	-63	-0.6	GT	Cross-shore
3.2	0.316	70	0.6	GB	Alongshore
3.0	0.329	-116	-1.0	GT	Cross-shore
Alongshore wind					
Period (hrs)	f (cycles / hour)	Phase °	Time Shift (hours)	Current meter	Current axis
17.1	0.059	62	2.9	GT	Alongshore
14.5	0.069	-61	-2.4	GB	Cross-shore
14.5	0.069	-157	-6.3	GB	Alongshore
14.4	0.069	143	5.7	GT	Cross-shore
10.6	0.095	71	2.1	GT	Cross-shore
7.8	0.128	103	2.2	GT	Alongshore
3.1	0.318	85	0.7	GB	Cross-shore
3.1	0.321	153	1.3	GT	Alongshore
2.8	0.362	-87	-0.7	GB	Cross-shore
2.5	0.405	-126	-0.9	GT	Cross-shore

Table 4-4. Frequency, period, phase and time-shift of *current* data coherent at the 95% significance level, in the range $T = 2.5$-24 hours. Positive phase and time-shift indicates that GT leads GB, and *vice versa*.

Period (hrs)	f (cycles / hour)	Phase °	Time Shift (hours)	Direction
18.0	0.056	-176	-8.8	Alongshore
18.0	0.056	-177	-8.9	Cross-shore
14.5	0.069	-177	-7.1	Cross-shore
11.4	0.088	175	5.5	Alongshore
8.8	0.113	96	2.4	Cross-shore
7.8	0.128	-75	-1.6	Alongshore
5.9	0.169	0	0.0	Cross-shore
3.8	0.2611	-170	-1.8	Cross-shore
3.7	0.2722	166	1.7	Cross-shore
3.5	0.2879	-179	-1.7	Alongshore

Table 4-5. Observed Poverty Bay circulation during ADP surveys, along with corresponding wind and shelf-current conditions. Up-coast and Down-coast refer to southwest and northeast flowing currents respectively.

Date (1998)	Circulation in Poverty Bay	Wind	Mid-water (GT)	Near-bed (GB)
13-Sep	Anticyclonic	Off-shore 2hr <3 m s^{-1}, Onshore 4hr >3 m s^{-1}	Down-coast	Off-shore
17-Sep	Anticyclonic	Off-shore < 2 m s^{-1}	Up-coast	Off-shore
24-Sep	Anticyclonic	Off-shore > 2 m s^{-1} then onshore > 2 m s^{-1}	Down-coast	Off-shore
26-Sep	Anticyclonic	Off-shore 3-6 m s^{-1}	Up-coast	Off-shore
28-Sep	Anticyclonic, offshore in inner bay at depth	On-shore < 5 m s^{-1}	Up-coast	Off-shore
15-Sep	Offshore at surface, onshore at depth	Off-shore > 5 m s^{-1}	Off-shore	Off-shore
21-Sep	Offshore at surface, complex at depth near reef	Off-shore > 5 m s^{-1}	Off-shore	Down-coast
22-Sep	Offshore at surface, onshore at depth	Off-shore 4 m s^{-1} then onshore 3 m s^{-1}	Off-shore	Down-coast
19-Sep	Up/downwelling, anticyclonic/cyclonic with changing wind	Off-shore < 3 m s^{-1} then onshore 3 m s^{-1}	Up-coast	Off-shore

4.11 FIGURES

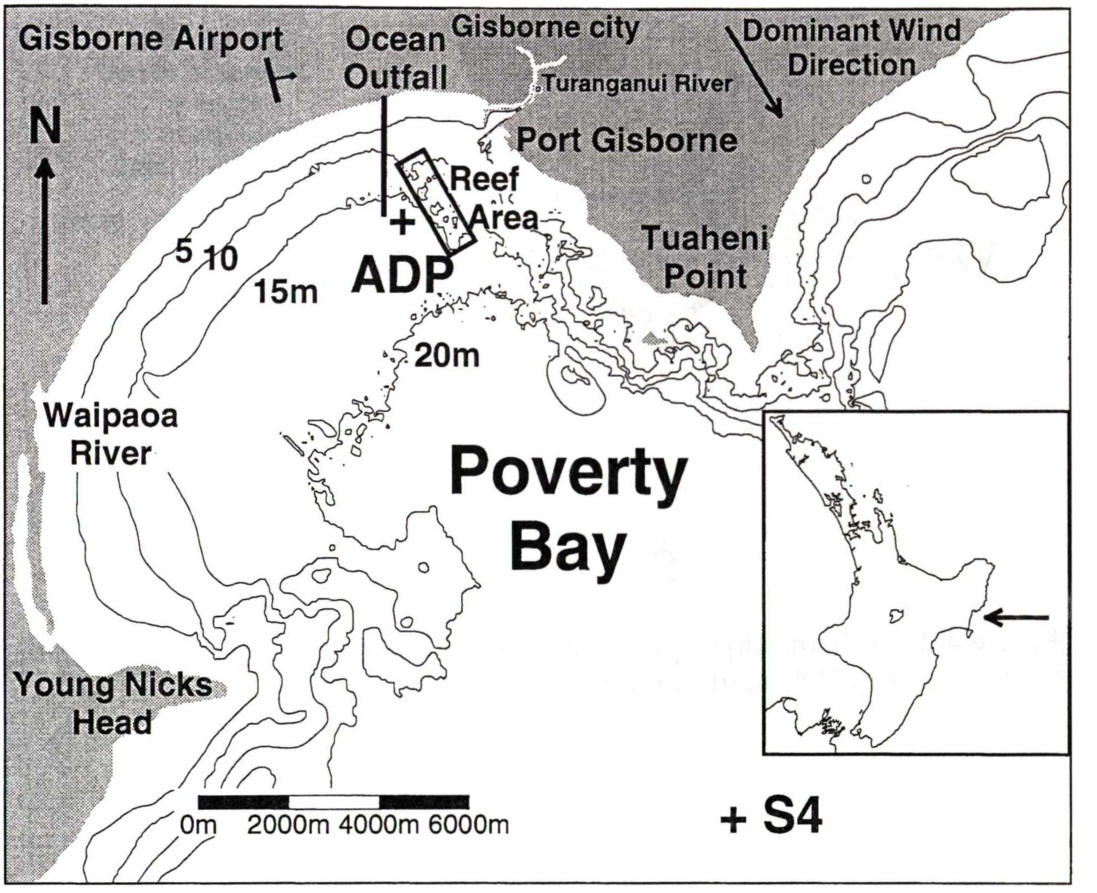

Figure 4-1. Poverty Bay location and bathymetry, showing sites of ADP (during Deployment-A) and S4 current-meters.

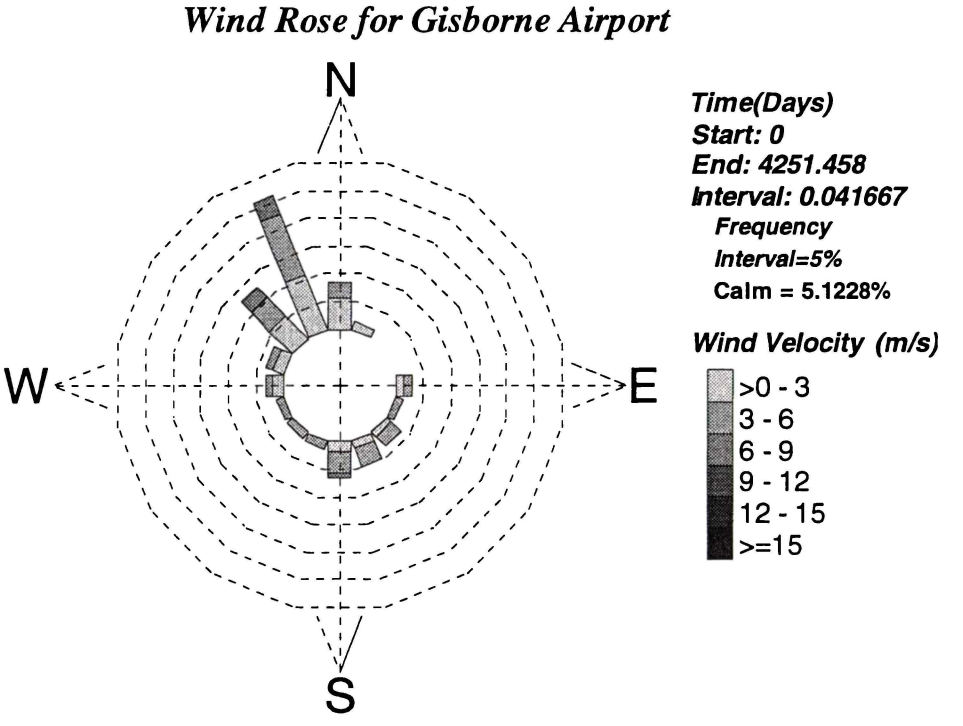

Figure 4-2. Gisborne airport wind rose from 86,046 hourly recordings, beginning 01:00, 1 January 1988 until 11:00, 8 August 1999.

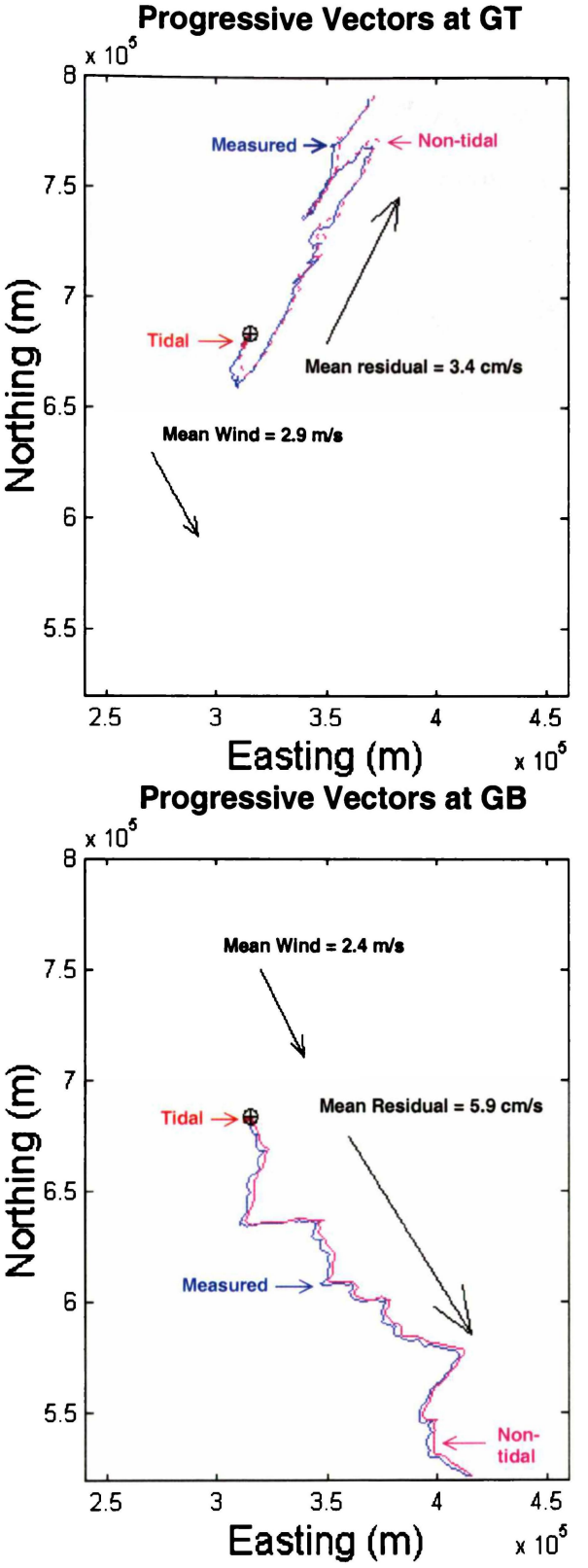

Figure 4-3. Progressive vector plots for S4 current-meter deployments GT (mid-water-column) and GB (near-bed), 9 September to 23 October 1998. Tidal currents have little or no net transport.

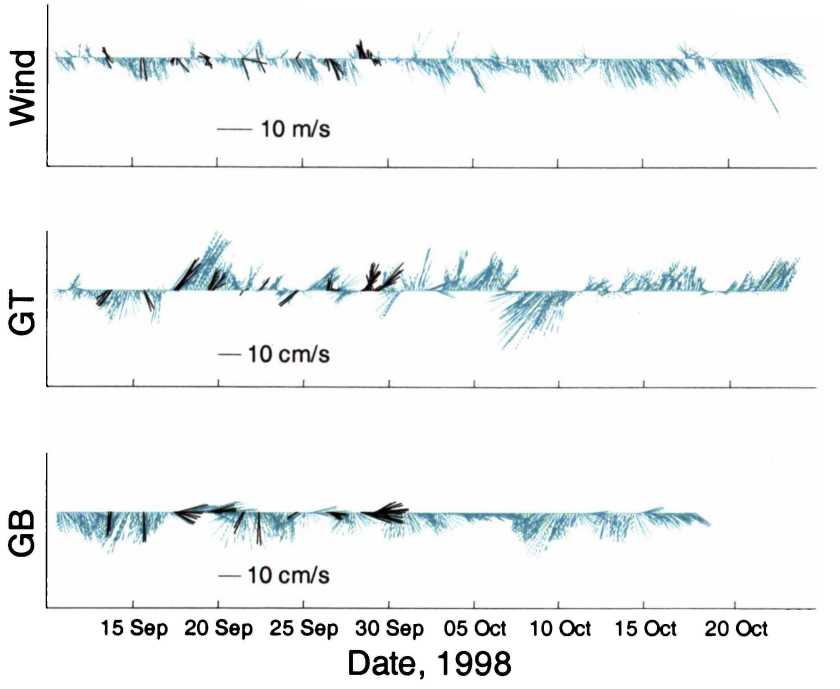

Figure 4-4. Wind at Gisborne Airport (directions inverted to true vectors convention), and residual current velocity at current-meters GT and GB. Wind and currents have been bolded at times coinciding with ADP surveys. True north is in the vertical direction.

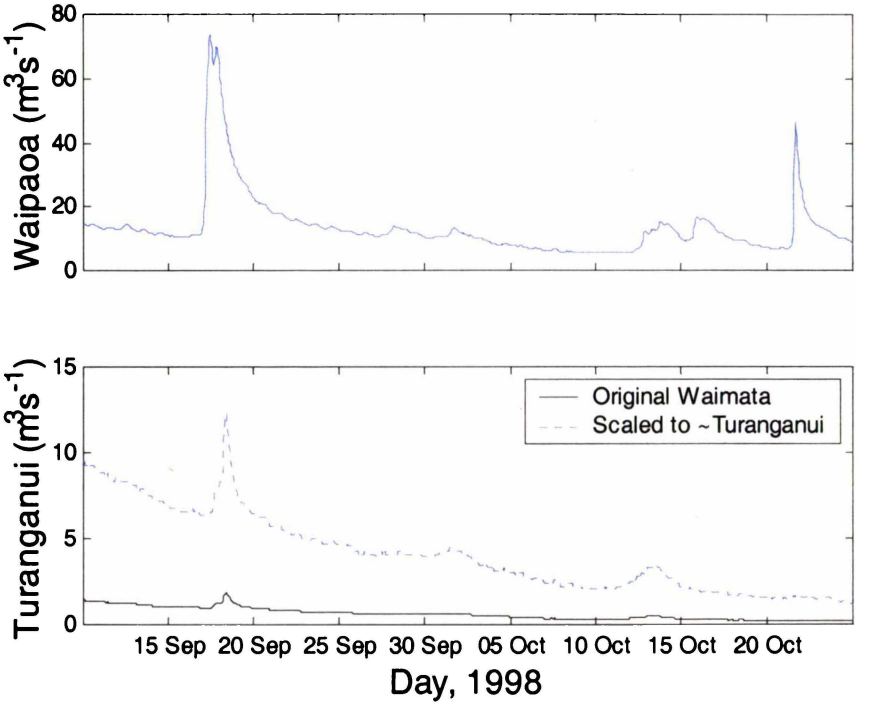

Figure 4-5. River discharge into Poverty Bay during the study period, 10 October – 23 September 1998. The Waimata River is the main tributary of the Turanganui River that discharges adjacent to Port Gisborne. An estimate of the Turanganui River discharge is shown based on Waimata River discharge, scaled to approximately one sixth of the Waipaoa River (Gorman et al., 1997).

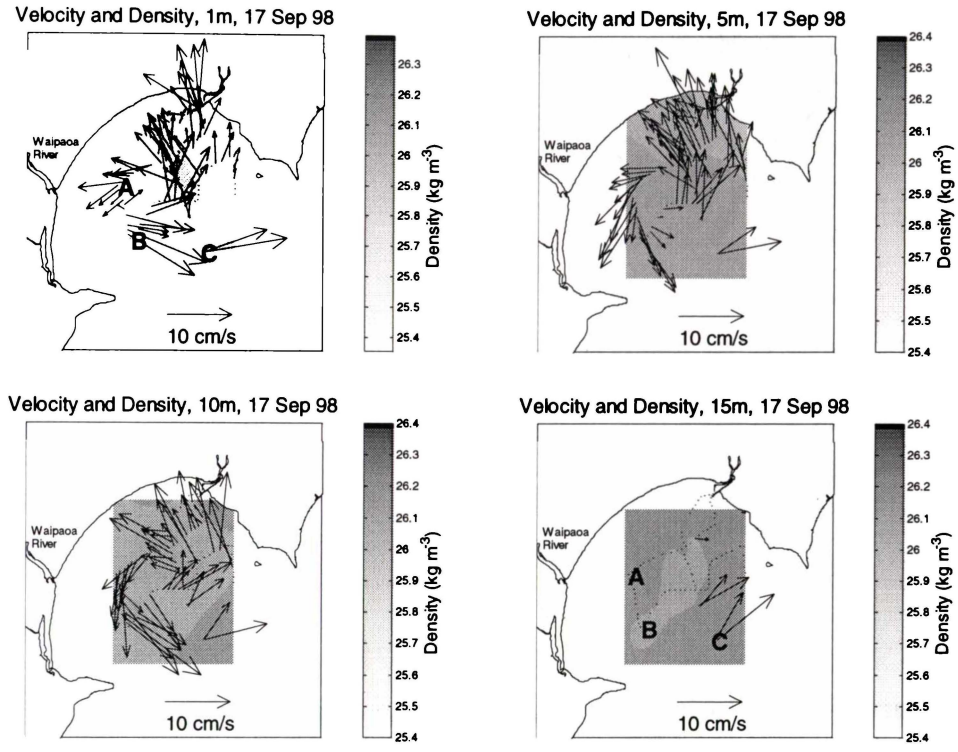

Figure 4-6. Velocity and water density anomaly (-1000) measured by vessel-mounted real-time ADP and CTD, 8:54-15:21, 17 September 1998. Wind was northerly < 2 m s^{-1} (Figure 4-4). Depths are relative to lowest astronomical tide. CTD cast sites A, B and C (refer **Figure 4-12**) are marked on plots a and d.

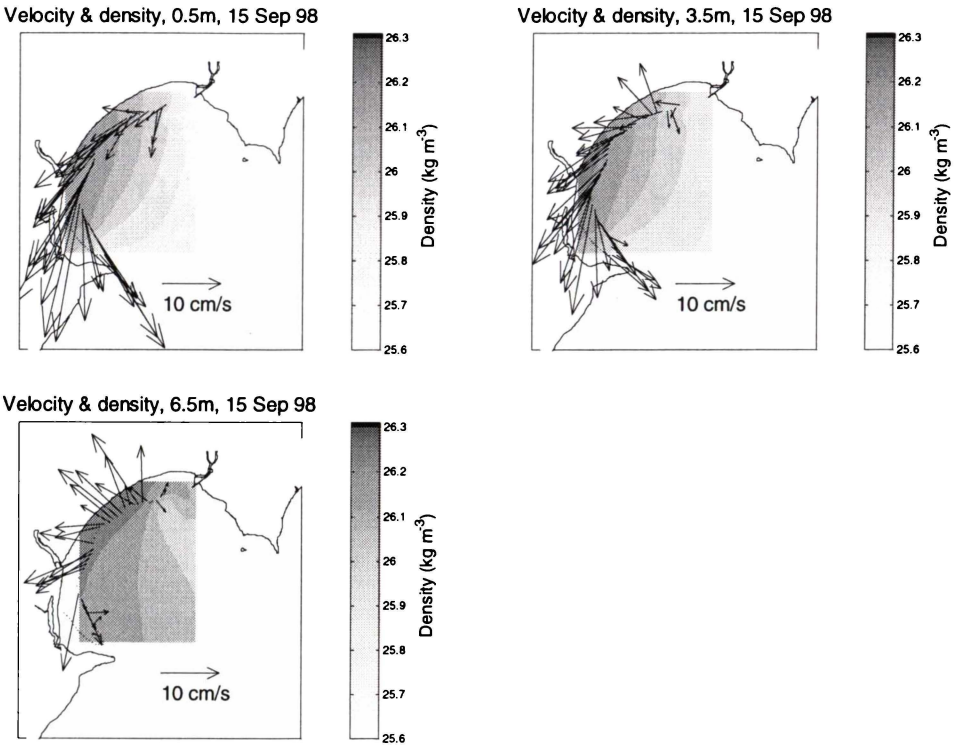

Figure 4-7. Velocity and water density anomaly (-1000) measured by vessel-mounted real-time ADP and CTD, 13:50-15:54, 15 September 1998, under northerly wind of > 5 m s^{-1} (Figure 4-4). Depths are relative to lowest astronomical tide.

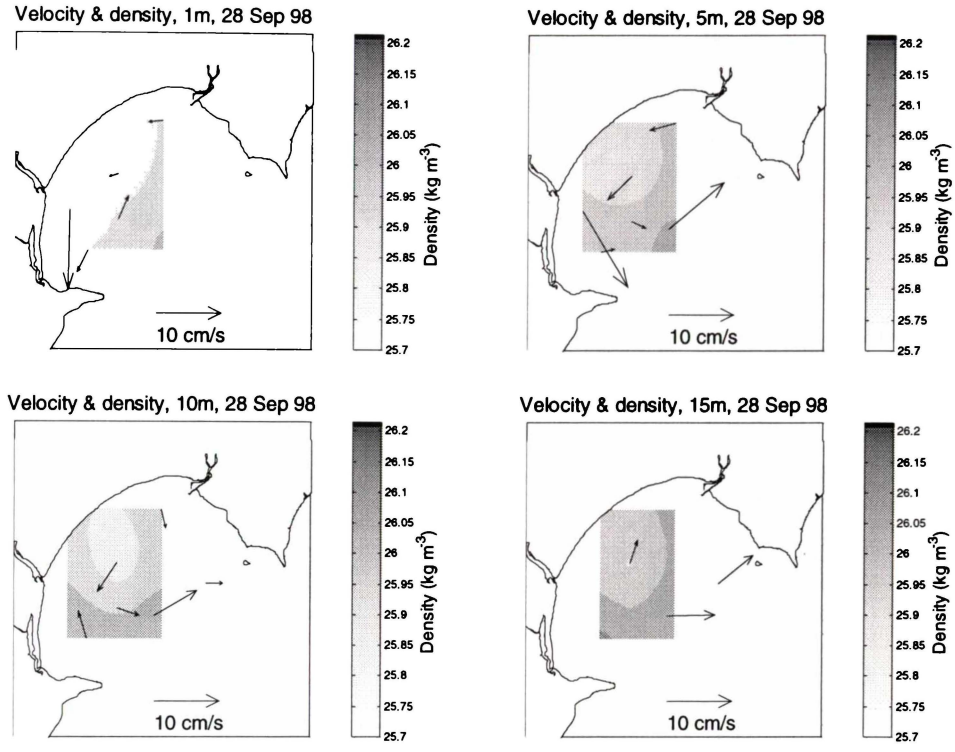

Figure 4-8. Velocity and water density anomaly (-1000) measured by bottom-mounted ADP and CTD, 7:25-11:52, 28 September 1998. Wind was southerly 3-4 m s^{-1} (Figure 4-4). Depths are relative to lowest astronomical tide.

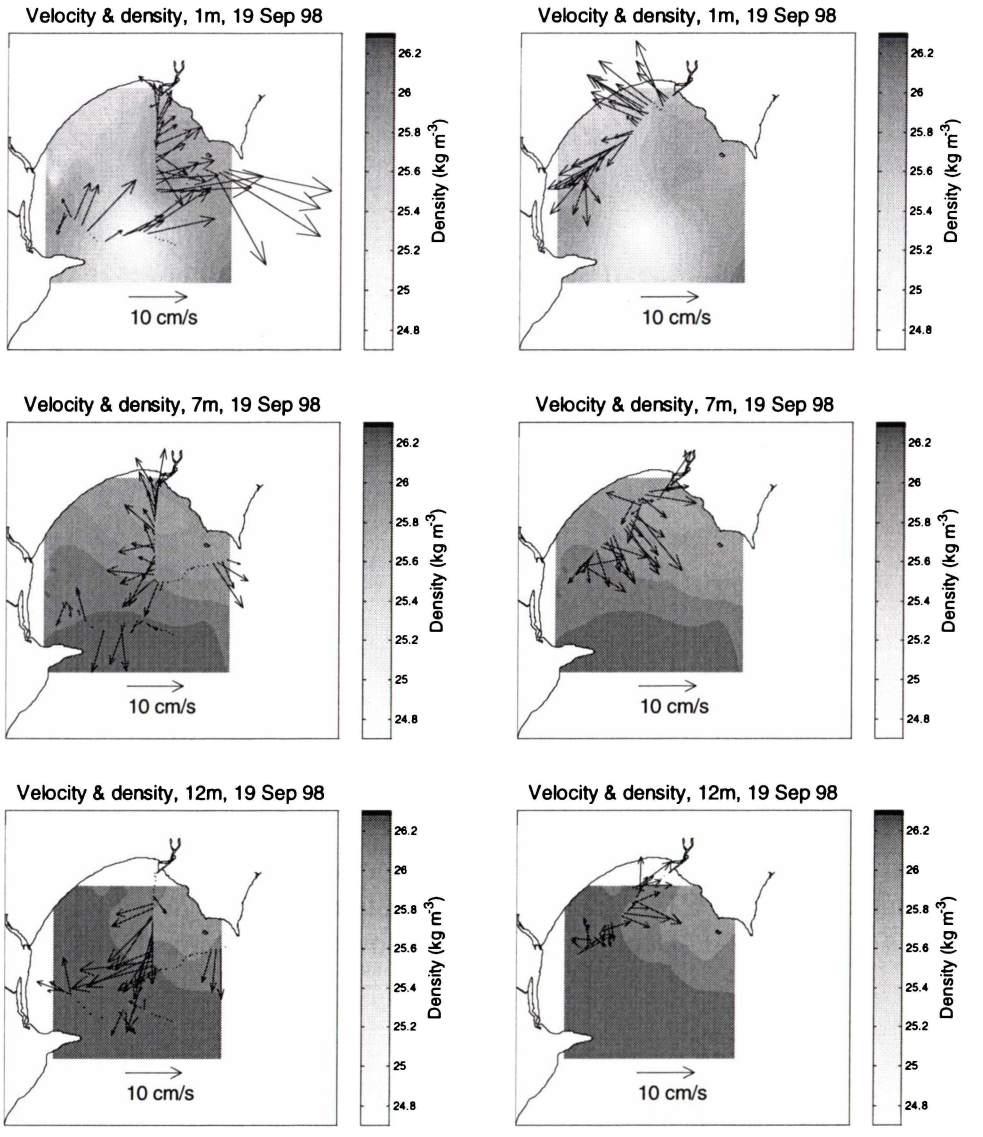

Figure 4-9. Velocity and water density anomaly (-1000) measured by vessel-mounted real-time ADP and CTD, 7:59-15:21, 19 September 1998. The left-hand plots relate to the morning during an offshore breeze (< 3 m s^{-1}), while plots on the right relate to early afternoon during a southeast sea breeze of ~ 3 m s^{-1}. Densities relate to CTD casts spanning morning and afternoon, and are identical in both left and right-hand plots. Depths are relative to lowest astronomical tide.

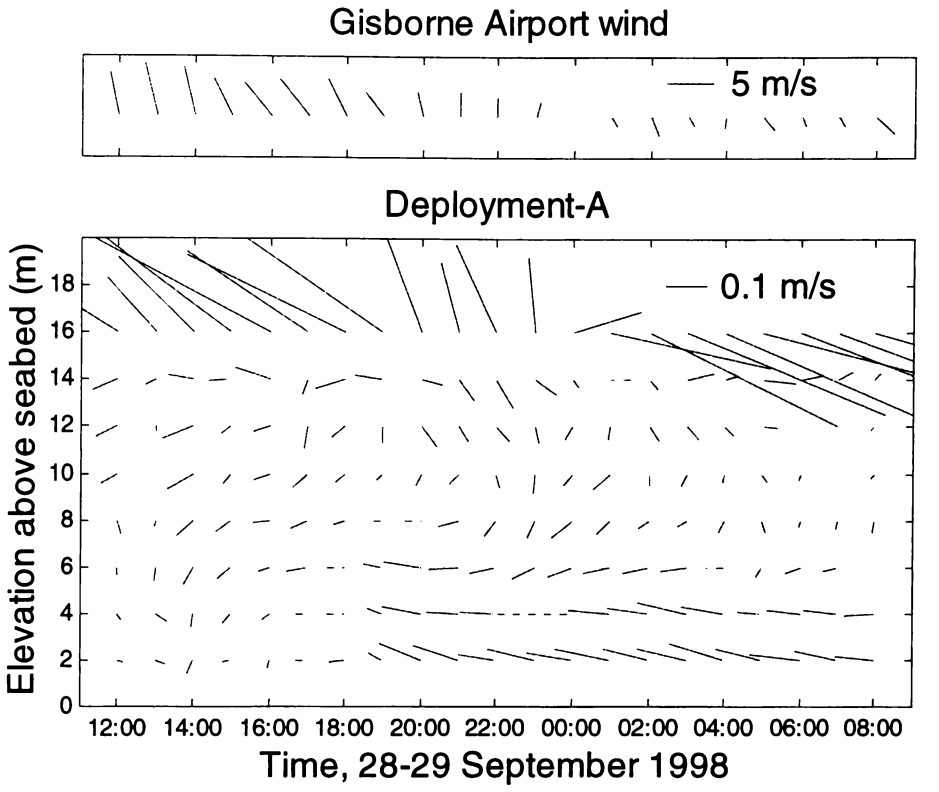

Figure 4-10. Feather plots of hourly wind and current, over the duration of ADP bottom-mounted Deployment-A, 12:00, 28 September – 08:00, 29 September, 1998. Wind velocities have been inverted to true vectors convention. Speed magnitudes at 16 m elevation are overestimated due to acoustic interference with the water surface, but nonetheless are in close directional agreement with wind. True north is vertically up the page.

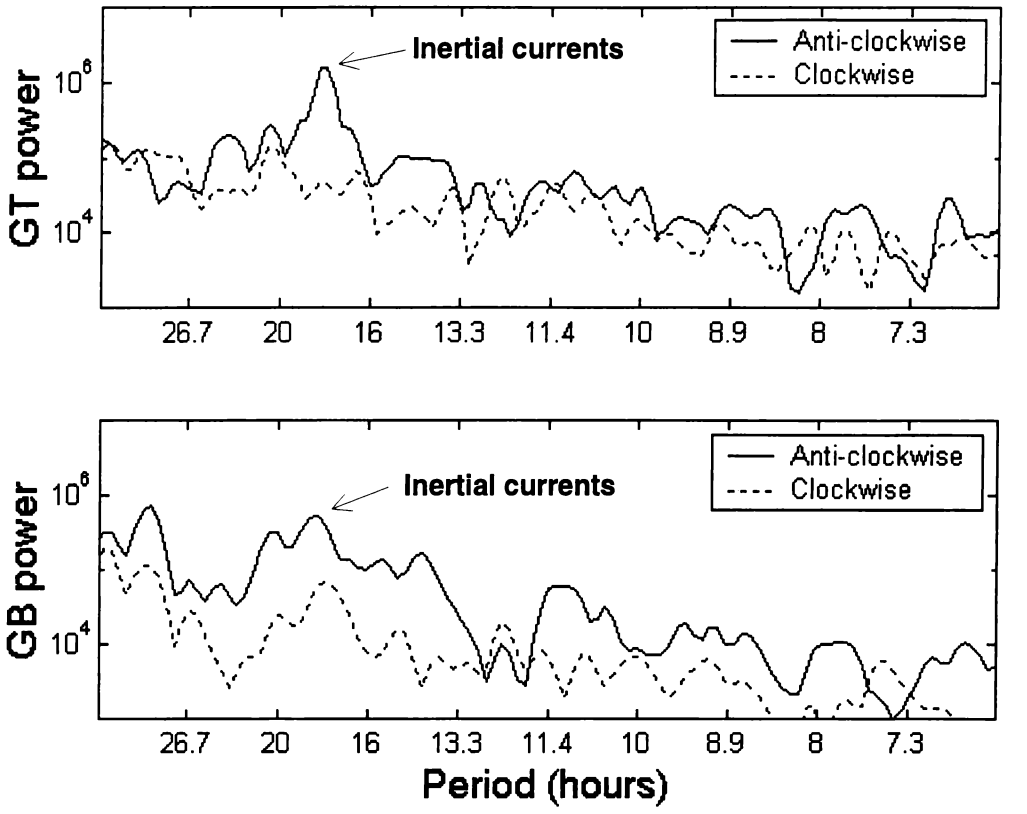

Figure 4-11. Rotary spectra of residual currents at GT (mid-water) and GB (near-bed).

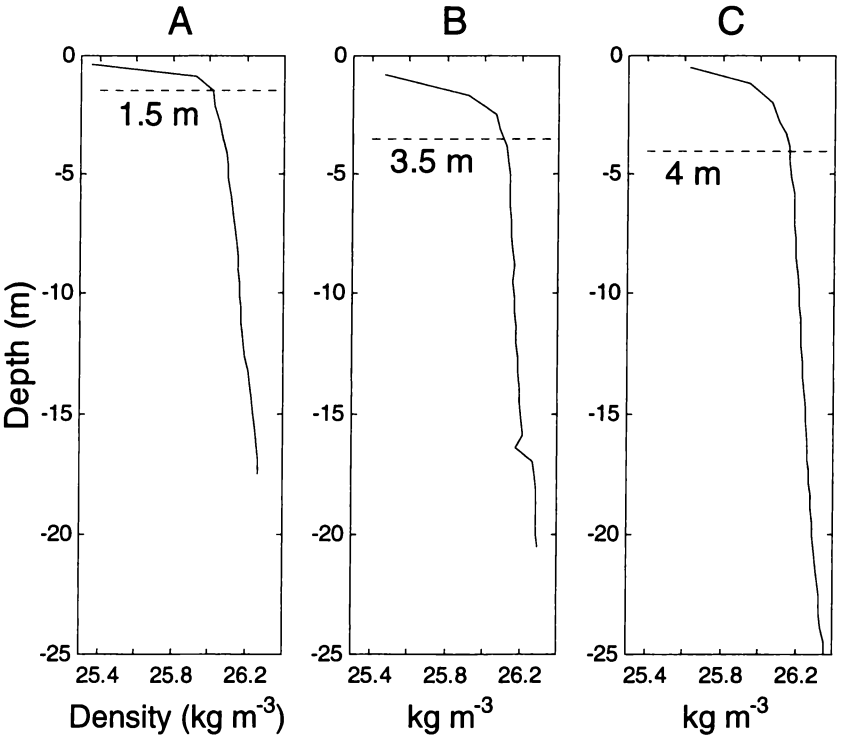

Figure 4-12. Vertical density profiles A, B and C at distances 3000, 4300 and 7500 m respectively from the Waipaoa River, as measured from CTD casts taken at sites A, B and C (**Figure 4-6**a,d), on 17 September. The horizontal dashed line represents the approximate river plume depth.

5

5.1 CONTEXT OF THE PAPER WITHIN THE THESIS

The paper presented in Chapter 4 used data analyses to infer hydrodynamic forcing and typical circulation patterns within Poverty Bay. The paper also addressed continental-shelf-current forcing and an outcome of this was the identification of significant low-frequency motion in the shelf sea-level and current record, the source of which was not investigated. Low-frequency motion is often associated with coastal-trapped-waves (CTWs) (Csanady, 1997) that can provide significant hydrodynamic forcing in coastal embayments (Wright et al., 1987; Black et al., 1993). Coastal-trapped-waves (CTWs) are a possible source of low-frequency energy at Gisborne, having been identified along the South Island west coast after generation in the Cook Strait region (Stanton, 1995). An investigation of CTW activity at Poverty Bay is therefore undertaken in this paper (specific thesis aim 2), employing wind and water level data obtained during the field study and from south of Poverty Bay including Cook Strait. It was anticipated that successful prediction of Cook-Strait-forced CTW activity might provide a boundary condition component for future three-dimensional simulation of Poverty Bay, but CTWs are not sufficiently well predicted with the simple model. However, it is demonstrated that they do propagate northward from the Cook Strait region to Poverty Bay.

Coastal-trapped waves on the east coast of the North Island, New Zealand

S. A. STEPHENS[1]
K. P. BLACK[1]
R. G. BELL[2]
T. R. HEALY[1]
[1]Coastal Marine Group, Department of Earth Sciences, The University of Waikato, Private Bag 3105, Hamilton, New Zealand, email: scotts@waikato.ac.nz, k.black@waikato.ac.nz, t.healy@waikato.ac.nz
[2]National Institute of Water and Atmospheric Research Ltd, P. O. Box 11 115, Hamilton, New Zealand, email: r.bell@niwa.cri.nz

Abstract The coastal ocean response to remote sea-level variation and wind forcing, on the east coast continental shelf of North Island, New Zealand, was examined using current, sea-level and wind observations, combined with barotropic numerical simulations. Correlation and regression analyses showed that CTWs generated by wind-driven water flux through Cook Strait, could account for up to 40% of variance in Gisborne shelf-currents, at timescales of 2-20 day period. Numerical simulations indicated that CTWs forced by a through-strait flux dominated low-frequency motion at Riversdale, but although these remotely-forced waves were reaching as far north as Gisborne, they were not dominating low-frequency motion there. Simulated sea-levels showed 88% energy attenuation occurred as CTWs exited Cook Strait, but only 3% attenuation occurred as CTWs travelled up-coast from Riversdale, therefore a barotropic CTW generated by a Cook Strait flux had approximately 9% its original energy on reaching Gisborne.

Keywords alongshore wind; wind stress; continental shelf; coastal flux; inverse barometer; weather band; cross-correlation; spectral analysis; numerical modelling

5.2 INTRODUCTION

The alongshore propagation of sea-level changes and associated flow patterns on the continental-shelf are often the result of coastal-trapped waves (CTWs), and these phenomena have received considerable attention since Hamon (1962) first identified their signature (Csanady, 1997). Since then CTWs have been identified in numerous field studies and theoretical advances have been made in modelling these features. Csanady (1997) provides a thorough review. CTWs are a form of Kelvin wave, so called because the Coriolis force traps them at the coast. As they propagate, water is set up at the coast by Coriolis, giving rise to an offshore horizontal pressure gradient force that balances the Coriolis force and keeps the wave moving parallel to the coast (The Open University, 1989). In the Southern Hemisphere CTWs must propagate with the coast on the left, and therefore move northward on the east coast of New Zealand and southward on the west coast. The offshore extent of the wave is governed by the Rossby radius of deformation, of order 2000 km for barotropic and 20 km for baroclinic waves, at latitude 40°S (The Open University, 1989). CTWs are distinguished from other Kelvin waves (such as initiated when tides or Rossby waves encounter land boundaries) by their generation mechanism. CTWs are generated over the shelf either by alongshore wind stress (Hamon, 1976; Clark and van Gorder, 1986) or by a coastal flux pulsing through a coastal strait (Buchwald and Kachoyan, 1987).

In New Zealand, Heath (1978) observed 0.1 m s^{-1} mean currents in the Taranaki Bight/western Cook Strait region, generated by wind stresses associated with passing meteorological pressure systems. Cahill et al. (1991) and Stanton (1995) later showed this region to be important for the forcing of CTWs that propagate southward along the west coast of South Island, New Zealand. The likelihood exists that CTWs also propagate northward up the east coast of the North Island, having been generated by a wind-driven coastal flux through Cook Strait. Some support for this hypothesis comes from Goring (1995) and Schwarz (1997), who identified the possible signature of a storm-generated CTW propagating from Gisborne around East Cape to the Bay of Plenty. Alongshore current data presented by Chiswell (2000) from two sites on the lower North Island east coast show a staggered pulse of north-directed velocities between 7-12 February 1998, that might be CTW related. The pulses coincide with strong north-westerly winds measured in Cook Strait and at Castlepoint (up to 25 m s^{-1}).

This paper investigates the hypothesis that CTWs propagate up the east coast of North Island New Zealand, from Cook Strait to Gisborne. Cook Strait is known for having strong through-strait winds (Reid, 1996). Strong wind stresses through Cook Strait generate associated through-strait currents. These currents provide the coastal flux necessary for CTW generation via the Buchwald and Kachoyan (1987) theory. Cahill et al. (1991) found coherence between through-strait wind stress and CTW motion on the upper South Island that matched the Buchwald and Kachoyan (1987) *coastal flux* theory. Further away from Cook Strait on the lower South Island west coast, Stanton (1995) showed that *longshore wind stress* was highly correlated with sea-level and appeared to be the dominant forcing mechanism.

This paper presents evidence for CTWs on the North Island east coast and addresses both forcing mechanisms. Sea-level and current data are examined first, to identify low-frequency correlation representative of CTW activity. A simple barotropic model is then used in an attempt to reproduce northward CTW propagation along the North Island east coast. Data acquisition and treatment is discussed first, results of time-domain analyses and numerical simulations are presented, and the occurrence of CTWs is then considered.

5.3 METHODS

The data set for the investigation comprised of current and total-pressure measurements on the shelf off Gisborne, sea-level at Wellington Harbour and at Riversdale, and wind measured at Brothers Island in Cook Strait, Castlepoint and Gisborne Airport (Figure 5-1). Abbreviations referring to these data are listed in Table 5-1. Detailed flow information is necessary to identify the structure of both barotropic and baroclinic CTWs and since only one set of current measurements were available, modal composition or changing cross-shore structure of the CTWs is not addressed. The results of Stanton (1995) suggest that even if this data were available, the considerable alongshore variation in bathymetry between Cook Strait and Gisborne (Figure 5-3) would likely cause changes in CTW modal

structure, requiring a comprehensive current meter array to resolve. The available sea-level and wind stress data at three sites is suited to the identification of barotropic waves, which have a large surface expression, therefore the study concentrates on barotropic CTWs and uses a barotropic numerical model.

Analyses are restricted to a 38-day time frame (Sep-Oct, 1998) for which Gisborne current and pressure data is available. Therefore, factors that influence seasonal and interannual sea-level fluctuations such as water temperature, ENSO and offshore sea-level differences (Burrage et al., 1995) can be ignored.

Hourly wind and barometric data for 1998 were obtained for three stations, Gisborne Airport (W_G), Castlepoint (W_C), and Brothers Island (W_B) in Cook Strait (Figure 5-1). Wind velocities were adjusted to 10 m above sea-level (Beer, (1983). Wind stresses were calculated for all stations using the method of Large and Pond (1981), and their directions were inverted to true vectors convention for direct comparison with current data. Cook Strait wind stresses are approximately four times those of the up-coast stations (Figure 5-2). Currents on the continental shelf adjacent to Gisborne (Figure 5-1) were measured by two S4 current-meters, deployed at the same site between 10 September and 23 October 1998, 6 km offshore from Gisborne, on the continental shelf in 35 m water depth (η_G, Figure 5-1). The *near-bed* S4 was mounted 2 m above the seabed and is hereafter referred to as V_b to signify *cross-shore* and *alongshore* velocity components respectively. The *mid-water* S4DW, here-on referred to as V_t, was deployed approximately 24 m above the bed on a taut mooring. The S4DW also contained a total pressure sensor, and adjusted sea-levels from this instrument are hereafter referred to as η_G. Sea-level and barometric pressure at five-minute intervals were obtained for Riversdale and Wellington Harbour, and corresponding inverse-barometer adjusted sea-levels are hereafter referred to as η_R and η_W respectively (Figure 5-1). Linear interpolation was used over gaps of less than two time steps in wind and sea-level records. Data was then filtered and decimated (see below) and the process repeated. Since most gaps were small, this proved successful in all but one case, W_G having a significant gap of over two days. This gap was filled using the CLEAN algorithm of Baisch and Bokelmann (1999).

Atmospheric pressure (hPa) may be converted to an equivalent inverse barometer (IB) sea-level in mm using the commonly used barometric factor (h) of -10 mm hPa^{-1} (Goring, 1995). Sea-level records from Wellington Harbour (η_W) and Riversdale (η_R) were measured using vented sea-level recorders, which require adjusting for IB. A linear regression between IB and sea-level at Wellington showed almost isostatic conditions, with a linear regression slope (barometric factor, h) of -9.8 and squared correlation coefficient $r^2 = 0.88$, whereas Riversdale gave $h = -8.6$, $r^2 = 0.76$. Based on high barometric factor it was decided to treat sea-level at Wellington as isostatic, and a straight subtraction of IB from sea-level was performed. At Riversdale, the barometric factor $h = -8.6$ mm hPa^{-1} was used for IB and subtracted from raw sea-level to give an adjusted sea-level. The adjusted sea-levels are used below in cross-correlation analyses with other data sets. At Gisborne, sea-level was not measured directly, but total pressure was recorded by the mid-water shelf current-meter. Sea-level (η_G) was then calculated using the hydrostatic equation (Gill, 1982). Total pressure gauges measure the combined effect of atmospheric and water pressure, as atmospheric pressure increases, so the water pressure decreases. On conversion therefore, total pressure gauges essentially give an adjusted sea-level, requiring no correction for IB (Harms and Winant, 1994). Thus on subtraction of the mean sea-level, η_G could be directly compared with adjusted sea-levels η_W and η_R.

CTWs are associated with weather patterns, being driven by alongshore wind stress or coastal fluxes that are themselves forced by meteorological conditions. CTWs are therefore low-frequency motions, Wright et al. (1987) found CTWs influenced the Labrador Shelf response in the energetic "meteorological band" of ~2-6 days. Cahill et al. (1991) found CTWs to affect the continental shelf response on the west coast of South Island New Zealand, in the "weather band" of ~6-20 days. In the present study it was decided to examine low-frequency motions on the scale of ~2-20 days. All current, sea-level and wind data presented here were band-pass filtered, using a tapered boxcar filter (Goring, 1995). The half-power frequencies were 0.033 and 0.6 cycles per day (cpd), corresponding to periods of 30 days and 40 h respectively, thus tidal influences

were removed from oceanographic data. Since interest centred on frequencies contained within the weather band, > 0.05 cpd (Cahill et al., 1991), the band-pass filter was chosen in preference to a low-pass filter, in order to remove the long term trend from the data, that can influence correlation and spectral analysis between records (Goring, 1995). Decimation to 12-hour intervals was undertaken on all data sets to reduce auto-correlation and computation time in the following analyses. Times at which decimated data from all stations were simultaneously available were 00:00, 11 September – 00:00, 18 October 1998, giving 75 × 12-hourly spaced data points.

CTW's are forced by alongshore stresses and through-strait fluxes, so the alongshore components of all directional data collected on the North Island east coast were determined, while the through-strait direction was determined for directional data collected in Cook Strait.

Time-domain cross-correlation analyses were undertaken (Chatfield, 1980), and although auto-correlation was largely removed by prior filtering and decimation, timeseries were first converted to white noise using a linear filter, so that significantly non-zero correlations were greater than $2/\sqrt{}$(sample size), (Jenkins and Watts, 1968). Following cross-correlation analyses and subsequent alignment, linear regression between variables was undertaken to determine relationships in the time domain. Frequency-domain analyses were undertaken, but provided no advantage over simple time-domain analyses when compared with model output, therefore frequency-domain analyses are omitted for simplicity.

CTWs were simulated using the two-dimensional (barotropic) form of Model 3DD (Black, 1995). The two-dimensional form of model 3DD has been successfully applied and verified in a diverse range of situations (Black, 1987; Black and Gay, 1987; Black et al., 1989; Black and Gay, 1991; Black et al., 1993; Young et al., 1994), including CTW simulation on the Great Australian Bight (Middleton and Black, 1994). Density profiles measured off the North Island east coast in October 1996 showed no marked pycnocline, but exhibited a near constant density increase with depth (Chiswell, *pers. comms.*). Although the

barotropic model is therefore not ideal, results show it capable of reproducing CTW propagation and furthermore, data was not available to calibrate a baroclinic model.

Bathymetry was digitised from New Zealand Navy hydrographic charts, and rotated 35° anticlockwise to align the model grid with the North Island east coast (Figure 5-3). Simulations were forced using a combination of low-pass-filtered measured sea-level (η_W) and measured wind data (W_B, W_C and W_G). Since the model simulations were designed to test for the northward propagation of CTWs generated in the Cook Strait region, sea-levels were input at the western boundary only. The model was first run using only measured wind data (Figure 5-3), from which a simulated Wellington Harbour sea-level ($s\eta_W$) was obtained. It was observed that model simulations using only wind inputs gave poor correlation with η_W, η_R and η_G, therefore the model required a sea-level boundary component to accurately reproduce η_W. $s\eta_W$ was low-pass-filtered (< 0.6 cpd) and subtracted from similarly filtered measured η_W to give a residual sea-level not inclusive of wind effects. This low-frequency residual sea-level was used to force the western boundary, following application of a 2.5 amplitude magnification and a 5-hour time-lag (required to accurately reproduce itself at Wellington). Simulations including both the western sea-level boundary and measured winds showed that measured η_W was being accurately reproduced (Figure 5-4), with the residual sea-level having 4 times the variance of the local wind-induced sea-level. In using the residual sea-level boundary the model therefore assumes a pre-existing wave, not forced by wind stress in the straight itself. The source of this energy is discussed later. The sea-level open boundary condition is analogous to a wave form at the western boundary, which will produce a coastal flux through the eastern end of Cook Strait. Therefore the coastal flux theory (Buchwald and Kachoyan, 1987) is the dominant forcing mechanism for simulated barotropic CTWs on the lower North Island east coast. However, the longshore wind generation mechanism (Hamon, 1976) is also present through the inclusion of wind stress in the model.

Three simulations were then undertaken, all including sea-level forcing at the western boundary but having different wind inputs. This was done to determine

the importance of local wind forcing near Gisborne. Simulation SIM1 included measured winds from W_B, W_C and W_G, simulation SIM2 did not include W_G, and simulation SIM3 included only W_B. The model was forced with wind data applied at 18 sites (Figure 5-3). Model 3DD then uses inverse-interpolation to calculate wind stresses between wind input stations. Where data from W_C or W_G were not required, wind speeds of zero were input at the relevant stations (Figure 5-3). A major source of error in the model is likely to be the use of land-based winds that are applied across the ocean to more than 200 km offshore, but no alternative wind estimates were available. Simulated sea-level was output at three sites corresponding to η_W, η_R and η_G (Figure 5-3), and all output data was low-pass-filtered < 0.6 cpd. The 20-day period between Julian Day 255-275, 1998 was simulated.

5.4 RESULTS

5.4.1 Time-Domain Data Analyses: Cross-Correlation and Linear Regression

Sea-level variation at Gisborne is greater than at Wellington or Riversdale (Figure 5-2), η_G having 2.8 times the variance of η_R and 1.6 times the variance of η_W (Table 5-3).

The band-pass filtered (0.033-0.6 cpd) data are shown in Figure 5-2. Cross-correlation analyses were undertaken to determine if significant correlation existed between data sets and at what time lags (Chatfield, 1980). Analyses showed that decimation to 12-hour intervals had largely removed any auto-correlation. For directional (wind, current) data, cross-correlations were performed using the alongshore component. Following alignment, linear regression was performed between data sets and the results are presented in Table 5-2.

Alongshore winds from all stations are significantly correlated, as can be visualised from the data (Figure 5-2). This can be expected since the scale of

weather pressure systems is generally of greater size than the North Island. As expected, V_t and V_b are strongly correlated and in phase with each other with coefficient of determination $r^2 = 0.78$. Currents off Gisborne showed a better relationship to Cook Strait wind than to local Gisborne wind, in particular near the seabed with up to 40% of V_b variance explained by Cook Strait Winds W_B (Table 5-2). Sea-level off Gisborne (η_G) lagged V_t and V_b by 1 lag (12-hour), and up to 25% of V_t and 39% of V_b can be related to η_G (Table 5-2). Since northward currents lead the sea-level peak by 1 lag, this indicates a northward propagating geostrophic wave/current (The Open University, 1989).

A weak correlation between η_R and η_G ($r^2 = 0.22$) at 2 lags is consistent with the observation that energy appears to be propagating to the north. η_W and η_R are significantly correlated at zero lag, having $r^2 = 0.38$, however η_W is uncorrelated with η_G. Multiple linear regression on more than two data sets did not greatly improve r^2 values.

5.4.2 Numerical Simulations

In all three simulations (SIM1, SIM2 and SIM3), simulated and measured low-pass-filtered sea-levels at η_R were well correlated (Table 5-4, results 2, 5 & 8). Although measured η_R is not reproduced exactly, the simulations show reasonable agreement with measured amplitude, and lag by 2-hours (Figure 5-5). The model thus shows adequate calibration to demonstrate that a large proportion of the low-frequency energy at Riversdale is related to that in Cook Strait (Figure 5-5).

Simulated sea-levels at Riversdale and Gisborne are significantly correlated at 23 hours lag (Table 5-4, result 12), i.e. simulations indicate a CTW propagating up the North Island east coast from Riversdale to Gisborne. The model shows that most attenuation of the $s\eta_W$ water levels occurs on exiting Cook Strait and before the barotropic CTW reaches Riversdale (Table 5-5). Furthermore there is little energy loss between Riversdale and Gisborne (Table 5-5). Simulated sea-levels contain $\leq$10% of the measured sea-level variance at Gisborne, but they show significant correlation for all three simulations, although the relationship is much

weaker than at Riversdale (Table 5-4 (results 3, 6 & 9), Figure 5-6). The correlation also becomes weaker (corr. coef. 0.48→0.46→0.33) as first Gisborne wind then Castlepoint wind are removed from the simulations (SIM2, SIM3), indicating the importance of local wind effects on the coast north of Riversdale.

5.5 DISCUSSION

Other than CTWs propagating from the Cook Strait region, there are many possible sources of low-frequency energy at Gisborne including local wind forcing, coastal wind jets (Laing et al., 1997; Laing and Brenstrum, 1996), CTW modal scattering, continental-shelf-currents (Chiswell, 2000), and baroclinic effects.

For example, correlations were improved with the inclusion of wind stress over the continental shelf north of Riversdale, indicating an important contribution by the local wind-field. The largest source of error in the simulations is likely to be the extrapolation of land-based winds across the continental-shelf and open ocean, since this inaccuracy directly affects the models ability to simulate CTW forcing via longshore wind stress. Longshore wind stress could supply a large proportion of the extra low-frequency variance present at Gisborne compared with further south, but is possibly not well enough represented for the model to accurately simulate its effect. The most accurate wind stress inputs will be those measured at Brothers Island (W_B) and applied in the Cook Strait region, since Cook Strait experiences a high degree of topographic steering that causes winds to align themselves through the strait (Reid, 1996).

Despite these unaccounted-for processes, the data and model have shown evidence for CTW propagation between Cook Strait and Gisborne. Significant correlation between non-tidal sea-level and currents indicates the presence of a geostrophic wave/current at Gisborne, such as observed by Burrage et al. (1995). Alongshore currents at Gisborne had highest linear relationship (Table 5-2) with winds through Cook Strait, suggesting that CTWs are generated by a wind-driven water flux through Cook Strait. Using Cook Strait wind and sea-level data,

numerical simulations were able to closely reproduce measured Riversdale sea-levels (Figure 5-5), showing that energy released from Cook Strait was propagating to Riversdale.

A lower but significant correlation between numerical output and sea-level showed CTW propagation from Cook Strait to Gisborne (Figure 5-6). The model showed that 88% attenuation of Cook Strait water level variance occurred on exiting Cook Strait and prior to the CTW reaching Riversdale, but that little further attenuation occurred between Riversdale and Gisborne (Table 5-5). Without further wind energy inputs a barotropic CTW generated in Cook Strait had approximately 9% its original energy on reaching Gisborne, but lost only 3% travelling up-coast from Riversdale. On reaching Gisborne the simulated barotropic CTW contained $\leq$10% of measured sea-level variance due to additional energy inputs from other sources, but despite the energy difference there was still significant correlation to indicate CTW propagation from Cook Strait to Gisborne.

These observations support the presence of CTWs on the North Island east coast, generated by a flux of water through Cook Strait. The through-strait flux mechanism appears to dominate low-frequency motion at Riversdale, but the regression results suggest that although these remotely-forced waves are reaching as far north as Gisborne, they are not dominating low-frequency motion there. These results are analogous to the findings of Cahill et al. (1991) and Stanton (1995), who found the coastal flux generation theory to apply to CTW motion on the upper South Island west coast, but longshore wind stress generation to dominate further south from Cook Strait. Better representation of the longshore wind field in the model may have more closely reproduced Gisborne sea-level in the simulations.

Measured wind stress and sea-levels did not show strong linear relationships, and preliminary simulated sea-levels had poor correlation with all measured sea-levels when forced by wind stress only, necessitating the use of a western sea-level boundary. The use of the sea-level boundary to re-create measured water level at Wellington (η_W) assumes that there is a pre-existing low-frequency component in Cook Strait that is not generated locally by through-strait winds, and its presence

is justified in modelling terms by the calibration at η_R. Before the boundary multiplication factor was applied, the variance of the applied sea-level was 4 times that of the simulated wind-induced sea-level. This implies that wind stress (over the Cook Strait area modelled) supplies only ¼ of η_W low-frequency energy, the rest coming from existing sea-level energy.

The source of this energy is unknown, but wind generation over the wide Taranaki Bight continental-shelf and the shelf to the north is a likely candidate. Both Cahill et al. (1991) and Stanton (1995) found this region to be important in the generation of coastal fluxes that initiated South Island CTWs. Shirtcliffe et al. (1990) showed that the non-tidal Cook Strait flux could be closely approximated using a simple box-model driven by wind stress over Taranaki Bight and balanced by bottom friction in the strait. There is a large continental-shelf area ideal for CTW generation in this region that is not covered by the model domain used in this study, so the modelled response to through-strait wind forcing is likely to be smaller than experienced in reality. Some contributions from long period tidal energy can be expected (eg. Burrage et al. (1995)); tidal analysis on one years sea-level at Wellington showed that the MSM, MF, MSF fall inside the 40-hour – 30-day filtering cut-off periods and have amplitudes 0.005-0.017 m, i.e. up to 0.03 m variation. However these tides will be partially contaminated by non-tidal processes at the relevant timescales. Some remotely-forced low-frequency energy is likely to reach Cook Strait from CTWs forced either on the North Island west coast or on the South Island east coast, or by wind- or atmospheric pressure-induced seiching in Taranaki Bight (Shirtcliffe et al., 1990). The bathymetry on the upper South Island east coast exhibits rapid alongshore depth changes south of Cook Strait, and although this violates a basic assumption of simple CTW theory, Stanton (1995) observed some remotely forced CTW propagation to occur over similar bathymetry changes on the lower South Island west coast.

5.6 CONCLUSIONS

Simulation of barotropic CTWs combined with time-domain cross-correlation analyses of wind, sea-level and Gisborne current velocities, showed CTW

propagation from Cook Strait to Gisborne. Correlation and regression analyses showed that CTWs generated by wind-driven water flux through Cook Strait, could account for up to 40% of variance in Gisborne shelf-currents, at timescales of 2-20 day period. Numerical simulations forced from the Cook Strait region were able to partially reproduce low-frequency sea-level oscillations at Riversdale and Gisborne. The through-strait flux forcing mechanism of Buchwald and Kachoyan (1987) appeared to dominate low-frequency motion at Riversdale, but the regression results suggested that although these remotely-forced waves were reaching as far north as Gisborne, they were not dominating low-frequency motion there. Simulated sea-levels showed 88% energy attenuation occurred as CTWs exited Cook Strait, but only 3% attenuation occurred as CTWs travelled up-coast from Riversdale, therefore a barotropic CTW generated by a Cook Strait flux had approximately 9% its original energy on reaching Gisborne. Better representation of the longshore wind field in the model may have more closely reproduced Gisborne sea-level in the simulations.

5.7 RECOMMENDATIONS FOR FUTURE WORK

The data set used in this study was too sparse to identify CTW details such as modal structure and propagation speeds. This could be attempted in future given a comprehensive field programme and modern acoustic Doppler technology would provide an ideal tool for measuring the vertical current structure in the presence of CTWs. Future study could also employ wavelet analysis, which is a more suitable for examining the non-stationary wind-current relationship than spectral and time-domain analyses.

5.8 ACKNOWLEDGEMENTS

The authors wish to thank Dr. Basil Stanton of NIWA Wellington, for his advice at the initiation of this investigation. Thanks to Derek Goring of the National Institute of Water and Atmospheric Research (NIWA) who supplied wind data

and sea-level at Riversdale. Thanks to Wellington Regional Council who supplied sea-level data at Wellington Harbour.

5.9 REFERENCES

Baisch, S. and Bokelmann, G. H. R. 1999: Spectral analysis with incomplete time series: an example from seismology. *Computers and Geosciences 25*: 729-738.

Beer, T. 1983: Environmental Oceanography: an introduction to the behaviour of coastal waters, Pergamon Press, New York. 262 p.

Black, K. P. 1987: A numerical sediment transport model for application to natural estuaries, harbours and rivers. *In:* Noye, J. *ed.* Numerical modelling applications to marine systems, Vol. Elsevier, North Holland, pp. 77-105.

Black, K. P. 1995: The hydrodynamic model 3DD and support software. Department of Earth Sciences, The University of Waikato, Hamilton, Pp. 53.

Black, K. P. and Gay, S. L. 1987: Eddy formation in unsteady flows. *Journal of Geophysical Research 92(C9)*: 9514-9522.

Black, K. P. and Gay, S. L. 1991: Reef-scale numerical hydrodynamic modelling developed to investigate crown-of-thorns starfish outbreaks. *In:* Bradbury, R. *ed.* Acanthaster and the Coral Reef: A Theoretical Perspective, Vol. Springer-Verlag, pp. 120-150.

Black, K. P., Hatton, D. and Rosenberg, M. 1993: Locally and externally-driven dynamics of a large semi-enclosed bay in southern Australia. *Journal of Coastal Research 9(2)*: 509-538.

Black, K. P., Healy, T. R. and Hunter, M. 1989: Sediment dynamics in the lower section of a mixed sand and shell-lagged tidal estuary. *Journal of Coastal Research 5(3)*: 503-521.

Buchwald, V. T. and Kachoyan, B. J. 1987: Shelf waves generated by a coastal flux. *Australian Journal of Marine and Freshwater Research 38(3)*: 429-437.

Burrage, D. M., Black, K. P. and Steinberg, C. R. 1995: Long-term sea-level variations in the central Great Barrier Reef. *Continental Shelf Research 15(8)*: 981-1014.

Cahill, M. L., Middleton, J. H. and Stanton, B. R. 1991: Coastal-trapped waves on the west coast of South Island, New Zealand. *Journal of Physical Oceanography 21*: 541-557.

Chatfield, C. 1980: The analysis of time series: an introduction, Chapman and Hall, London. 268 p.

Chiswell, S. M. 2000: The Wairarapa Coastal Current. *New Zealand Journal of Marine and Freshwater Research 34(2)*: 303-315.

Clark, A. J. and van Gorder, S. 1986: A method for estimating wind-driven frictional, time-dependent, stratified shelf and slope water flow. *Journal of Physical Oceanography 16*: 1013-1037.

Csanady, G. T. 1997: On the theories that underlie our understanding of continental shelf circulation. *Journal of Oceanography 53*: 207-229.

Gill, A. E. 1982: Atmosphere-ocean dynamics, Academic Press, San Diego. 662 p.

Goring, D. G. 1995: Short level variations in sea level (2-15 days) in the New Zealand region. *New Zealand Journal of Marine and Freshwater Research 29*: 69-82.

Hamon, B. V. 1962: The spectrums of sea level at Sydney, Coff's Harbour and Lord Howe Island. *Journal of Geophysical Research 67(13)*: 5147-5155.

Hamon, B. V. 1976: Generation of shelf waves on the East Australian Coast by wind stress. *Memoires Societe Royale des Sciences de Liege 6*: 359-367.

Harms, S. and Winant, C. D. 1994: Synthetic Subsurface Pressure derived from bottom pressure and tide gauge observations. *Atmospheric and Oceanic Technology 11*: 1625-1636.

Heath, R. A. 1978: Atmospherically induced water motions off the west coast of New Zealand. *New Zealand Journal of Marine and Freshwater Research 12(4)*: 381-390.

Jenkins, G. M. and Watts, D. G. 1968: Spectral analysis and its applications, Holden-day, San Francisco. 525 p.

Laing, A. K. and Brenstrum, E. 1996: Scatterometer observations of low-level wind jets over New Zealand coastal waters. *Weather and Forecasting 11(4)*: 458-475.

Laing, A. K., Revell, M. J. and Brenstrum, E. 1997: ERS scatterometer observations of airflow around mountainous islands. *In:* Proceedings of the 3rd ERS Symposium on Space at the Service of our EnvironmentFlorence, Italy, Pp. 1579-1584.

Large, W. G. and Pond, S. 1981: Open ocean momentum flux measurements in moderate to strong winds. *Journal of Physical Oceanography 11*: 324-337.

Middleton, J. F. and Black, K. P. 1994: The low frequency circulation in and around Bass Strait: a numerical study. *Continental Shelf Research 14(13/14)*: 1495-1521.

Reid, S. 1996: Pressure gradients and winds in Cook Strait. *Weather and Forecasting 11*: 476-488.

Schwarz, M. A. 1997: Factors influencing storm surge variability on the New Zealand coast. Diploma in Applied Science (Meteorology) thesis, Victoria University, Wellington. 94 p.

Shirtcliffe, T. G. L., Moore, M. I., Cole, A. G., Viner, A. B., Baldwin, R. and Chapman, B. 1990: Dynamics of the Cape Farewell upwelling plume, New Zealand. *New Zealand Journal of Marine and Freshwater Research 24(4)*: 555-568.

Stanton, B. R. 1995: Sea level variability on the West Coast of New Zealand. *Journal of Physical Oceanography 25(6)*: 1265-1272.

The Open University 1989: Ocean Circulation, Pergamon Press, Oxford. 238 p.

Wright, D. G., Greenberg, D. A. and Majaess, F. G. 1987: The influence of bays on adjusted sea level over adjacent shelves with application to the Labrador Shelf. *Journal of Geophysical Research 92(C13)*: 14610-14620.

Young, I. R., Black, K. P. and Heron, M. L. 1994: Circulation in the Ribbon Reef region of the Great Barrier Reef. *Continental Shelf Research 14(2/3)*: 117-142.

5.10 TABLES

Table 5-1. Recording station abbreviations for current, sea-level and wind data, including the chosen alongshore direction.

W_B Wind at Brothers Island (Cook Strait), through-strait direction = 330°T

W_C Wind at Castlepoint, alongshore direction = 33°T

W_G Wind at Gisborne Airport, alongshore direction = 42°T

V_t Gisborne mid-water alongshore current at S4DW, alongshore direction = 33°T

U_b Gisborne near-bed alongshore current at S4, alongshore direction = 60°T

η_W Sea-level at Wellington Harbour

η_R Sea-level at Riversdale

η_G Sea-level at Gisborne, measured at S4DW

$s\eta_W$ Simulated sea-level in Wellington Harbour, model grid cell $I = 67$, $J = 54$, Figure 5-3

$s\eta_R$ Simulated sea-level at Riversdale, model grid cell $I = 94$, $J = 73$, Figure 5-3

$s\eta_G$ Simulated sea-level on the Gisborne continental shelf, model grid cell $I = 93$, $J = 180$, Figure 5-3

Table 5-2. Wind, current and sea-level, multi-linear regression analysis. $Y = aX_1 + bX_2 + c$, where Y = bolded variable, X_1 = A (alongshore component) and X_2 = C (cross-shore component). Prior to performing linear regression, data were aligned according to the shown lag. Lags were determined through cross-correlation in the time-domain, and refer to the lead of the bolded variable (Δt = 12-hours).

$\mathbf{W_B}$		a	b	c	r^2	lag
W_C	A	0.12	-0.11	0.00	0.56	0
	C	0.07	0.02	0.00	0.42	0
W_G	A	0.09	0.03	0.00	0.35	0
	C	0.10	0.14	0.00	0.31	0
V_t	A	0.49	-0.69	0.00	0.26	1
	C	0.09	0.09	0.00	0.15	1
V_b	A	0.52	-0.40	0.00	0.40	1
	C	-0.02	-0.01	0.00	0.01	1
η_W		0.10	0.18	0.00	0.22	-1
η_R		0.08	0.06	0.00	0.11	0
η_G		0.16	-0.16	0.00	0.14	2

$\mathbf{W_C}$		a	b	c	r^2	lag
W_G	A	0.59	-0.11	0.00	0.31	1
	C	0.35	0.86	0.00	0.23	1
V_t	A	3.63	-1.67	0.00	0.23	1
	C	0.38	-0.03	0.00	0.04	1
V_b	A	3.32	-0.68	0.00	0.37	1
η_G		0.87	0.14	0.00	0.09	2

$\mathbf{W_G}$		a	b	c	r^2	lag
V_t	A	2.55	-0.58	0.00	0.12	0
	C	0.91	0.20	0.00	0.35	0
V_b	A	2.14	0.48	0.00	0.23	0
	C	-0.26	-0.08	0.00	0.04	0
η_G		0.80	0.15	0.00	0.09	1

η_W		a	b	c	r^2	lag
η_R		0.52		0.00	0.38	0
η_G		0.08		0.00	0.00	-

η_R		a	b	c	r^2	lag
η_G		0.81		0.00	0.22	2
V_t	A	1.78		0.00	0.20	1
	C	0.19		0.00	0.04	1
V_b	A	1.66		0.00	0.31	1
	C	0.22		0.00	0.05	1

η_G		a	b	c	r^2	lag
V_t	A	1.29		0.00	0.25	-1
	C	0.21		0.00	0.10	-1
V_b	A	1.21		0.00	0.39	-1
	C	0.07		0.00	0.01	-1

Table 5-3. Measured sea-level variance as a percentage of measured η_G variance.

η_W	η_R	η_G
63%	39%	100%

Table 5-4. Cross-correlation results between real and simulated sea-levels.

Result index #	Simulation	Variable 1	Variable 2	Lag	Correlation Coefficient
1	SIM1	η_W	$s\eta_W$	0	0.97
2	SIM1	η_R	$s\eta_R$	2	0.63
3	SIM1	η_G	$s\eta_G$	9	0.48
4	SIM2	η_W	$s\eta_W$	0	0.96
5	SIM2	η_R	$s\eta_R$	1	0.62
6	SIM2	η_G	$s\eta_G$	18	0.46
7	SIM3	η_W	$s\eta_W$	0	0.96
8	SIM3	η_R	$s\eta_R$	1	0.59
9	SIM3	η_G	$s\eta_G$	23	0.33
10	SIM1	$s\eta_W$	$s\eta_R$	0	0.57
11	SIM1	$s\eta_W$	$s\eta_G$	13	0.48
12	SIM1	$s\eta_R$	$s\eta_G$	23	0.67
13	SIM3	$s\eta_W$	$s\eta_R$	0	0.56
14	SIM3	$s\eta_W$	$s\eta_G$	15	0.31
15	SIM3	$s\eta_R$	$s\eta_G$	33	0.62

Table 5-5. Predicted sea-level variance as a percentage of predicted $s\eta_W$ variance.

$s\eta_W$	$s\eta_R$	$s\eta_G$ (SIM1)	$s\eta_G$ (SIM2)	$s\eta_G$ (SIM3)
100%	12%	12%	9.5%	9.3%

5.11 FIGURES

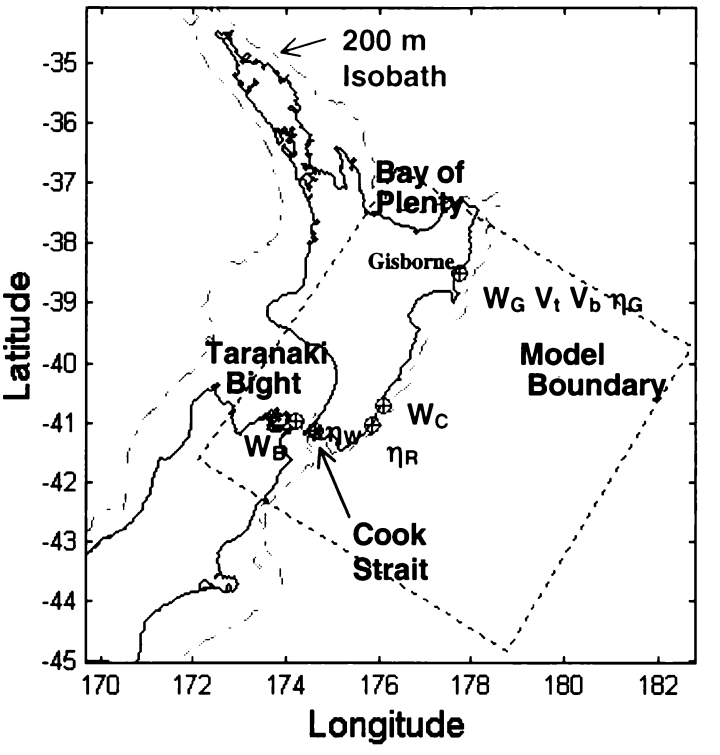

Figure 5-1. Map of New Zealand, the model grid boundary (orientated 35°T), and the 200 m isobath representing the continental shelf. An ⊕ marks data collection station sites, refer to Table 5-1 for full meaning of abbreviations.

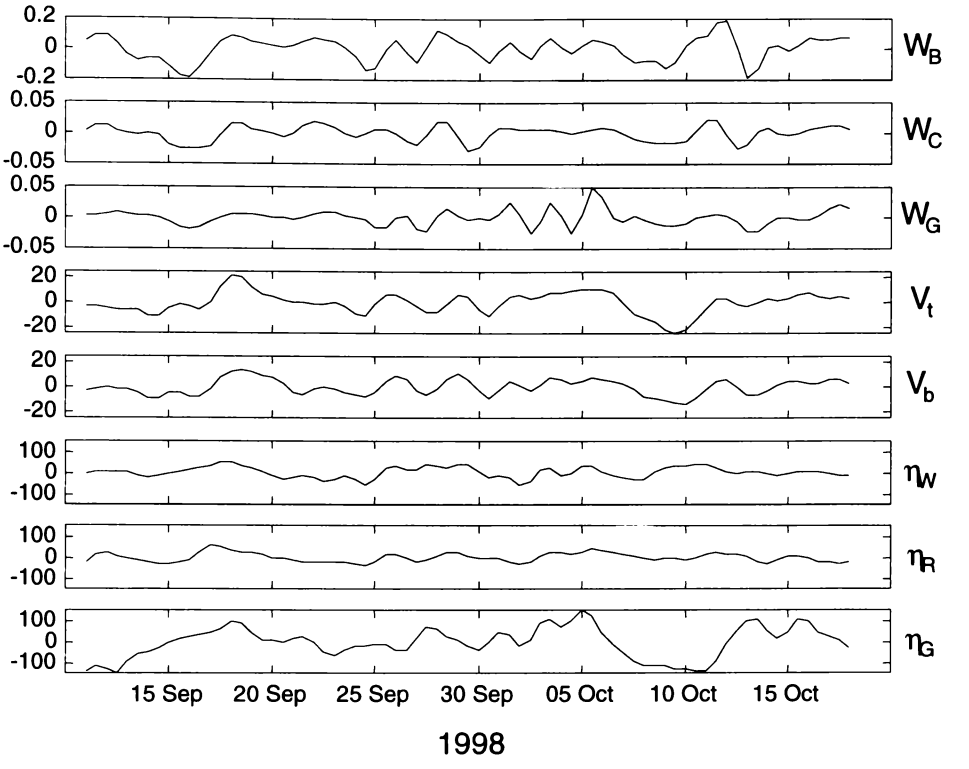

Figure 5-2. Band filtered (0.033 – 0.6 cpd) data. The vertical direction corresponds to the up-coast (north) direction for directional (wind and current) data, and to positive sea-level. Units for wind stress (W_B, W_C and W_G) are N m^{-2}, units for current (V_t and V_b) are cm s^{-1}, and units for sea-level (η_W, η_R and η_G) are mm. Refer to Table 5-1 for explanation of abbreviations.

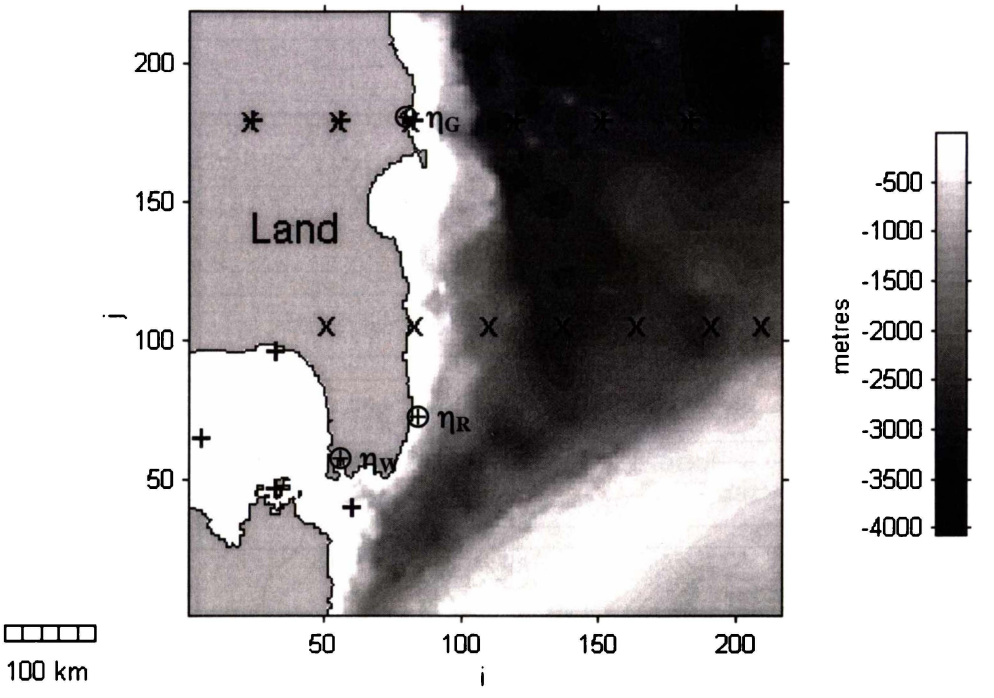

Figure 5-3. Model grid used for simulation of wind generated CTWs (simulations SIM1, SIM2 and SIM3). Input sites for winds measured at W_B, W_C and W_G are marked by +, × and * respectively. Colour shading indicates bathymetry depth.

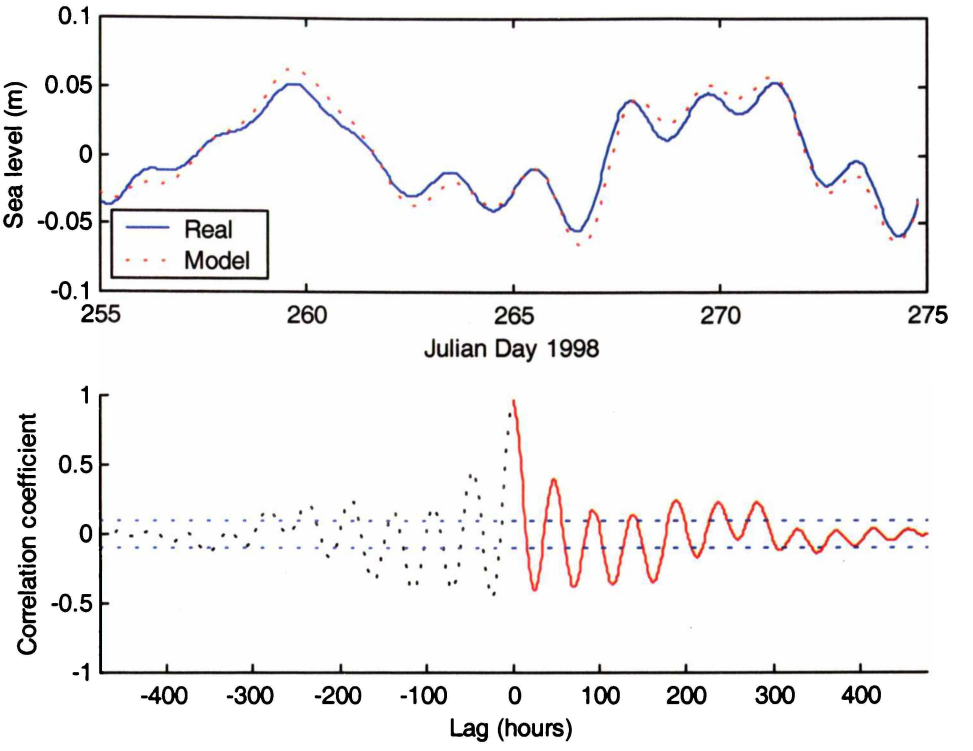

Figure 5-4. Raw time-series and cross-correlogram between low-pass-filtered real and simulated (SIM1) sea-level at Wellington Harbour (η_W). The correlation coefficient is 0.97 at lag 0, well above significance levels indicated by the horizontal dashed line.

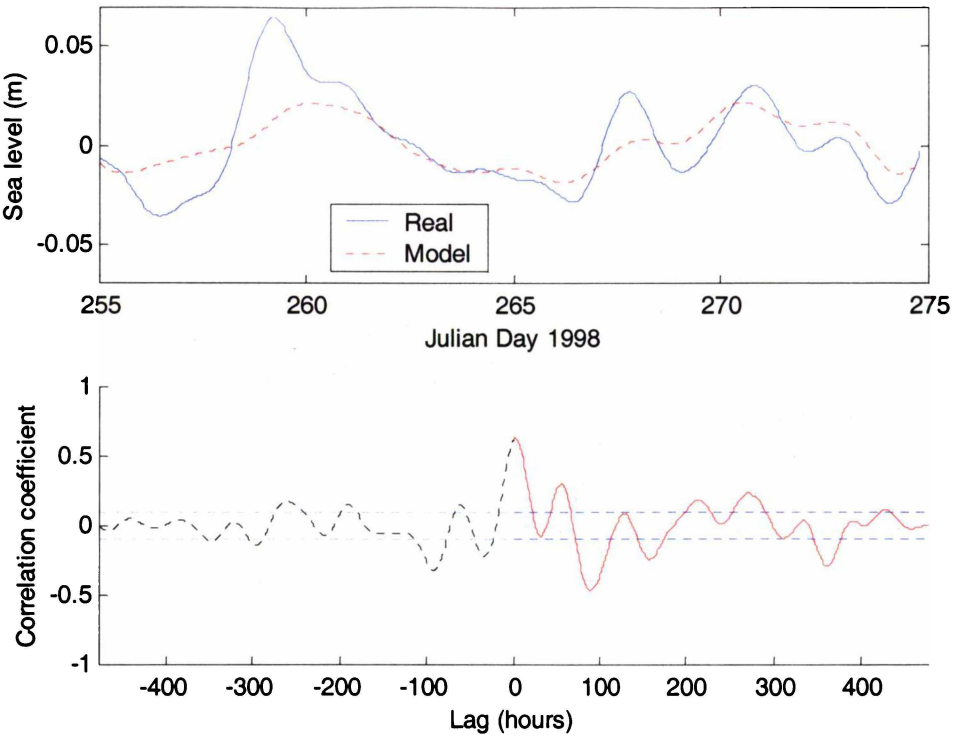

Figure 5-5. Raw time-series and cross-correlogram between low-pass-filtered real and simulated (SIM1) sea-level at Riversdale (η_R). The correlation coefficient is 0.63 at lag 2, well above significance levels indicated by the horizontal dashed line.

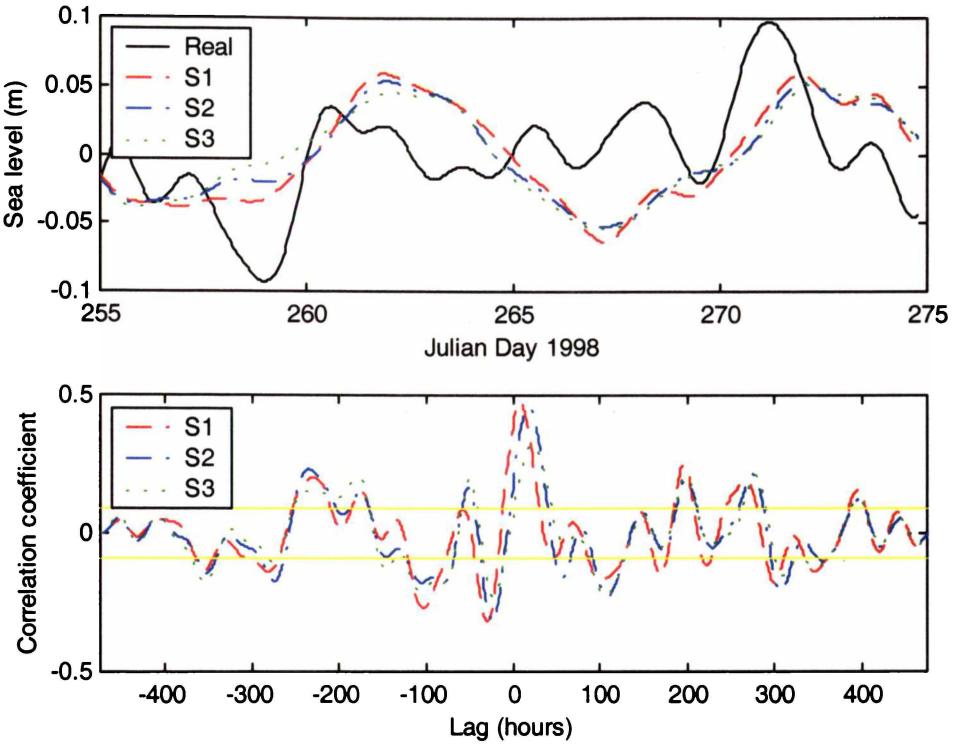

Figure 5-6. a) Gisborne real and simulated (SIM1, SIM2 and SIM3) low-pass-filtered sea-level (simulated data are multiplied by 3 for clarity) and b) cross-correlogram between real and simulated data. The correlation coefficient and lags for simulations SIM1, SIM2 and SIM3 are 0.48, 0.46, 0.33 and 9-, 18-, 23-hour lags respectively.

6 - Wavelet analysis of the wind-current relationship

6.1 INTRODUCTION

Near-surface current flow results from the transfer of energy from wind to water through frictional stress at their interface, and surface currents transfer momentum downward through turbulent diffusion, driving currents lower in the water column (Gill, 1982). Furthermore, the movement of surface water near a coastline can initiate bottom-return-flow known as upwelling or downwelling (The Open University, 1989). In Chapter 4 it was shown that the non-tidal component of the mid-water shelf-current record contained 81% of total current variance (energy). A logical mechanism for forcing non-tidal currents on the continental-shelf near Poverty Bay is through wind stress and in Chapter 4, cross-spectral analysis was used to investigate this relationship. While some correlation was identified, cross-spectral analysis had limited success in explaining the energetic non-tidal component through local wind forcing. Cross-spectral analysis is a traditional tool for time-series analysis and works by resolving a signal into its constituent frequencies. In doing so, spectral analysis assumes that the signal is stationary, i.e. no systematic change in mean or variance (no trend) such that the probability distribution tends towards a constant with time (Chatfield, 1980). This poses problems when dealing with signals that are seasonal, or whose relationship with another signal changes with time. The interaction between wind and current is certainly non-stationary (over the 43-day interval considered here), as wind speed and directions vary, and water conditions such as stratification alter with time. A comparatively new technique is wavelet analysis, designed specifically to deal with non-stationary signals and able to resolve the dominant modes of variability and how those modes vary with time (Goring and Bell, 1999). Since wind stress is a logical contributor to non-tidal motion on the Poverty Bay continental-shelf and as coastal-trapped-waves were found to contribute only a portion of non-tidal energy (Chapter 5), wavelet analysis is applied to further investigate the wind/current interaction.

6.2 METHODS

The continuous wavelet transform was used to analyse the wind and current signals. Torrence and Compo (1998) provide a comprehensive description of the method and discuss how to output the analysis in terms of statistical analysis. The method of Torrence and Compo (1998) has been adapted and used here, and the reader is referred to their paper for a comprehensive description.

The continuous wavelet transform provides a means of transforming a signal into frequency-time space, and therefore extracting information about how the magnitudes of the various scales in a signal change with time (Goring and Bell, 1999). An example is provided in Figure 6-1, where two digital signals have been wavelet-transformed using the method of Torrence and Compo (1998), with the wavelet function known as DOG 6 (6^{th} derivative of a Gaussian). The DOG is a real valued wavelet (compared with complex), so it gives no information on the phase of the signal, but captures both the positive and negative oscillations of the time-series (Torrence and Compo, 1998). The real valued DOG wavelet function was chosen to investigate the wind-current relationship because it gives detail at the finest scale. The colour contour maps are plots of the square of the wavelet coefficients $|W(a,t)|^2$, where a is the dilation scale, analogous to period in a Fourier transform (Goring and Bell, 1999). The bright patches represent high power (greater than the 95% significance level) and the dark patches represent low (insignificant) power. In Figure 6-1, peaks in the signal amplitude show up as bright patches, at scales (also termed frequencies or equivalent-Fourier periods T_F and located on the y-axis) matching the signal period, eg. T_F = 64 hours for Signal 1, which matches the input signal period (Signal 1 = 0.1 $\sin(2\pi/64\times t)$). The cross-power contour plot (A) shows covariance between the two signals at equivalent-Fourier periods of 64 hours, as expected since both signals contain a T = 64 hour component. The cross-power plot is damped where the T = 128 hour component of Signal 2 is out of phase with the T = 64 hour component, reducing its energy. Note there is a zone of influence (seen by blurring of the signal) near the ends of the contour plots where edge effects become important, due to the finite record length (Torrence and Compo, 1998).

Prior to wavelet analysis wind data was converted to true vectors convention and both wind and current data were rotated 36° clockwise to align them with the coast. The cross-wavelet transform was then computed and plotted between each (alongshore/cross-shore) component of the wind data and the two current-meter datasets (Figure 6-4 - Figure 6-19).

Wavelet analysis is usually performed on data series having length equal to some power of 2 (Torrence and Compo, 1998). Since the GT record consisted of 1025 hourly values and the GB record consisted of 900 hourly values, the GB record was padded with zeros and GT truncated by 1, so that both time-series consisted of 1024 data points (2^{10}). This gave a maximum resolvable period of 512 hours and a minimum of 2 hours.

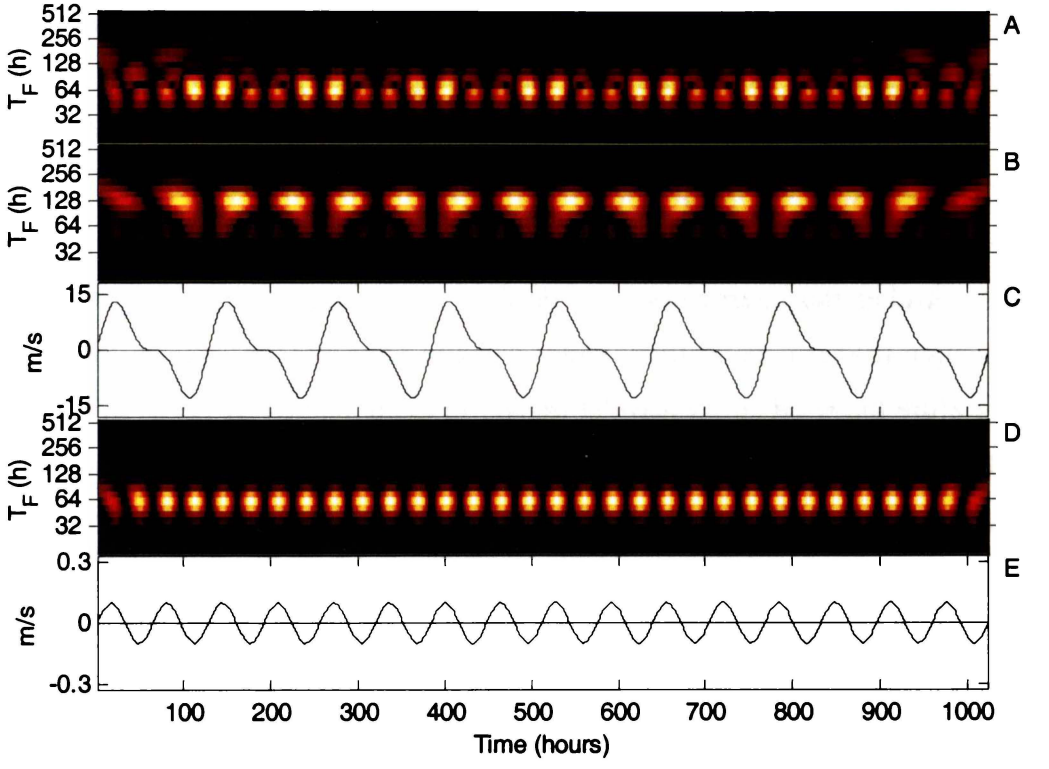

Figure 6-1. A wavelet analysis example: A) cross-power contour map, B) power contour map of Signal 2, C) Signal 2 time-series, D) power contour map of Signal 1, E) Signal 1 time-series. Signal 1 = 0.1 $\sin(2\pi/64 \times t)$ and Signal 2 = (5 × Signal 1 + 10 $\sin(2\pi/128 \times t)$).

6.3 RESULTS AND DISCUSSION

Plots of the wind and current time-series and wavelet power contour maps are shown in Figure 6-4-Figure 6-19. In each Figure, plots E and D contain the *current* time-series and wavelet power contour map respectively, plots C and B contain the *wind* time-series and wavelet power contour map respectively, and plot A contains the wind-current cross-power contour map, which is a plot of the covariance between wind and current.

Wind stress is a function of velocity squared $\tau = C_D \rho_a u^2$ (Gill, 1982), and so has a non-linear relationship to the wind speed. Wind stress forces circulation and not wind velocity, therefore wavelet transforms should be calculated with wind stress if a cause-effect relationship is to be established between wind and current. It was found that despite this non-linear relationship, cross-power wavelet transforms were similar when calculated using either wind velocity or wind stress, as demonstrated by the comparison made in Figure 6-2, plots 1-A and 2-A. For all the calculated wavelet transforms that follow, using either wind velocity or stress did not alter the interpretation of results. Wind stress has a greater standard-deviation-to-mean ratio than wind velocity, because of its u^2 relationship. Therefore the wind stress wavelet transform is dominated by peaks in the record (plots B and C), and less detail is shown of the weaker frequency-time signals. To show detail in the wind record, the plots shown are those calculated using wind velocities, but this hasn't altered the interpretation.

From examination of the cross-power wavelet plots (Figure 6-4 - Figure 6-19, plots A), an abundance of significantly correlated data is obvious, contrasting to the sparsely correlated data identified by spectral analysis (Chapter 4, Table 4-3). The wavelet analyses show that residual continental-shelf-current is largely a function of wind stress, with peaks in wind strength generally being accompanied by a reactive peak in the currents. Wind-forcing of continental-shelf-currents occurred throughout the field study period at the majority of resolvable periods between 8 – 512 hours. This helps to explain the large proportion of energy contained in the non-tidal (residual) shelf-current component (Chapter 4), suggesting that it is largely wind-forced.

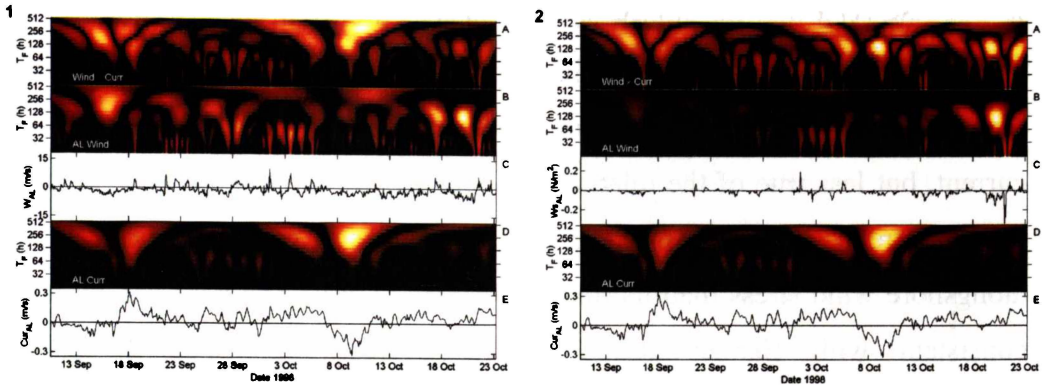

Figure 6-2. Wavelet analysis of the alongshore mid-water (GT) current component (time-series in plots E) and the alongshore wind component (time-series in plots C), for equivalent Fourier periods 2-512 hours, showing the cross-power in plots A. Plot 1 uses raw wind speed to compute the wavelet transform, while plot 2 uses wind stress calculated by the method of Wu (1982).

The power contour maps of wind (plots B) show how the energy contained in the wind signal at different scales varies with time. It can be seen that the wind exhibits non-stationary behaviour. For example in Figure 6-4 plot B, there is an episode between 25 September and 6 October where the alongshore wind contains significant energy at periods of approximately 2 days, but this does not persist throughout the record. Conversely, there is a semi-regular energy peak between 5-11 days (128-256 hours) that occurs throughout the time-series, but shifts in a subtle manner between periods of 128 to 256 hours, and therefore is not picked up by spectral analysis. Like the wind, the wavelet cross-power plots (A) illustrate the time-varying relationship between wind and current, showing that it is certainly non-stationary and therefore not well suited to spectral analysis.

In the 5-20 day weather-band (see Cahill et al., 1991), wind and mid-water current show the strongest relationship in the alongshore direction (Figure 6-4) and this is suggestive of coastal-trapped-wave (CTW) forcing, long-period waves being actively generated by alongshore wind stress (Buchwald and Adams, 1968). Wavelet analyses suggest that local forcing of CTWs is certainly occurring in the weather-band.

It was observed that the mid-water and near-bed current-meters showed similar correlation patterns with the wind. This is true of the alongshore wind with alongshore current, the cross-shore wind with both alongshore and cross-shore current, but less true of the relationship between the alongshore wind and cross-shore current. The near-bed cross-shore current responds more often to alongshore wind stress than its mid-water counterpart. The near-bed response is consistent with Ekman-induced upwelling/downwelling under geostrophic adjustment of a wind-generated alongshore current (Pond and Pickard, 1983) and is typical along straight sections of the coast. The mean of the alongshore wind component was near zero for the field period suggesting that neither Ekman upwelling nor downwelling prevails.

Generally the wind-driven current response is similar between current-meters and this is true for lower frequency signals in particular. Low-frequency wind events therefore affect the entire water column, driving three-dimensional circulation near the coast. Since the wind commonly drives circulation on the continental-shelf in 35 m water depth it is likely to be dominant in adjacent Poverty Bay, which is shallow and confined. This concurs with the findings of Chapter 4 that showed wind and river induced circulation to dominate in the bay. The DOG wavelet function chosen for the wavelet analysis does not provide details on the phase relationship so it is unclear if near-bed flows have an inverse phase relationship with wind. However, spectral analysis often showed ~180° phase differences between the mid-water and near-bed currents (Chapter 4, Table 4-4), suggesting that this may commonly be the case.

At shorter periods (2-32 hours) mid-water currents generally showed more correlation with wind than near-bed currents (Figure 6-12 - Figure 6-19). The mid-water column is expected to show more high frequency wind response due to its proximity to the water surface. Very little near-bed wind-current response is seen at periods less than 8 hours, indicating that longer time scales are required to initiate near-bed motion on the continental-shelf. Spectral analysis showed a diurnal wind signal (Figure 6-3), likely to be associated with the pronounced Gisborne land-sea breeze cycle that results from the katabatic effect of the nearby Raukumara ranges (Hessell, 1980). The high-frequency wavelet plots show a

diurnal shelf-current response to the wind sea-breeze cycle (Figure 6-12 - Figure 6-19), that should be even greater in Poverty Bay due to stratification, which increases vertical current shear.

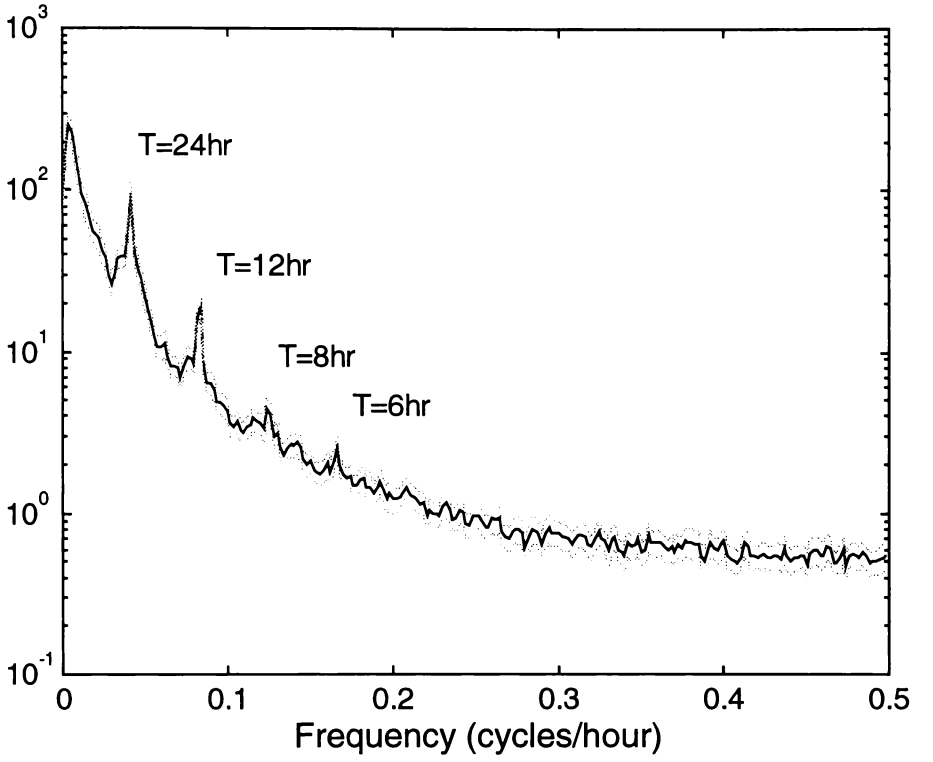

Figure 6-3. Auto-spectrum of Gisborne Airport wind along its principle axis 334/154°T. The spectrum contains 102036 hourly records from 1/1/88 – 22/8/99. Dashed lines show 95% confidence intervals.

6.4 CONCLUSIONS

Wind stress is a non-stationary time-series, therefore wavelets are a more suitable tool to analyse the wind-forced current response than spectral analysis. Wavelet analysis outperformed spectral analysis in illustrating the wind-driven influence on shelf-currents adjacent to Poverty Bay. Wavelet analyses showed that wind-forcing of continental-shelf-currents occurred throughout the field study period, at the majority of resolvable frequencies. This explains the large proportion of energy contained in the non-tidal (residual) shelf-current component (Chapter 4).

A strong alongshore relationship between wind and current in the 5-20 day band was suggestive of local CTW forcing and explains some of the low-frequency energy in the shelf sea-level unaccounted for in Chapter 5.

The response to wind-forcing was similar throughout the water column for motion with periods greater than ~32 hours, showing that the wind is affecting the entire water column on the shallow continental-shelf and will therefore be dominant in shallow and confined Poverty Bay. Ekman-induced upwelling/downwelling appears to be a common occurrence on the shelf.

At shorter periods (<32 hours), the wind has less influence at depth, and very little wind-forced near-bed shelf-current response is seen at periods less than 8 hours. Mid-water column currents respond to the wind at short periods and the strong diurnal wind signal is transferred to the upper water column. In Poverty Bay this is likely to be an important forcing mechanism.

6.5 ACKNOWLEDGEMENTS

Wavelet software was provided by C. Torrence and G. Compo, and is available at URL: http://paos.colorado.edu/research/wavelets/. Thanks to Dr. Rob Bell for supplying his wavelet routines, appropriate literature and his demonstration of the technique.

6.6 FIGURES

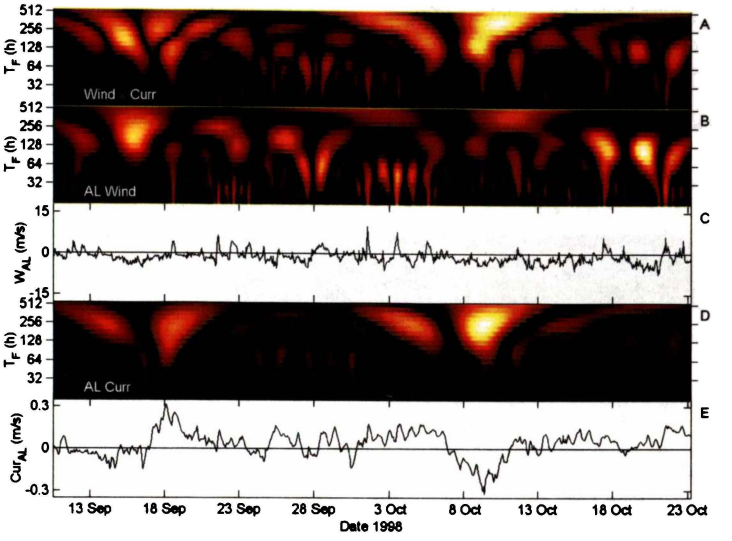

Figure 6-4. Wavelet analysis of the alongshore mid-water (GT) current component (time-series in plot E) and the alongshore wind component (time-series in plot C), for equivalent Fourier periods 2-512 hours, showing the cross-power in plot A.

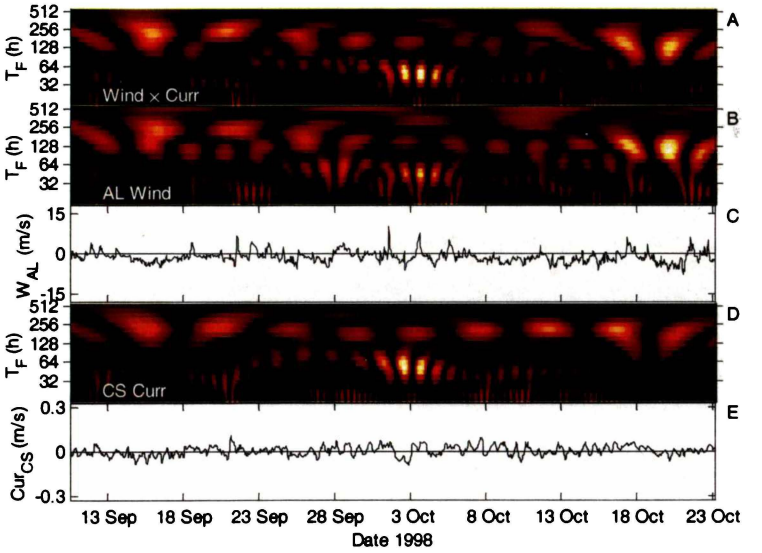

Figure 6-5. Wavelet analysis of the cross-shore mid-water (GT) current component (time-series in plot E) and the alongshore wind component (time-series in plot C), for equivalent Fourier periods 2-512 hours, showing the cross-power in plot A.

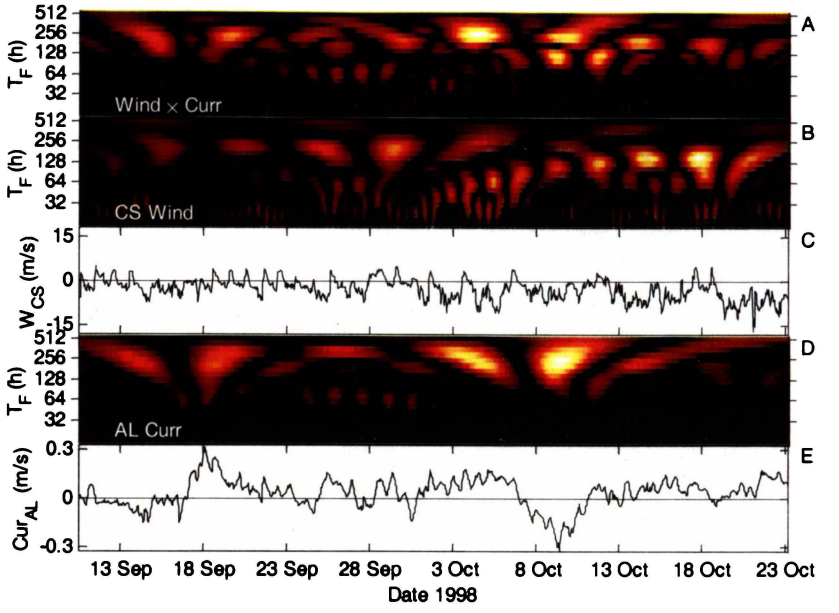

Figure 6-6. Wavelet analysis of the alongshore mid-water (GT) current component (time-series in plot E) and the cross-shore wind component (time-series in plot C), for equivalent Fourier periods 2-512 hours, showing the cross-power in plot A.

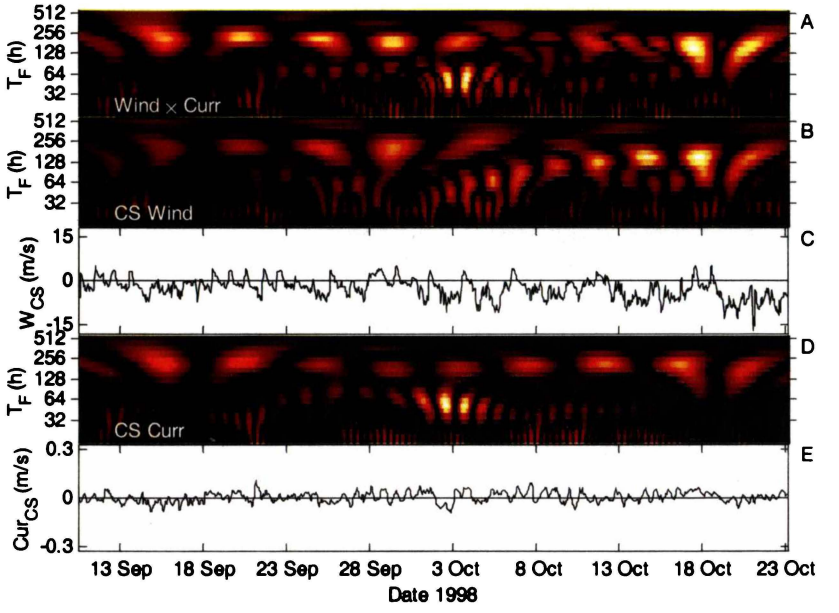

Figure 6-7. Wavelet analysis of the cross-shore mid-water (GT) current component (time-series in plot E) and the cross-shore wind component (time-series in plot C), for equivalent Fourier periods 2-512 hours, showing the cross-power in plot A.

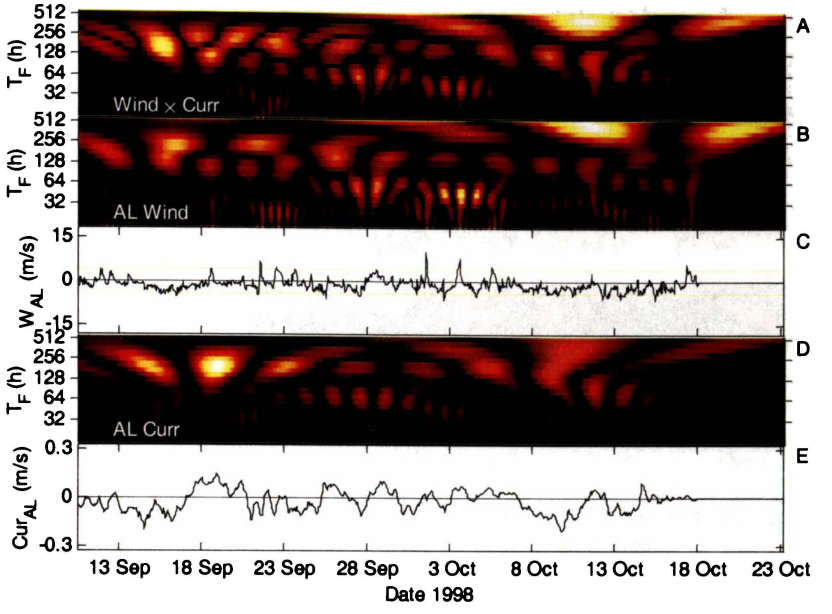

Figure 6-8. Wavelet analysis of the alongshore near-bed (GB) current component (time-series in plot E) and the alongshore wind component (time-series in plot C), for equivalent Fourier periods 2-512 hours, showing the cross-power in plot A.

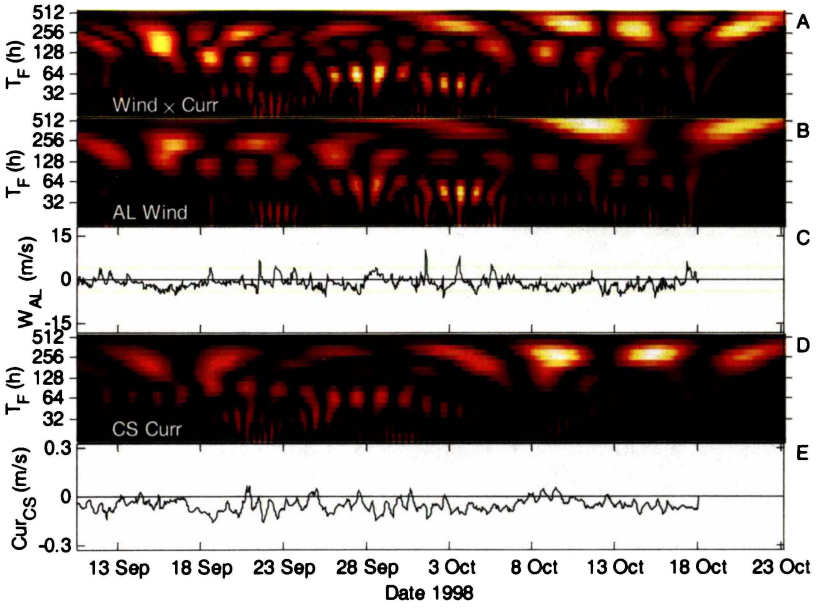

Figure 6-9. Wavelet analysis of the cross-shore near-bed (GB) current component (time-series in plot E) and the alongshore wind component (time-series in plot C), for equivalent Fourier periods 2-512 hours, showing the cross-power in plot A.

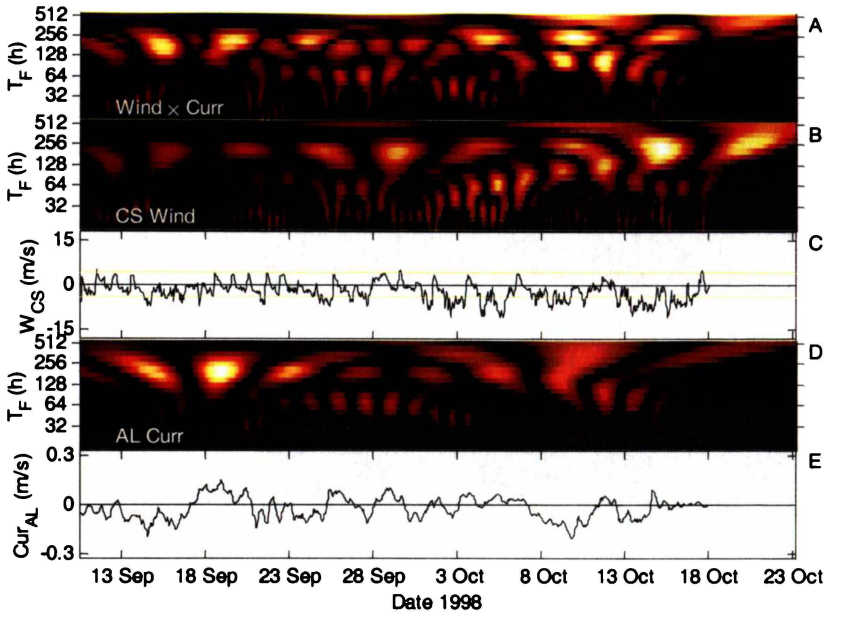

Figure 6-10. Wavelet analysis of the alongshore near-bed (GB) current component (time-series in plot E) and the cross-shore wind component (time-series in plot C), for equivalent Fourier periods 2-512 hours, showing the cross-power in plot A.

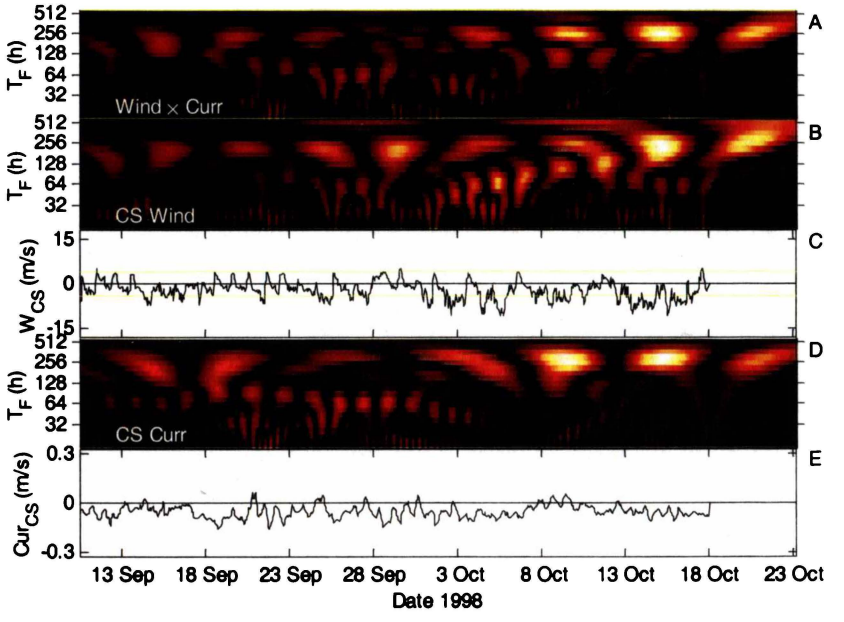

Figure 6-11. Wavelet analysis of the cross-shore near-bed (GB) current component (time-series in plot E) and the cross-shore wind component (time-series in plot C), for equivalent Fourier periods 2-512 hours, showing the cross-power in plot A.

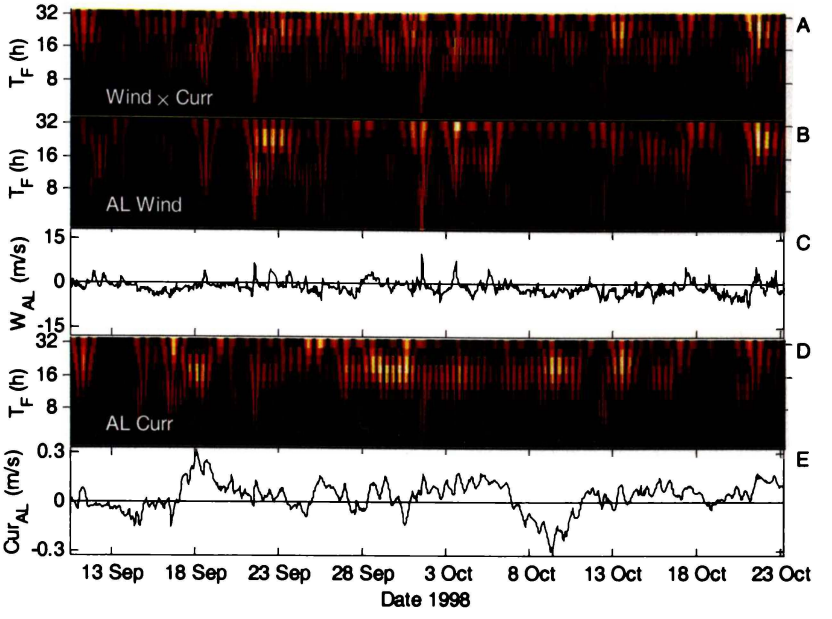

Figure 6-12. Wavelet analysis of the alongshore mid-water (GT) current component (time-series in plot E) and the alongshore wind component (time-series in plot C), for equivalent Fourier periods 2-32 hours, showing the cross-power in plot A.

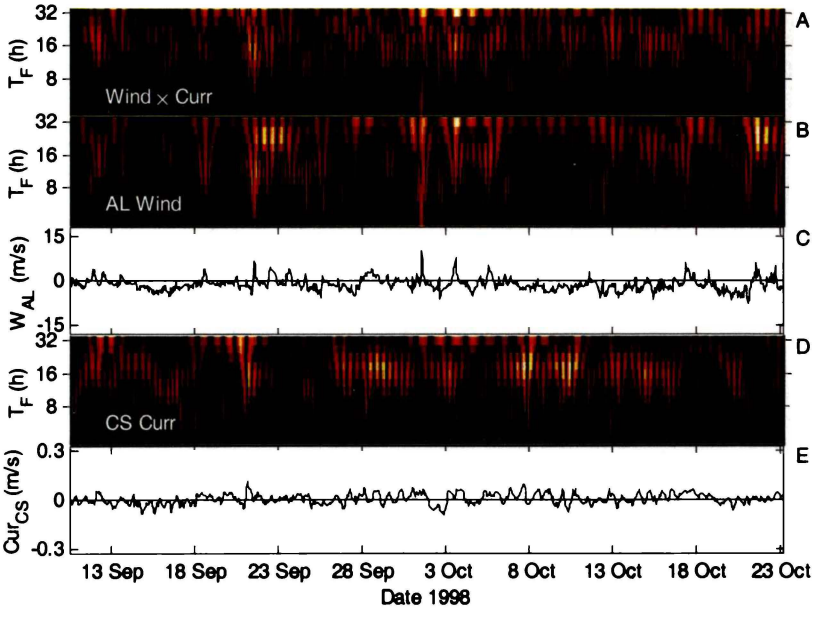

Figure 6-13. Wavelet analysis of the cross-shore mid-water (GT) current component (time-series in plot E) and the alongshore wind component (time-series in plot C), for equivalent Fourier periods 2-32 hours, showing the cross-power in plot A.

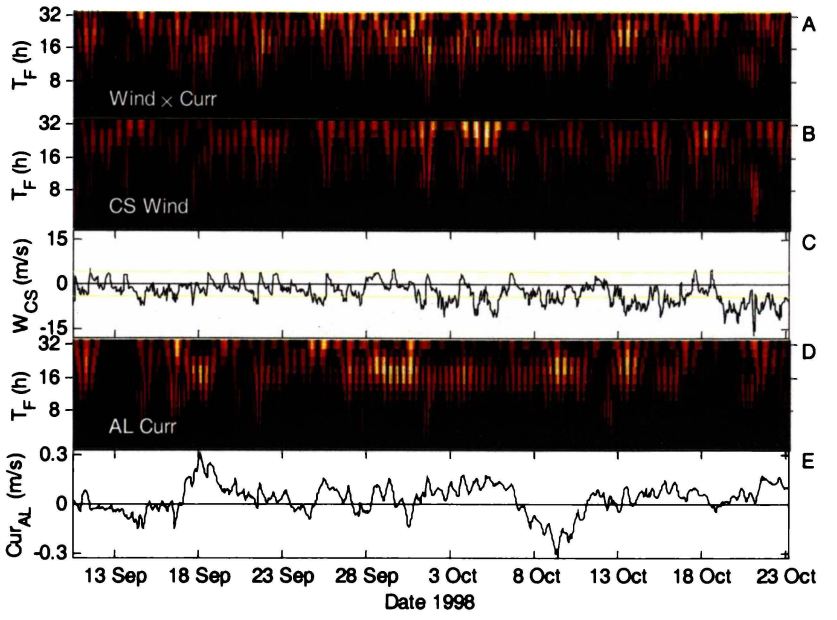

Figure 6-14. Wavelet analysis of the alongshore mid-water (GT) current component (time-series in plot E) and the cross-shore wind component (time-series in plot C), for equivalent Fourier periods 2-32 hours, showing the cross-power in plot A.

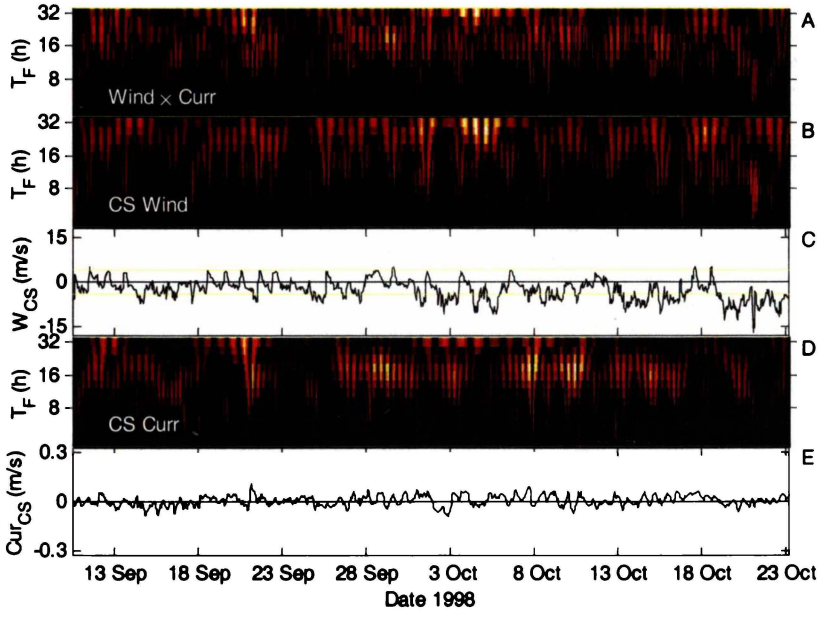

Figure 6-15. Wavelet analysis of the cross-shore mid-water (GT) current component (time-series in plot E) and the cross-shore wind component (time-series in plot C), for equivalent Fourier periods 2-32 hours, showing the cross-power in plot A.

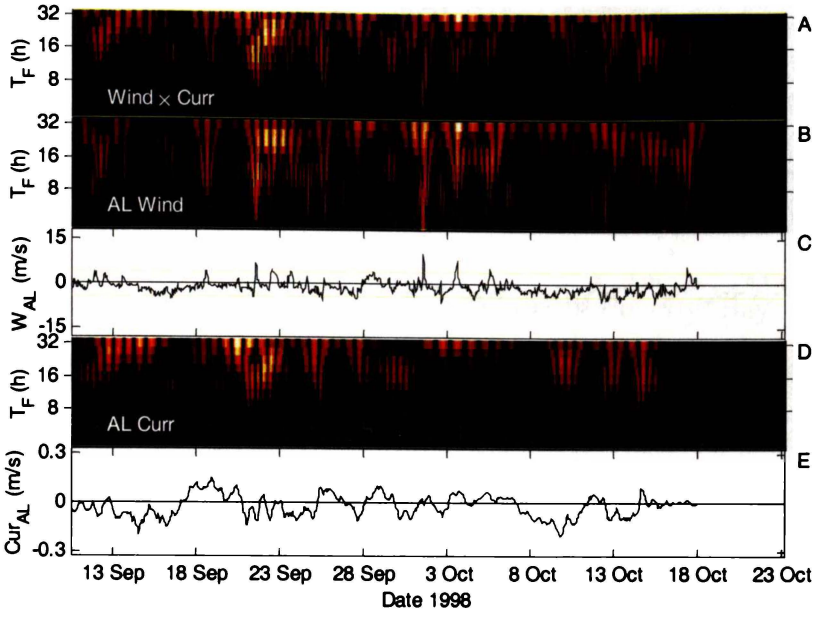

Figure 6-16. Wavelet analysis of the alongshore near-bed (GB) current component (time-series in plot E) and the alongshore wind component (time-series in plot C), for equivalent Fourier periods 2-32 hours, showing the cross-power in plot A.

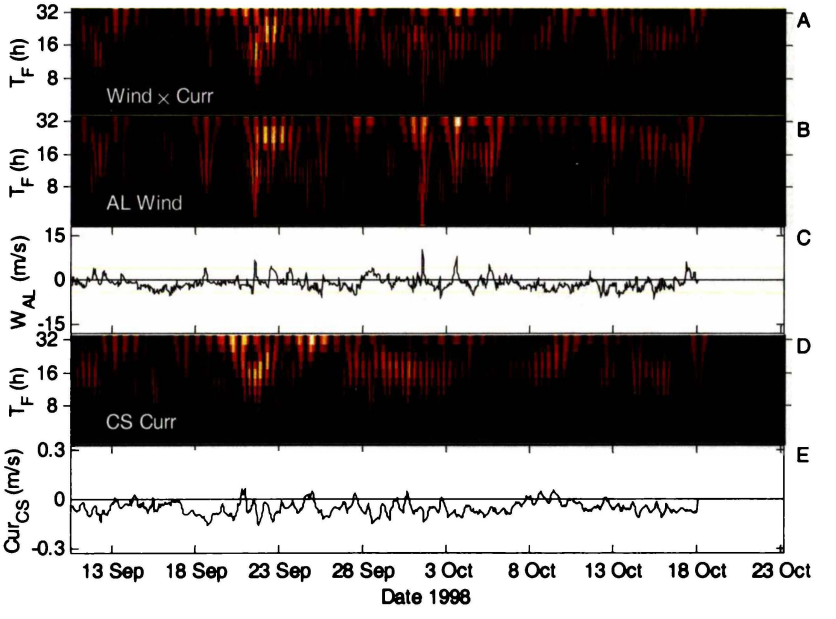

Figure 6-17. Wavelet analysis of the cross-shore near-bed (GB) current component (time-series in plot E) and the alongshore wind component (time-series in plot C), for equivalent Fourier periods 2-32 hours, showing the cross-power in plot A.

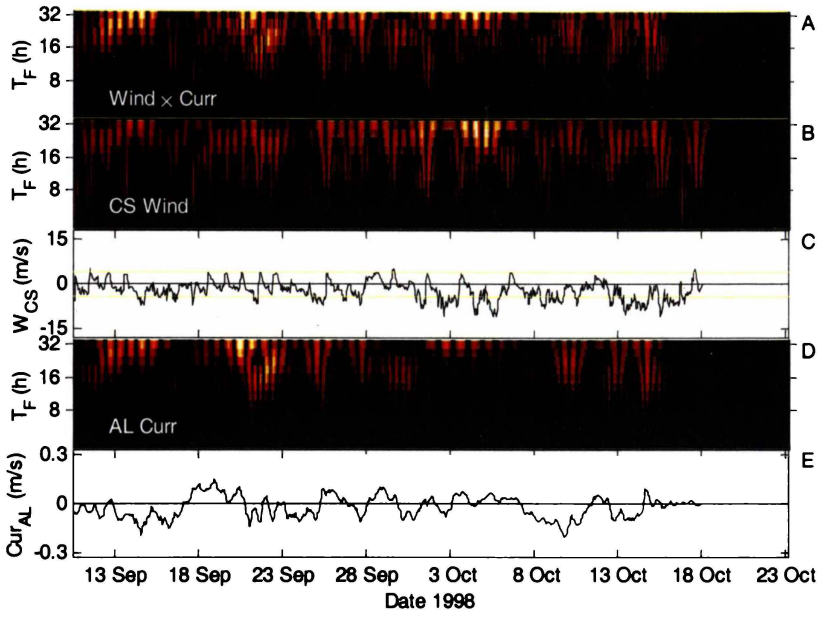

Figure 6-18. Wavelet analysis of the alongshore near-bed (GB) current component (time-series in plot E) and the cross-shore wind component (time-series in plot C), for equivalent Fourier periods 2-32 hours, showing the cross-power in plot A.

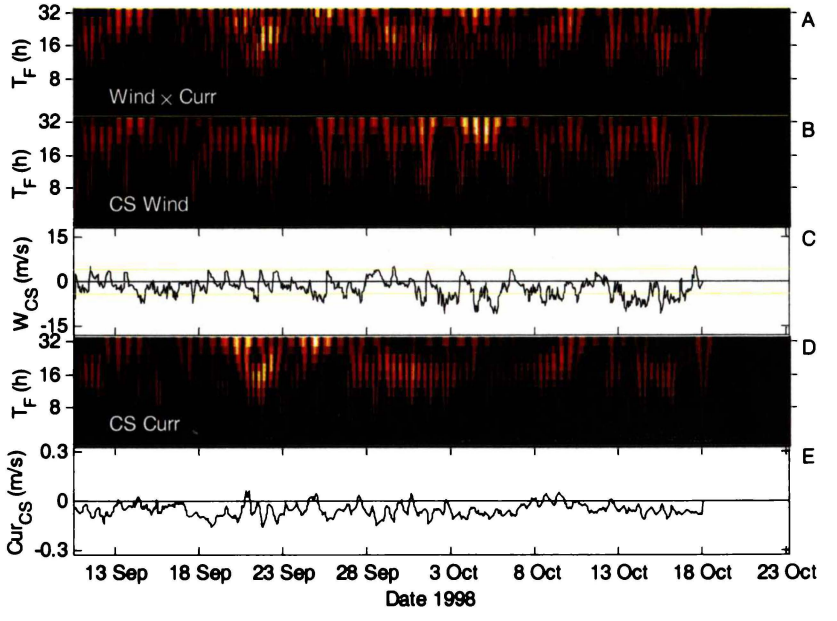

Figure 6-19. Wavelet analysis of the cross-shore near-bed (GB) current component (time-series in plot E) and the cross-shore wind component (time-series in plot C), for equivalent Fourier periods 2-32 hours, showing the cross-power in plot A.

7 - Three-dimensional simulation of Poverty Bay

7.1 INTRODUCTION

Field surveys highlighted the variability of Poverty Bay hydrodynamics and showed that the forcing in the bay was dominated by the interaction of fluvial discharge and surface wind stress (Chapter 4). The shelf-current was demonstrated to have little effect on Poverty Bay circulation, contrary to previous simulations (Black et al., 1997). In light of this knowledge, it was decided to re-run three-dimensional simulations of Poverty Bay, to calibrate the model using real shelf-currents. Furthermore, the ADP measurements provided a better spatial resolution for model calibration than moored current-meters used in the 1997 AEE investigation. The calibration of a Poverty Bay numerical model allows circulation to be broken down into its shelf-current, river discharge and wind stress driven constituents, providing insights that the field study could not. The model accounts for the relative magnitude of wind-stress- and river-discharge-forced circulation, the effect of floods, and the most prominent bathymetric controls on circulation. Thus the modelling chapter addresses specific thesis aims 1, 2, 4 and 5 in detail. Model 3DD (Black, 1995) was used for the simulations and is described in Appendix 2. The model bathymetry, boundary files and other inputs used for both two and three-dimensional simulations are described in the methods section.

7.2 METHODS

Model simulations covered the period 10-30 September 1998, coinciding with calibration data provided by ADP and CTD surveys on 15, 17, 19, 26 and 28 September. This period included variable winds (Figure 7-6), a quickflow discharge event from the Waipaoa River (Figure 7-5), and shelf-currents exhibited considerable variability (Figure 7-10). The simulation period therefore comprised an adequate test of the model over a range of typical Poverty Bay hydrodynamic conditions. Water temperature was essentially constant during the simulation

period (Figure 7-7), simplifying the modelling, but solar inputs may need to be accounted for in future if summer periods are simulated.

7.2.1 Model Bathymetry

The hydrodynamics of a coastal embayment arise from a balance of the accelerative forces acting to drive the water body and its interaction with the underlying bathymetry. In coastal environments where the water is shallow, deceleration due to bed-friction is high and with respect to model 3DD Black (1995) observes that the quality of the bathymetry representation in the model is more important than everything else.

A version of the 200 × 200 m Poverty Bay grid used by Black et al. (1997) was modified for this study. The original grid was constructed from digitised Navy Chart NZ5613 (Kohl, 1989) using both the published charts and the original fair sheets (from sounding data used with permission of the Hydrographer RNZN). These data were supplemented by data recorded in hydrographic surveys during 1996. The process then involved:

- inspection of the data in Matlab™ to identify mismatches between data sets
- interpolation with the Kriging method onto an evenly-spaced grid using Surfer™
- output from Surfer of an ASCII file in X (Easting),Y (Northing) and Z (depth) format
- hand editing to resolve remaining anomalies
- output using a Fortran™ code to files in "Bath" format, which is accepted by model 3DD.

The model provides the option to define an average depth at the cell mid-point only, or on all of the cell walls. The latter was chosen as it doubles the resolution.

The original grid used by Black et al. (1997) contained 75 × 64 (I, J), 200 m square cells, incorporated a flat continental-shelf of 25 m depth, and did not

extend to the S4 deployment location. Therefore modification was required for this study and the model grid was extended to 75 × 69 (*I*, *J*), 200 m square cells (Figure 7-1). Body-force simulations (discussed below) gave better results when the flat continental-shelf was replaced with real depths digitised from Navy Chart NZ55 (Gerrard, 1989).

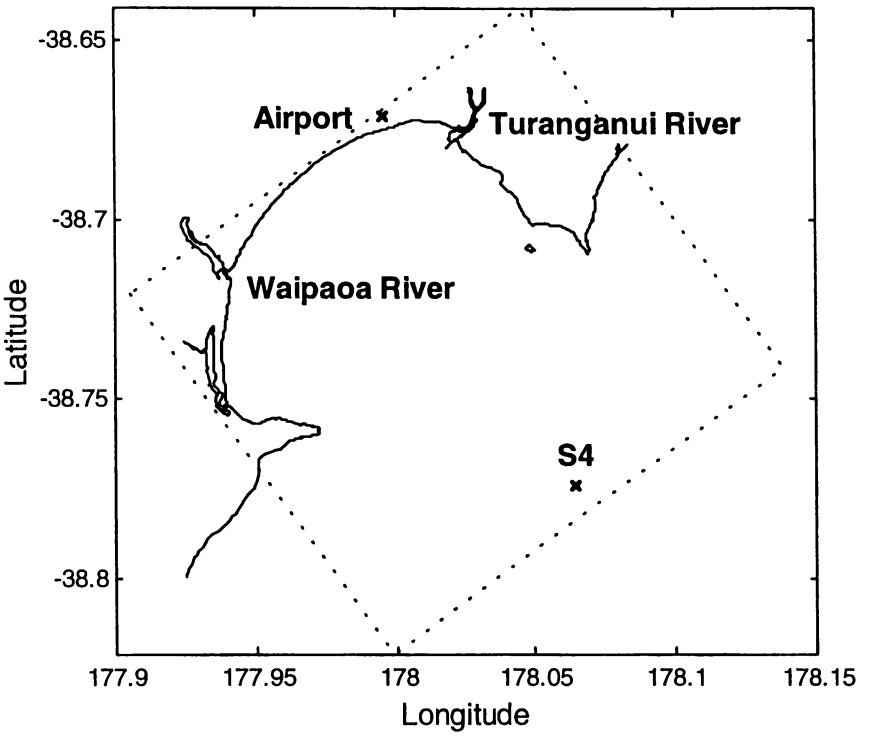

Figure 7-1. Extent of the Poverty Bay hydrodynamic model grid, including the location of boundary data sources: the S4 current-meters, Gisborne Airport and rivers.

Initial model runs using the 200 m horizontal grid spacing took about 32 hours real-time to complete a 468-hour simulation. Since 54 simulations were eventually required to achieve satisfactory calibration, the bathymetry horizontal grid spacing was increased from 200 to 400 m to reduce simulation times. Initial trials showed close results using the two grids, and the model was found to be more sensitive to vertical structure than to the horizontal spacing. Simulations were thereafter undertaken using the 400 m grid, reducing simulation times by one eighth.

The 400 m grid (Figure 7-2) contained 38 × 36 (*I*, *J*), cells and was rotated 36° clockwise relative to the land, about grid origin *I* = -4.25, *J* = 10.5 (corresponding to Easting/Northing 306000/680600 and latitude/longitude –38.7994/177.9547). This was done so that the *I* and *J* directions corresponded to the alongshore and cross-shore directions respectively.

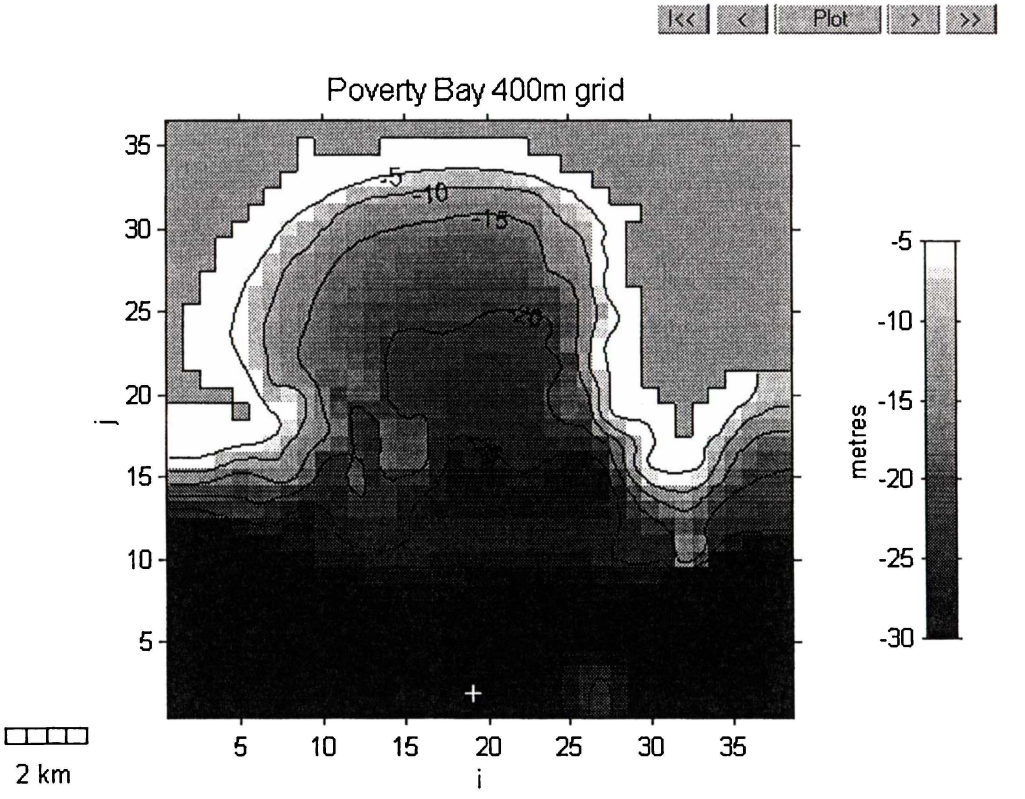

Figure 7-2. Poverty Bay 400 m bathymetry grid, used for hydrodynamic simulations, showing S4 deployment site (+).

7.2.2 Body-force

Accurate simulations require adequate representation of open boundary conditions (Black, 1995) and the Poverty Bay model has three open sea boundaries (Figure 7-2). Since current-meters were deployed in just one site, an obvious problem is a lack of data to represent these boundaries. On open coastlines, geostrophic currents are associated with sea-level gradients, and water level boundaries therefore provide an effective means of driving a numerical model.

When planning the field study, it was recognised that bottom pressure gauges could be used to provide open boundary conditions for the numerical model, if placed on the continental-shelf to the north and south of the bay. This was prevented by a lack of resources; accurate tide gauges were not available during the field study window. Ideally, pressure gauges would be deployed many kilometres apart, to minimise sea-level-gradient measurements errors, and the gauges would be levelled in to a known datum. Black et al. (1997) used pressure gauges placed approximately 1 km either side of the bay to close the sea-level boundary condition, but the instruments were not levelled in to a datum, and sank into the soft bottom at varying rates, creating errors in the sea-level gradient measurement that resulted in over-prediction of shelf-current velocities. To accurately level pressure gauges many kilometres apart on the remote Poverty Bay coast would have created a large resourcing problem by itself. Instead the model relied upon the current measurements made at a single location for calculating the open boundary conditions.

Where existing current data exists, a body-force acceleration can be calculated to provide a surrogate for sea-level gradients and therefore force the model. The body-force is obtained by inverting the vertically-averaged momentum equation and solving using measurements of currents and winds. The body-force F is:

$$F_x = \frac{g\partial\varsigma}{\partial x} = [-\frac{\partial u}{\partial t} + \frac{\rho a \gamma W_x |W|}{\rho(d+\varsigma)} - \frac{gu(u^2+v^2)^{1/2}}{C^2(d+\varsigma)} + fv]$$

$$F_y = \frac{g\partial\varsigma}{\partial y} = [-\frac{\partial v}{\partial t} + \frac{\rho a \gamma W_y |W|}{\rho(d+\varsigma)} - \frac{gv(u^2+v^2)^{1/2}}{C^2(d+\varsigma)} - fu]$$

where g is the gravitational acceleration constant, ς is sea-level, u, v, W_x and W_y are current and wind velocities in the x, y directions, ρ_a and ρ are the densities of air and seawater respectively, γ (= *(0.8+0.065.*W)/1000*) is the wind stress coefficient, d is water depth, C is Chezy's C and f is the Coriolis parameter (Black, 1995). The body-force is recognised by 3DD but is calculated in a separate program (Appendix 3). The body-force was calculated using an average current between the mid-water and near-bed current-meters (GT and GB), since

the body-force is a vertically-averaged calculation. Directional data (current and wind) were first rotated 36° clockwise, in order that data should match the model grid orientation. A continental-shelf bed roughness length 0.002 m and depth 30 m were assumed.

Because the body-force is reproduced from a single point measurement, it inherently assumes that flow is uniform across the domain surrounding the instrument location. Therefore, the body-force acceleration is applied uniformly to the entire model grid. In the situation presented here, currents on the open shelf are well represented (Figure 7-3), but currents inside the bay that are forced as a direct result of the body-force, are expected to be erroneous. Fortunately, increased frictional effects reduce the direct impact of the body-force acceleration in the shallow bay, and the momentum and sea-level gradients created by the body-force current on the outer shelf, tend to override the direct body-force impact at the bay entrance. Furthermore, it is shown below that currents forced by wind stress and river discharge dominate inside the bay.

In an open ocean, the model will exactly reproduce the measured currents using the body-force technique. In more complex bathymetry, some deviations (at the measurement site) occur due to neglected bathymetric effects and local sea gradients within the model grid. In addition, the body-force does not account for the three-dimensional structure about the vertically-averaged condition. Thus, some errors can be expected (Black, 1995). An advantage of using the body-force is that because it is re-created from measured current time-series, it incorporates all processes contributing to its forcing. Therefore tides, coastal-trapped-waves, and inertial currents are all represented.

A disadvantage is that since the body-force is a surrogate for acceleration due to sea-level pressure gradients and replaces sea-level boundaries, water level changes (eg. tidal rise and fall) are not represented in the model. During simulations, the water level remains essentially fixed at zero, with small sea-level changes induced mainly by wind stress and locally near the rivers, small (< 0.03 m) compared to the mean tidal range in Gisborne of ~1.4 m. Since the surface area of the bay is ~62 km^2, the mean tidal water exchange volume is

~86.8×10^6 m^3. This poses the question of whether it is justified to ignore such substantial volume changes in the model? As demonstrated later, the skill of the model in predicting bay hydrodynamics suggests that it is. Due to the wide exposure of the bay to the continental-shelf, tidal waves entering and leaving the bay create only minor currents of ~0.02 m s^{-1} (Gorman et al., 1997). The greater importance of non-tidal currents suggests that the rise and fall of the tide simply acts to translate the water column up and sideways, inside which the response to non-tidal forcing continues largely unaffected. This is fortunate since a lack of sea-level boundaries compelled the use of the body-force, leaving no real choice for the modeller. The important factor is that although the volume exchange is not present, current accelerations due to tidal processes are still represented by the body-force.

Comparison of measured and simulated depth-averaged continental-shelf-currents show that the body-force is satisfactorily reproducing measured shelf-currents (Figure 7-3). Since not constrained by the nearby land boundary, alongshore flows are fastest and therefore of greatest importance to circulation in Poverty Bay. Figure 7-3 shows that although there are some large deviations of ~0.1 m s^{-1}, the body-force generally reproduces measured alongshore currents well. These deviations predominantly result from the uneven bathymetry used in the model grid that cannot be accounted for by the body-force calculation (in which it was assumed the continental-shelf was a uniform 30 m depth). Despite these errors the use of a body-force to represent shelf-currents was necessitated in the absence of accurate sea-level measurements on the open boundaries.

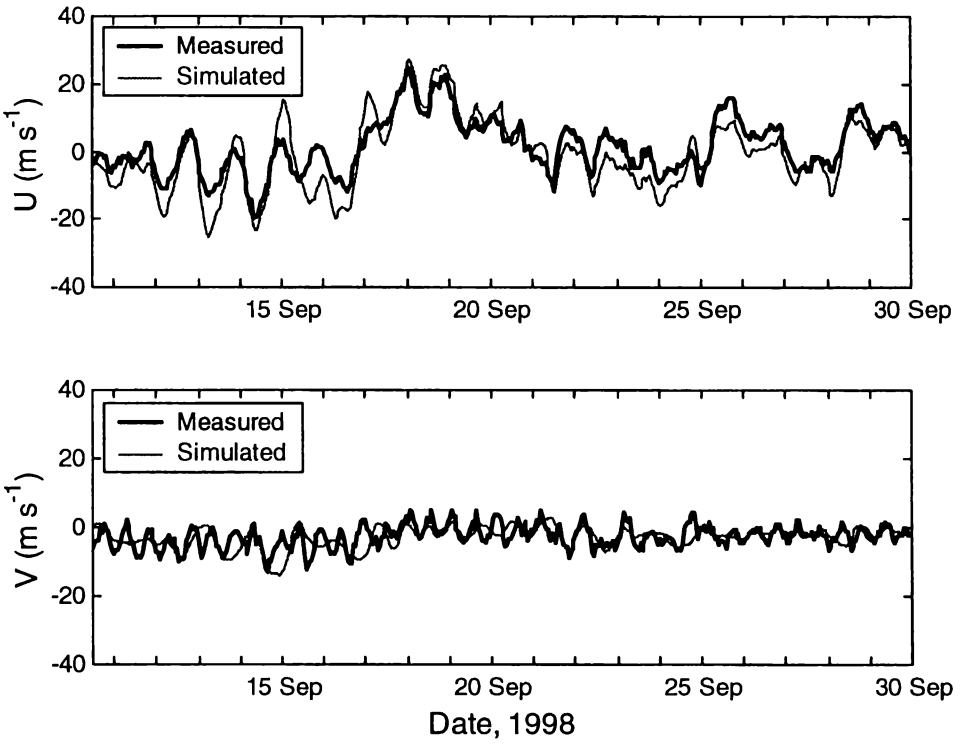

Figure 7-3. Comparison between measured and simulated depth-averaged shelf-current, using just the body-force to drive the model.

7.2.3 Ocean boundaries

The body-force is used as a surrogate for sea-level boundaries where data is unavailable for those boundaries. Therefore the western, southern and eastern open sea-level boundaries were clamped at zero, and the body-force acceleration was used to simulate shelf-current response to sea-level gradients.

7.2.4 River discharge

Poverty Bay receives freshwater from the Waipaoa and Turanganui Rivers, resulting in a stratified water body and necessitating a three-dimensional numerical model for accurate simulation (Chapter 4). Therefore the northern model boundary included freshwater input time-series from the Waipaoa and Turanganui Rivers (Figure 7-5) and the treatment of these boundaries is discussed below. The Waipaoa River has approximately 6 times the discharge of the Turanganui River (Bruce Walpole, Gisborne District Council, *pers. comm.*) and preliminary simulations showed it to dominate stratification in the bay. Waipaoa

River discharges were obtained from the Kanakanaia automatic flow gauging station at Te Karaka (map reference: NZMS260 Y17 359 923), located ~27 km from the bay, and the river follows a meandering course of ~47.5 km over this distance (Hawkey, 1984). No major tributaries join the Waipaoa below this station, however a time delay can be expected between flow passing the station and entering the bay. Figure 7-4 gives the relationship between Waipaoa River discharge and flow velocity, while Table 7-1 gives the time lags for flow between the gauging station and Poverty Bay. Since river baseflow does not vary rapidly, preliminary model simulations showed the model to be most sensitive to the arrival of the quickflow event, 17-19th September (Figure 7-5). From Table 7-1, this gives a time lag at peak flow of 12.6 hours between flow passing the gauging station and entering the bay. Allowing for slightly lower discharge during the majority of the quickflow event, a time lag of 15 hours was applied to the river boundaries (Figure 7-5). This delay was not accounted for in Chapter 4.

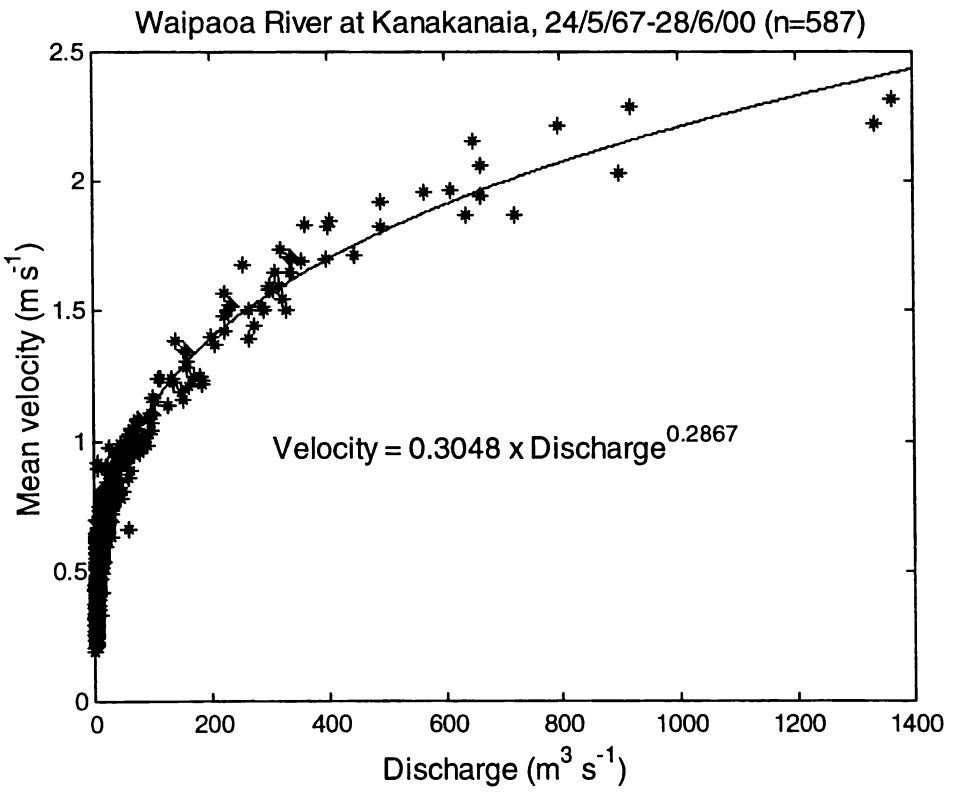

Figure 7-4. The relationship between Waipaoa River discharge and velocity, from 587 gaugings undertaken since 1967: velocity = 0.3048 × discharge$^{0.2867}$.

From 233,302 mean hourly values collected since 11 November 1972, the mean Waipaoa River discharge is 32.29 $m^3 s^{-1}$, standard deviation 68.83 $m^3 s^{-1}$, maximum 2821.30 $m^3 s^{-1}$, and minimum 0.68 $m^3 s^{-1}$. With a mean discharge of 13.67 $m^3 s^{-1}$ the simulation period therefore covers a period of relatively low flow. Flows exceeding 2000 $m^3 s^{-1}$ were recorded twice in the 18-year record, although Cyclone Bola was not recorded due to gauge failure and there may similar unrecorded events. Discharges exceeding 200 $m^3 s^{-1}$ occurred 3.5 times per year on average while flows greater than 60 $m^3 s^{-1}$ occurred approximately 14 times per year. The mean river discharge not including flows in excess of 60 $m^3 s^{-1}$ was 17 $m^3 s^{-1}$. The longest recorded duration of discharges less than 3 $m^3 s^{-1}$ was 47 days.

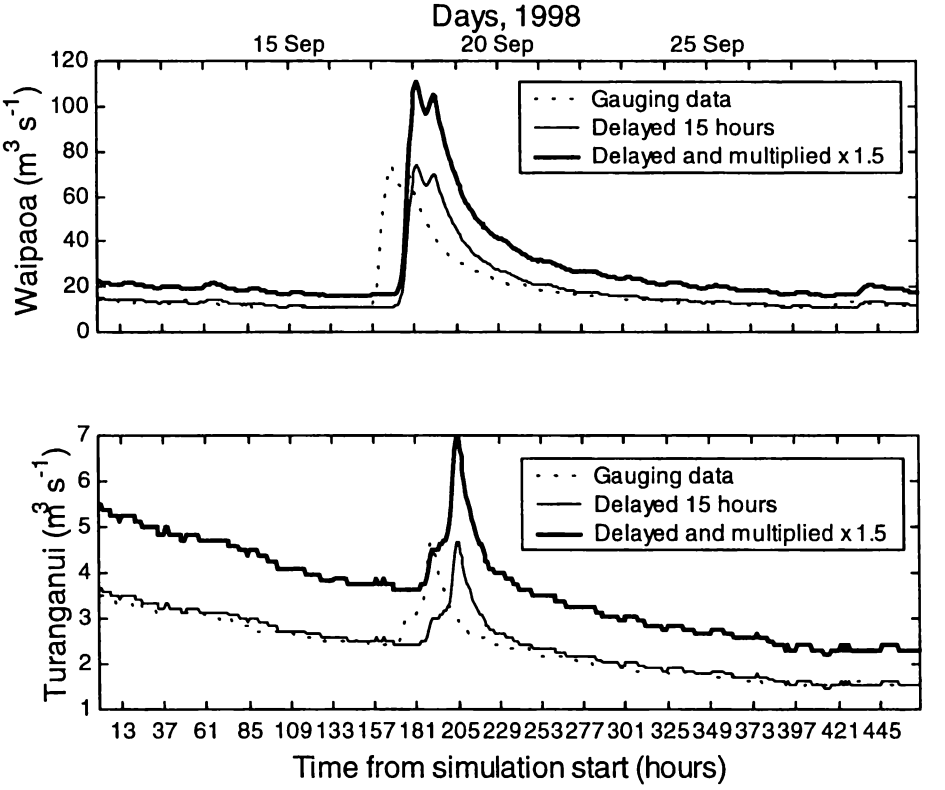

Figure 7-5. River flow during the simulation period, dashed line is discharge measured at the up-river gauging station, light solid line is discharge delayed 15 hours and heavy solid line is discharge used in calibrated simulations (delayed 15 hours and multiplied by 1.5).

The Turanganui River time-series was reconstructed from the Waimata River flow gauging station, the Waimata River being the major tributary. Since the Waimata

gauging station is located toward the headwaters and far from its confluence with the Turanganui River, a multiplication factor of 2.5 was applied to bring its baseflow to approximately 1/6 that of the Waipaoa River and a time lag of 15 hours was also applied. The model proved relatively insensitive to the Turanganui River discharge, salinity patterns being dominated by the larger Waipaoa River.

Table 7-1. Waipaoa River *discharge*, *velocity* and *time lag* from gauging station to bay, for the 486 hour model simulation window.

	Discharge ($m^3 s^{-1}$)	Velocity ($m s^{-1}$)	Time lag (hours)
Mean	13.67	0.645	20.46
Maximum	73.90	1.047	12.60
Minimum	5.32	0.492	26.82

7.2.5 Wind input

ADP and CTD surveys indicate that wind stress has significant influence on Poverty Bay hydrodynamics (Chapter 4). Model 3DD accepts wind inputs in meteorological convention, at user specified grid cells. The model uses inverse interpolation to calculate wind stresses between stations, but since only one wind station was used in simulations, the model applied the wind stress over the entire grid. Wind data input to model 3DD were recorded at the Gisborne Aero recording station (Figure 7-1) and are shown in Figure 7-6. It is well known that wind speeds measured on land are less than across an adjacent water body, due to boundary layer friction (Hsu, 1986). Therefore the correction

$$W_{sea} = 1.62 + 1.17_{land}$$

(Hsu, 1986) was applied to Gisborne Aero wind speeds prior to simulation, as used by Black et al. (1996) and by Galperin and Mellor (1990) with an observational adjustment. The use of the formula was justified by more accurate velocity and salinity patterns during simulations.

While the Hsu (1986) formulae is well accepted for the adjustment of wind velocities over land to those over the adjacent sea, there is much debate over the

drag coefficient C_d used to convert wind speed into wind stress. Model 3DD uses the Wu (1982) wind stress coefficient

$$C_d = (0.8 + 0.065|W|) \times 10^{-3},$$

but many others have been proposed. Pickard and Emery (1990) give a range of C_d increasing from 0.98×10^{-3} to 2.04×10^{-3} as wind speeds increase from 2 to 25 m s^{-1}. Large and Pond (1981) propose two different C_d formulations for wind speeds above and below 11 m s^{-1}, while modern numerical models often use two C_d formulations with a cut-off wind speed of ~4-5 m s^{-1} (eg. Ivey and Patterson, 1984; Wang and Symonds, 1999).

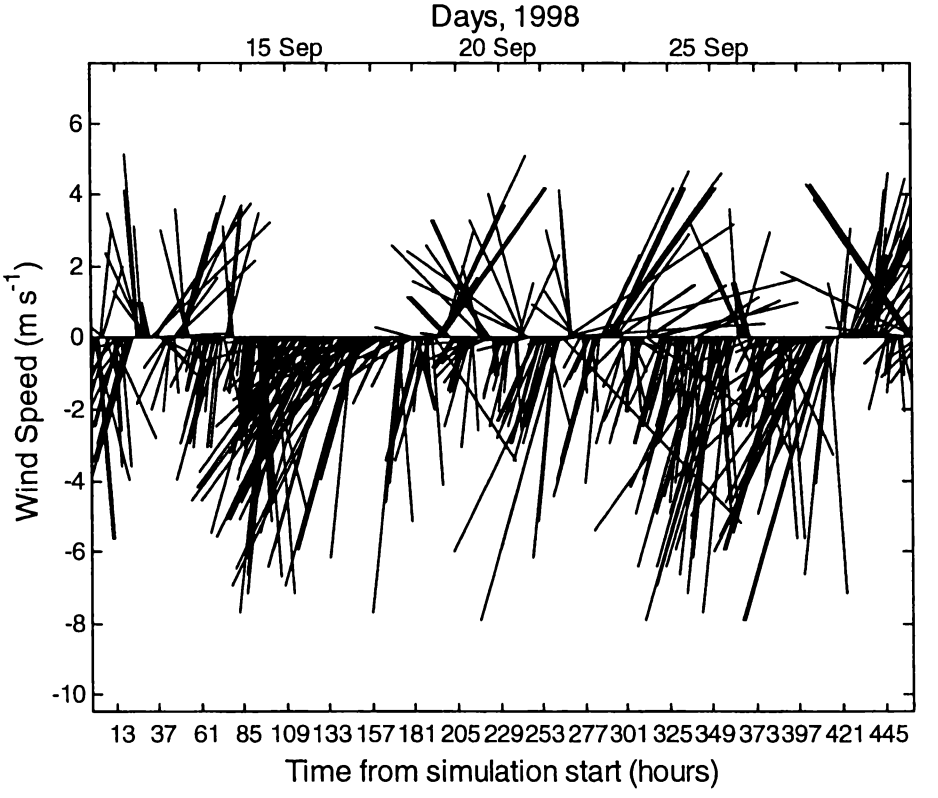

Figure 7-6. Wind recorded at Gisborne Aero during the simulation period, shown in true vectors convention and rotated +36° to match model grid orientation.

7.2.6 Seabed friction

Side-scan-sonar images show the Poverty Bay seabed to be devoid of bedforms and predominantly composed of fine sand and mud (Healy et al., 1997). The

frictional roughness length z_0 was therefore unable to be calculated based on bedform size, but was estimated to be 0.0001 m. This is small compared with the typical estuarine value of around 0.001 m (Black et al., 1989), but is in keeping with the fine and smooth sedimentary features in the bay. (Foster and Carter, 1997) showed that continental-shelf sediment adjacent to Poverty Bay also contains substantial mud proportions, but due to the uncertainty of bedform sizes on the continental-shelf, z_0 was estimated at 0.002 m, a value used by (Black, 1989). A sensitivity test showed that the model gave near-identical results if z_0 = 0.0001 m was used everywhere, provided that the body-force used to drive shelf-currents was calculated using matching z_0.

7.2.7 Stratification and model type

Model 3DD allows a choice of inputs to control stratification in its three-dimensional form. The model will work with inputs of density, salinity, temperature or a combination of salinity and temperature. The choice depends on the dominant parameter and on the data available to drive the model. Over the fieldwork and simulation period, river discharge provided data for a salinity boundary and appeared to dominate stratification, therefore a salinity model was the logical choice.

On the continental-shelf, temperature was observed to remain close to 13°C, with less than 1°C variation at both mid-water and near-bed S4 sites during the simulation period (Figure 7-7). The background temperature was therefore set to 13°C for the model simulations. Salinity was set to 34.8 ppt at the open sea boundaries, based on CTD casts taken on the continental-shelf during the 1998 field study, while river water was set to 4 ppt to allow for some dissolved salts in the typically high suspended sediment load rivers (Foster and Carter, 1997).

In combination with the near constant continental-shelf temperatures observed, CTD surveys showed density to be dominated by salinity (Figure 7-8), indicating that during the field period, stratification was dominated by freshwater inputs to the bay and not thermal inputs via solar radiation. Significant temperature changes were observed in the surface layer at times, but these were associated

with the river plumes and not with solar inputs (Figure 7-9). Based on these results a salinity-stratified model was chosen, with temperature set to constant 13°C.

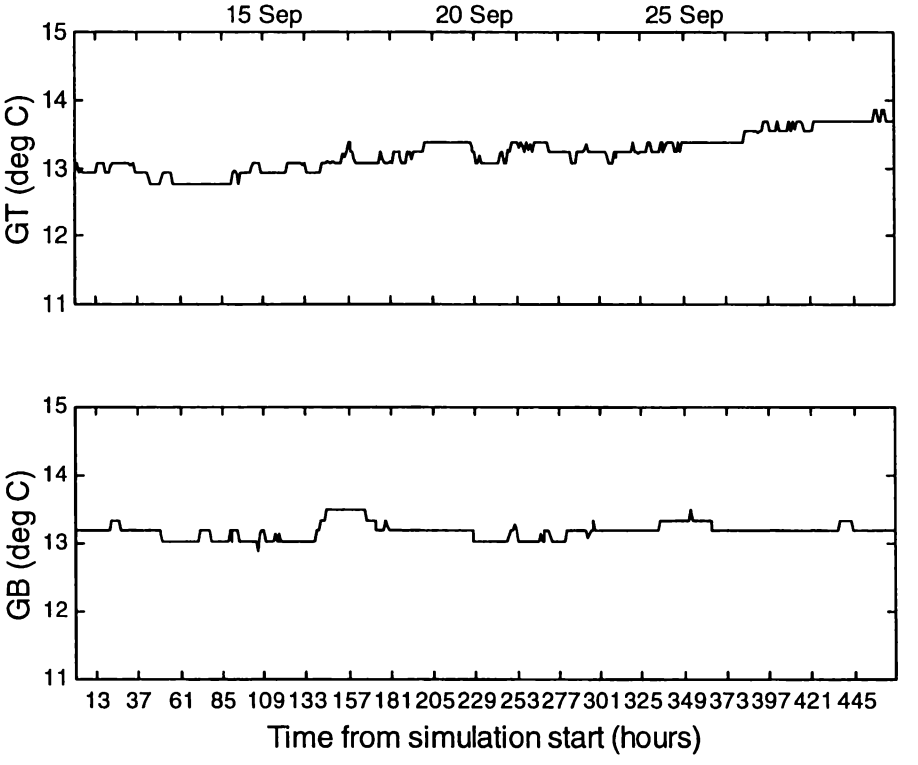

Figure 7-7. Temperature on the continental-shelf during the simulation period, at the current-meter locations GT (mid-water) and GB (near-bed).

Conversely, Black et al. (1997) used a temperature-salinity type model to simulate an August 1996 period. Like the 1998 field survey used for this study, 1996 CTD calibration data showed that in general, patterns of temperature stratification closely matched that of salinity, suggesting that they were river-induced temperature changes and not caused by solar radiation inputs (Gorman et al., 1997). The calibration simulation undertaken by Black et al. (1997) supported this; although heating and cooling occurred near the bay margins, river discharge, wind and strong shelf-currents dominated circulation, and temperatures in the bay at large were dominated by the river plumes. Therefore Black et al. (1997) could also have used a salinity-only model for their winter simulations with equivalent success.

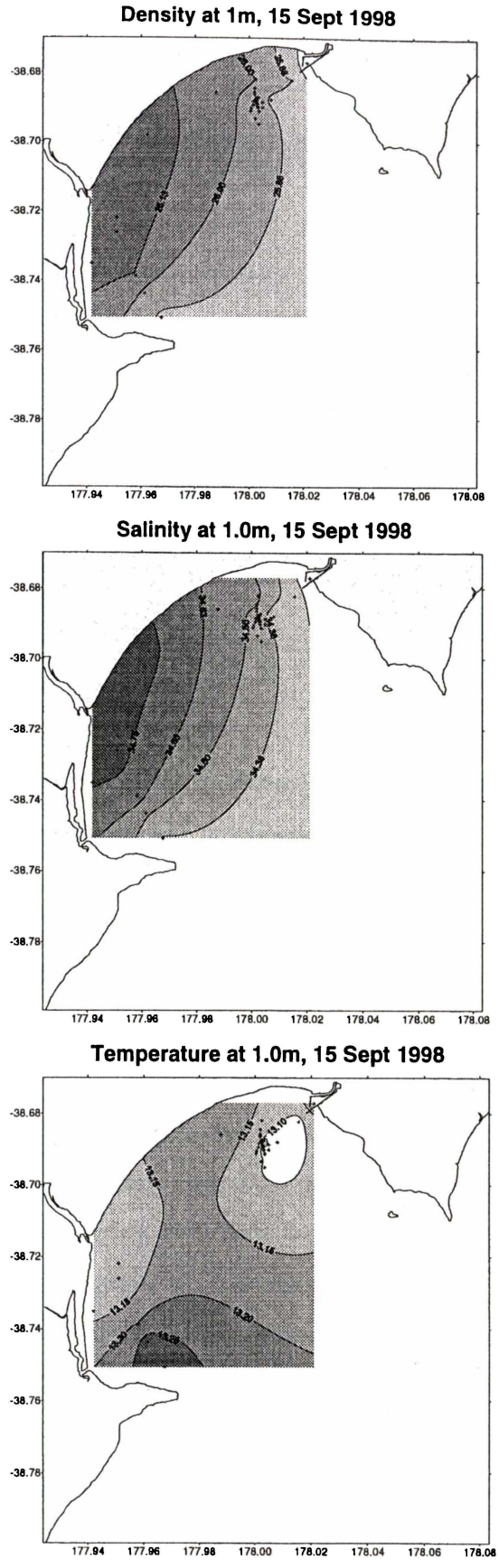

Figure 7-8. Density, salinity and temperature at 1 m depth, 15 September 1998, showing the dominance of salinity on density distribution.

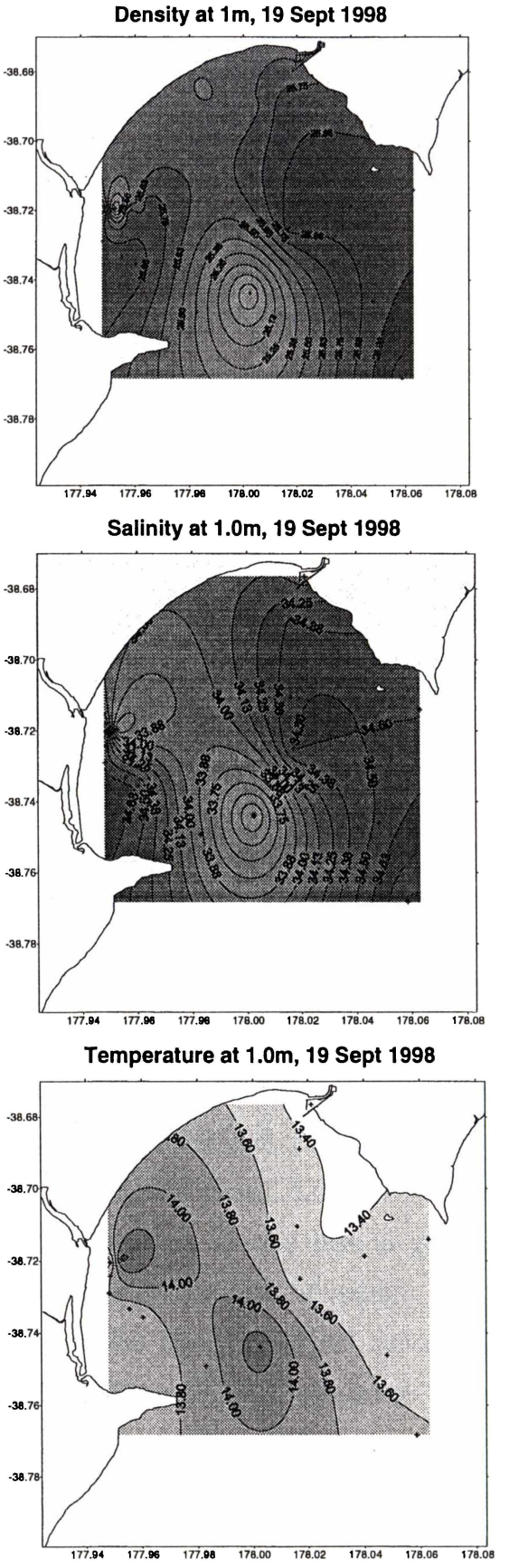

Figure 7-9. Density, salinity and temperature at 1 m depth, 19 September 1998.

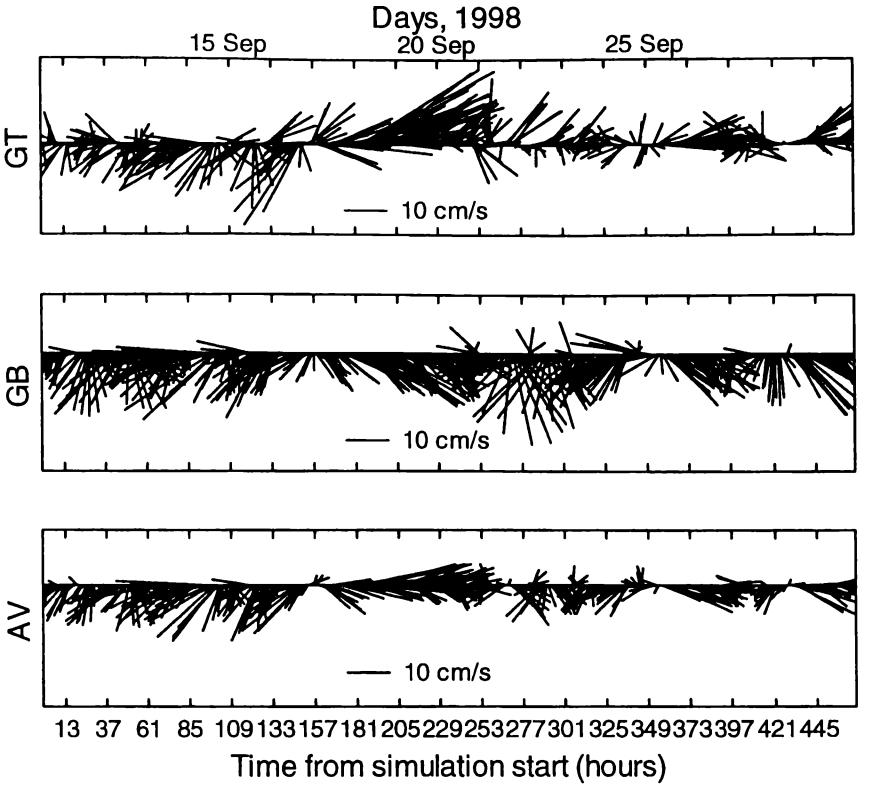

Figure 7-10. Continental-shelf-currents rotated +36° to match model grid orientation. GT is mid-water, GB is near-bed and AV is the mean.

7.2.8 Model layers

Model 3DD allows for a user-specified vertical layer structure. Since vertical shear and mixing occurs at the layer interfaces, the number and thickness of vertical layers in the model should be chosen to represent the natural stratification. Poverty Bay responds primarily to wind stress and river discharge forcing (Chapter 4), therefore the choice of surface layer thickness is most important. Examination of CTD casts taken during field surveys showed that freshwater was mixed with marine water ~1-10 m from the water surface at times, but with a surface-mixed layer commonly around 2 m depth. Therefore the surface layer was chosen to be 2 m thick. Substantial vertical current shear was observed to occur at depths up to ~10 m (Chapter 4, Figure 4-7 & Figure 4-9) during the field study, so a total of 8 model layers were chosen to adequately represent stratification (Table 7-2). Sensitivity tests were also undertaken using a model incorporating 10 layers with 4 × 1 m near-surface layers, and a 7-layer model using 3 m thick near-surface layers. Results showed that excessive stratification

and limited vertical mixing in the 10-layer model prevented downward momentum transfer, while the 7-layer model predicted overly diffused salinity patterns.

Table 7-2. Model vertical layer description

Layer #	Layer thickness (m)	Layer sub-surface range (m)	Layer mid-point (m)
1	2	0-2	1
2	2	2-4	3
3	2	4-6	5
4	3	6-9	7.5
5	3	9-12	10.5
6	4	12-16	14
7	4	16-20	18
8	20	20-40	30

7.2.9 Horizontal eddy viscosity

The horizontal eddy viscosity term (Appendix 2, eqn A2.1) behaves as a velocity smoothing algorithm, the higher the horizontal eddy viscosity coefficient A_H, the greater the velocity smoothing (Black et al., 1997). This term has little influence when velocity gradients are smooth, and has little appreciable influence at values less than 1 on a grid size of ~100 m (Black, 1989). Simulations showed sharp velocity gradients only occasionally at the headlands of the bay, therefore A_H was set to 1. A sensitivity test using A_H = 5 showed that increased horizontal shear (internal friction in the water column) caused some damping of current speeds, too slow compared with measured velocities, confirming A_H = 1 as the better choice.

7.2.10 Vertical eddy viscosity

The downward transfer of momentum is controlled through the vertical eddy viscosity term $\frac{\partial}{\partial z}\left(N_z \frac{\partial u}{\partial z}\right)$, where N_Z is the vertical eddy viscosity coefficient (Appendix 2). Thus the correct value for N_Z is of fundamental importance to

successful model calibration. Several options are available: fixed values for N_Z can entered by the modeller, using either one depth-averaged value or a different value for each model layer, or a formulation for N_Z can be applied. Model 3DD offers the choice of a parabolic formulation, whereby N_Z increases near the surface and bottom boundaries (Appendix 2). Also offered is the modification $N_Z = N_0 \, e^{-C'Ri}$, where N_0 is N_Z predicted by the parabolic formulation and R_i is a gradient Richardson number that parameterises the degree of stratification between each layer. The result is that as stratification increases, R_i increases and N_Z decreases. This represents the natural situation where stratification inhibits vertical mixing and thus limits the downward transfer of momentum from the surface. C' is set separately for both salinity diffusion and the transfer of momentum, the model defaults being $C'_S = 12$ for salinity and $C'_M = 4$ for momentum. Sensitivity tests showed that decreasing C'_S caused increasing vertical diffusion of salinity (a result opposite to that desired), whereas the model was insensitive to increases in C'_S above the default value. The default value $C'_S = 12$, therefore provides the most restrictive possible limit to salinity diffusion. Using larger C'_M values served to increase mixing between layers, transferring momentum down through the water column and providing a means to increase predicted current velocities. This resulted in decreased surface layer speeds and increased speeds in the lower water column, but did not change the general circulation patterns. Unfortunately, this also increased the vertical transfer of salinity, and a significant increase in near-bed velocity was associated with too much vertical disruption of stratification. Since disruption of stratification in the bay was unacceptable, the final calibration used a value of $C'_M = 5$, slightly larger than the default, but making little difference to the simulation. A further improvement to the model may have been the use of a minimum N_Z. In the presence of large R_i values due to high salinity stratification, this may have increased the transfer of momentum at the low end of the scale, without transferring too much salinity, but this was unable to be factored into the model.

7.3 RESULTS AND DISCUSSION

The results of numerical simulations have been transformed from the standard model output (eg. Figure 7-2) into the same format used to view the measured data (Figure 7-12). Since field surveys were conducted over a period of a few hours, model output was averaged over the corresponding period prior to plotting.

The following results and discussion address firstly the model calibration run, i.e. the most accurate reproduction of Poverty Bay hydrodynamics as measured in the field. The model calibration simulation included the most appropriate choices for parameters such as A_H, N_Z, K_H, K_Z, C', and included appropriate adjustments to the wind speed and timing of river discharge, as discussed in the methods section. Following calibration the model is used to determine the comparative contribution to circulation of the three forcing components: shelf-current, wind and river discharge.

7.3.1 Model calibration

Model output is compared with measured data in Figure 7-11 - Figure 7-17. Velocity data measured by ADP have been superimposed on salinity contour plots, measured by CTD. For ease of comparison with model output, the measured data have been plotted at depths (relative to the water surface) that correspond to model output mid-layer depths. The measured salinity data have been contoured onto a 100 × 100 grid by the Kriging method, using Surfer™ (Golden Software, 1996). Consequently the contoured salinity plots of the measured data contain some interpolated information that may not be strictly true. On days where CTD sampling coverage was comprehensive (eg. 17, 19 and 26 September, Figure 7-13, Figure 7-14 and Figure 7-15), then salinity contours can be assumed roughly correct, but on 15 and 28 September (Figure 7-12 and Figure 7-16) the contoured salinities must be viewed with caution.

The best model calibration after 54 model runs reproduced the general velocity and salinity patterns well, but tended to over-predict salinity diffusion and under-predict current speeds (Figure 7-11). The under-predicted velocities suggested

that the forcing in the model was overly weak. It is shown below that circulation in Poverty Bay is forced mainly through surface wind stress and by river discharge effects. Further model calibration runs were undertaken using river discharge multiplied by 1.5 and 2, and wind (over sea) magnitudes multiplied by 1.3, 1.5, and 1.7. The best calibration was obtained using river discharge multiplied by 1.5 and wind magnitudes multiplied by 1.5. Both wind magnitudes and river discharge volumes had to be increased in unison to improve calibration. While an increase in wind speeds alone produced faster currents, predicted circulation patterns deteriorated if river discharge was not correspondingly increased, illustrating the interdependence of the two forcing mechanisms in driving Poverty Bay hydrodynamics.

Since the Waipaoa River gauging station is located ~27 km from Poverty Bay, it is reasonable to assume that the river receives some catchment runoff between the gauging station and the bay. Thus discharges entering the bay are expected to be greater than those measured by some unknown factor, and the factor of 1.5 applied in the model provides the best calibration results.

The wind speed multiplication factor is likely to result from a combination of: 1) the inadequacies of using land-based wind measurements in place of those over the sea; 2) the inapplicability of the Wu (1982) wind drag coefficient C_d used to calculate wind stress in the model. Sea-based wind measurements were not available for the study, and neither were ECWMF predictions. Therefore land-based winds measured at Gisborne airport were applied, using the standard land-to-sea wind speed correction factor of Hsu (1986). The Gisborne airport weather station is located on plains away from steep topography and close to Poverty Bay (Figure 7-1), therefore the Hsu (1986) multiplication factor should have accounted for most of the magnitude difference between land and sea, but cannot substitute for the accuracy provided by direct wind measurements. As discussed in the methods section, many different formula for calculating C_d are available, later versions commonly recognising that a change in C_d is required for wind speeds above and below ~4-5 m s^{-1} (not included in the Wu (1982) formula). A better formula for calculating C_d at Poverty Bay was not investigated, but a wind speed

multiplication factor of 1.5 was applied instead, and this provided good model calibration results.

The simulations in Figure 7-12 - Figure 7-16 therefore represent the best model calibration after 60 runs. The model reproduces the general velocity and salinity patterns well, but tends to over-predict salinity diffusion. The model shows a marked freshwater plume at all times in the surface layer, but this was not always present during the field surveys (Figure 7-12).

During the 15th September field survey, the wind blew strongly toward the southwest (Figure 7-6), restricting the survey to low chop areas along the inner bay margin (Figure 7-12). ADP and CTD results show surface wind-driven flow and an associated upwelling bottom return flow in the nearshore, while circulation in the wider bay is unknown due to the limited spatial coverage of the survey (Figure 7-12). In the surface layer (0-2 m), the model shows that the buoyant fresh Waipaoa River plume is forced to the southwest of the bay by the prevailing wind-driven surface current, however this plume was not identified during the field survey. In model layer 2 (2-4 m) both the velocity and salinity pattern closely match the measured situation, with currents flowing out past Young Nicks Head and saline marine water located nearshore, brought onshore as part of the wind-induced bottom-return-flow. Current magnitudes are well predicted, but the upwelling slug is more widespread than measured, although contoured measured salinities are unlikely to be exact either, due to limited spatial coverage. Therefore on the 15th September the model shows good calibration for velocities although the speeds are under-predicted, while upwelling is also represented in the salinity patterns. A broader upwelling slug and uniform salinity in deeper layers may indicate excessive numerical eddy diffusion of salinity.

During the 17th September field survey, winds were lightly offshore (Figure 7-6) and river flows were low (Figure 7-5). An anticyclonic gyre consumed the bay (~0.1 m s^{-1}), with upwelling marine water near the centre of the gyre and the Waipaoa River plume evident in the western bay surface (Figure 7-13). The anticyclonic gyre transported fresh-mixed water offshore in the western bay while bringing saline water onshore in the east. In model layers 1 and 2 a high salinity

slug is also predicted near the bay centre, although this is broader than that measured. The model reproduces the measured anticyclonic circulation, but while predicted speeds are good in the lower water column they are under-predicted in the mid and upper water column. At the bay entrance a southeast flow draws water out of the bay and prevents a strong anticyclonic gyre developing. It is later demonstrated below that the near-entrance flow is driven by the body-force, and this period coincides with an over-predicted body-force (Figure 7-3). Therefore on the 17th September the velocity calibration is good in the lower water column but less accurate in the mid and upper water column.

During the 19th September field survey, the wind was light offshore in the morning and light onshore during the afternoon as part of the sea-breeze cycle (Figure 7-6). River flows were returning toward normal (baseflow) after a recent quickflow event that peaked at 111 $m^3 s^{-1}$ (multiplication factor applied, Figure 7-5). Measurements showed the freshwater river plume to be confined largely to the north-eastern side of the bay and to extend deep to model layer 5 (9-12 m), apart from two surface readings that showed a freshwater surface slug positioned near Young Nicks Head (Figure 7-14). Following the quickflow discharge the bay contained considerably more freshwater than 15th and 17th September. Measured velocities appeared to show a switch in circulation between morning and afternoon that was consistent with wind direction, suggesting wind-driven surface flow and associated bottom-return flow (Chapter 4). In the surface layer the model shows a more prominent surface plume emanating from the Waipaoa River than measured and does not predict the freshwater slug by Young Nicks Head. However, for subsurface layers the predicted salinities are very close to measured, showing good calibration. Velocities in model layers 2 and 3 are also well calibrated in both speed and direction, showing anticyclonic horizontal circulation. In deeper layers the model remains well calibrated with velocities measured in the morning (although speeds are under-predicted), but it does not match the afternoon transect across the inner bay (velocity vectors shown in white, Figure 7-14). Even in comparison to morning currents, the model shows a gradual velocity transition between layers and does not reproduce the rapid shear in current directions observed between layers 3 and 4 (5-7.5 m). Therefore on 19th September the model is generally well calibrated, closely reproducing salinity and

velocity patterns. However, the model seems too insensitive to wind-driven effects, particularly after the onset of the seabreeze in the shallow inner bay.

The 26th September field survey encompassed a low discharge period (Figure 7-5) and above average strength offshore winds, following an onshore period (Figure 7-6). The current survey was undertaken by successively placing a bottom-mounted ADP at 14 sites – hence the plots show fewer current vectors (Figure 7-15). A freshwater surface slug was present near the entrance of the bay and the Waipaoa River plume was evident at the surface. A weak anticyclonic circulation was evident. Except for the surface layer, where the freshwater slug is not represented, the model generally predicts salinity patterns well, although with too much horizontal dispersion (perhaps responsible for absence of the freshwater slug). The velocity calibration is good, with both speed and direction close to measured. Therefore the model generally shows good calibration on 26th September.

The 28th September field survey encompassed low river discharge (Figure 7-5) and was undertaken during onshore winds (Figure 7-6). The measured salinity distribution clearly shows downwelling freshwater close to land and offshore-directed currents in the lower water column (Figure 7-16). Winds blow surface water inshore where it downwells to flow offshore near the bottom. The model also shows downwelling currents in the centre of the northern shoreline, and evidence for a small anticyclonic gyre in the western half of the bay, as measured. Downwelling is not so obvious in the predicted salinity patterns as for measured salinity, and as for other days salinity diffusion appears too great in the horizontal, dispersing any sharp salinity gradients. Predicted onshore velocities appear over-predicted in the upper 5 m, indicating that the wind speed multiplication factor of 1.5 may be too strong for onshore wind conditions.

The ADP was left beside the sewage outfall (Figure 1-2) between 12:00, 28 September – 08:00, 29 September, 1998 (deployment A, Chapter 4) and constituted the only long-term bottom-mounted ADP record from the field study. Since deployment A encompassed a wind directional swing from onshore to offshore it provides an excellent calibration record (Figure 7-17). Predicted

currents generally compare favourably with measured currents at the deployment A location site, showing good model calibration throughout the water column (compare Figure 7-17 and Figure 7-18).

Overall, the model calibrated well when forced by a combination of body-force, river discharge × 1.5 and wind stress calculated from wind speeds × 1.5. Circulation is less well predicted on 17th September when an erroneous body-force influences the continental-shelf and outer bay and on 28th September when surface current magnitudes are too high. Salinity patterns are also generally good, although plume boundaries are not sharp and the freshwater influence sometimes extends further onto the shelf than measured, indicating too much horizontal diffusion. Black et al. (1997) explains that the mass conserving (Eulerian) advection/dispersion scheme exhibits some numerical diffusion. During these simulations the horizontal eddy diffusivity coefficient K_H (Appendix 2) was set to 0.0005 $m^2 s^{-1}$, a physically realistic value (Black et al., 1997). However, sensitivity tests showed that due to the inherent Eulerian diffusion, K_H only became effective when increased by ~2 orders of magnitude, and so it was impossible to decrease horizontal salinity diffusion.

As was demonstrated in Chapter 4 and is reinforced by modelling below, circulation in Poverty Bay is mainly forced from the surface, through wind stress and the buoyant discharge of freshwater from the rivers. Under-predicted velocities in the lower water column are therefore a result of insufficient momentum transfer from the water surface downward.

Comparison of model predictions with measured data shows that a reasonable level of calibration has been achieved, with the model generally predicting velocity and salinity patterns successfully. Following calibration the most appropriate values for the various constant parameters (eg. A_H, N_Z, K_H, K_Z, C') have been selected for the Poverty Bay situation. The model is therefore simulating near-correct responses to forcing from the three sources, including shelf-current, wind and river discharge. The calibrated model can therefore be used to investigate forcing from these processes individually, and to make

predictions for hydrodynamic situations not encountered during the field survey, such as Waipaoa River flood events.

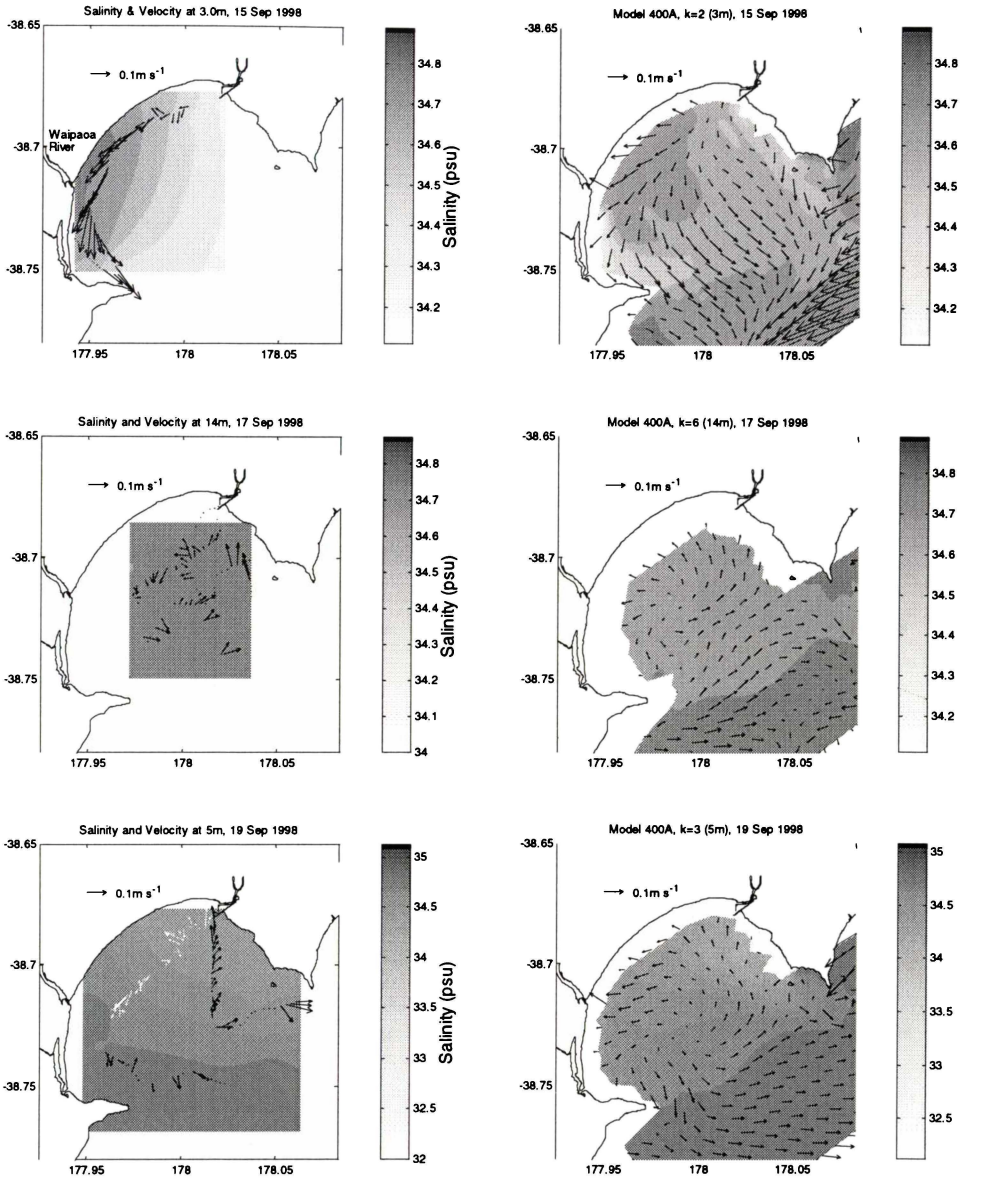

Figure 7-11. Measured data (left) compared with model output averaged over the time corresponding to the survey (right). Velocity vectors were measured using vessel-mounted ADP. Salinity and velocity patterns are generally well predicted but current magnitudes are under-predicted.

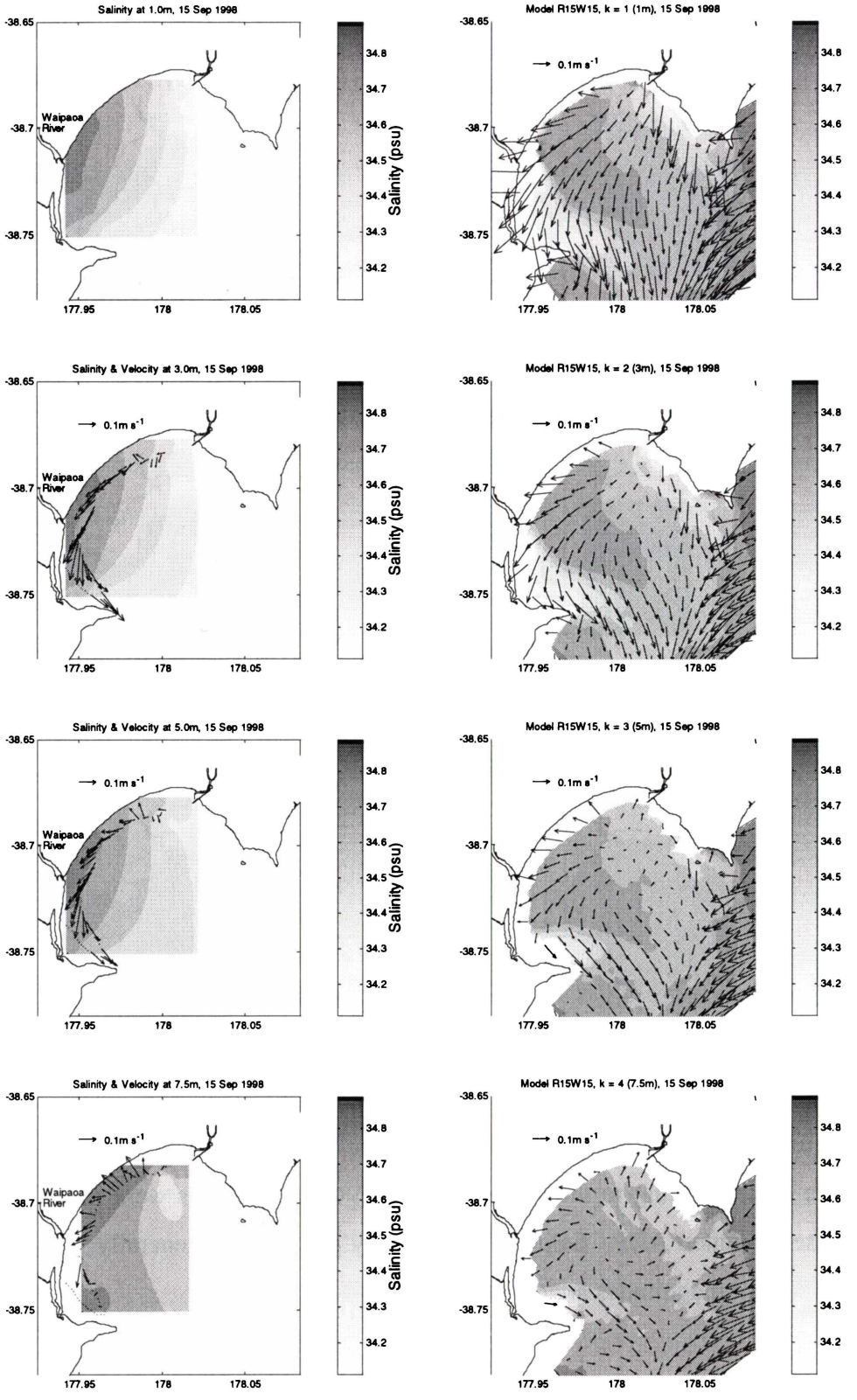
Salinity at 1.0m, 15 Sep 1998
Model R15W15, k = 1 (1m), 15 Sep 1998
Salinity & Velocity at 3.0m, 15 Sep 1998
Model R15W15, k = 2 (3m), 15 Sep 1998
Salinity & Velocity at 5.0m, 15 Sep 1998
Model R15W15, k = 3 (5m), 15 Sep 1998
Salinity & Velocity at 7.5m, 15 Sep 1998
Model R15W15, k = 4 (7.5m), 15 Sep 1998
0.1m s-1
Waipaoa River
Salinity (psu)
-38.65
-38.7
-38.75
177.95
178
178.05
34.8
34.7
34.6
34.5
34.4
34.3
34.2

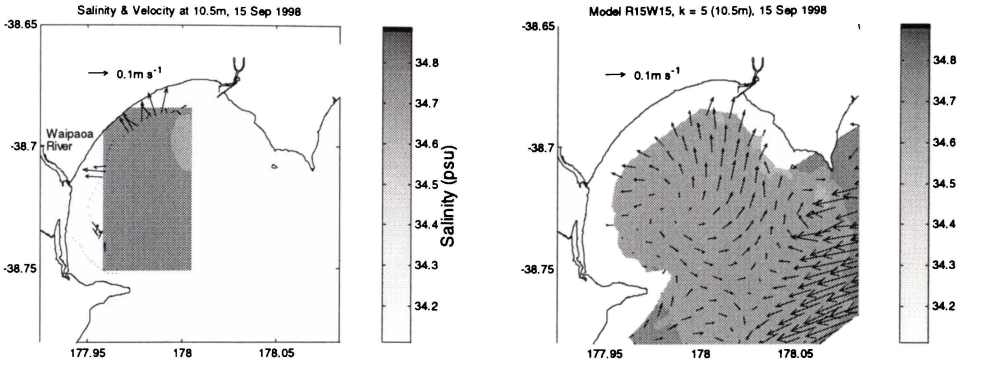

Figure 7-12. Measured data on 15th September 1998, compared with model output from the calibration simulation averaged over the time corresponding to the survey. Velocity vectors were measured using vessel-mounted ADP.

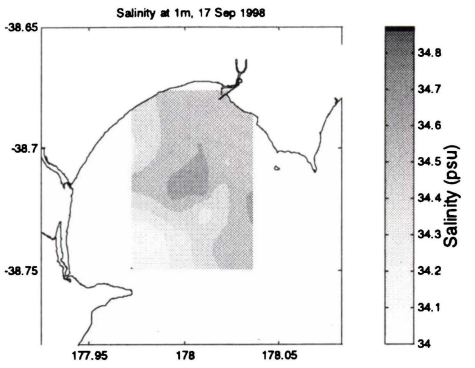
Salinity at 1m, 17 Sep 1998
-38.65
-38.7
-38.75
177.95
178
178.05
Salinity (psu)
34.8
34.7
34.6
34.5
34.4
34.3
34.2
34.1
34

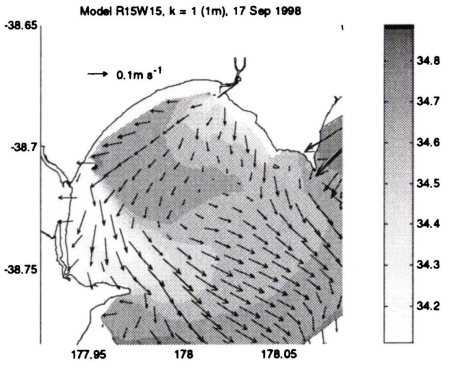
Model R15W15, k = 1 (1m), 17 Sep 1998
0.1m s-1
-38.65
-38.7
-38.75
177.95
178
178.05
34.8
34.7
34.6
34.5
34.4
34.3
34.2

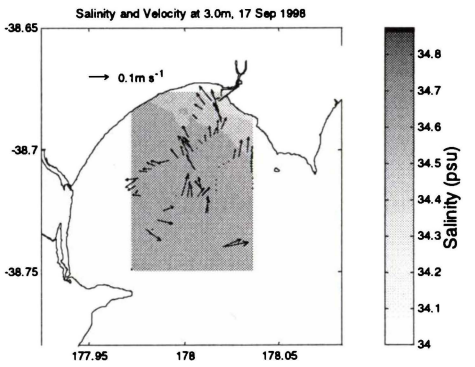
Salinity and Velocity at 3.0m, 17 Sep 1998
0.1m s-1
-38.65
-38.7
-38.75
177.95
178
178.05
Salinity (psu)
34.8
34.7
34.6
34.5
34.4
34.3
34.2
34.1
34

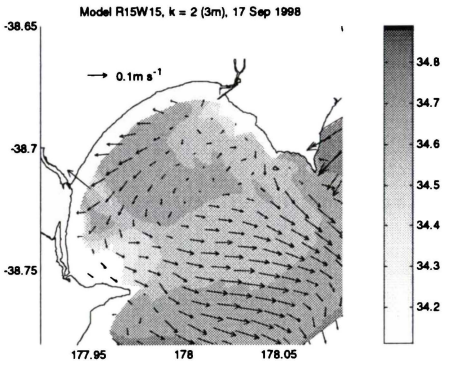
Model R15W15, k = 2 (3m), 17 Sep 1998
0.1m s-1
-38.65
-38.7
-38.75
177.95
178
178.05
34.8
34.7
34.6
34.5
34.4
34.3
34.2

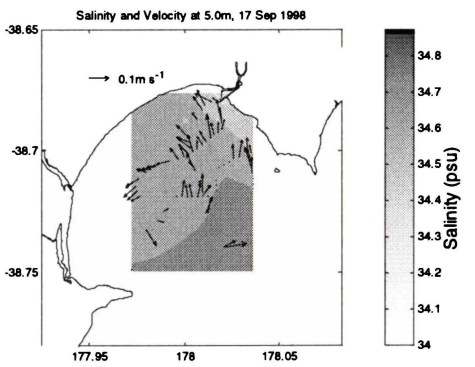
Salinity and Velocity at 5.0m, 17 Sep 1998
0.1m s-1
-38.65
-38.7
-38.75
177.95
178
178.05
Salinity (psu)
34.8
34.7
34.6
34.5
34.4
34.3
34.2
34.1
34

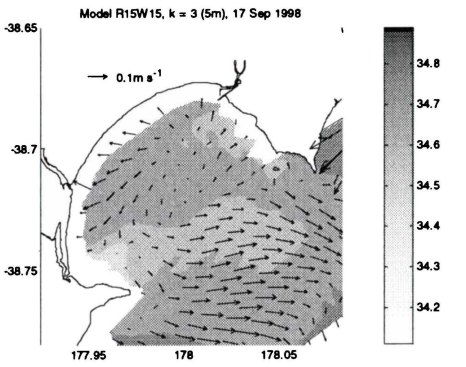
Model R15W15, k = 3 (5m), 17 Sep 1998
0.1m s-1
-38.65
-38.7
-38.75
177.95
178
178.05
34.8
34.7
34.6
34.5
34.4
34.3
34.2

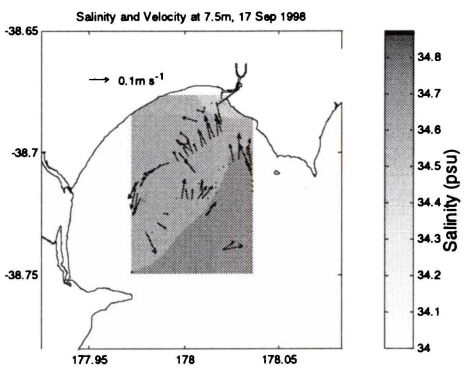
Salinity and Velocity at 7.5m, 17 Sep 1998
0.1m s-1
-38.65
-38.7
-38.75
177.95
178
178.05
Salinity (psu)
34.8
34.7
34.6
34.5
34.4
34.3
34.2
34.1
34

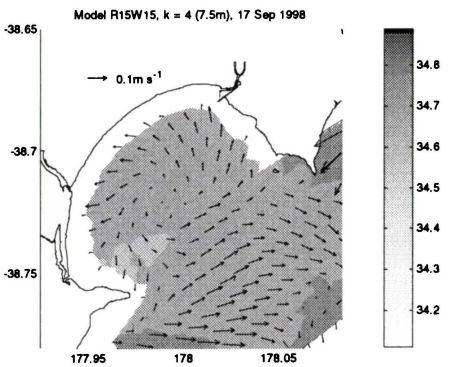
Model R15W15, k = 4 (7.5m), 17 Sep 1998
0.1m s-1
-38.65
-38.7
-38.75
177.95
178
178.05
34.8
34.7
34.6
34.5
34.4
34.3
34.2

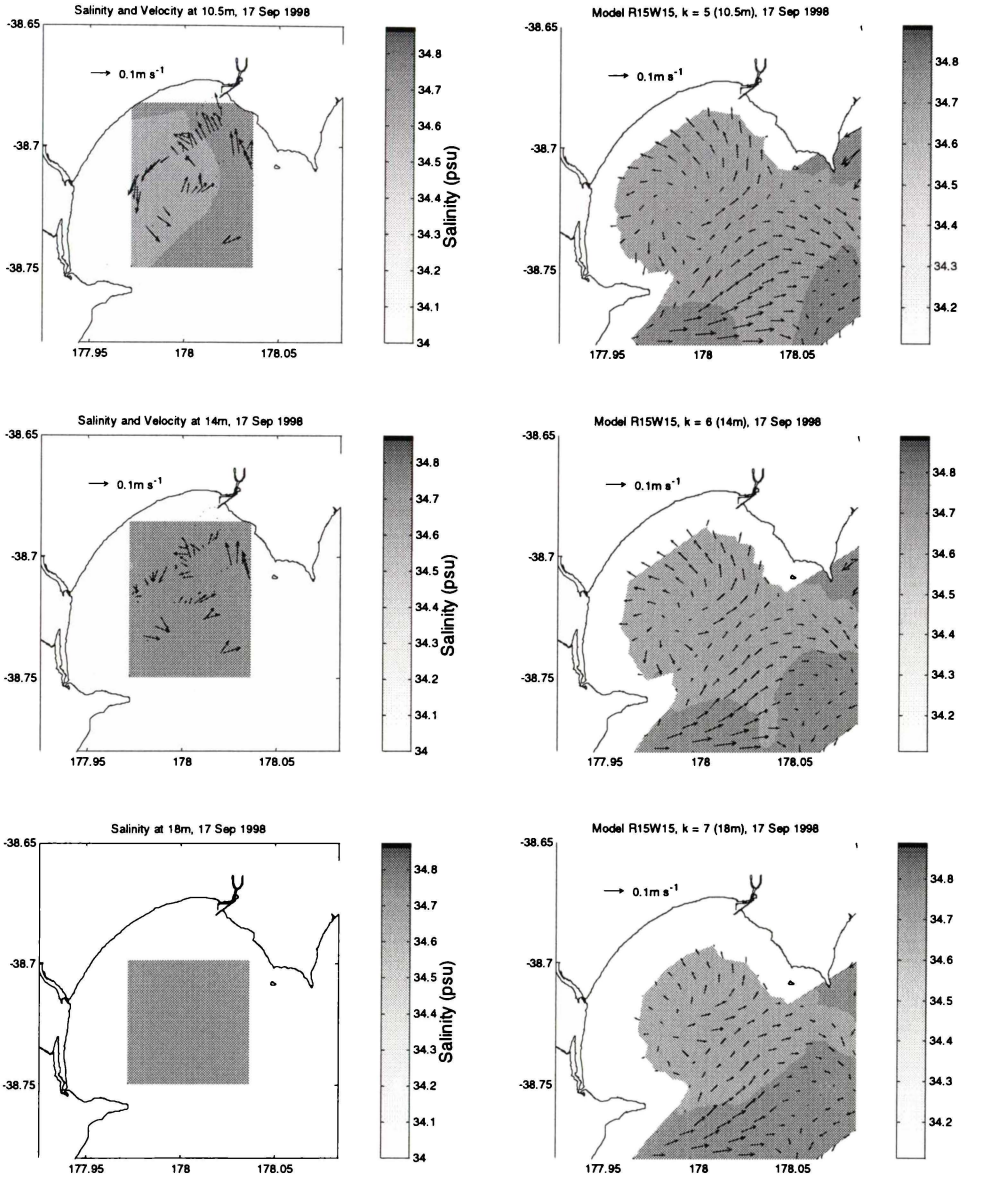

Figure 7-13. Measured data on 17th September 1998, compared with model output from the calibration simulation averaged over the time corresponding to the survey. Velocity vectors were measured using vessel-mounted ADP.

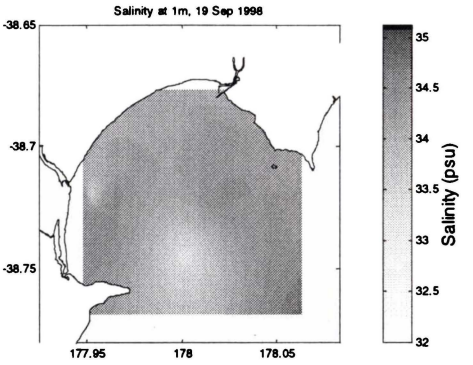
Salinity at 1m, 19 Sep 1998
-38.65
-38.7
-38.75
177.95
178
178.05
35
34.5
34
33.5
33
32.5
32
Salinity (psu)

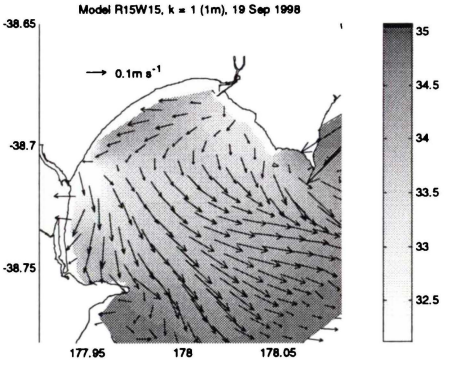
Model R15W15, k = 1 (1m), 19 Sep 1998
0.1m s-1
-38.65
-38.7
-38.75
177.95
178
178.05
35
34.5
34
33.5
33
32.5

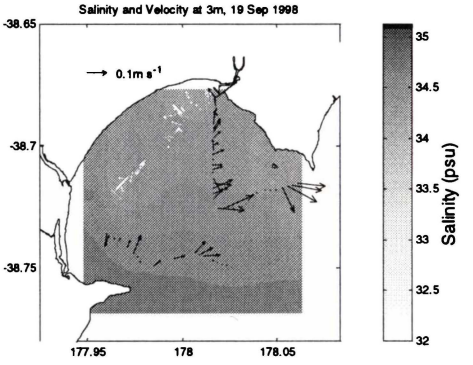
Salinity and Velocity at 3m, 19 Sep 1998
0.1m s-1
-38.65
-38.7
-38.75
177.95
178
178.05
35
34.5
34
33.5
33
32.5
32
Salinity (psu)

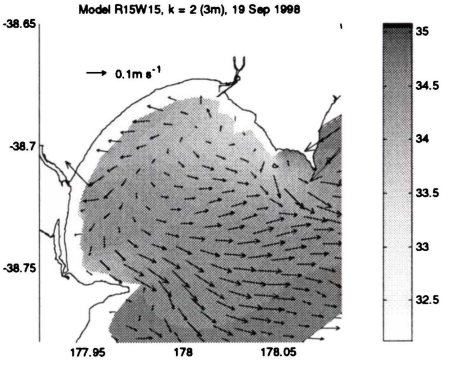
Model R15W15, k = 2 (3m), 19 Sep 1998
0.1m s-1
-38.65
-38.7
-38.75
177.95
178
178.05
35
34.5
34
33.5
33
32.5

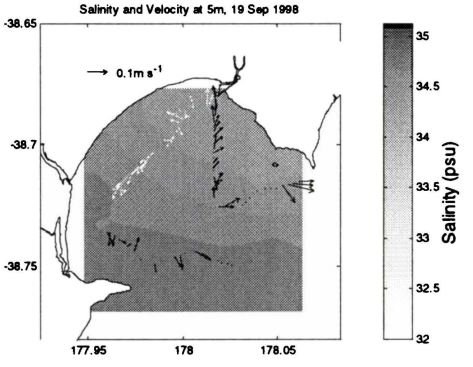
Salinity and Velocity at 5m, 19 Sep 1998
0.1m s-1
-38.65
-38.7
-38.75
177.95
178
178.05
35
34.5
34
33.5
33
32.5
32
Salinity (psu)

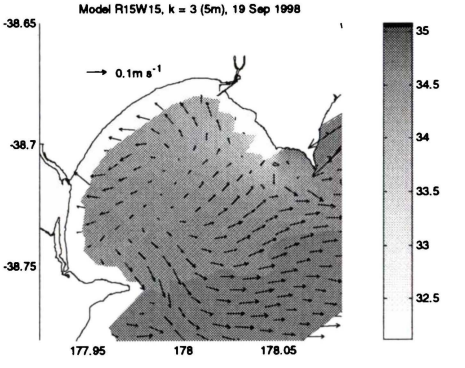
Model R15W15, k = 3 (5m), 19 Sep 1998
0.1m s-1
-38.65
-38.7
-38.75
177.95
178
178.05
35
34.5
34
33.5
33
32.5

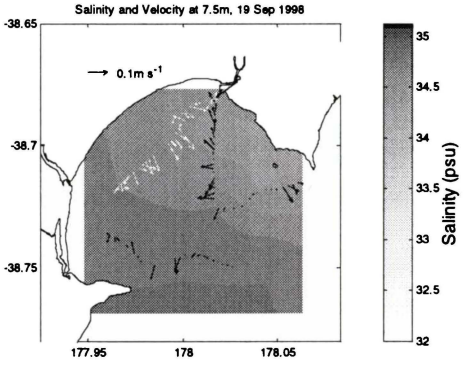
Salinity and Velocity at 7.5m, 19 Sep 1998
0.1m s-1
-38.65
-38.7
-38.75
177.95
178
178.05
35
34.5
34
33.5
33
32.5
32
Salinity (psu)

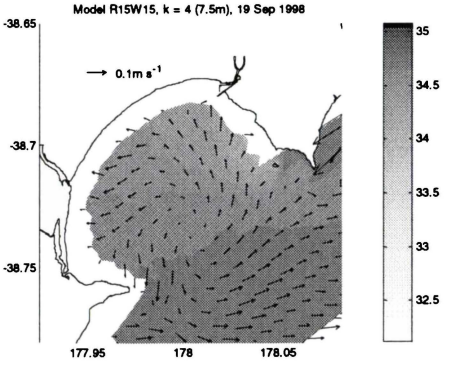
Model R15W15, k = 4 (7.5m), 19 Sep 1998
0.1m s-1
-38.65
-38.7
-38.75
177.95
178
178.05
35
34.5
34
33.5
33
32.5

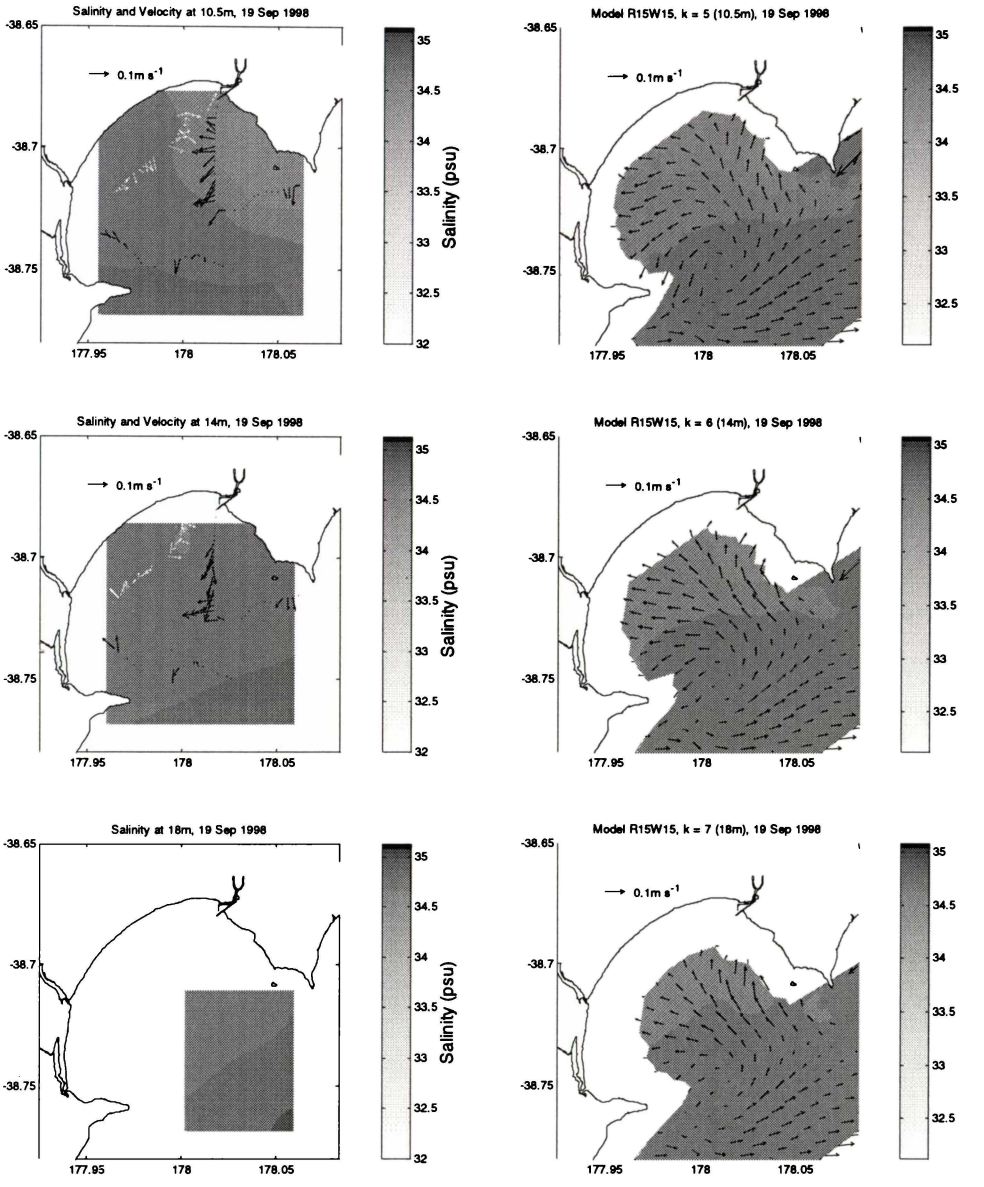

Figure 7-14. Measured data on 19th September 1998, compared with model output from the calibration simulation averaged over the time corresponding to the survey. Velocity vectors were measured using vessel-mounted ADP, morning data shown in black (offshore wind), afternoon data shown in white (onshore wind).

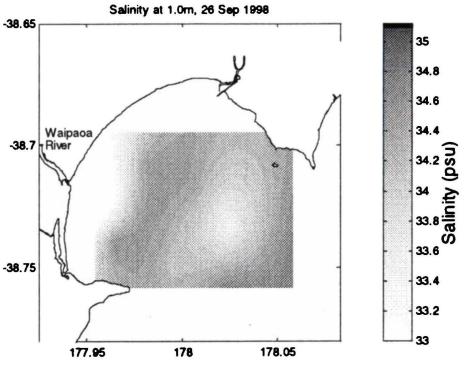
Salinity at 1.0m, 26 Sep 1998
-38.65
-38.7
-38.75
Waipaoa River
177.95
178
178.05
Salinity (psu)
35
34.8
34.6
34.4
34.2
34
33.8
33.6
33.4
33.2
33

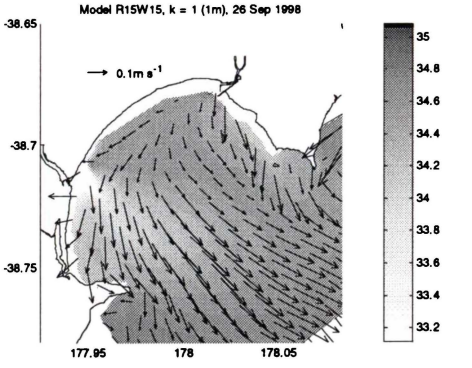
Model R15W15, k = 1 (1m), 26 Sep 1998
0.1m s-1
-38.65
-38.7
-38.75
177.95
178
178.05
35
34.8
34.6
34.4
34.2
34
33.8
33.6
33.4
33.2

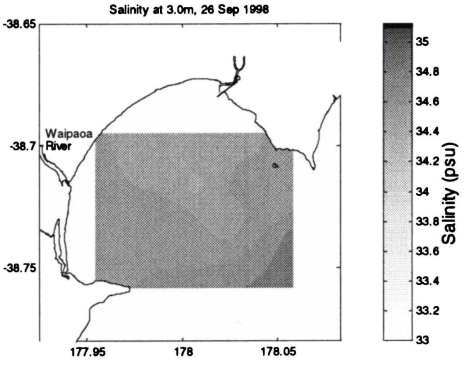
Salinity at 3.0m, 26 Sep 1998
-38.65
-38.7
-38.75
Waipaoa River
177.95
178
178.05
Salinity (psu)
35
34.8
34.6
34.4
34.2
34
33.8
33.6
33.4
33.2
33

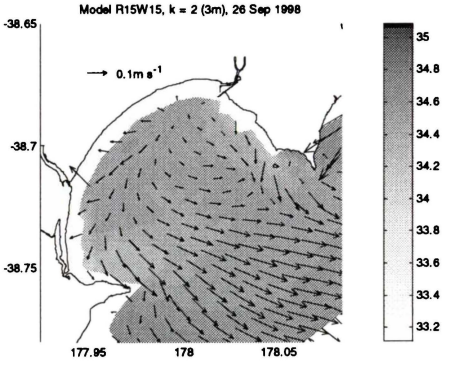
Model R15W15, k = 2 (3m), 26 Sep 1998
0.1m s-1
-38.65
-38.7
-38.75
177.95
178
178.05
35
34.8
34.6
34.4
34.2
34
33.8
33.6
33.4
33.2

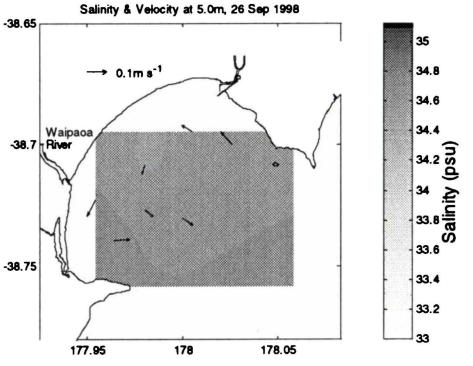
Salinity & Velocity at 5.0m, 26 Sep 1998
0.1m s-1
-38.65
-38.7
-38.75
Waipaoa River
177.95
178
178.05
Salinity (psu)
35
34.8
34.6
34.4
34.2
34
33.8
33.6
33.4
33.2
33

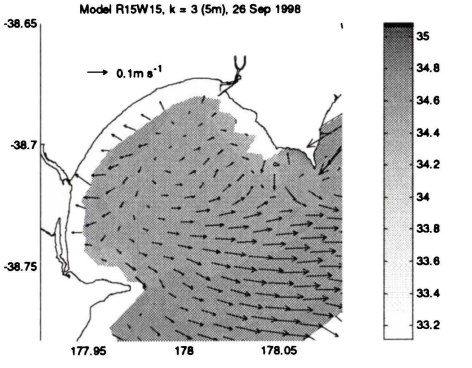
Model R15W15, k = 3 (5m), 26 Sep 1998
0.1m s-1
-38.65
-38.7
-38.75
177.95
178
178.05
35
34.8
34.6
34.4
34.2
34
33.8
33.6
33.4
33.2

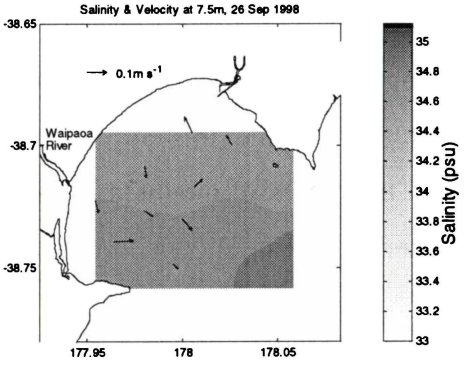
Salinity & Velocity at 7.5m, 26 Sep 1998
0.1m s-1
-38.65
-38.7
-38.75
Waipaoa River
177.95
178
178.05
Salinity (psu)
35
34.8
34.6
34.4
34.2
34
33.8
33.6
33.4
33.2
33

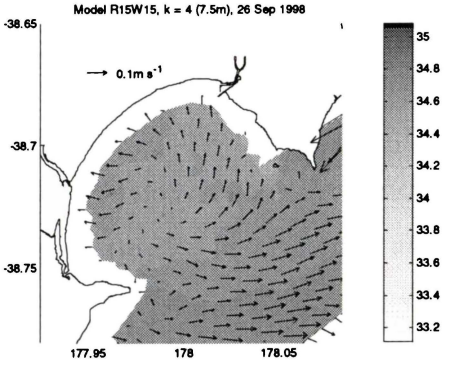
Model R15W15, k = 4 (7.5m), 26 Sep 1998
0.1m s-1
-38.65
-38.7
-38.75
177.95
178
178.05
35
34.8
34.6
34.4
34.2
34
33.8
33.6
33.4
33.2

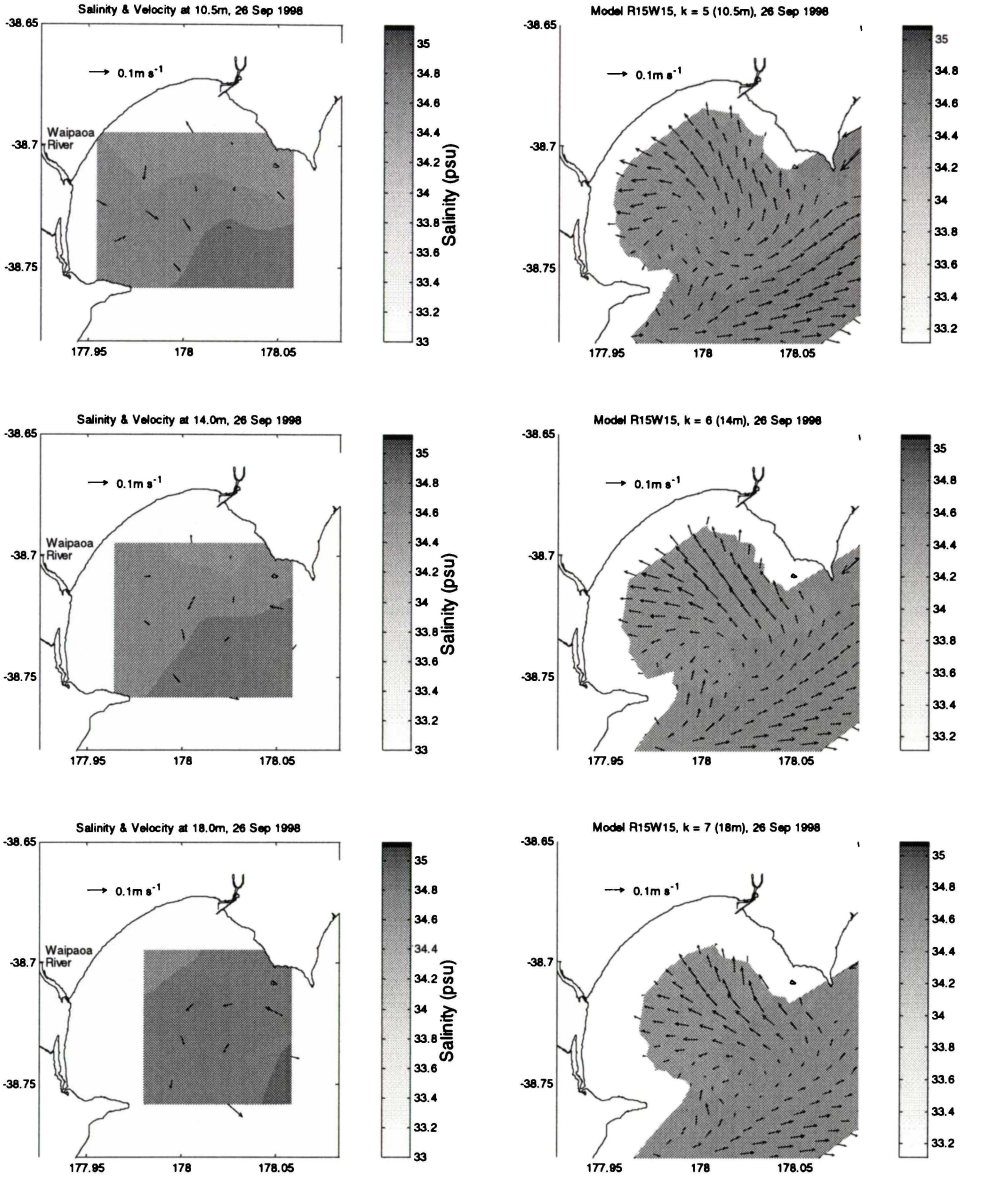

Figure 7-15. Measured data on 26th September 1998, compared with model output from the calibration simulation averaged over the time corresponding to the survey. Velocity vectors were measured using bottom-mounted ADP; therefore data are only available within the instruments 15 m range from the seabed.

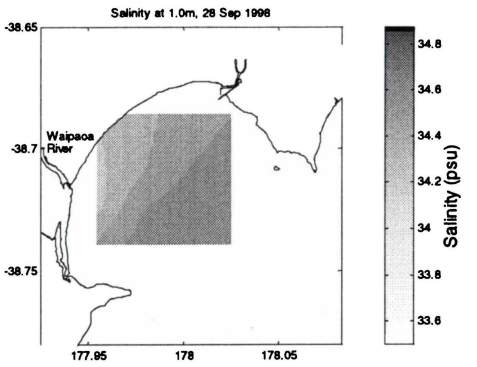
Salinity at 1.0m, 28 Sep 1998
-38.65
-38.7
-38.75
Waipaoa River
177.95
178
178.05
Salinity (psu)
34.8
34.6
34.4
34.2
34
33.8
33.6

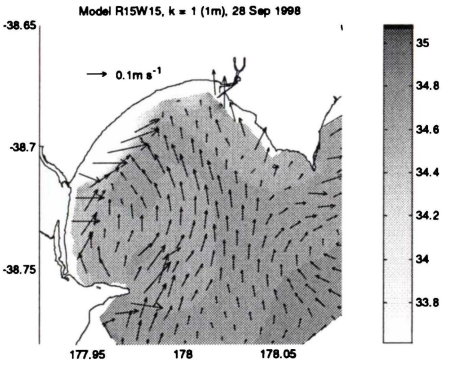
Model R15W15, k = 1 (1m), 28 Sep 1998
0.1m s-1
-38.65
-38.7
-38.75
177.95
178
178.05
35
34.8
34.6
34.4
34.2
34
33.8

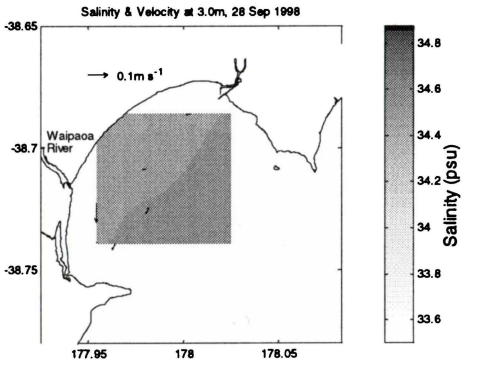
Salinity & Velocity at 3.0m, 28 Sep 1998
0.1m s-1
Waipaoa River
-38.65
-38.7
-38.75
177.95
178
178.05
Salinity (psu)
34.8
34.6
34.4
34.2
34
33.8
33.6

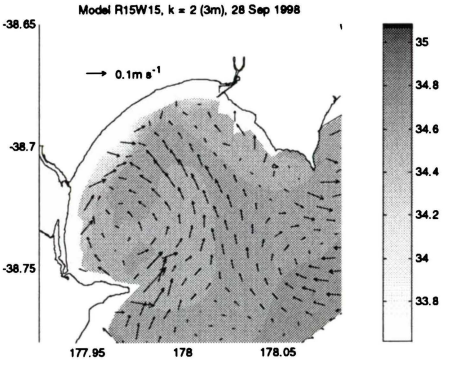
Model R15W15, k = 2 (3m), 28 Sep 1998
0.1m s-1
-38.65
-38.7
-38.75
177.95
178
178.05
35
34.8
34.6
34.4
34.2
34
33.8

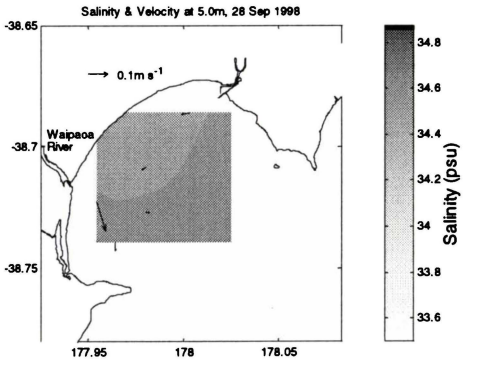
Salinity & Velocity at 5.0m, 28 Sep 1998
0.1m s-1
Waipaoa River
-38.65
-38.7
-38.75
177.95
178
178.05
Salinity (psu)
34.8
34.6
34.4
34.2
34
33.8
33.6

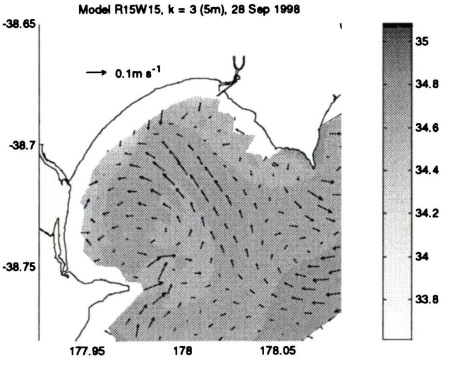
Model R15W15, k = 3 (5m), 28 Sep 1998
0.1m s-1
-38.65
-38.7
-38.75
177.95
178
178.05
35
34.8
34.6
34.4
34.2
34
33.8

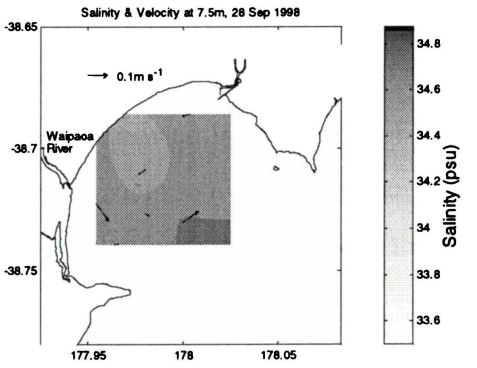
Salinity & Velocity at 7.5m, 28 Sep 1998
0.1m s-1
Waipaoa River
-38.65
-38.7
-38.75
177.95
178
178.05
Salinity (psu)
34.8
34.6
34.4
34.2
34
33.8
33.6

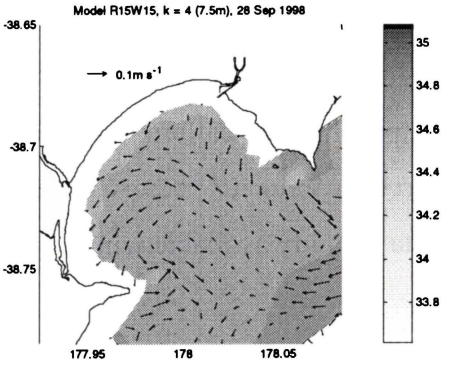
Model R15W15, k = 4 (7.5m), 28 Sep 1998
0.1m s-1
-38.65
-38.7
-38.75
177.95
178
178.05
35
34.8
34.6
34.4
34.2
34
33.8

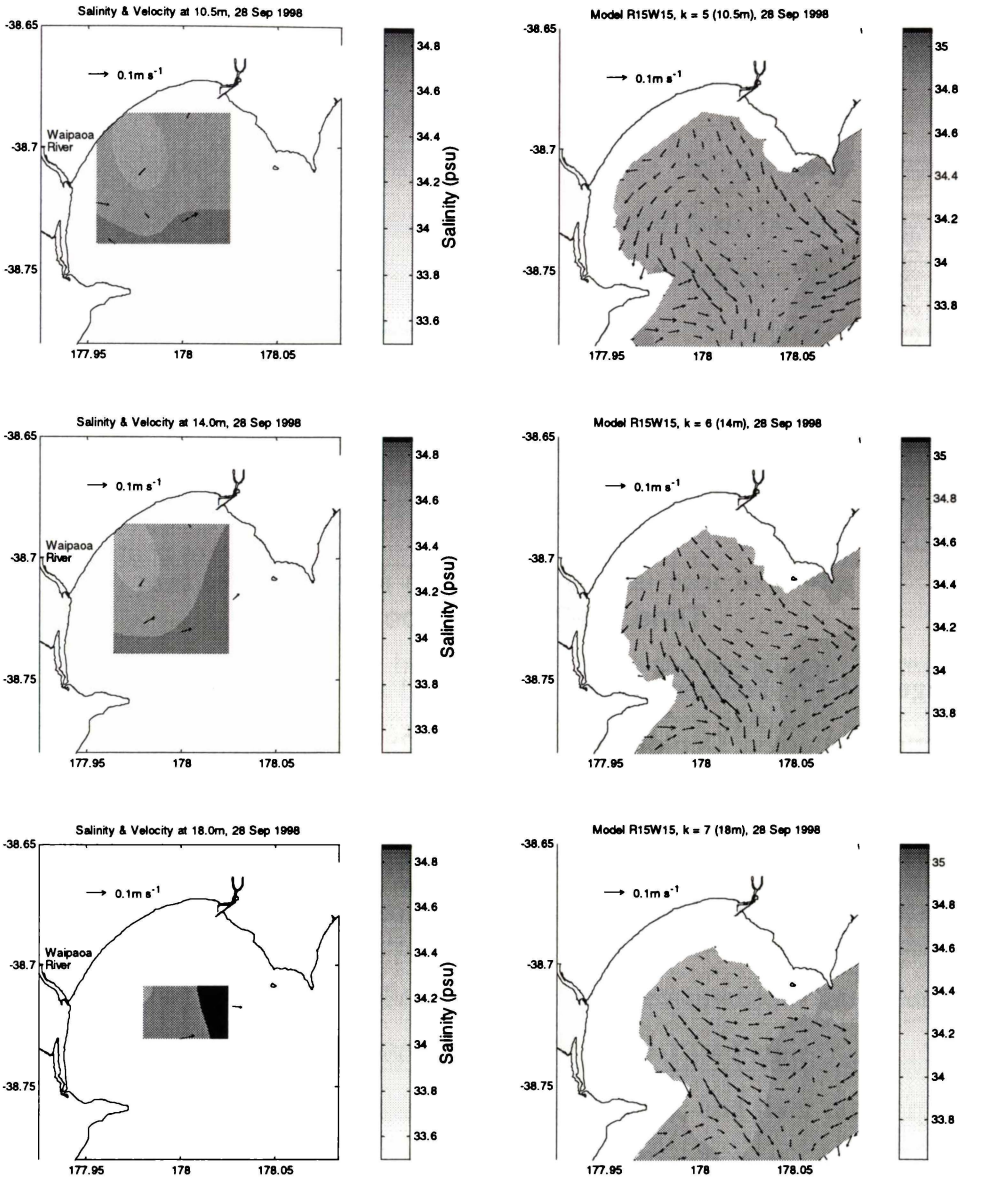

Figure 7-16. Measured data on 28th September 1998, compared with model output from the calibration simulation averaged over the time corresponding to the survey. Velocity vectors were measured using bottom-mounted ADP; therefore data are only available within the instruments 15 m range from the seabed.

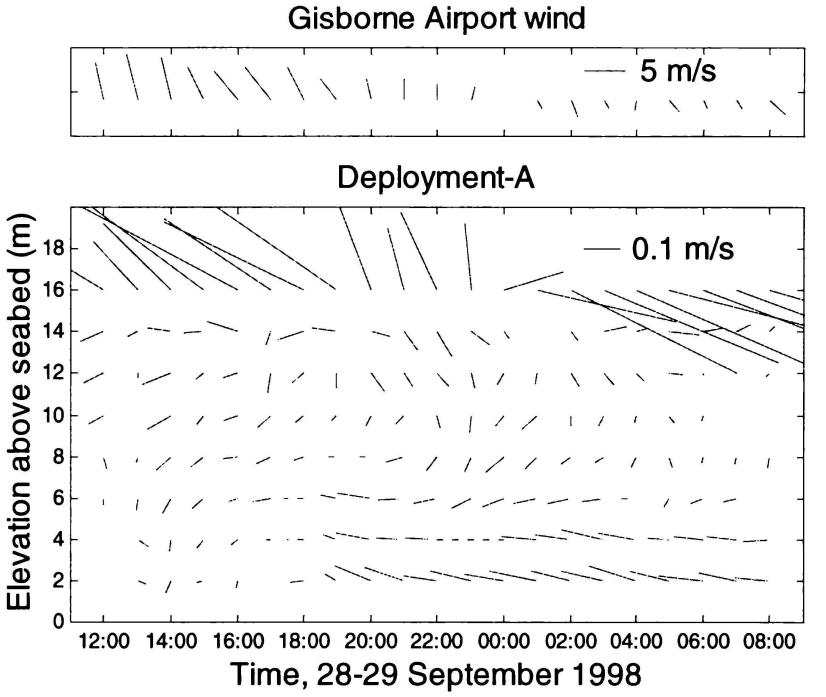

Figure 7-17. Feather plots of hourly wind and current, over the duration of ADP bottom-mounted Deployment-A, 12:00, 28 September – 08:00, 29 September, 1998. Wind velocities have been inverted to true vectors convention. Speed values at 16 m elevation are unreliable due to acoustic interference with the water surface, but nonetheless are in close directional agreement with wind.

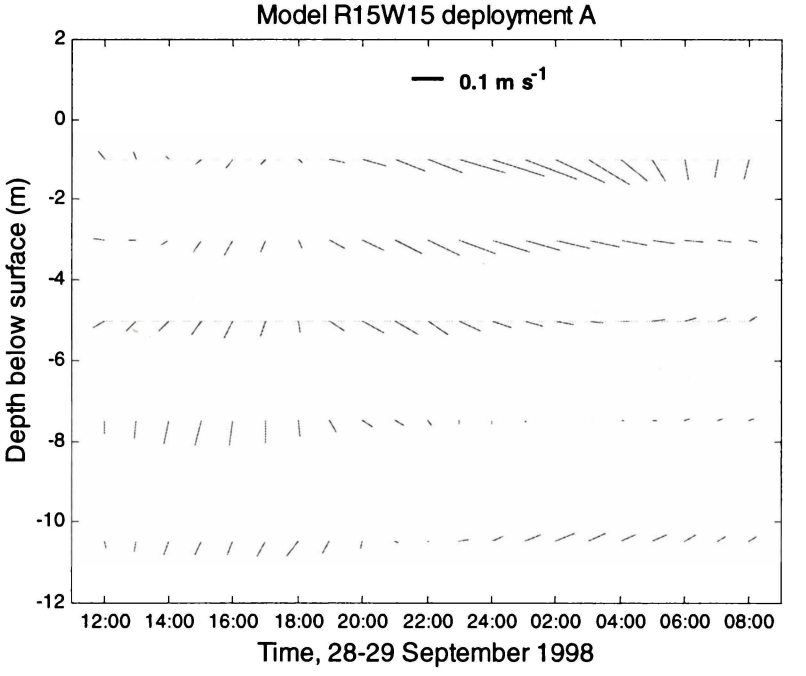

Figure 7-18. Model predicted currents at the ADP deployment A site 12:00, 28 September – 08:00, 29 September, 1998.

7.3.2 Body-force only

Following calibration, the model was successfully combining shelf-current (through the body-force), wind and river discharge to reproduce circulation in Poverty Bay. The model can then be used to isolate these three forcing components to determine the peculiarities and relative importance of each to circulation in the bay. The first component examined was the shelf-current, represented by the body-force. The body-force was calculated using depth-averaged equations (Appendix 3), using the near-average continental-shelf depth of 30 m. Therefore, although the body-force acceleration was applied universally to the model grid, its effect is small in shallow areas of the shelf and bay due to high frictional damping, and it mainly affects currents on the continental-shelf, which it is designed to represent.

A simulation was run using just the body-force to drive the model and the results show that although shelf-currents are significant at the bay entrance, they drive only minor currents inside the bay (Figure 7-19). The maximum shelf-current speed occurred on 18th September, reaching 0.25 m s^{-1} (Figure 7-3). This drives currents in the bay entrance of 0.1 m s^{-1}, but in the inner bay at depths <18 m, speeds are $\leq$0.02 m s^{-1} (Figure 7-19). Shelf-currents are clearly insignificant in forcing the inner bay, since the calibrated model and measurements show current speeds well above 0.02 m s^{-1} in depths <18 m (Figure 7-12 - Figure 7-18). This supports the findings of Chapter 4 that showed wind stress and river discharge to be of primary importance to Poverty Bay circulation. However, the shelf-current does influence circulation in the deep outer bay and this is observed on 17th September where the shelf-current-induced flow is offshore past Tuaheni Point (Figure 7-19). The shelf-current is not well predicted on 17th September (Figure 7-3) and it was observed that this outer bay flow disrupted predictions in the mid and upper water column (Figure 7-13). The shelf-current was observed to have a significant influence in the outer bay when speeds were approximately greater than 0.1 m s^{-1}, this being about 25% of the time. Due to directional dependence (i.e. a shelf-current flowing into the bay has more effect than one flowing past the entrance), this was reduced to around 15%, although the reverse was true on occasions. Thus the shelf-current can influence Poverty Bay circulation at times, but it is generally insignificant.

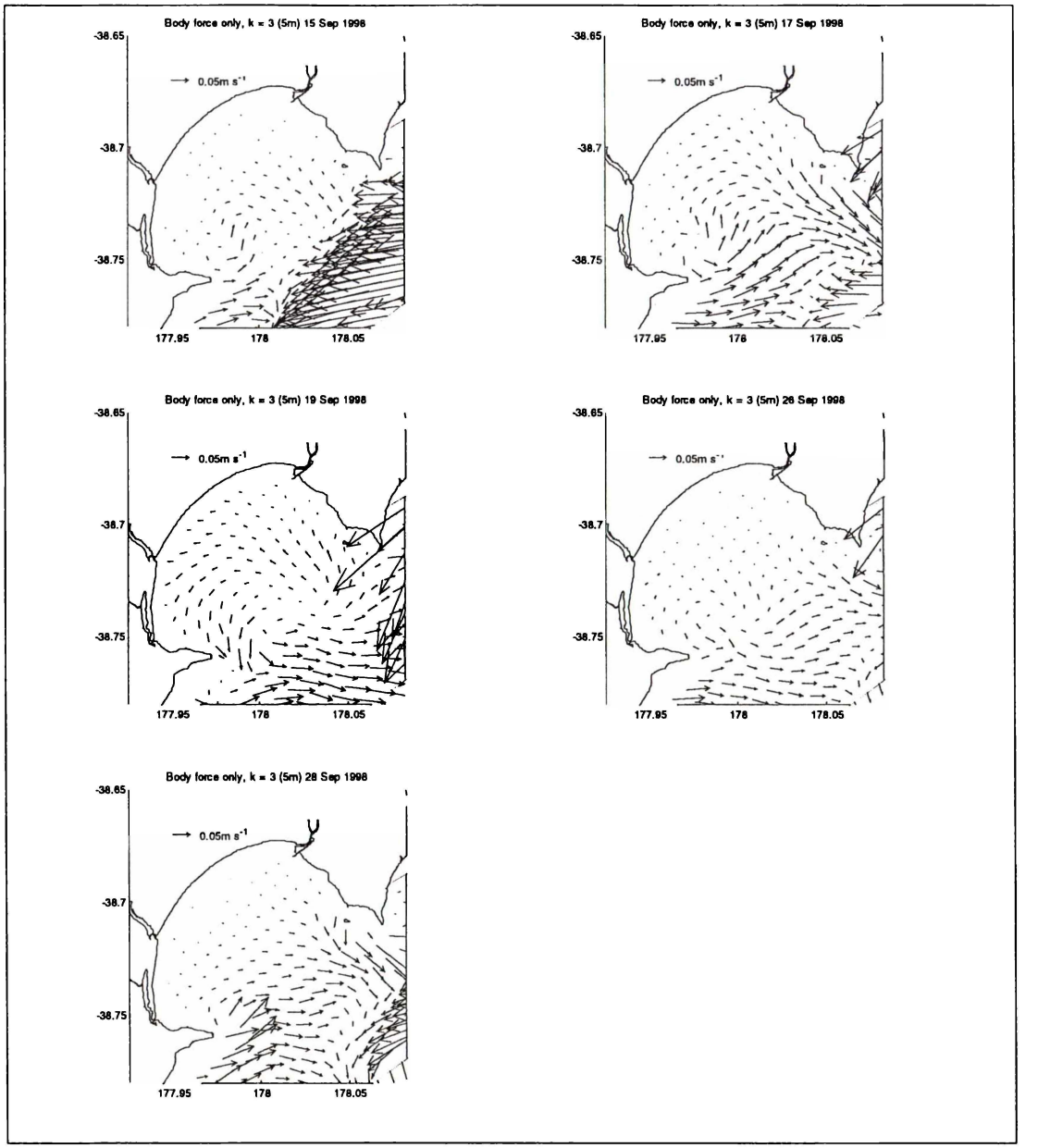

Figure 7-19. Model output in layer 3 (4-6 m) at times coinciding with data surveys, using only the body-force as input. Since the body-force acceleration is applied uniformly to all vertical layers in the model, circulation in other layers is very close to that shown for layer 3.

7.3.3 No shelf-current

The simulation using only the body-force to drive the model showed that the shelf-current has little impact on circulation in Poverty Bay. Therefore a simulation was run including both wind stress and river discharge, but not including the body-force (i.e. not including shelf-currents). Sea-level was clamped to zero at the open boundaries. On comparing the simulation with the

calibration model run, it was observed that both velocity and salinity patterns were very similar, confirming that the combined influence of wind and river discharge were dominating circulation. There were some differences; on occasions the velocity patterns were closer to those measured while sometimes they were slightly worse. For example, on 17th September, the removal of the erroneous shelf-current influence allowed the river/wind combination to develop anticyclonic circulation as measured, although current speeds suffered the general problem of being under-predicted (Figure 7-20). However, there were occasions where removal of the shelf-current decreased simulation accuracy (Figure 7-21), although the general circulation patterns were still reasonably close.

The results of this section and the one above show that the combined influence of wind stress and river discharge dominates circulation in Poverty Bay, and that future numerical simulations could be undertaken to a reasonable degree of accuracy without requiring continental-shelf-current data.

These results also concur with the findings of Chapter 4, when no relationship was found between shelf-currents and circulation in Poverty Bay, but disagree with the results of Chapter 1, whose hydrodynamic conclusions were largely based on simulations by Black et al. (1997). Simulations by Black et al. (1997) were limited by the absence of water level and current data on the continental-shelf, against which to calibrate the model. Consequently shelf-current speeds were over-predicted and had a much greater influence on circulation in outer Poverty Bay than the field surveys (Chapter 4) and present simulations have shown to exist.

Figure 7-22 presents output from two simulations set up similarly to the calibration run, but using the measured depth-averaged alongshore current to drive shelf-currents from the western shelf boundary as a velocity boundary, instead of using the body-force. In the second simulation (right-hand plots in Figure 7-22) the shelf-current velocities were multiplied by 5 times, to increase them toward speeds predicted by Black et al. (1997), often over 1 m s^{-1}. Fast shelf-currents disturb currents in outer Poverty Bay, particularly where eddies form adjacent to the headlands, and these are sources of error in the simulations. Notably however,

current patterns in the inner bay (depths < ~18 m) remained largely undisturbed by the fast shelf-currents, although speeds were raised inside the bay in general through transfer of momentum from the intruding shelf-currents. This is further evidence that shelf-currents are generally of little consequence to the hydrodynamics of the bay. It also lends credibility to the previous simulations by Black et al. (1997) that predicted the general circulation patterns well despite fast shelf-currents. The zone of most variability between the two simulations is that around the 20 m depth contour where the level of shelf-current influence varies the most. This explains why Black et al. (1997) obtained poor directional calibration against a current-meter deployed in this zone.

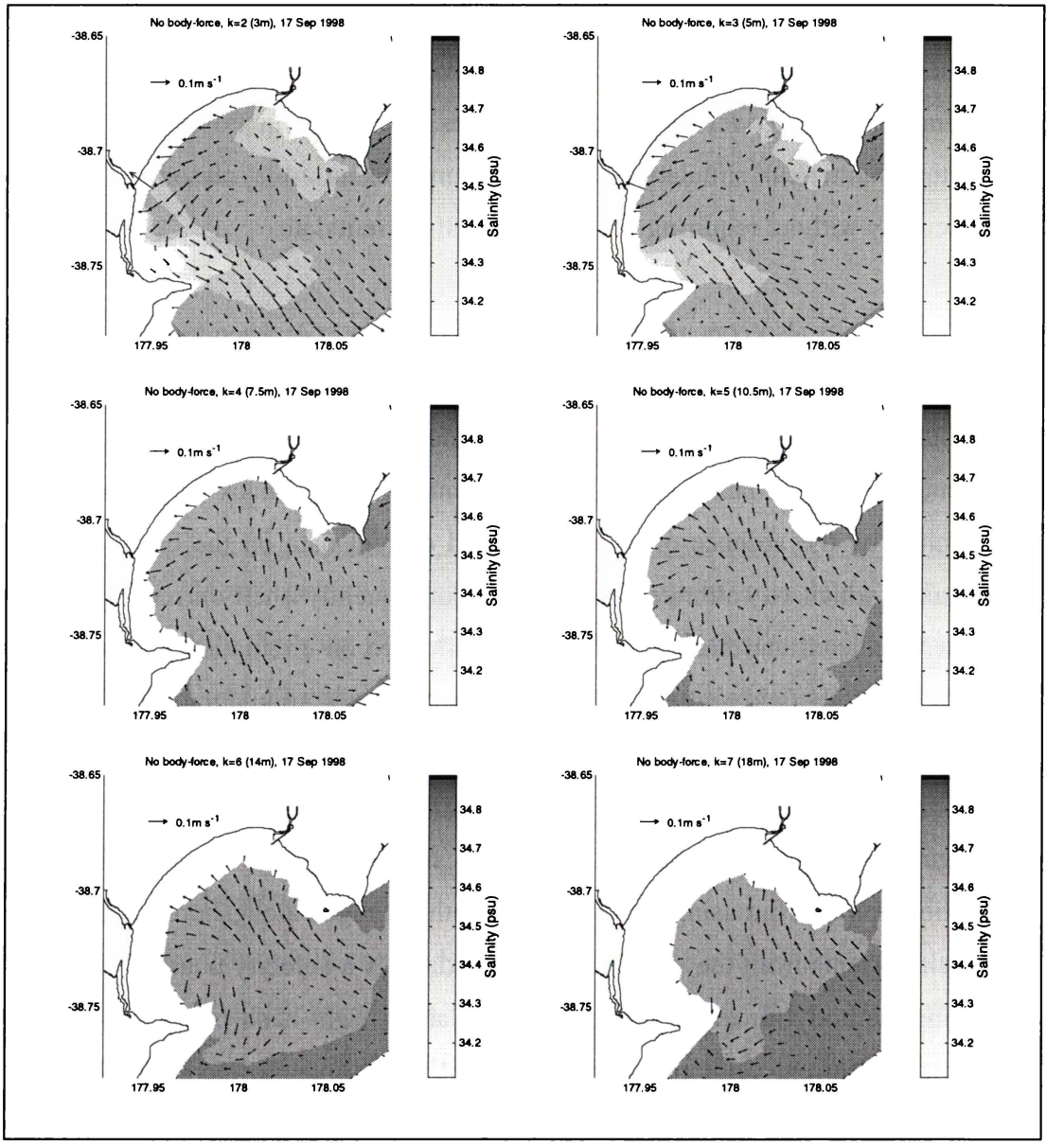

Figure 7-20. Model output coincident with the 17th September field survey, using wind and river discharge to force the model, and no body-force.

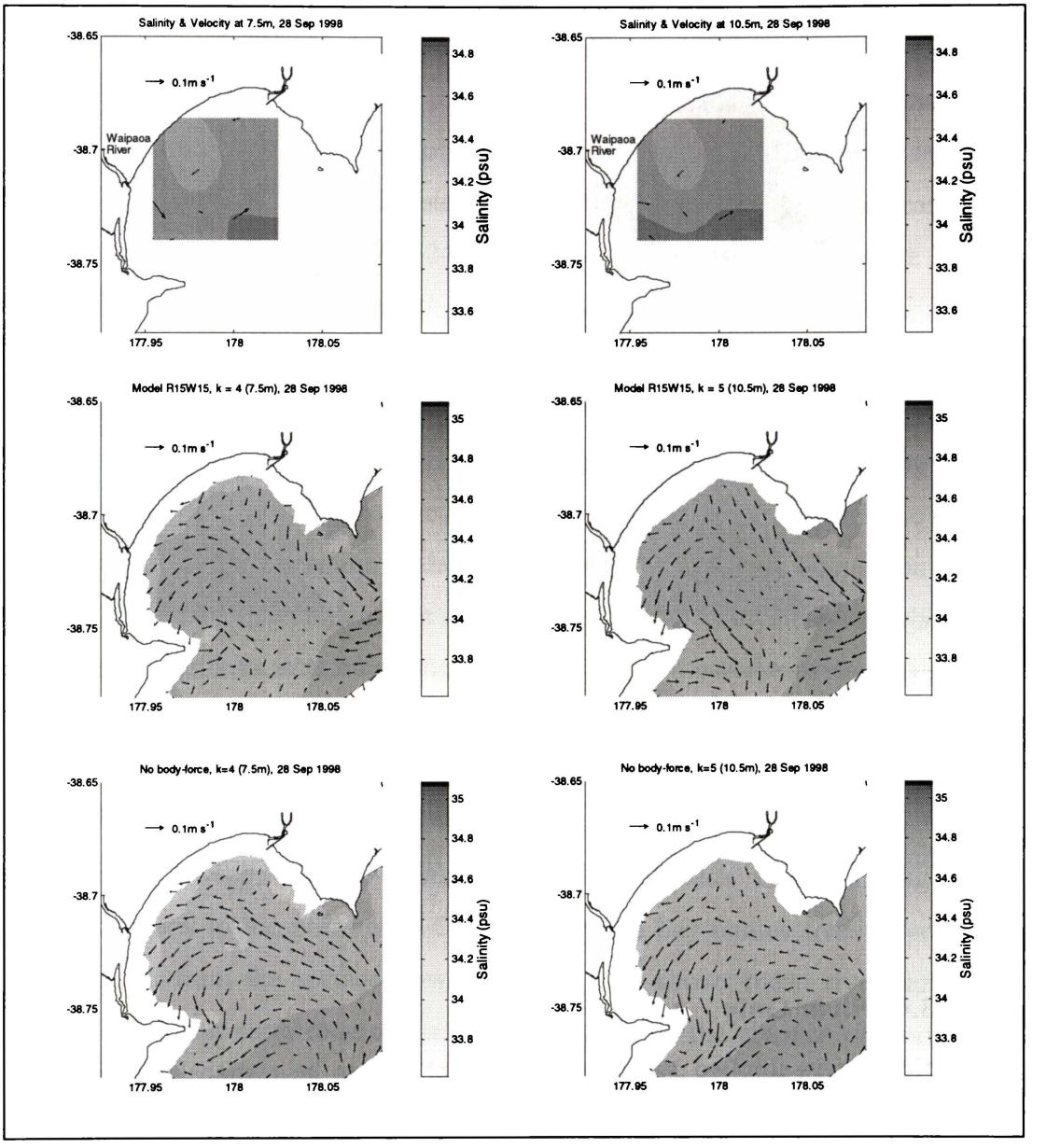

Figure 7-21. Comparison between measured data (top), the calibration simulation (middle) and simulation using only wind and river discharge as boundary conditions (bottom) at 6-9 m depth (left) and 9-12 m depth (right), 28th September 1998.

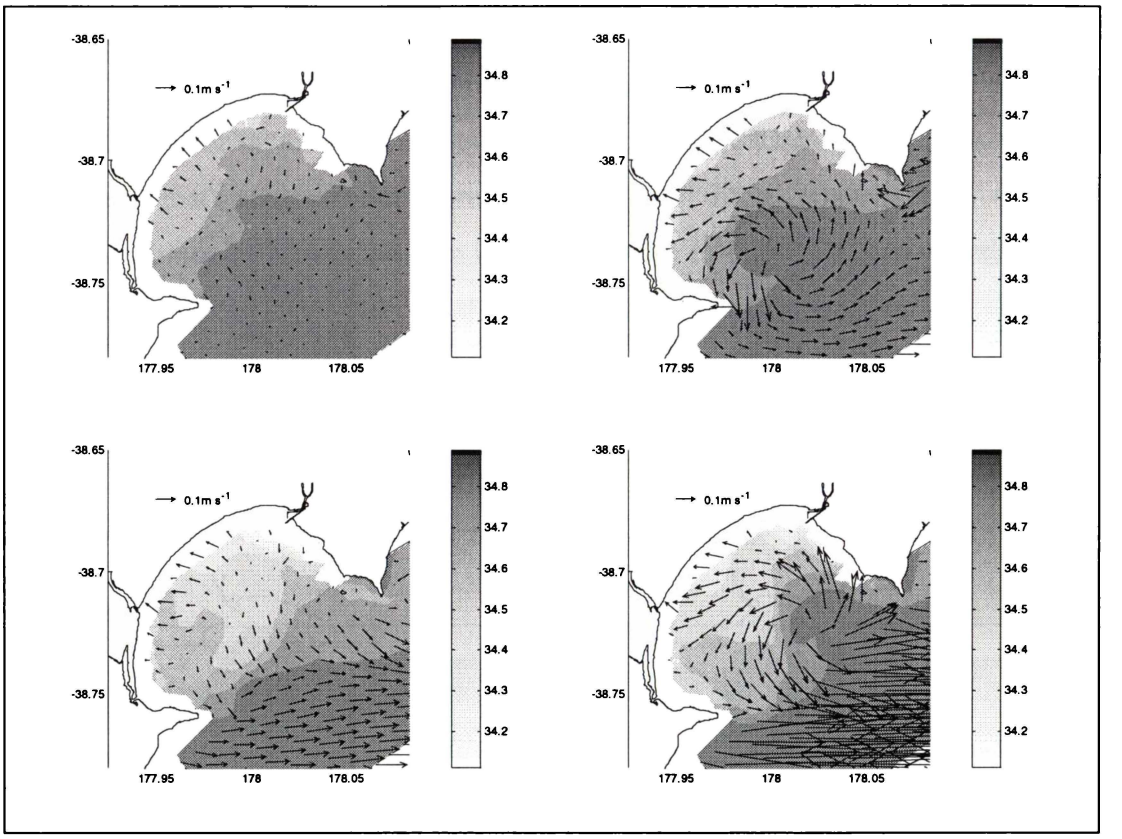

Figure 7-22. Model output using a shelf-current velocity boundary in place of the body-force. Plots on the left use measured shelf-current, while plots on the right use shelf-current multiplied by 5. Upper plots correspond to 59-hours and lower plots to 206-hours. Right-hand plots show that fast shelf-currents induce eddies.

7.3.4 River Only

Field surveys implied Waipaoa River discharge to be responsible for the long-term forcing of the prevailing anticyclonic circulation in Poverty Bay (Chapter 4). The numerical model allows the isolation of river forcing, by including river discharge as the only boundary condition. This section compares model simulation results with the field study findings of Chapter 4. The model results presented in the following two paragraphs show that Coriolis is an important control on plume dynamics, causing the plume to rotate. This is at odds with Chapter 4, and highlights aspects of the model grid size used, and of the numerical diffusion scheme, which prevent accurate simulation of plume dynamics. It is demonstrated later that wind stress drives most of the bay hydrodynamics, and the river inputs are more important for their role in stratifying the bay.

Figure 7-23 shows model output coincident with the 17th September field survey. The buoyant Waipaoa River discharge drives surface currents offshore past Young Nicks Head in the south. Simultaneously, Coriolis acts to rotate the plume toward the left, initiating anticyclonic circulation. Momentum from the surface layer is transferred down through the water column, mixing fresh and marine water. This initiates anticyclonic flow throughout the bay at all depths and serves to draw saline continental-shelf water into the bay along the deep northeastern side. It can be seen from Figure 7-24 that this pattern persists for the entire field survey period and in fact it occurs for the entire simulation.

These results show that river discharge drives anticyclonic circulation in Poverty Bay even in times of low flow and this supports Chapter 4 in suggesting that Waipaoa River discharge is likely responsible for the long-term anticyclonic gyre in Poverty Bay. To determine if the river-induced anticyclonic circulation was purely a function of hydrodynamic interaction with the bathymetry or whether earth rotational effects were more important, a simulation was run using only river discharge to force the model and with latitude set to zero to negate the Coriolis force. Figure 7-25 shows the mean river-induced circulation over the simulation, with rotational effects included. A mean anticyclonic circulation exists and this has acted to sweep offshore-flowing plume water back inshore along the northeastern bay to the port area. Consequently the bay retains freshwater and this is mixed from the surface down. Figure 7-26 shows mean river-induced circulation without earth rotational effects included. In the absence of Coriolis, the mean trend is for surface water to flow straight offshore, inducing a bottom-return-flow directly onshore in layers 3-down, i.e. below 4 m depth. The anticyclonic circulation is absent and mean currents below the surface layer are very weak, because the surface plume that forces the bay is heading straight over the top to sea and is mixing very little, as shown by the mean salinity patterns.

This shows that earth rotational effects are important to Poverty Bay circulation, acting to turn the Waipaoa River plume counter-clockwise and initiate anticyclonic circulation. However, in Chapter 4 under plume-driven circulation, it was calculated that the Waipaoa River plume has a low Kelvin number and therefore should exhibit *non-rotational* behaviour (Garvine, 1987). Increasing

plume depth was measured toward the frontal boundary providing further evidence that the Waipaoa River plume is non-rotational (Chapter 4). Non-rotational plumes have strong boundary fronts and concentrate their greatest layer depth and mass transport near the front, whereas rotating plumes have boundary fronts that weaken soon after discharge in a turning region, where Coriolis deflects the plume toward shore forming a coastal current (Garvine, 1987). The simulated plume weakens with distance from the river and rotates under Coriolis to flow back into the bay along the northeastern (port) side, showing rotating plume behaviour that is clearly at odds with the findings of Chapter 4. There are two inadequacies in the model that explain this occurrence. The first is that the (Eulerian) advection/dispersion scheme exhibits some numerical diffusion, which prevents formation of a sharp plume boundary such as exhibited by non-rotational plumes. The second is that the 400 m model grid is too coarse to accurately represent the river width at its confluence with the bay. The width of the river mouth w is one of two length scales that strongly influence plume structure, the other being the internal Rossby radius r_0 (Garvine, 1987). Furthermore, using a wide river mouth reduces the simulated river flow velocity as it enters the bay, affecting r_o and thus the Kelvin number $K = w/r_0$ is raised from $<<1$ to ~1 for the simulations. As mentioned in Chapter 4 and Garvine (1987), rotating plumes can be expected if $K \approx 1$ and non-rotating plumes if $K << 0$. The model predictions therefore make dynamical sense when the simulated river width is taken into account.

To accurately simulate river width would have required a horizontal grid scale of ~20 m that would have been hugely computationally expensive and not possible given the large number of simulations undertaken. The relative success of the model calibration suggests that accurate representation of plume rotational characteristics is in any case not essential to the simulations. It is intuitively obvious from the unchanging river-forced circulation and demonstrated lack of shelf-current influence that the wind must provide most hydrodynamic variability in Poverty Bay, and this is shown below to be the case. Instead the strength of the surface freshwater discharge and its role in stratifying the bay are important.

It is interesting to compare model predictions of river-induced circulation with those calculated from field surveys in Chapter 4. The calibration simulation showed that during the 17th September survey, the mean volume of water inside the bay having salinity < 34.5 psu (plume water) was 5.3×10^7 m^3, which compares closely to 5.6×10^7 m^3 calculated in Chapter 4. In Chapter 4 the Waipaoa River plume was calculated to have increased its volume 24 times by entrainment of seawater on 17th September 1998, but this was based on gauging data without making allowance for the approximately 15-hour flow delay between the gauging station and the bay, or the multiplication factor of 1.5 used for model calibration. Since mean discharge over the same period used for Chapter 4 calculations was ~17 m^3 s^{-1} and not 66 m^3 s^{-1} as used, the plume had in fact entrained around 100 times its original volume. Both the calculations of Chapter 4 and the simulations in this chapter show that the river plume on 17th September occupied over 5% of the total bay volume. On the 19th September following the quickflow event, the calibration simulation showed 29% of the bay was mixed with plume water. Both the field survey and simulations show that the river plume mixes with a significant proportion of the total bay volume and therefore has considerable potential to drive circulation. The relative importance of river-induced circulation compared with wind-induced circulation is addressed later.

In Chapter 4 a density-driven plume dispersion stress was calculated and equated to an equivalent wind stress, by the method of Visser (1996). This calculation accounted for density-driven dispersion (baroclinic pressure gradients) but pressure gradients created by the seaward sloping of the plume water surface (barotropic pressure gradients) were not accounted for, because sea-level gradients were not measured in the field. Model output includes both sea-levels and densities, allowing barotropic and baroclinic pressure gradients to be compared. The results indicate that the dominant parameter driving plume dispersion is the barotropic pressure gradient. For example, on 19th September 1998 during the final stages of a Waipaoa River quickflow event (Figure 7-5), the barotropic pressure gradient from the river mouth (cell *I* 9, *J* 33) to outside the plume (cell *I* 9, *J* 22) was 0.761 N m^{-3}, while the baroclinic pressure gradient was 0.054 N m^{-3} in the surface layer over the same distance. The maximum baroclinic pressure gradient in layer 2 was approximately 0.004 N m^{-3}.

Similar results throughout the calibration simulation show that the seaward sloping of the plume water surface is more important to plume spreading than the self-induced shear created by density gradients within the water column. This opposes the suggestion made in Chapter 4 that density-driven dispersion was likely to dominate, based on a calculated density-gradient-induced stress equivalent to a 7 m s^{-1} wind-induced stress. However, it is shown below in section 8.3.8 that the density-gradient-induced stress calculated in Chapter 4 was over-predicted, and hence the erroneous suggestion.

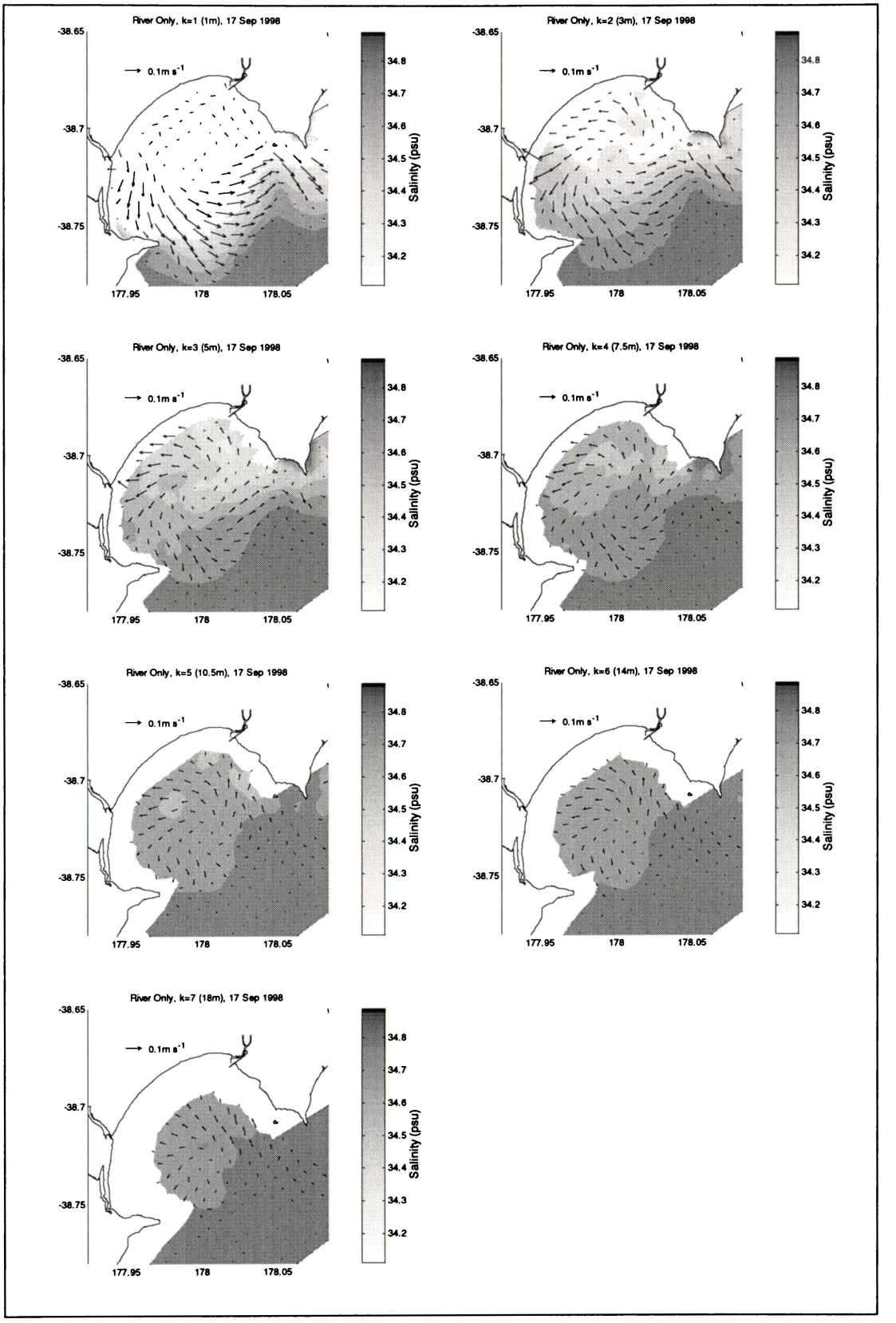

Figure 7-23. Model output coincident with the 17th September field survey, with Waipaoa and Turanganui River discharge the only boundary condition.

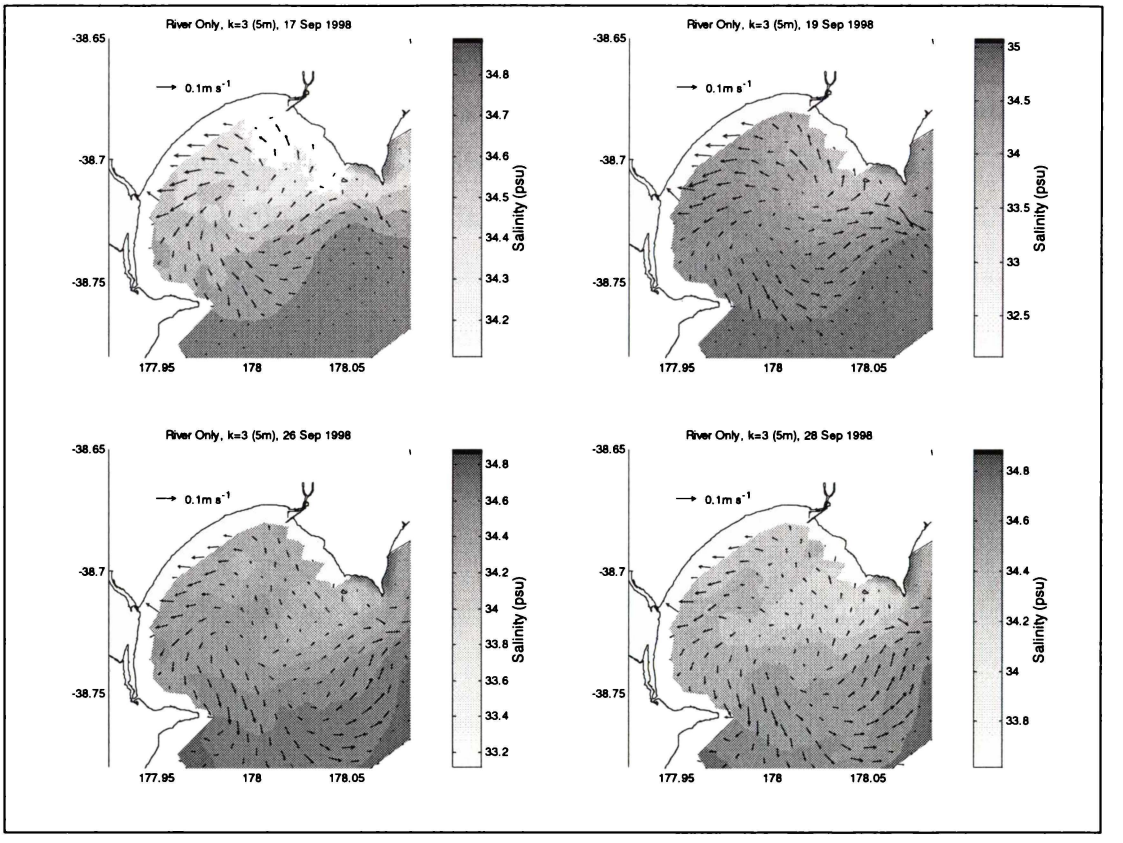

Figure 7-24. Model output in layer k = 3 (4-6 m depth) at times coincident with field survey data, with Waipaoa and Turanganui River discharge the only boundary condition.

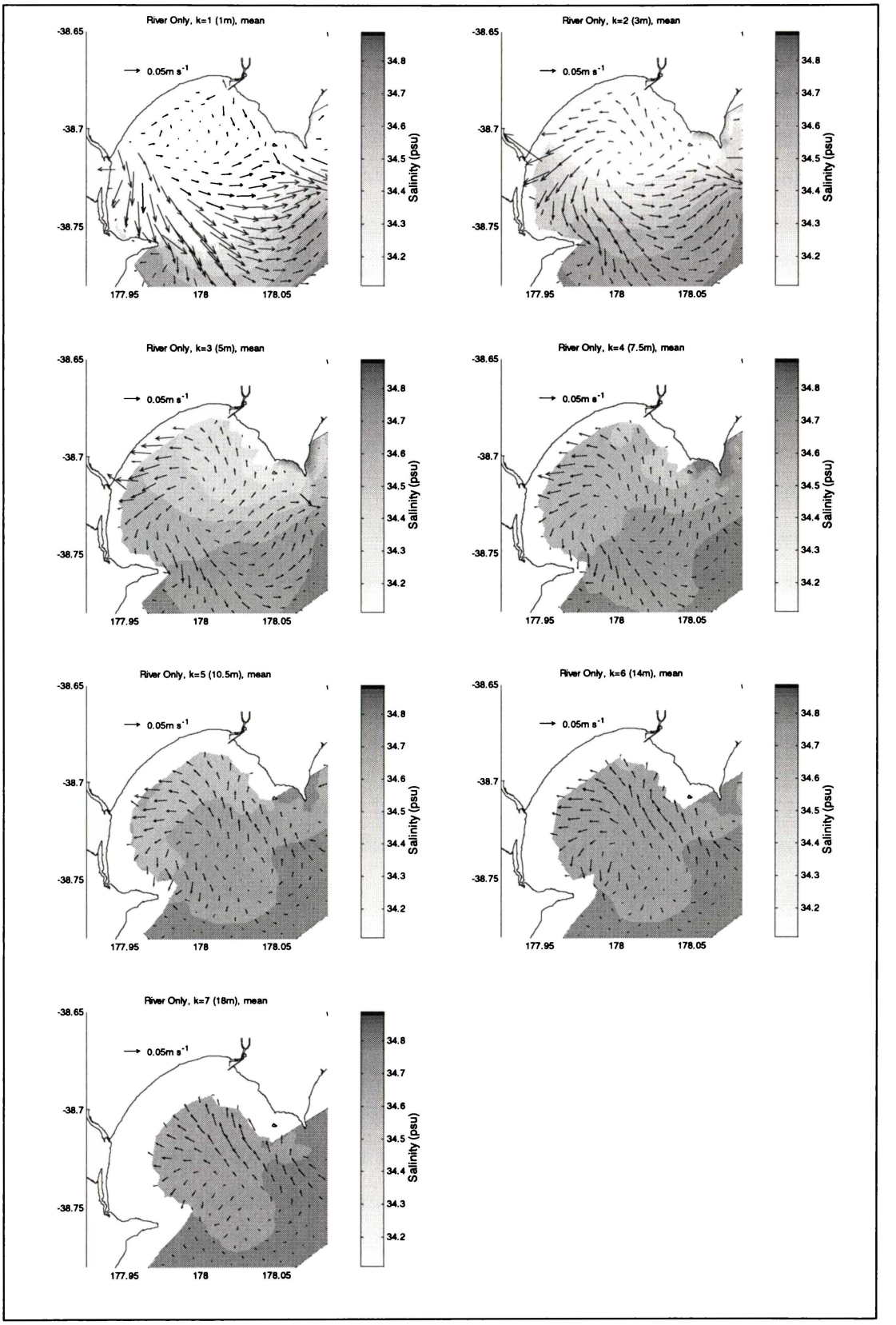

Figure 7-25. Mean river-induced circulation over the simulation period.

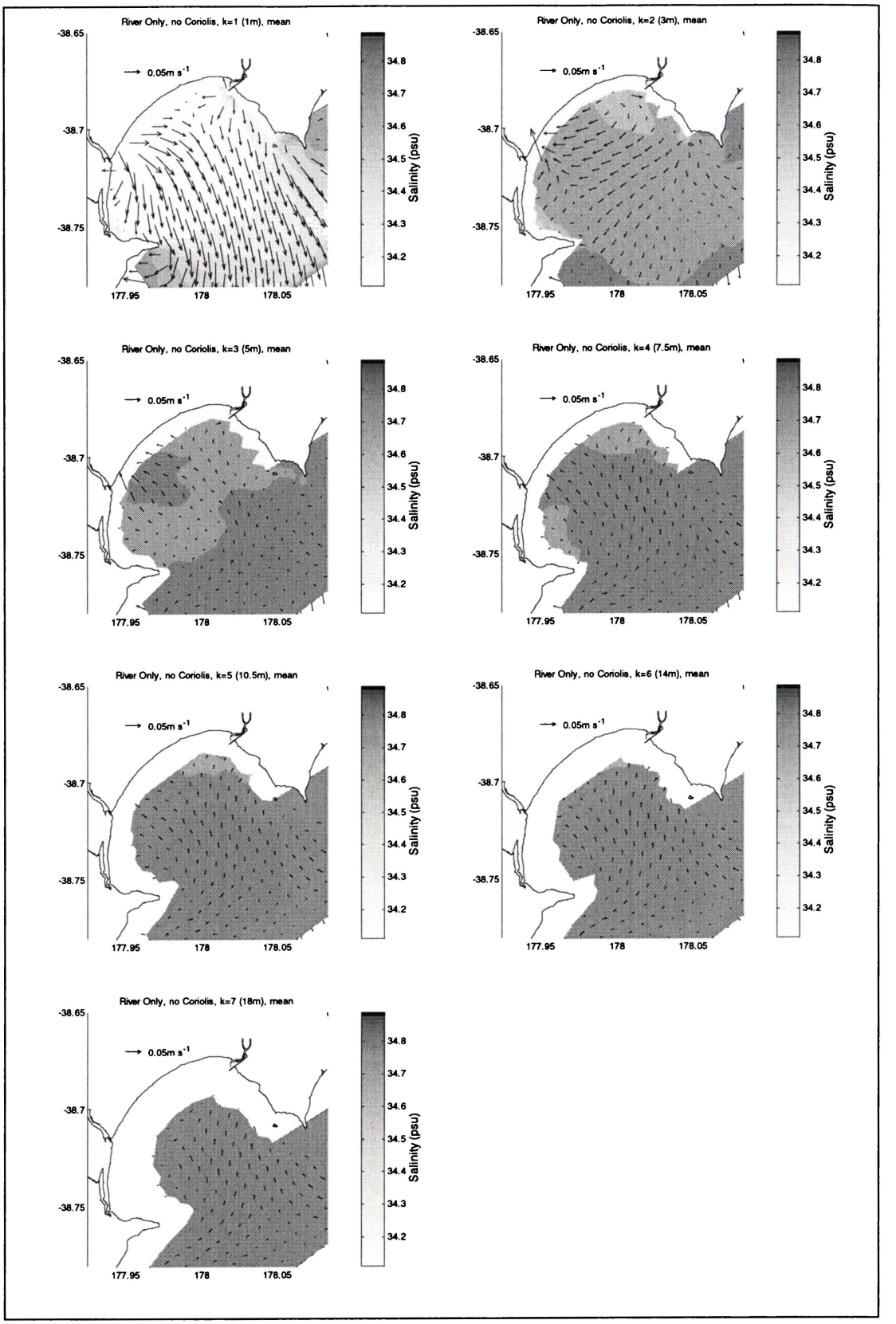

Figure 7-26. Mean river-induced circulation over the simulation period, with rotation effects not included.

7.3.5 Wind Only

Surface wind stress is an important forcing mechanism in Poverty Bay, so to isolate its effect on circulation a simulation was run using only wind stress to force the model. When compared to the simulation including both wind and river discharge there are two significant results, the first being that circulation patterns are similar both with and without river discharge included. The second significant result is that currents speeds are considerably slower in the absence of stratification, throughout the water column.

In all but negligible winds (< 2 m s^{-1} at Gisborne Airport), circulation patterns are similar both with and without river discharge, indicating that the wind dominates current direction and therefore the circulation pattern (eg. compare plots A & B, Figure 7-27). In offshore wind situations, anticyclonic circulation is present (Figure 7-12) but this is disturbed during onshore winds, with the near-surface currents in particular being swept onshore (Figure 7-27). Since offshore winds predominate in Poverty Bay, the mean wind-induced circulation is an anticyclonic gyre, as seen in the mean current record (Figure 7-28). Therefore the commonly observed anticyclonic gyre in Poverty Bay is a favoured by both Waipaoa River discharge and the mean wind stress.

Unlike river-induced flows where the surface layer is driven from a point source and is thereafter free to rotate under the Coriolis force, surface wind-driven flows remain coupled to the wind direction. Even on removal of Coriolis from the simulations, net anticyclonic circulation is still observed, forced by the predominantly offshore wind stress (Figure 7-29). This occurs because the prevailing offshore winds blow from slightly north of northwest (Chapter 4, Figure 4-2), which is not directly through the cross-shore axis of Poverty Bay, but more from the port to Young Nicks Head. This tends to create stronger seaward currents along the shallow southwest coast, forcing more water out past Young Nicks Head than past Tuaheni Point. Additionally, shoreward-directed bottom-return-flows tend to move onshore in the north-eastern half of the bay to replace water pushed offshore at the surface. It is shown in the discussion chapter (Chapter 8) that wind-driven bottom-return-flows favour deeper water in an

embayment, and since Poverty Bay is deeper in its north-eastern half, this is the preferred channel for these phenomena.

Although circulation patterns in Poverty Bay are dominated by wind stress, current speeds are reduced to unrealistic values in the absence of stratification (Figure 7-27). This occurs because stratification inhibits vertical mixing between layers and facilitates vertical shear in the water column. In a stratified water column, turbulent eddies must overcome a buoyancy gradient in order to vertically mix parcels of water (Dera, 1992). Therefore vertical mixing is reduced, so that momentum transferred to the water surface by wind stress remains concentrated in a narrow surface layer, and thus the surface layer develops faster horizontal velocities. The reduced vertical turbulent mixing between layers, is analogous to reduced turbulent friction at the seabed, and can be conceptualised as reducing friction between layers. This explains why the wind is ineffective in forcing Poverty Bay without river discharge included and shows that stratification-induced vertical shear is an important process in Poverty Bay.

In central Poverty Bay (model grid cell I = 16, J = 26, Figure 7-2) current speeds in the surface layer had a mean of 0.6% of the wind speed and a maximum of 1.3% of the wind speed, when the model was forced by wind stress only. This is slower than the 1-2% typically experienced in shallow coastal situations (Prandle and Matthews, 1990). In the simulation forced by both wind stress and river discharge, surface-layer currents had a mean of 1.8% and maximum of 6.7% of the wind speed, more in line with expected values. Again this indicates that stratification aids wind-driven currents, and that the two processes act in unison to control Poverty Bay hydrodynamics.

During the simulation period, stratification was provided by river discharge, but there are times during summer when high solar radiation levels temperature-stratify the water column. CTD measurements taken in February show evidence for thermal heating of surface water during daylight hours (Chapter 3, Figure 3-5 & Figure 3-6). However, as shown in Appendix 1, salinity still dominates stratification. A salinity-only model was chosen for the present simulations to

simplify simulations and because the field surveys providing calibration data showed no evidence for significant thermal stratification. Nevertheless, since correct representation of stratification is important, summer simulations of Poverty Bay would best use a model that accounts for both temperature and salinity, to account for temperature-stratification.

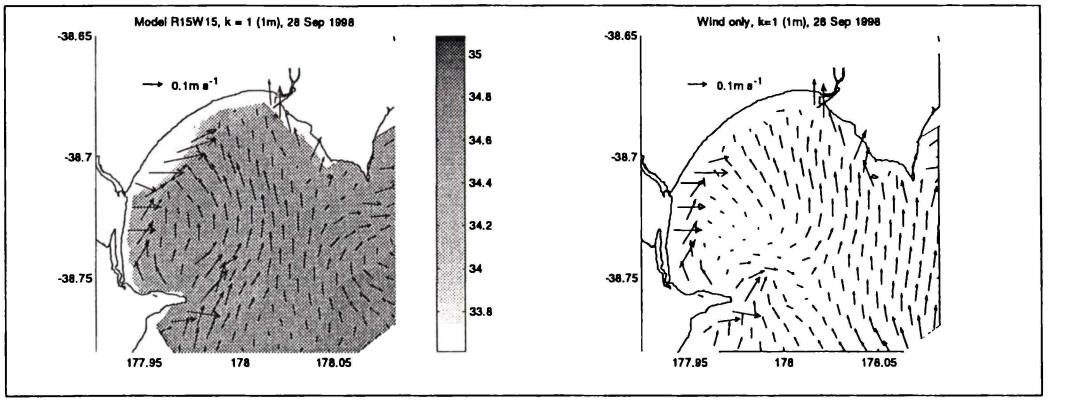

Figure 7-27. Circulation in layer 1 (near-surface) coincident with the 28th September field survey: A) calibration simulation, B) model is forced by wind only. Note that surface velocities are reduced in B.

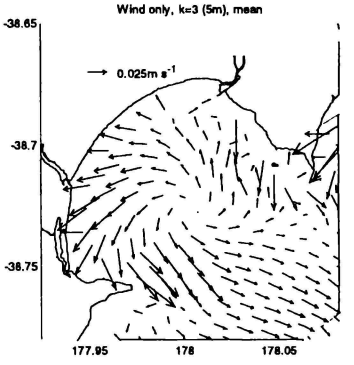

Figure 7-28. Mean wind-induced circulation in model layer 3 (4-6 m), the simulation includes wind stress as the only forcing mechanism (no stratification).

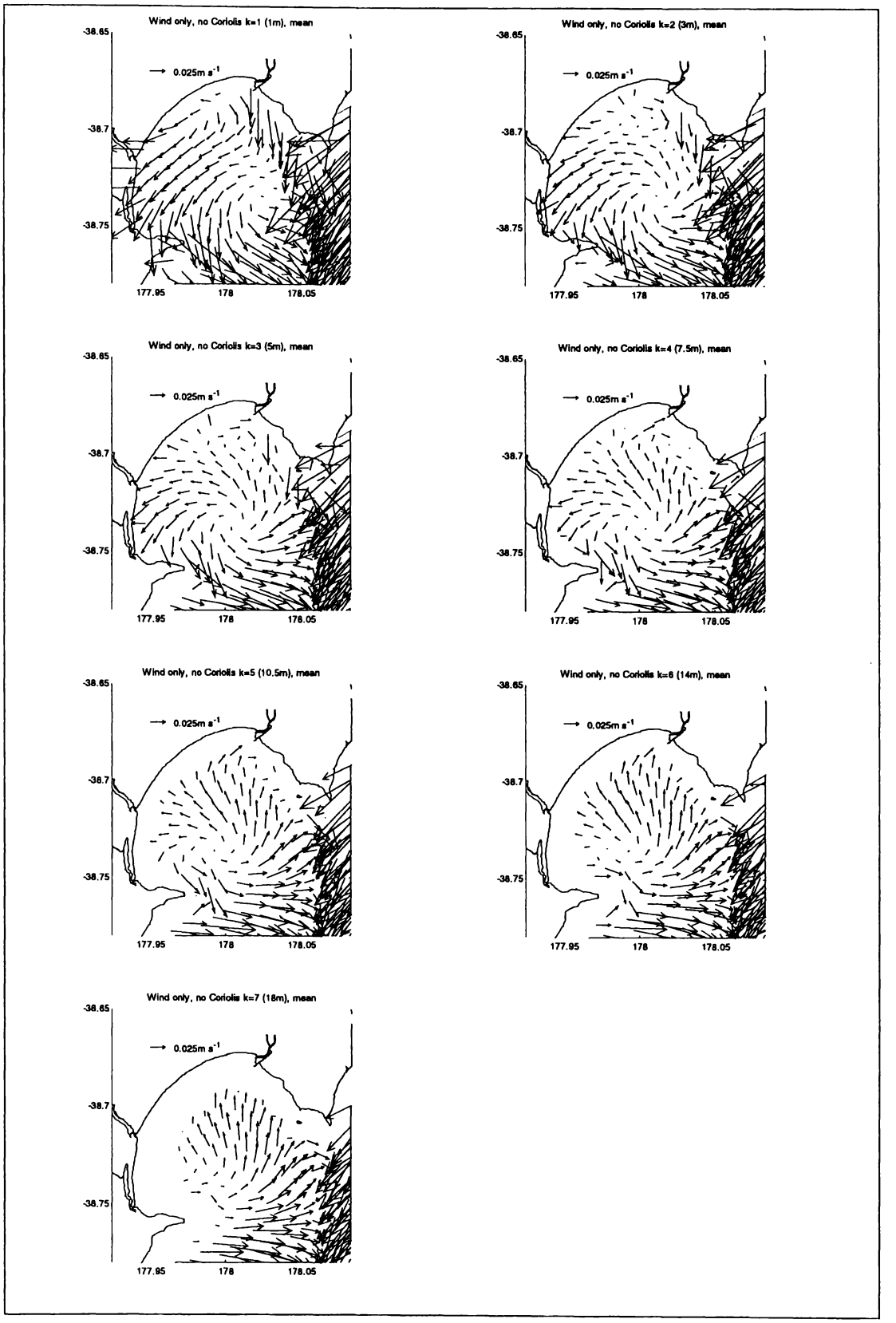

Figure 7-29. Mean wind-induced circulation over the simulation period, with rotation effects not included.

7.3.6 Wind-induced circulation patterns

In the above section it was recognised that the general circulation pattern in Poverty Bay was governed by wind direction. During the predominating offshore wind conditions, surface currents moved offshore, an anticyclonic gyre dominated circulation in the bay and continental-shelf water was drawn in near the seabed to counteract offshore surface flow. Three-dimensional circulation is best illustrated using a combination of horizontal and vertical profiles through the bay. The typical circulation pattern under offshore winds is shown in Figure 7-32. The horizontal profiles show anticyclonic circulation inside the bay, while cross-shore profiles (through I cells) show offshore wind-driven surface flow with marine water upwelling to replace it. Offshore surface flow is fastest in the Waipaoa River plume (I = 9) due to the combined influence of wind stress and river discharge, and this causes rapid uplift of marine water as it is entrained into the plume. The pattern is similar through the deep northeast bay section (I = 20), although offshore flow is slower away from the river plume. The shallow alongshore cross-section (J = 33) again demonstrates near-shore upwelling and shows a trend for east to west flow, consistent with the anticyclonic gyre. Currents are weak through the central bay cross-section (J = 25) but are generally upwelling as currents flow inshore along rising bathymetric contours.

Since the wind dominates Poverty Bay circulation under most conditions (section 8.3.8) and dominant wind direction is offshore, the time-averaged circulation pattern is similar to that induced by offshore winds (Figure 7-32). The time-averaged vertical circulation is characterised by the offshore flow of buoyant surface water and onshore flow of dense marine water. Time-averaged offshore surface flow ranges from 0.03-0.10 m s^{-1}, being fastest in the Waipaoa River plume (southwest) and slowest in the northeast. Shoreward near-bed return flow (time-averaged) ranges from < 0 (seaward) in the southwest to 0.05 m s^{-1} in the northeast, i.e. shoreward bottom-return flows are concentrated in the northeast of the bay. Since most water flows offshore in the southwest and onshore in the northeast, there must be anticyclonic time-averaged horizontal circulation associated with the vertical upwelling. The time-averaged horizontal circulation in the mid-water column is characterised by an anticyclonic gyre of velocity ~0.04 m s^{-1} as water flows in past Tuaheni Point, circles the bay and flows out

past Young Nicks Head (Figure 7-34). In shallow water along the eastern (port) side of the bay, a seaward return flow acts against the anticyclonic horizontal circulation. The time-averaged surface salinity/density pattern is characterised by fresher plume water extending offshore in the vicinity of the two rivers, and a high salinity/density area in the central and inner bay between the river plumes. In the mid-water column, freshwater tends to accumulate in the northeast corner of the bay by the port, trapped by the anticyclonic horizontal circulation.

A study was made of circulation during onshore winds, since these disrupt the typical circulation under offshore winds (Table 7-3). Onshore winds were classified as any wind approaching from 90° either side of the approximate cross-shore axis of Poverty Bay, i.e. any wind from 54-234°T. During the simulation period, the wind was onshore for 110 of the 468 hours, 24%. From 86046 hourly Gisborne Aero wind records between 1988-1999, onshore winds with a consecutive duration of at least 6 hours occurred 23% of the time. This concurs with the wind-rose in Chapter 4 that shows a predominance of off-shore winds. Column 2 (Table 7-3) indicates that during the simulation period, all except two onshore wind periods occurred in the afternoon, consistent with the strong diurnal sea-breeze signal in the Poverty Bay wind record. The other two onshore wind events were associated with the passage of southerly wind fronts. During the calibration simulation, surface layer current directions were closely coupled to wind directions and so onshore wind periods were associated with onshore near-surface flow (Table 7-3). The change in near-surface current direction instigated by onshore winds caused an associated switch from onshore to offshore currents near the seabed at the bay entrance (Table 7-3, column 5), usually with a 1-2 hour delay. This is part of a downwelling circulation system driven by sea-level gradients, as onshore wind stress sets water up against the coast (Figure 7-31). Some near-entrance offshore flows were also observed in the absence of onshore winds, due to shelf-current influence. The anticyclonic gyre that predominates in the Poverty Bay mid-water column was disturbed following most onshore wind episodes, as demonstrated for model layer 3 (4-6 m), (Table 7-3, column 4). Circulation in the mid-water column is less susceptible to wind-driven influences and often has a longer response time than the surface and near-bed layers, typically taking ~5 hours to respond to changing wind stresses. On occasions,

onshore winds actually strengthened the anticyclonic gyre even though near-bed layers exhibited the expected bottom-return-flow, but this was rare.

The typical onshore-wind-induced three-dimensional circulation is depicted in Figure 7-33. Surface currents (K = 1) are pushed onshore and the Waipaoa River plume is turned to flow alongshore toward the port. Contrary to the offshore wind situation, onshore winds do not form a gyre in the bay, and immediately below the surface layer (K = 3) currents show variability in both speed and direction. The cross-shore sections (I = 9,20) show wind-induced downwelling to occur and the lower horizontal sections (K = 5,7) correspondingly show offshore flow with a trend for downwelling currents to exit through the deep section near Tuaheni Point. The shallow alongshore cross-section (J = 33) shows eastward plume migration and entrainment of marine water upward into the plume. Near the port, the plume converges with water blown inshore along the northern coast and is forced to downwell. The central bay cross-section (J = 25) shows downwelling in the west, and a strong downwelling zone in deep water near I = 20, where water forced inshore from the continental-shelf meets return-flow from the port area. This is associated with upwelling in the shallow western margin where the wind sucks surface water away.

Figure 7-32 and Figure 7-33 show typical circulation patterns under offshore and onshore winds, but there were times when circulation showed considerable complexity, typified by Figure 7-39. These episodes were associated with wind shifts when the bay was adjusting to the new forcing direction, and they were consequently short-lived, usually 1-3 hours.

The above results demonstrate that wind direction is the primary control on hydrodynamic *variability* in Poverty Bay. In particular, onshore winds are required to disrupt the typical anticyclonic gyre and upwelling circulation that is initiated by Waipaoa River discharge but also by the prevailing offshore wind. Onshore wind events in Gisborne tend to be of short duration (< 12 hours) because the wind-rose is dominated by the regional katabatic flow off the Raukumara Ranges (Hessell, 1980) and so episodes of non-anticyclonic circulation will consequently be short-lived in Poverty Bay. Wind-induced

variability will be more common in summer, when the diurnal sea breeze is better established (Hessell, 1980).

Table 7-3. Onshore wind periods and associated circulation patterns during the calibration simulation.

Onshore wind periods (simulation hours)	Onshore wind coincides with afternoon (* = yes)	Periods of onshore surface-layer current (simulation hours)	Periods of non-anticyclonic circulation in model layer 3, 5 m (simulation hours)	Periods of offshore near-entrance flow in model layer 7, 18 m (simulation hours)
25 – 40	*	25 – 41	33 – 42	26 – 37
47 – 55	*	47 – 55	49 – 60	49 – 60
75 – 80	*	75 – 81	80 – 87	76 – 85
193 – 198	*	193 – 199	200 – 208	194 – 202
217 – 224	*	218 – 222		219 – 224
240 – 245	*	241 – 244	243 – 246	244 – 246
266 – 274	*	266 – 276	273 – 276	268 – 278
287 – 297		287 – 297	295 – 303	288 – 298
313 – 320	*	313 – 320	315 – 322	
364 – 374	*	365 – 373		366 – 375
420 – 445		420 – 444	426 – 451	420 – 448
457 – 463	*	455 – 462	460 – 468	457 – 463
				107 – 115
				155 – 170
				179 – 184

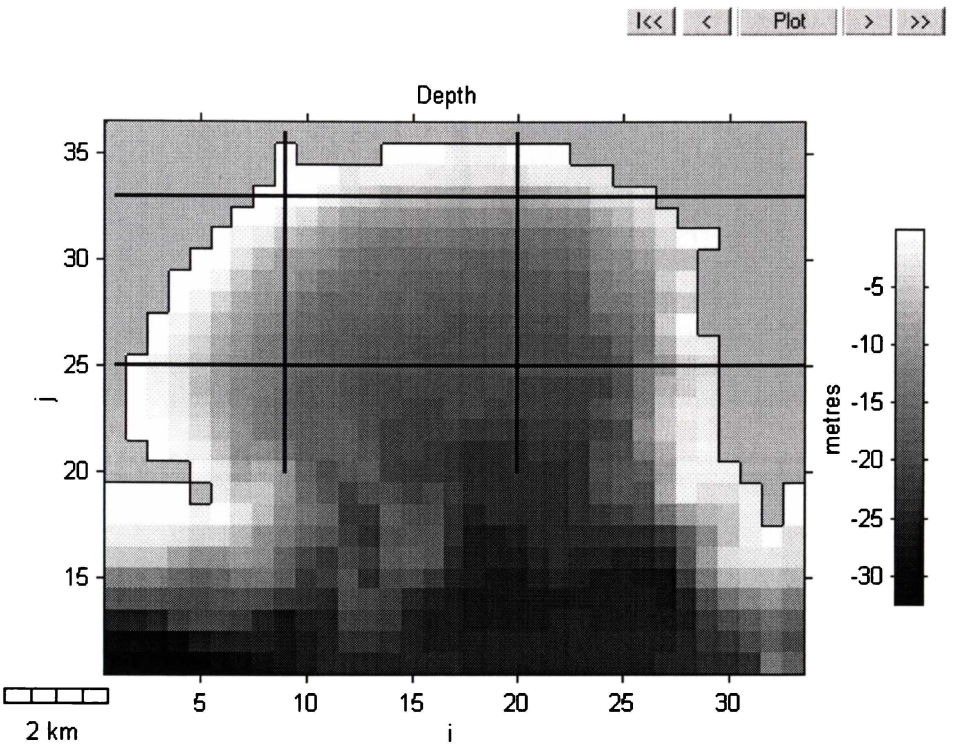

Figure 7-30. Poverty Bay model bathymetry showing the location of vertical cross-sections incorporated in Figure 7-32 and Figure 7-33.

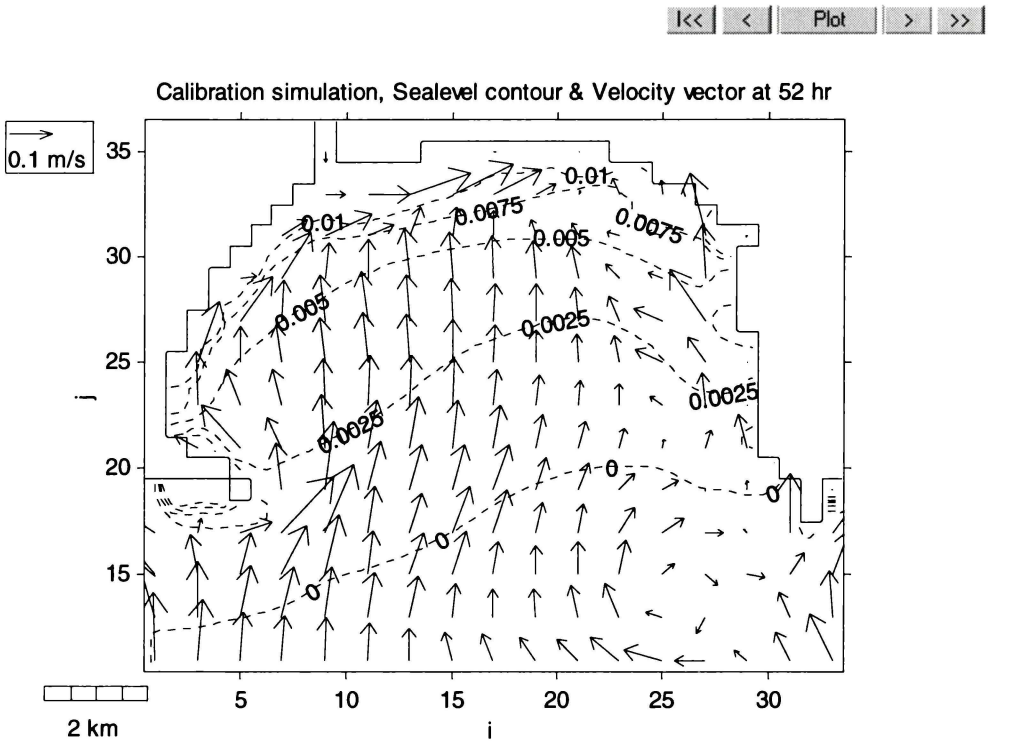

Figure 7-31. Velocity vector and sea-level contour coinciding with an onshore wind period at 52 hours in the calibration simulation.

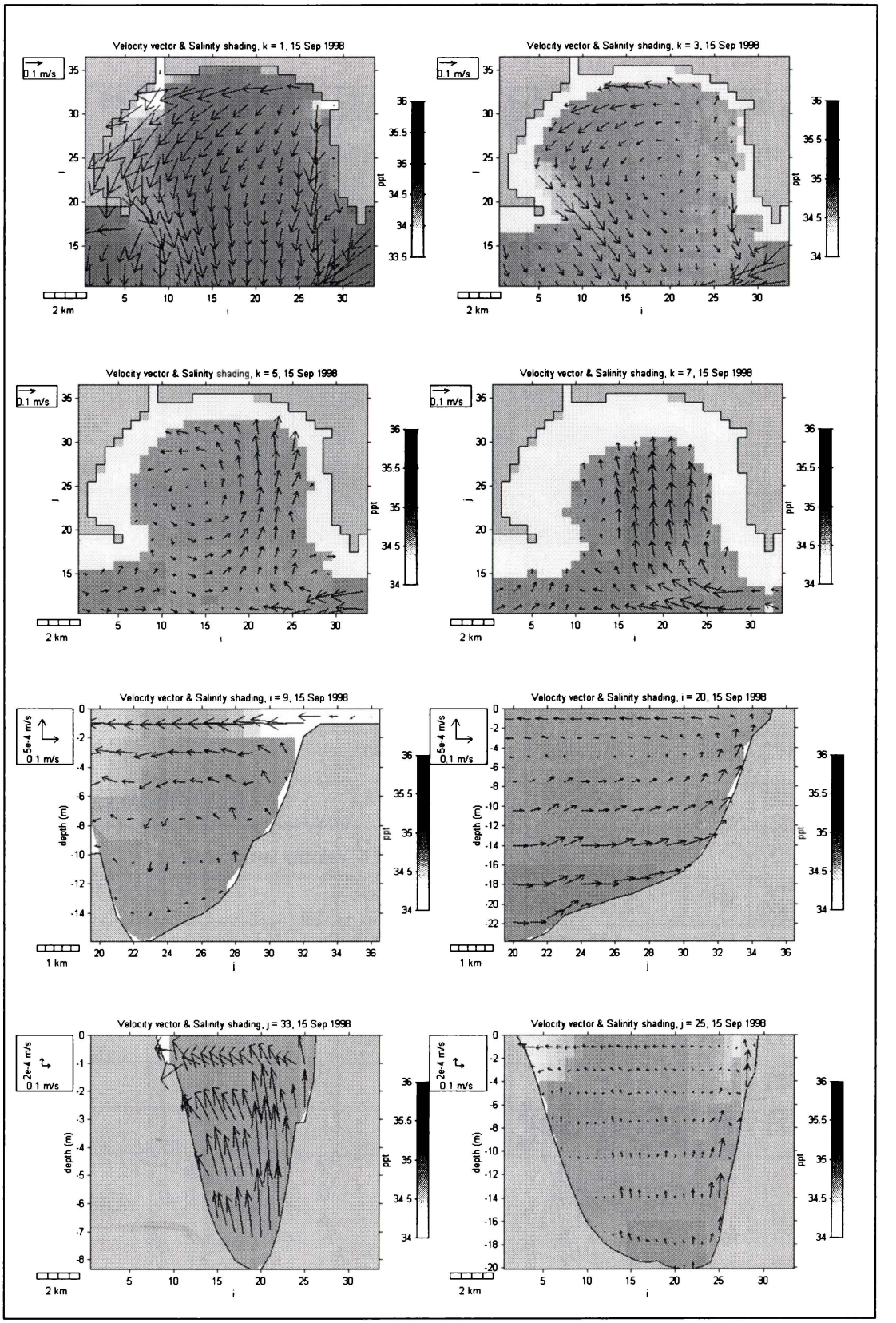

Figure 7-32. Model output from the calibration simulation, coincident with 15th September field survey during offshore winds of > 5 m s^{-1}. Figure 7-30 gives *I* and *J* transect locations.

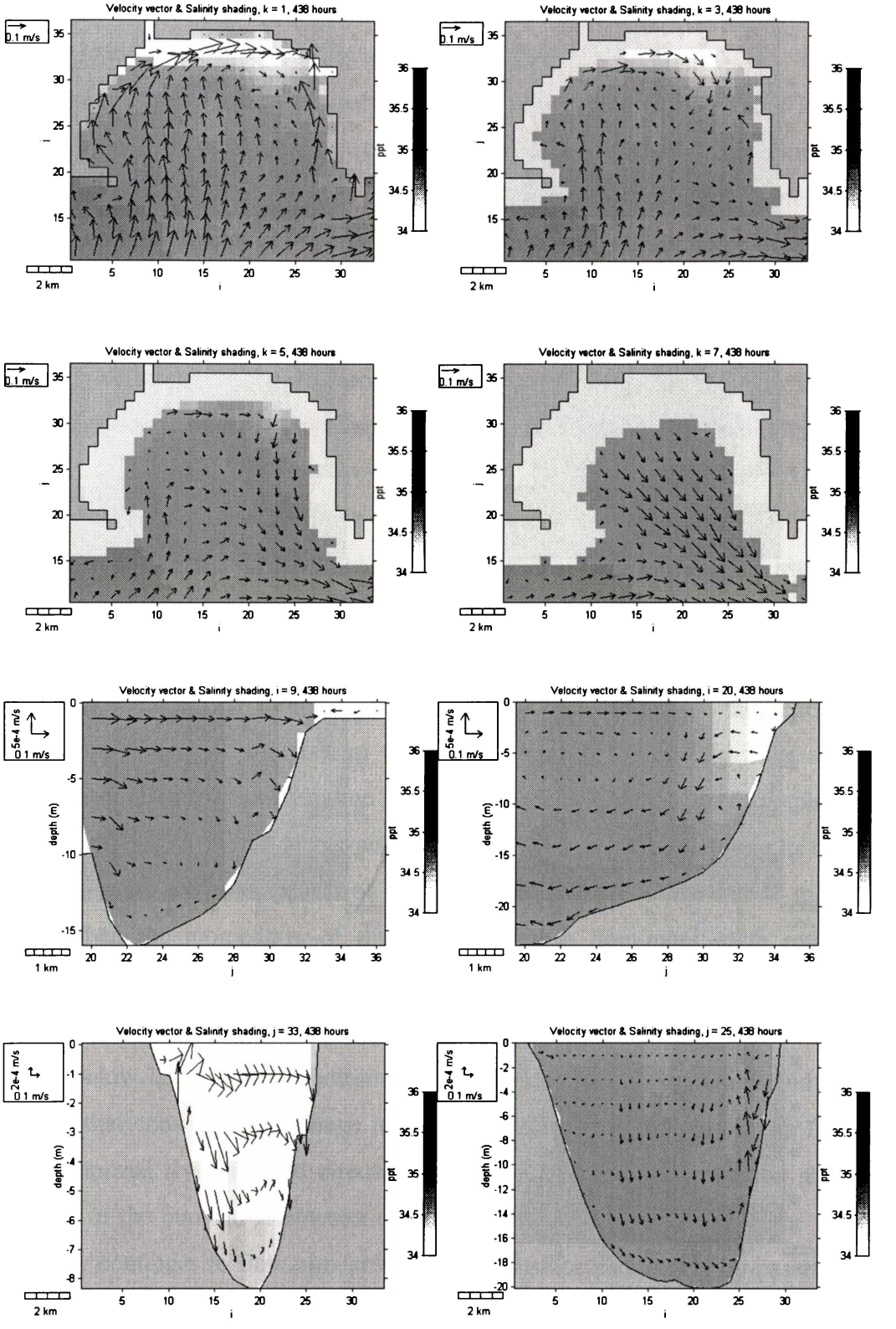

Figure 7-33. Model output from the calibration simulation at 438 hours, following the 28th September field survey (428-431 hours) when winds had been onshore for 18 hours (Figure 7-6).

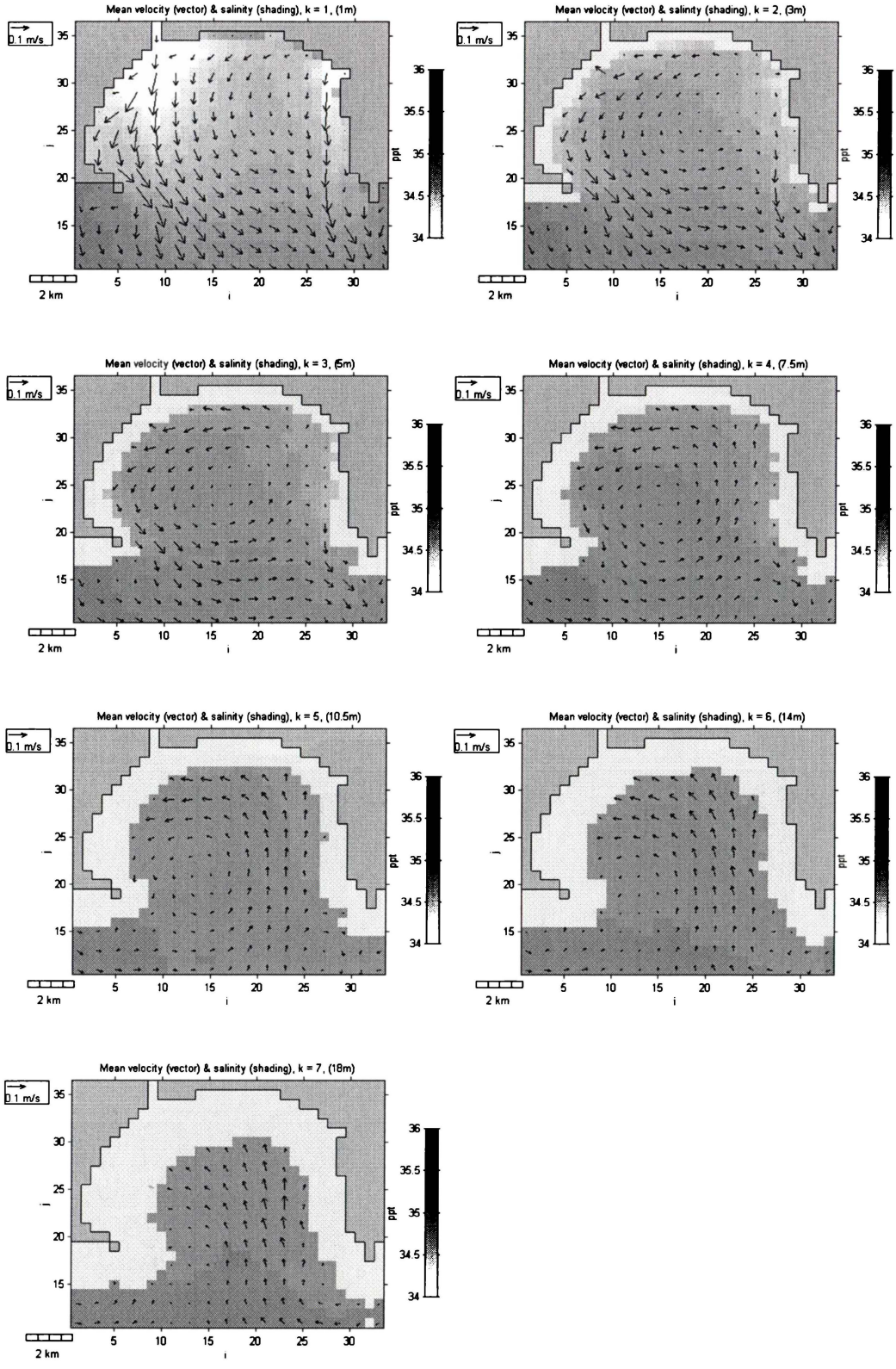

Figure 7-34. Time-averaged circulation and salinity in Poverty Bay during the calibration simulation.

7.3.7 Floods

The simulation including just river-forcing showed that Waipaoa River discharge initiates offshore surface flow, onshore return-flow near the seabed at the bay entrance and an anticyclonic gyre in the mid-water column. The model calibration period included a typical minor quickflow discharge from the Waipaoa River of 74 $m^3 s^{-1}$ (at the gauging station), but this discharge was small compared with typical flood events (Figure 7-35). A large flood was simulated to determine the effects on circulation in Poverty Bay, and to determine if discharge dominates over wind-forcing during flood events. A flood event of 1079 $m^3 s^{-1}$ peak discharge was chosen for simulation because it contained a single quickflow peak (Figure 7-35), although larger floods are known to have occurred, the largest during Cyclone Bola when discharge was estimated at 5300 $m^3 s^{-1}$ (Gisborne District Council, 1994).

Figure 7-36 demonstrates that flood events drive fast surface currents, up to 2 m s^{-1} at the river mouth and 0.25 m s^{-1} near the entrance of the bay. Turbulent mixing transferred momentum directly to layer 2 although currents were much slower than at the surface. By model layer 3 the plume had little direct influence on currents via downward momentum transfer and currents were beginning to be drawn onshore to replace marine water entrained into the surface plume. However, the plume mixed deeper and had strong offshore velocities near its outer boundary front, a pattern typical of non-rotational plumes. This shows that in floods, when the momentum of the flood discharge dominates earth rotation effects and horizontal numerical dispersion, the model will simulate non-rotational plume characteristics, despite its limitations discussed in section 8.3.4 above. Below layer 3 (6 m), bottom-return-flow dominates circulation and it is observed that considering the huge increase in discharge, this is not much faster than for normal river-induced circulation (Figure 7-23). The simulation shows that most of the buoyant freshwater remains in the surface layer and so the river essentially continues to flow outward across the surface and largely by-passes the bay without mixing, so subsurface velocities are not greatly affected. Whereas during lesser discharges the Waipaoa plume loses momentum rapidly after discharge and rotates under Coriolis to initiate anticyclonic circulation, during floods the plume has sufficient momentum to drive the entire surface layer

offshore. This causes bottom-return-flow to act across the width of the bay and prevents formation of an anticyclonic gyre, leaving a straight upwelling-type circulation. An anticyclonic gyre was observed to reform once river discharge reduced to approximately 120 $m^3 s^{-1}$. From the 28-year record, discharges were less than 120 $m^3 s^{-1}$ 96% of the time; therefore the model suggests anticyclonic river-induced circulation will be the norm, although this result must be viewed with caution since the model cannot reproduce non-rotational plumes for low discharges.

The Waipaoa River is known to carry high suspended sediment loads during floods that Foster and Carter (1997) suggest deliver large quantities of fluid mud to the continental-shelf as hyperpycnal flows. Hyperpycnal river flows occur when the density of the river discharge exceeds that of marine water, due to the suspended sediment content. Thus the river plume would flow underneath the water surface along the seabed and not across the surface as simulated. According to Foster and Carter (1997), the threshold for hyperpycnal Waipaoa River discharge occurs when flow exceeds 2000 $m^3 s^{-1}$, which is approximately a decadal event. The simulated flood event was considerably less than 2000 $m^3 s^{-1}$ and can be assumed reasonably accurate. However, a hyperpycnal flood discharge would considerably alter circulation in the bay compared with the buoyant flood discharge simulated here. A density model would be required should hyperpycnal discharges wish to be simulated in future, as opposed to the salinity model used here.

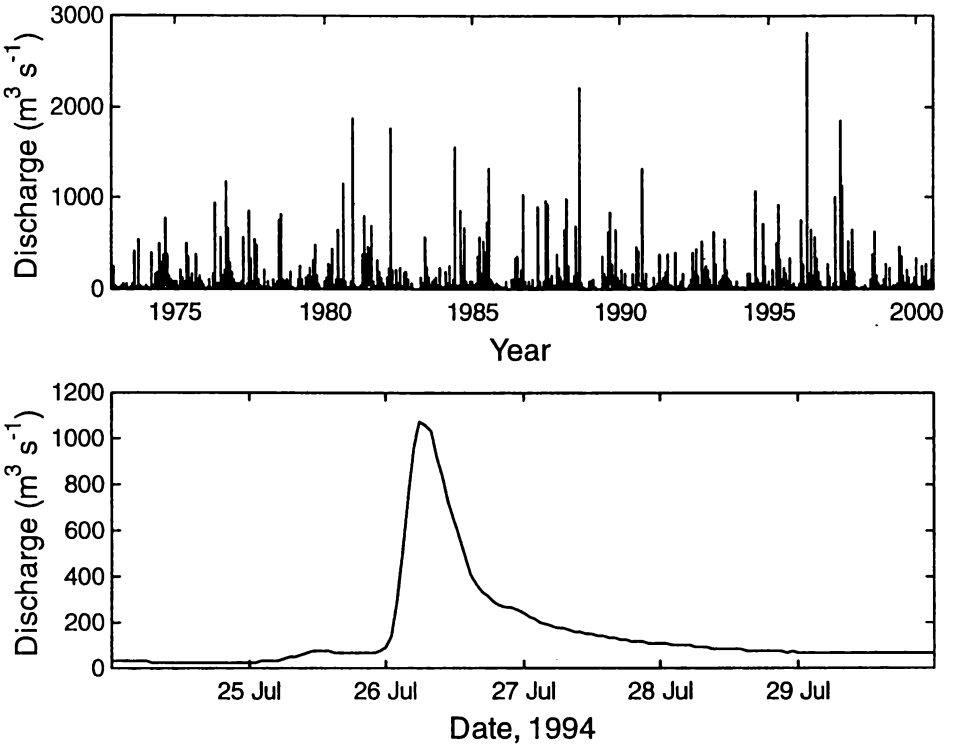

Figure 7-35. Waipaoa River discharge: A) discharge history (contains gaps), B) flood discharge used for flood simulation (peak = 1079 $m^3 s^{-1}$).

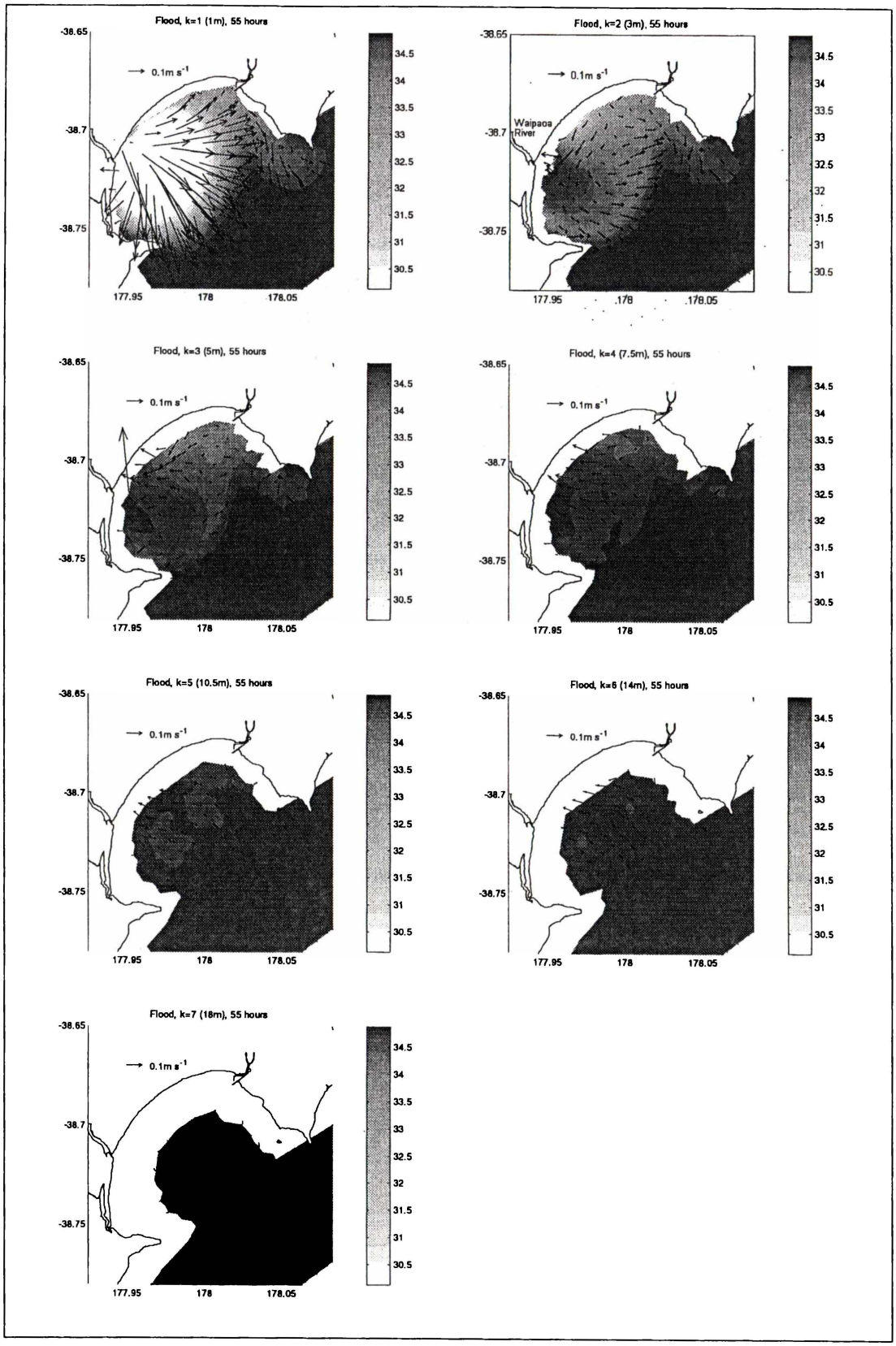

Figure 7-36. Flood simulation of the Waipaoa River 26/7/94 storm (Figure 7-35, B), shown at time coinciding with peak 1079 $m^3 s^{-1}$ discharge. River discharge is the only forcing used in the simulation.

7.3.8 Wind-influence versus river-influence

A balance between wind and river discharge has been shown to control Poverty Bay hydrodynamics. In section 8.3.4 it was shown that the river plume entrained substantial amounts of water and had a significant effect on the bay. The plume forced offshore flow near the surface, onshore near-bed flow at the bay entrance and an anticyclonic gyre in the mid-water column. In section 8.3.5 it was shown that a similar circulation pattern is created by the prevailing offshore wind, but that episodic onshore wind events provided hydrodynamic variability. In this section the question is posed as to which of wind-stress and river discharge is the dominant forcing mechanism in Poverty Bay.

Both the wind and river mobilise and mix significant water volumes within the bay. On 19th September 1998 simulations showed that 29% of the total bay volume was mixed with freshwater. Over the calibration period the wind had an instantaneous affect on currents in the surface layer (Table 7-3), which comprised 13% of the bay volume. In addition, model layer 7 near the seabed had a short ~1 hour response time to the wind (Table 7-3), therefore the wind mobilised 23% of the bay within 1 hour. Average response times in the mid-water column (layer 3) were ~5 hours, showing wind to dominate circulation in the entire bay over an ~5 hour time frame. Under the range of river discharges and wind stresses experienced during the model calibration period the wind clearly dominated river discharge in its influence on the bay. However, river discharge was very dominant during the simulated flood event (Section 8.3.7).

To further investigate the balance between wind and river induced circulation a series of simulations was undertaken where a constant-speed southerly wind was applied, and the river discharge steadily increased by 1 $m^3 s^{-1}$ per hour, up to 200 hours. A southerly wind was chosen since this is known to force the Waipaoa plume alongshore toward the port and induce circulation opposite to the anticyclonic river-induced pattern (section 8.3.6). The first graph in Figure 7-37 examines the relationship between southerly wind speed and the time and discharge required to reverse near-bed upwelling at the bay entrance. The occurrence of near-bed downwelling shows that the river-induced circulation has overcome wind-induced circulation (downwelling at the bay entrance) to instigate

anticyclonic circulation. When wind stress and discharge are working against each other the Waipaoa River begins to dominate once discharges reach 60 $m^3 s^{-1}$ (Figure 7-37). This value is dependent on the rate of discharge and the rate of spreading of the plume, but gives an approximate indication of the Waipaoa River volume required to compete with wind-forcing. Below this level the wind dominates circulation, and if > 5 m s^{-1} it can continue to dominate even larger discharges.

By introducing a river discharge into a bay where southerly-wind-induced circulation is already present, the river discharge must overcome the pre-existing momentum of the water column before circulation alters and this explains the minimum 60 (hour, $m^3 s^{-1}$) requirement to induce anticyclonic circulation. Flood discharge in the section above induced very strong surface currents, therefore a second series of southerly wind speeds were imposed to gauge the point at which wind begins to dominate circulation imposed by a receding flood event. The second graph in Figure 7-37 examines the relationship between receding flood discharge and the southerly wind speed required to steer the entire discharging plume along the coast toward the port. A strong 9 m s^{-1} wind was able to overcome a 220 $m^3 s^{-1}$ discharge, but for lesser wind speeds of 5-7 m s^{-1}, discharge was required to drop to ~65 $m^3 s^{-1}$. Winds of < 5 m s^{-1} did not prevent the plume flowing out past Young Nicks Head.

These results suggest that a Waipaoa River discharge of approximately 60 $m^3 s^{-1}$ is required before river-induced flow will begin to dominate wind-induced circulation. Conversely, winds of speed < 5 m s^{-1} may have little effect once the Waipaoa River discharge has reached this level. From 233,302 mean hourly values collected since 11 November 1972, the mean Waipaoa River discharge was 31 $m^3 s^{-1}$ and it exceeded 60 $m^3 s^{-1}$ just 11% of the time. The river is therefore only likely to dominate circulation during flood events.

From these results it is seen that at most times wind stress will dominate circulation in Poverty Bay. River discharge will dominate during episodic flood events, although strong winds may continue to dominate small freshes.

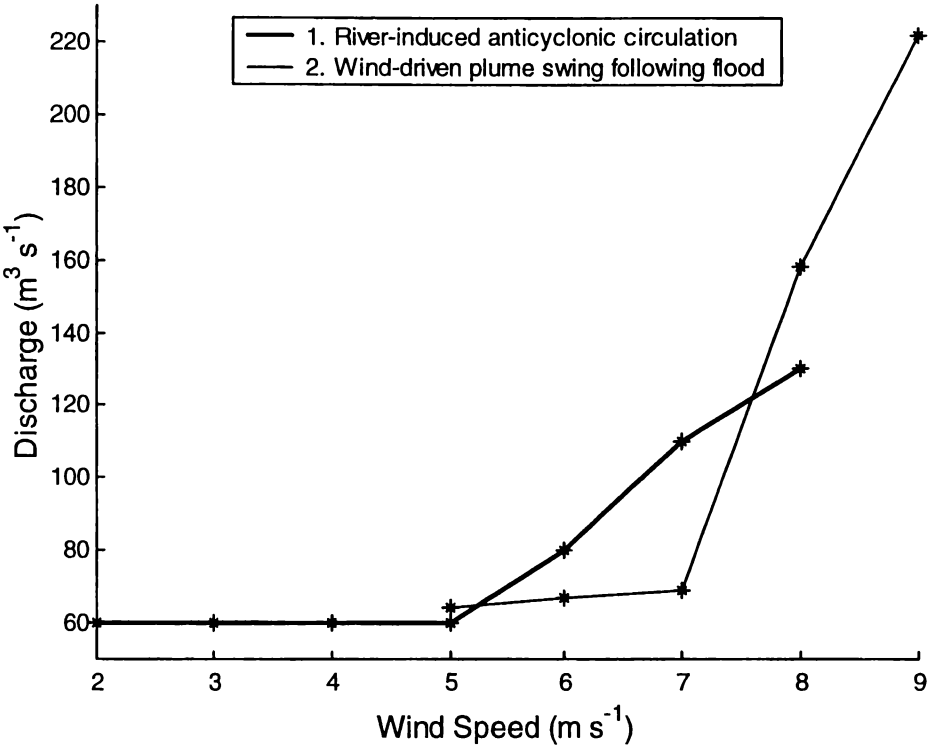

Figure 7-37. Simulation results showing: 1) the relationship between southerly wind speed and the time and discharge required to induce anticyclonic circulation, 2) the relationship between receding flood discharge and the southerly wind speed required to steer the entire discharging plume along the coast toward the port.

In Chapter 4 it was calculated that density-driven dispersion caused plume spreading at a rate equivalent to 7 m s^{-1} wind stress on 17th September 1998, yet discharge was well below mean conditions at just 11 m^3 s^{-1}. This seems excessive when compared to the above simulation results. The bulk vertical eddy viscosity N_Z = 0.012 m^2 s^{-1} used in the Chapter 4 calculation assumed a roughness length z_0 = 0.002 m, a typical value for sandy seabeds (Black and Hatton, 1992) and slightly coarser than that used by Black et al. (1997). The calibration simulation showed that in the vicinity of the plume, depth-averaged N_Z was considerably smaller at ~0.0006 m^2 s^{-1}. A more representative z_0 value for Poverty Bay is 0.0001 m, calculated in section 8.2.6 above. By the method of Visser (1996) this leads to bulk vertical eddy viscosity N_Z = 0.0008 m^2 s^{-1}, which is considerably closer to that of the simulations. Using the same parameters as in Chapter 4 but using N_Z = 0.0008 m^2 s^{-1}, the re-calculated wind speed that would exert surface stress equal to that of density-driven dispersion is 1.8 m s^{-1} on 17th September

1998. This value makes more sense in context with the low discharge on that day and the simulation results just presented.

From these calculations, density dispersion plus the light offshore wind should have combined to drive currents of ~0.05 m s^{-1} in the plume vicinity on 17th September (Prandle and Matthews, 1990). This compares favourably with measured velocities at 3 m depth (Figure 7-13). However, the circulation pattern was uniform throughout the water column on 17th September 1998 indicating little vertical shear and suggesting that vertical momentum transfer between layers initiated circulation. If this were the case and forcing was primarily from the surface, then currents would be expected to weaken with depth, but they grow stronger toward the mid-water column (Figure 7-13). In hindsight and with the benefit of the model it can be shown that the circulation measured on 17th September 1998 was generated by several days of offshore winds including some that reached over 10 m s^{-1} (Figure 7-6), combining with weak river-induced circulation. It was shown in Table 7-3 that the southerly wind events that are the main cause for altering circulation, typically take around 5 hours to change mid-water flow patterns. Clearly the water column maintains considerable momentum that sustains circulation during light forcing conditions such as were present on 17th September.

7.3.9 Eddies

Simulations by Black et al. (1997) showed transient eddies forming adjacent to the headlands of Young Nicks Head and Tuaheni Point, and eddy-formation was subsequently investigated in Chapter 2. The eddies simulated by Black et al. (1997) were large at times and consumed much of outer Poverty Bay, but these were driven by unrealistically large shelf-currents, often exceeding 1 m s^{-1}. However, the calibration simulation still showed transient eddies, such as observed in satellite images of the Waipaoa River plume (Foster and Carter, 1997), although these were small and short-lived in comparison to those of Black et al. (1997), (Figure 7-38). Eddies generally formed when wind shifts caused general hydrodynamic variability in the bay and lasted only 1-2 hours (Figure 7-39), and their rapid growth and decay is consistent with that of phase eddies (Chapter 2). More phase eddies were observed next to Tuaheni Point than Young

Nicks Head and eddies of several hours duration (steady-state eddies, Chapter 2) were observed on three occasions adjacent to Tuaheni Point (Figure 7-38). Tuaheni Point projects further into the current flow field than Young Nicks Head and continues its form underwater as a rocky point reef, and both these features were shown to be conducive to eddy formation in Chapter 2. The simulations show that eddies are short-lived features that occur adjacent to the headlands and particularly near Tuaheni Point, but have little influence on circulation inside Poverty Bay as a whole.

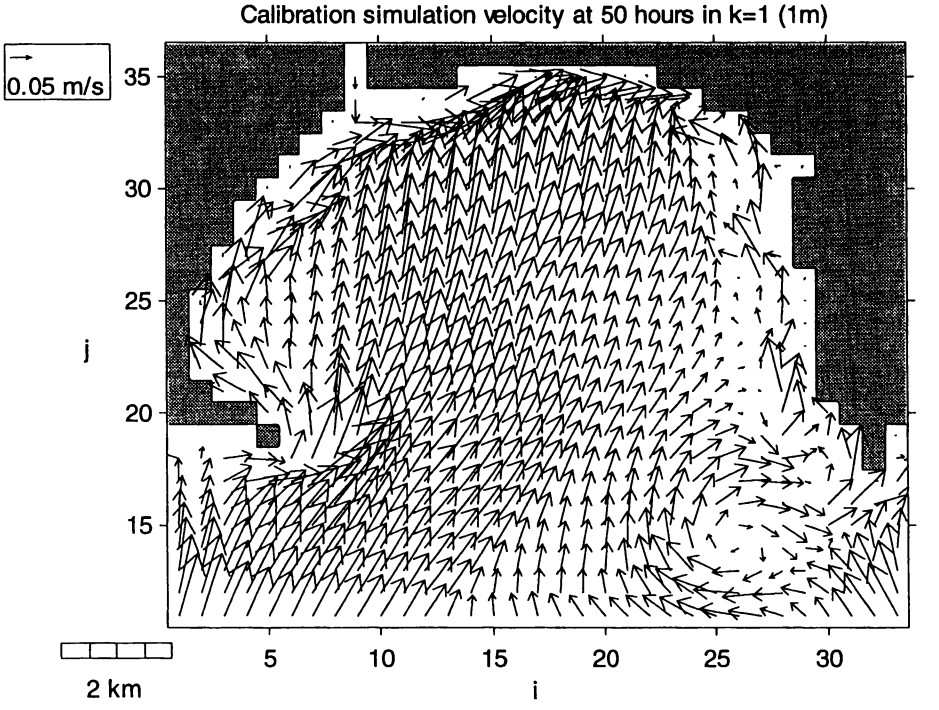

Figure 7-38. Transient eddy formation adjacent to Tuaheni Point during the model calibration simulation. The steady-state eddy shown existed for over 11 hours, during onshore wind conditions.

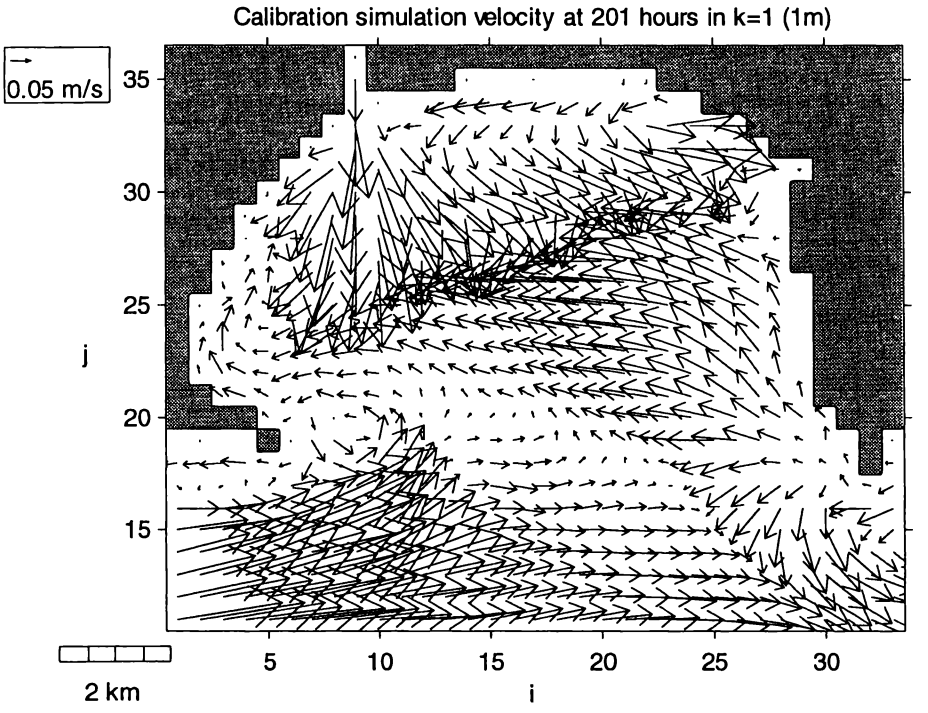

Figure 7-39. Transient eddy formation adjacent to Young Nicks Head during the model calibration simulation. The phase eddy shown formed during a wind shift from on to offshore and existed for 2 hours. Note the general hydrodynamic variability.

7.3.10 Bathymetric effects

In Chapter 2 the interaction between continental-shelf-currents and simplified embayment geometries was studied, with emphasis on eddy formation in the embayments. The bathymetric features having most effect on eddy formation inside the bay were the headlands flanking the bay entrance. An underwater reef projecting from the headlands was found to have a similar although lesser effect.

Having calibrated the three-dimensional model it was decided to simulate circulation over simplified bathymetries, but using the calibration data to force the model. The aim was to determine if the basic features of Poverty Bay circulation could be reproduced using simple bathymetries, and which bathymetric features had the biggest effect on circulation. The bathymetric features investigated were

the rounded nature of the bay (in the horizontal), the depth of the bay and the shape of the flanking headlands (Table 7-4).

Following Chapter 2, two basic simple bathymetries were used, a bluff-body embayment (Figure 7-40), and a smooth embayment (Figure 7-41). The simple bathymetries have dimensions similar to those of Poverty Bay (Figure 7-2), with an entrance width of 9.2 km and cross-shore extent of 6.8 km. The bathymetry representing the real bay (used for calibration modelling) had a volume of 9.7×10^8 m^3 from rows J = 20:34 (Figure 7-2), and the bluff-body bay had a similar volume of 10.0×10^8 m^3. The smooth bay had a lesser volume of 8.6×10^8 m^3 when calculated inside I = 9:30, J = 14:34.

Two variations were made to the bluff-body bathymetry. Firstly it was modified to include a flat seabed, and the depth was set to 15 m depth to keep the bay volume similar to the real Poverty Bay (Figure 7-42a). Secondly, the eastern headland was extended to mimic Tuaheni Point (Figure 7-42b).

Comparisons between the calibration simulation and the bluff-body bathymetry show that circulation patterns and salinities are remarkably similar, particularly during offshore wind conditions when the pattern of offshore surface flow, near-bed return flow and anticyclonic mid-water circulation are all reproduced (Figure 7-43). The main differences occur in the inner corners of the bluff-body bay and near the outer headlands in the lower water column. The square inner corners act as pockets to trap water and alter circulation compared to the real bay, while shelf-current-driven eddies form readily inside the bluff headlands, at depths below 10 m. This concurs with Chapter 2 where it was shown that abrupt headlands were conducive to eddy formation. Circulation was not so well predicted in the bluff-body bay during onshore winds (Figure 7-44), because under these conditions the inshore bathymetry is critical for directing downwelling bottom-return-flow, and the square inner bathymetry does not perform well. Nevertheless, surface and near-bed currents were still reasonably similar, suggesting that the rounded bay shape is not the most important bathymetric feature.

Model predictions deteriorated on removal of the sloping seabed from the bluff bathymetry (experiment 2, Table 7-4, Figure 7-42a), as can be seen from comparison of Figure 7-45 with Figure 7-43. Surface currents remained similar because they were directly forced by wind and river discharge, but the mid-water response was inaccurate. The reason for this is best illustrated by viewing time-averaged vertical sections through the water column (Figure 7-46). Since the prevailing wind was offshore during the simulation period, the time-averaged circulation is offshore at the surface, with associated upwelling through bottom-return-flow. The sloping seabed in the original bluff-body (experiment 1, Table 7-4) is a close representation of the real bay in the cross-shore direction, and bottom-return-flows follow the bathymetry up through the water column while moving inshore (Figure 7-46a,b). Conversely, the flat seabed (experiment 2, Table 7-4) allows bottom-return-flows to flow inshore without rising until they reach the abrupt inshore wall (Figure 7-46c). As a consequence, mid-water column flows are weaker and less responsive to changes in surface forcing. Poverty Bay also has an alongshore depth disparity between the east and west side of the outer bay (Figure 7-2), but the relative success of the simulation in experiment 1 (uniform alongshore depth) indicates that the depth disparity does not greatly effect circulation. This is not surprising since the cross-shore depth variation is much greater than that alongshore.

These results demonstrate that the basic features of circulation in Poverty Bay can be reproduced by simple bathymetries, and that the bluff-body embayment (experiment 1, Table 7-4) contains the main features necessary to simulate circulation in the bay, so long as accurate forcing data is used.

However, as was shown in Chapter 2, the headlands flanking the bay play an important role in eddy formation and in the abrupt bluff-body bathymetry they can disrupt circulation. This is seen in Figure 7-43 where eddy formation adjacent to Young Nicks Head disrupts circulation in the lower half of the outer bay. As explained in Chapter 2, this occurs because flow separation between the shelf-current and the bay is more sudden past an abrupt bluff headland, creating a more defined wake, a stronger shear zone and stronger recirculation-favourable sea-level gradients. However, although the bluff-body embayment is more conducive

to eddy formation at Young Nicks Head, it is less so at Tuaheni Point. Comparison between bathymetries in experiments 1, 2 and 3 (Table 7-4) reveals the importance of the projecting headland and reef at Tuaheni Point (Figure 7-47). When shelf-currents flow to the southwest with sufficient strength, the Tuaheni Point headland and reef creates a sheltered zone (wake), causes strong horizontal shear, and results in eddy formation (Figure 7-47a). To reproduce the strength and location of this eddy in the bluff-body embayment a point that projects into the shelf-current is required (experiment 3, Table 7-4, Figure 7-47c). A simulation was also run using the original bluff-body bay (experiment 1), but with frictional resistance increased by raising the frictional roughness length from z_0 = 0.002 m to z_0 = 0.1 m in the same area as the shelf promontory in experiment 3 (experiment 4, Table 7-4). As expected from Chapter 2, this was found to have very little effect on circulation compared with the processes (wake formation and horizontal shear) associated with flow separation at the nearby bluff headland. This demonstrates that at Poverty Bay, the physical presence of the Tuaheni Point headland and reef is more important than the increased frictional effect that may occur above the reef.

Since shelf-current flow had a net north-eastward flow (Chapter 4) and eddy formation was not commonly observed during the calibration simulation, the disruptive effect of eddies forming at Young Nicks Head was more noticeable than the lack of eddy formation adjacent to Tuaheni Point when the bluff-body bathymetry was used.

The smooth bathymetry (experiment 5, Table 7-4) lacked sufficient internal volume for circulation to develop as simulated for the real bay and favoured the formation of a single gyre. Therefore the smooth bathymetry was not a good representation of natural Poverty Bay and was unable to reproduce key circulation features. It was demonstrated in Chapter 2 that recirculation in the smooth embayment was influenced by a reef at its outer margin, when circulation was driven by shelf-currents. Since forcing in these simulations was dominated by wind stress inside the bay, outer reefs had no effect making the smooth bathymetry redundant. However the general pattern of anticyclonic circulation

during offshore winds was reproduced (Figure 7-48a), while cyclonic circulation was produced during onshore winds (Figure 7-48b).

After simulating circulation in simple bathymetries with similar volumes and horizontal dimensions to Poverty Bay, the bathymetric features having largest influence on circulation were the cross-shore seabed gradient and the shape of the headlands. The alongshore depth gradient was less important. Correct depth representation was more important in the inner bay, where headland effects were minor or non-existent, whereas the headlands influenced currents closer to the bay entrance, particularly in the lower water column. Tuaheni Point was best represented by an abrupt projecting headland, whereas Young Nicks Head would be best represented by a smooth headland. The physical presence of the Tuaheni Point headland and reef is more important than the increased frictional effect that may occur above the reef. The rounded shape of the bay (in the horizontal) was the least important bathymetric feature investigated.

Table 7-4. Index of simple bathymetries used in simulations with calibration data

Experiment #	Bathymetry type	Bathymetry description
1	Bluff	Sloping seabed
2	Bluff	Flat seabed
3	Bluff	Sloping seabed and projecting east point
4	Bluff	Sloping seabed, z_0 increased at Tuaheni Point
5	Smooth	–

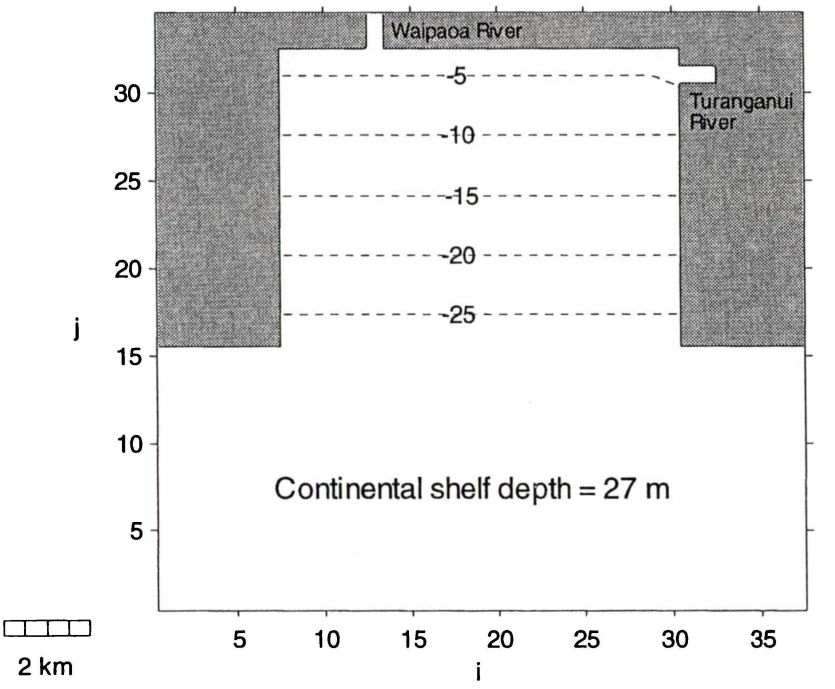

Figure 7-40. Plan view of simple bluff-body bathymetry, depth contours shown by dotted lines.

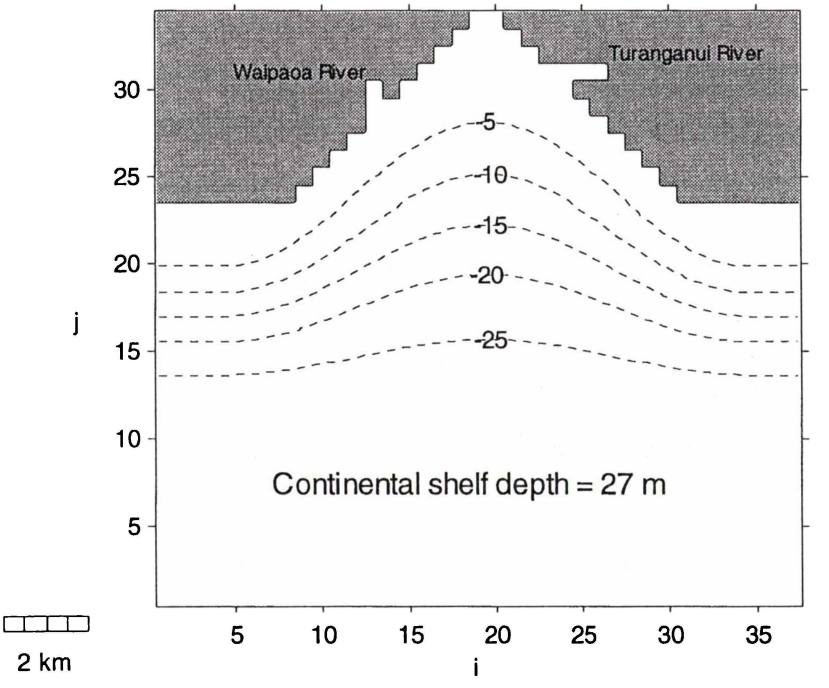

Figure 7-41. Plan view of simple smooth bathymetry, depth contours shown by dotted lines.

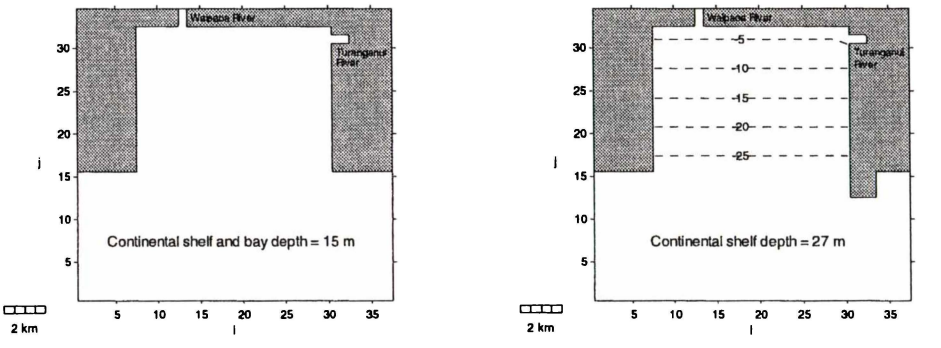

Figure 7-42. Plan view of simple bluff-body bathymetry: A) of constant 15 m depth, B) with sloping bay seabed and projecting east point.

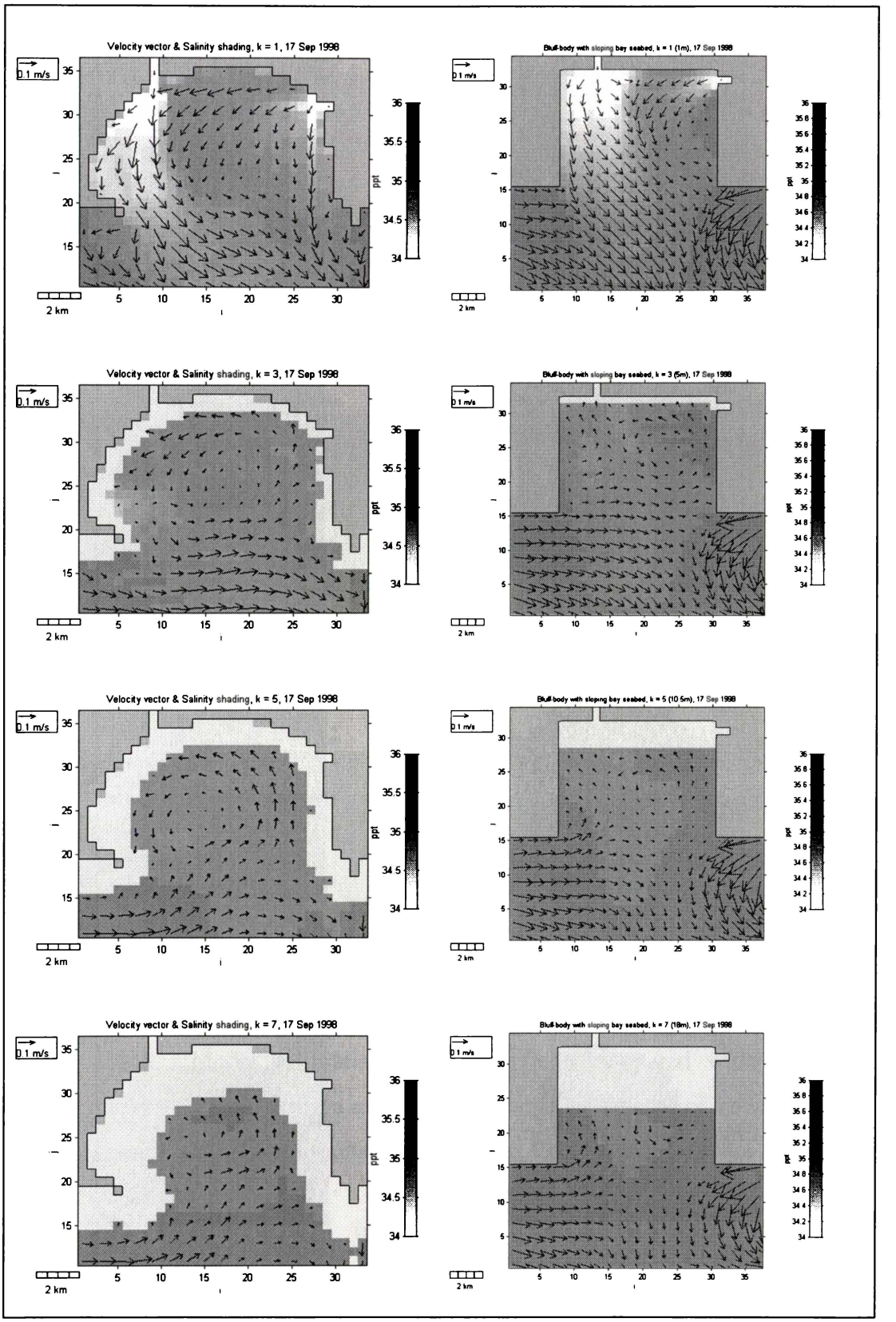

Figure 7-43. Model calibration simulation (left) compared with a similar simulation (right), but using a simple bluff-body bathymetry (Figure 7-40), at time coincident with the 17 September 1998 field survey during offshore winds.

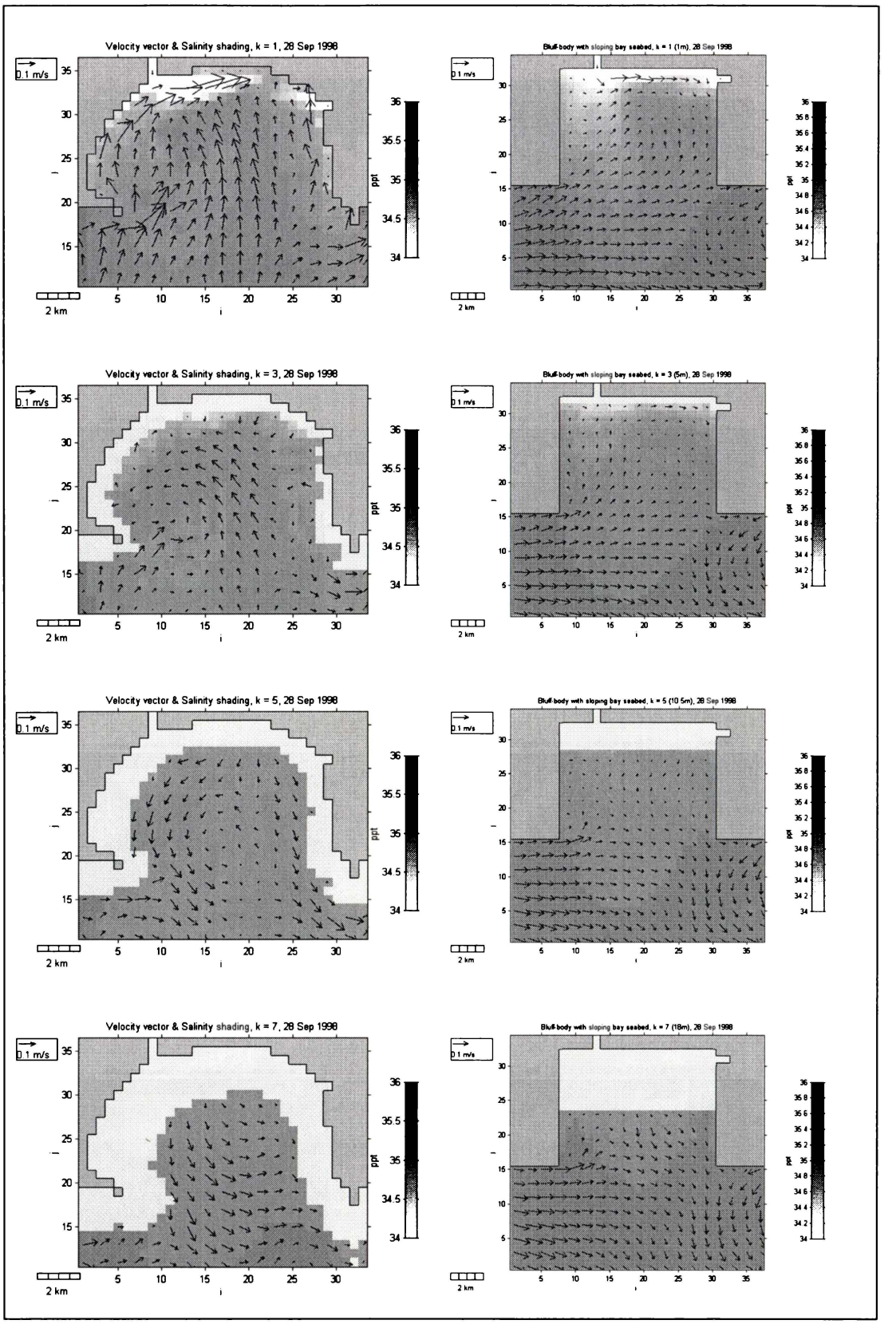

Figure 7-44. Model calibration simulation (left) compared with a similar simulation (right), but using a simple bluff-body bathymetry (Figure 7-40), at time coincident with the 28 September 1998 field survey during offshore winds.

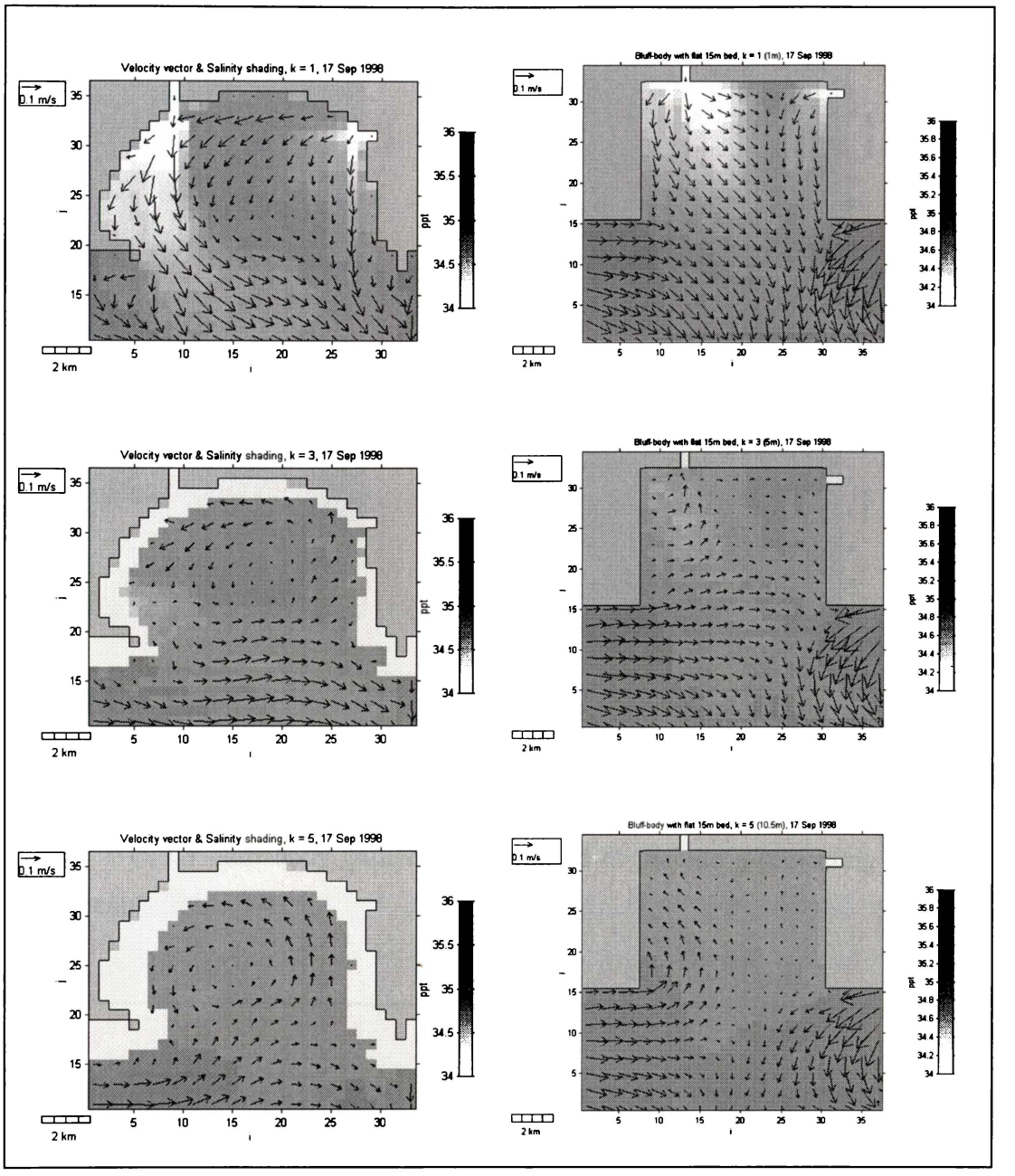

Figure 7-45. Model calibration simulation (left) compared with a similar simulation (right), but using a simple bluff-body bathymetry of constant 15 m depth (Figure 7-42), at time coincident with the 17 September 1998 field survey during offshore winds.

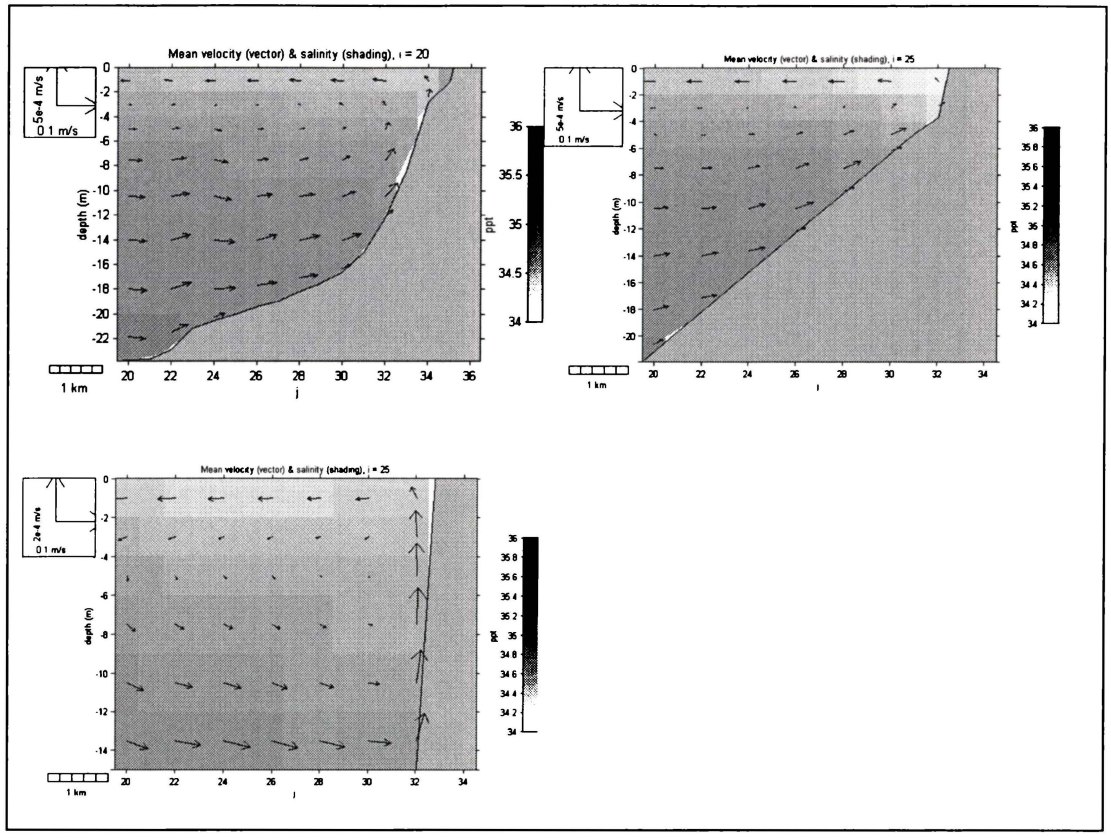

Figure 7-46. Time averaged cross-shore vertical sections through the water column: A) calibration simulation, B) bluff-body with sloping seabed, C) bluff-body with flat seabed.

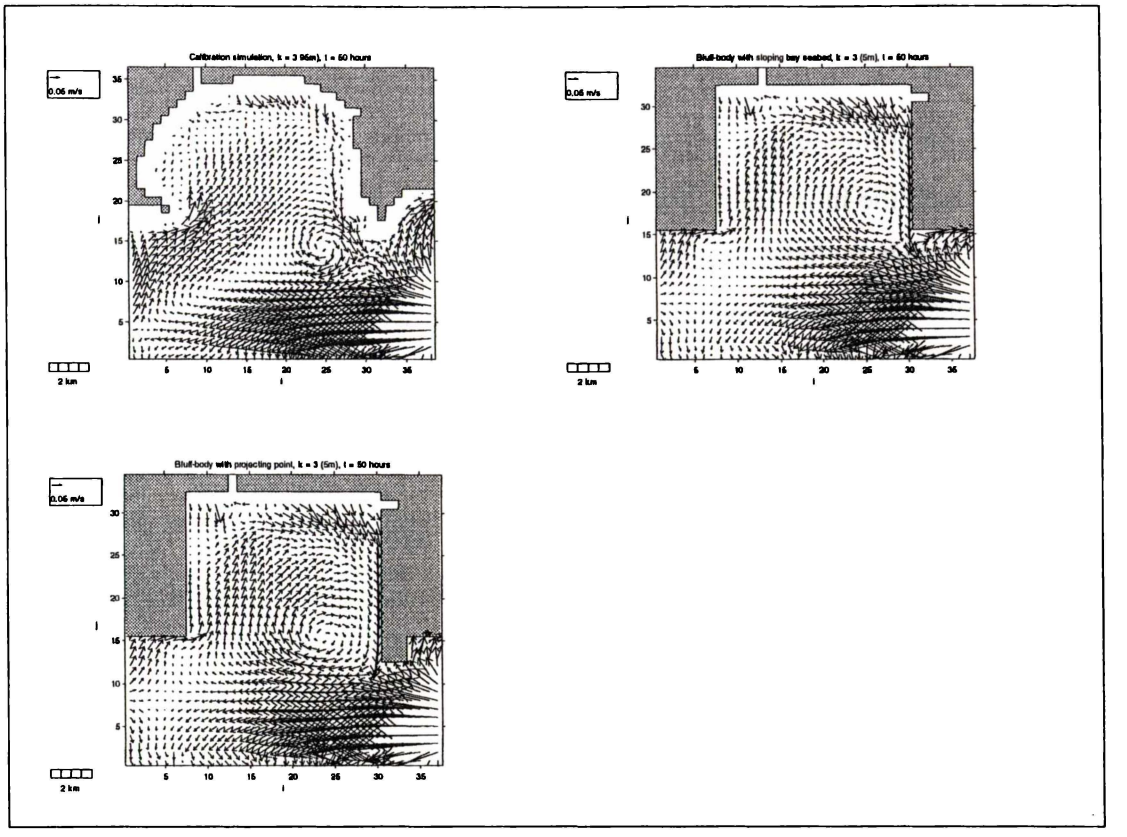

Figure 7-47. Model simulations at 50 hours using calibrated real forcing data, when continental-shelf-currents exhibit swift (~0.2 m s^{-1}) southwest flow past Tuaheni Point: A) calibration simulation, B) bluff-body bathymetry (experiment 1, Table 7-4), C) bluff-body bathymetry modified to include a projecting point (experiment 3, Table 7-4).

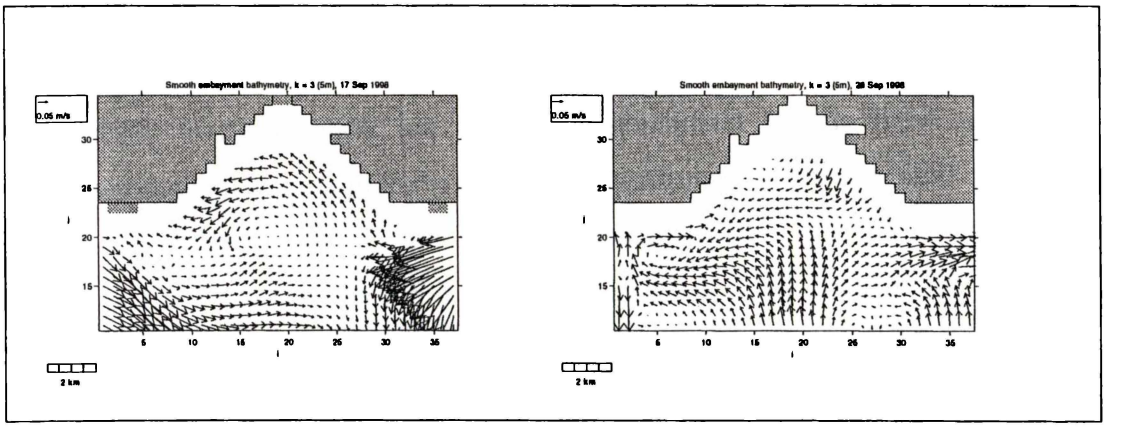

Figure 7-48. Circulation at 5 m depth in the simple smooth bathymetry (experiment 5, Table 7-4, Figure 7-41): A) during offshore winds on 17 September 1998, B) during onshore winds on 28 September 1998.

7.4 CONCLUSIONS

Model calibration involved the comparison of 60 simulations with measured data, during which the most appropriate values for A_H, N_Z, K_H, K_Z, C' were determined. Calibration also included appropriate adjustments to the wind speed and timing of river discharge. A reasonable level of calibration was achieved, with the model generally predicting velocity and salinity patterns successfully, although occasional disruptions arose from inaccuracies in the body-force used to drive the model. Excessive horizontal diffusion created further inaccuracies. However, circulation was sufficiently well predicted to use the calibrated model for separation and analysis of the processes contributing to Poverty Bay hydrodynamics, primarily shelf-currents, wind and river discharge.

Simulations showed that the combined influence of wind stress and river discharge dominates circulation in Poverty Bay, and that future numerical simulations could be undertaken to a reasonable degree of accuracy without requiring continental-shelf-current data. Shelf-currents had a minor impact on outer Poverty Bay and contributed little to circulation in depths less than 18 m.

Waipaoa River discharge caused offshore flow near the surface, onshore near-bed flow at the bay entrance and an anticyclonic gyre in the mid-water column.

Surface wind stress controlled hydrodynamic variability in the Poverty Bay. The prevailing wind created circulation similar to the Waipaoa River discharge; therefore both processes contributed to the prevailing anticyclonic horizontal circulation in the bay. River-induced anticyclonic circulation in Poverty Bay occurred due to earth rotational forces (Coriolis), but anticyclonic wind-induced circulation occurred due to the alignment of the prevailing wind with respect to the bay, generally forcing water out past Young Nicks Head and drawing it in past Tuaheni Point.

Under most conditions, the wind was the most important contributor to circulation with a response time of 1 hour for the upper and lower layers and ~5 hours in the mid-water column. The long-term wind-record suggested that offshore winds

prevail 77% of the time, and these have been shown to drive a time-averaged upwelling vertical circulation and an anticyclonic mid-water gyre. Variability to the typical circulation occurred during times of onshore wind stress, approximately 23% of the time. However, simulations suggested that once Waipaoa River discharge is greater than 60 $m^3 s^{-1}$ it can begin to dominate wind-induced circulation, but this is only likely during flood events (11% of the time). Conversely, winds of speed less than 5 $m s^{-1}$ may have little effect once the Waipaoa River discharge has reached this level.

Although wind stress dominated circulation during non-flood periods, river discharge was also found to be important for its role in stratifying the water column. This reduced vertical mixing, enhanced vertical shear, and facilitated faster horizontal velocities.

Simulation of simple bathymetries showed that the bathymetric features having largest influence on circulation were the cross-shore seabed gradient and the shape of the headlands. Correct depth representation was more important in the inner bay, where headland effects were minor or non-existent, whereas the headlands influenced currents closer to the bay entrance, particularly in the lower water column. Tuaheni Point was best represented by an abrupt projecting headland, whereas Young Nicks Head would be best represented by a smooth headland. The physical presence of the Tuaheni Point headland and reef has more influence than increased friction associated with the reef.

7.5 FUTURE WORK

The modelling study encountered a winter period when solar temperature inputs were small and stratification was dominated by freshwater river discharges. Future simulations during a summer period may require a density model that accounted for both temperature and salinity variation. Foster and Carter (1997) suggest that dense hyperpycnal Waipaoa River discharges occur above 2000 $m^3 s^{-1}$. Future simulation of this type of discharge would also require a density model. The langrangian version of model 3DD does not suffer from inherent numerical diffusion, as does the eulerian version used here. Future use of a lagrangian

model would facilitate more accurate simulation of river plume dispersion and mixing features, such as non-rotating plumes.

7.6 ACKNOWLEDGEMENTS

Model bathymetry was partially constructed from sounding data used with permission of the Hydrographer RNZN. The National Institute of Water and Atmospheric Research (NIWA) supplied wind data. Gisborne District Council supplied river discharge data, as did NIWA. Thanks to Professor Kerry Black for supplying the numerical model, appropriate literature and demonstration of its use.

8 - Discussion

8.1 INTRODUCTION

The central focus of this thesis has been investigation of the complexity of Poverty Bay hydrodynamics, relating to the unique bathymetric features and influences of wind, river discharge and continental-shelf-current driven circulation. This discussion chapter aims to broadly summarise the three-dimensional hydrodynamics of Poverty Bay in context of its bathymetry, forcing parameters and typical circulation patterns. The chapter compares the results of this study with similar studies in other coastal embayments, to explicate principles of circulation in an exposed and stratified coastal embayment with small tidal flows.

8.2 CIRCULATION IN POVERTY BAY

Poverty Bay is approximately 10 km wide at its confluence with the continental-shelf and 7 km in cross-shore extent, with a rounded planform and a mean sea-level volume of approximately 1×10^9 m^3 calculated from the digitised numerical model grid (Chapter 7). The Poverty Bay seabed slopes downward from its shoreline to approximately 25 m depth at the bay entrance (Figure 1-2), and the wide and deep entrance allows for free exchange with continental-shelf water throughout the water column. The bay is nearly symmetrical about its cross-shore axis, but is deeper in the northern half near the bay entrance. The biggest asymmetrical feature occurs between the headlands flanking the bay entrance. Although not so obvious terrestrially, below the water surface the rocky reef associated with Young Nicks Head is comparatively rounded and unobtrusive, whereas the Tuaheni Point reef extends further onto the continental-shelf and is abruptly contoured (Figure 1-2).

Tidal currents in Poverty Bay were shown by Gorman et al. (1997) to be small in comparison to the non-tidal component (Chapter 1). Subsequent continental-shelf measurements showed a similar trend; non-tidal flow contained 81% of the shelf-current variance and reached 0.32 m s^{-1}, whereas tidal currents never exceeded 0.12 m s^{-1} during field measurements (Chapter 4). Since tidal currents in inner Poverty Bay were commonly only 0.02-0.03 m s^{-1} compared with non-tidal currents of order 0.10 m s^{-1} (Gorman et al., 1997), it followed that circulation must be driven from some combination of non-tidal shelf-currents, wind and river discharge, with possible further contributions from heating and cooling and nearshore wave-driven littoral currents.

With respect to waves, Poverty Bay is exposed to open ocean wave energy from 60-185°T (Kensington, 1990) and has an energetic wave climate with a mean significant deep-water wave height of 1.2 m (Gorman et al., 1997). Wave action mixes the water column and increases frictional affects in shallow water (Davies et al., 1988). When superimposed on a current, near-bed wave orbital motion enhances the peak instantaneous bed shear stress, acting to increase bed-friction and damp the current (Davies et al., 1988). Providing that wave data are available, allowance can be made in numerical models by increasing the drag coefficient (Glorioso and Davies, 1995). A shortcoming of the present study was the absence of wave data during ADP field surveys, which prevented quantification of wave mixing effects on circulation. However, Glorioso and Davies (1995) showed that inclusion of wind-wave effects using a frictional drag coefficient reduces velocities, but does not significantly alter the pattern of wind-driven circulation. Additionally, Signell et al. (1990) showed that wave-current interaction with wind-driven circulation in a narrow, shallow embayment acted to increase bottom friction. Increasing effective bottom friction reduced the strength of the circulation, while the along-bay surface slope, bottom stress and the structure of the current profiles remained nearly unchanged. Furthermore, Black et al. (1996) showed that wave orbital motion explained only 11% variance in vertical temperature gradient on the Gippsland continental-shelf, compared with 37% from wind stress and 52% from surface temperature. While this is significant, it is not major. Based on these affirmations it is concluded that although unaccounted wave orbital motion will have introduced some error into

the simulations in Chapter 7, it is unlikely to have a huge impact on circulation in the bay, which has been shown to largely depend on wind and river discharge. The effect of wave mixing on stratification was not accounted for in this study. However, the 2 m surface vertical-layer used during modelling was based on observed surface mixed layer depth from CTD profiles, and sensitivity studies showed it to give best results. Wave mixing is assumed to be inherent in stirring this upper layer, but its effects were not otherwise accounted for since wave data was unavailable.

Wang and Symonds (1999) demonstrated that surface-cooling-induced downwelling was the most efficient flushing mechanism in Jervis Bay Australia, a bay with many similarities to Poverty Bay including similar horizontal dimensions, deep outer bay and wide exposure to the continental-shelf. However, although heating and cooling is active in Poverty Bay (Chapter 3), it is unlikely to be significant in comparison to other circulation forcing factors. Black et al., 1997 simulated Poverty Bay circulation, including both salinity and temperature in the model, finding that "temperature gradients are small" and "temperature influences... appear to be small relative to other processes". Heating and cooling during the day and night was more significant in the shallow margins of the bay than elsewhere and "in the absence of salinity effects, this cooler water would presumably downwell beneath the warmer waters offshore" (Black et al., 1997). CTD profiles showed that stratification in Poverty Bay was dominated by freshwater inputs from the Waipaoa and Turanganui Rivers (Figure 7-8 & Figure 7-9, Chapter 7), rather than by thermal radiation through the water surface. This was true even in February when solar radiation levels were high, water temperatures warm and river discharges were low (Appendix 1), showing that thermal heating and cooling had a minor impact on stratifying the water column and was unlikely to result in significant vertical circulation. This does not rule out the possibility of episodic cooling events causing inverse stratification (dense water at surface), but this would be extremely rare since Poverty Bay receives a nearly continuous supply of surface freshwater. Jervis Bay is similar to Poverty Bay in many ways, but has very little freshwater input, leaving stratification to evolve from thermal processes.

Non-tidal continental-shelf-currents off Poverty Bay commonly exceeded 0.1 m s^{-1} and had a maximum of 0.32 m s^{-1} during the field programme (Chapter 4). Local wind stress on the ocean surface is a logical forcing mechanism for non-tidal continental-shelf-currents, and this is the case at Poverty Bay. Observed continental-shelf-current directional swings following strong offshore winds provided some evidence for this, but spectral analysis showed little relationship (Chapter 4). Spectral analysis results showed sparse relationship between local wind and current at periods less than two days, but had higher coherences at longer periods that were suggestive of coastal-trapped-waves (CTWs). The subsequent investigation in Chapter 5 showed that CTWs were propagating up-coast from Cook Strait to Poverty Bay, although the modal structure of these waves was not resolved due to insufficient current data. CTWs therefore contribute to shelf-current forcing (specific thesis aim 2). Despite this finding there remained more energy in the Poverty Bay water level record than could be explained by propagation of CTWs. Following the CTW investigation, the use of wavelet analysis uncovered a convincing wind-current relationship on the Poverty Bay continental-shelf, at most resolvable frequencies between 8 and 512 hours (Chapter 6). This relationship had not been identified by spectral analysis because it is a tool designed for stationary time-series, whereas the wind and its relationship with the wind-affected water body are non-stationary in time. The coherence at weather-band frequencies suggested that CTWs were being locally forced, and this explains higher energy in the Gisborne long-period water levels than was present further south.

Although long-period CTW activity occurred at Poverty Bay, the lack of bay response to tidal forcing indicates that the response of Poverty Bay to CTW sealevel changes is also likely to be small. Poverty Bay has a wide entrance and no throat to restrict the adjustment of the bay to shelf sealevel changes such as are associated with CTWs. This allows smooth transition of sea-level changes between the bay and shelf, with little phase lag as a consequence and minimal associated currents. This contrasts with the findings of Black et al. (1993) in Port Phillip Bay, which exhibited a noticeable response to CTW forcing, at 3% of the total variance over 1 year. This was likely influenced by the narrow entrance to

Port Phillip Bay, whereby sea-level changes resulted in jetting through the bay entrance (3 m s^{-1} tidal currents).

As discussed above, tides and CTWs have a minor effect on Poverty Bay circulation, as does thermal heating and cooling. Wave orbital motion has not been investigated but is estimated to be of minor importance to circulation. In the absence of strong tidal currents, the hydrodynamics of Poverty Bay are dominated by wind stress and river discharge effects, with a lesser influence from predominantly non-tidal continental-shelf-currents (which include CTW effects). Accordingly, the following discussion focuses on circulation driven by these three mechanisms and so addresses specific thesis aims 2, 4 and 5. Although not addressed directly in this chapter, the thesis met specific thesis aim 3 by gathering data of sufficient spatial coverage and quality to calibrate Model 3DD, which was then used to reproduce and analyse circulation in Poverty Bay.

Time-averaged circulation in Poverty Bay was shown to occur ~77% of the time (Chapter 7) and is similar to that typically experienced under offshore winds (Figure 8-1). The time-averaged vertical circulation is characterised by the offshore flow of buoyant surface water and onshore flow of dense marine water. Time-averaged offshore surface flow ranges from 0.03-0.10 m s^{-1}, being fastest in the Waipaoa River plume (southwest) and slowest in the northeast. Shoreward near-bed return flow (time-averaged) ranges from < 0 (seaward) in the southwest to 0.05 m s^{-1} in the northeast, i.e. shoreward bottom-return flows are concentrated in the northeast of the bay. The time-averaged horizontal circulation in the mid-water column is characterised by an anticyclonic gyre as water flows in past Tuaheni Point, circles the bay and flows out past Young Nicks Head. A seaward return-flow occurs in shallow water along the eastern (port) side of the bay. The time-averaged surface salinity/density pattern is characterised by fresher plume water extending offshore in the vicinity of the two rivers, and a high salinity/density area in the central and inner bay between the river plumes. This saline slug has been measured on several occasions (Chapter 4 and Gorman et al. (1997)). In the mid-water column, freshwater tends to accumulate in the northeast corner of the bay by the port, trapped by the anticyclonic horizontal circulation.

A feature of Poverty Bay is the continuous influx of freshwater from the Waipaoa and Turanganui Rivers, and this is the primary difference compared with the otherwise very similar Jervis Bay, Australia. This stratifies the water column and promotes a classic estuarine-type circulation, where buoyant plume water flows seaward at the surface and saline marine water returns beneath (Kjerfve et al., 1992). However, even in estuaries with modest river inflows, tidal stirring can create a well-mixed system if sufficiently strong, eg. Broken Bay (Kjerfve et al., 1992) and Delaware Bay (Galperin and Mellor, 1990). In these situations tidal stirring breaks down the vertical structure and the systems can be successfully simulated in two dimensions (Kjerfve et al., 1992). Poverty Bay has small tidal flows, and so remains river-stratified even during relatively low flow discharge periods (Appendix 1), necessitating three-dimensional simulation (Chapter 7). Chapter 7 showed that in the absence of wind forcing, the Waipaoa River input would permanently drive an estuary-like upwelling circulation. River plume dispersion was driven predominantly by the seaward slope of the plume water surface (barotropic pressure gradient) rather than self-induced shear created by density gradients within the water column (baroclinic pressure gradient), similar to the Indian River Lagoon (Liu et al., 1997).

The following paragraph summarises the balance between wind stress and river discharge induced circulation (specific thesis aim 4). Although the time-averaged vertical circulation in Poverty Bay is similar to classical time-averaged estuarine circulation, the bay has several non-estuarine characteristics. The bay is deep compared to most estuaries, which allows for more complex internal circulation in the water column. The biggest disparity between the bay and an estuary is that classical time-averaged estuarine-type circulation is driven by the prevailing offshore wind and not by buoyant river influx. Therefore, at first glance the river appears more important than in reality, hence the conclusion by Black et al. (1997) that the Waipaoa River plume had a dominant effect on surface circulation. Simulations in Chapter 7 showed similar surface circulation patterns to those obtained by Black et al. (1997), both with and without river discharge included in the model. While the Waipaoa River discharge certainly contributes to estuarine-type time-averaged circulation, the wind dominates circulation under low river discharge conditions, with an almost instantaneous response at the water surface

and with associated bottom-return-flows responding in 1-2 hours (Chapter 7). Therefore, if the prevailing wind were onshore in Poverty Bay, then the classical time-averaged estuarine-type circulation would be reversed. Above ~60 $m^3 s^{-1}$, river discharge becomes the dominant forcing mechanism in the bay, and this occurs only about 11% of the time (Chapter 7). The river discharge is however, fundamental to stratification in the bay. In a stratified water body, buoyancy differences act to prevent mixing between layers and this facilitates vertical shear in the water column. The buoyancy gradient inhibits vertical turbulent mixing so that momentum from surface wind stress is concentrated into a narrower vertical layer, and this allows the development of faster horizontal velocities. The reduced vertical mixing is analogous to reduced turbulent friction at the seabed, and can be conceptualised as reducing friction between layers. Therefore it was seen in Chapter 7 that the wind was less effective in forcing Poverty Bay circulation without river discharge included in the simulation. Poverty Bay receives a near continuous freshwater supply and therefore stratification is likely to be re-established quickly following strong wind or wave-driven mixing events. Stratification is strongest near the water surface since it is dominated by freshwater influx, and the surface layer therefore shears easily across the bay and is particularly prone to wind-driven effects. The response to surface-layer movement is bottom-return-flow in the semi-enclosed bay, so stratification is important to circulation throughout the water column.

It was observed above that the wind dominates Poverty Bay circulation under low river discharge conditions (< 60 $m^3 s^{-1}$), which occur about 89% of the time. Of particular interest from the wind stress - current wavelet analyses (Chapter 6) was the transfer of a strong diurnal wind signal to the water column, a signature of the sea-breeze cycle first recognised as characteristic of the Poverty Bay area by Hessell (1980). This sea-breeze cycle was witnessed during ADP surveys and was hypothesised to have caused an observed vertical circulation overturn on 19th September 1998 (Chapter 4). Since Poverty Bay was shown to be highly responsive to wind forcing on short time scales of 1-5 hours (Chapter 7), the regular diurnal wind signature is clearly an important forcing mechanism in the bay. Aside from the sea-breeze cycle, winds are characterised by a prevailing northwest (offshore) wind, punctuated by occasional southerly fronts (Hessell,

1980). Since the prevailing wind is offshore, the observed time-averaged upwelling is of course also characteristic of circulation induced in real-time by offshore winds (Figure 8-1). However, onshore winds provide variability and force surface water into the bay. Simulations show that this often forces the Waipaoa River plume along the inshore coast toward the port, where it converges with water moving onshore along the Tuaheni Point side and is forced to downwell (Figure 8-2). This results in a downwelling slug of freshwater in the central bay, opposite to the time-averaged upwelling usually observed in this area. The pattern of wind-induced up- and downwelling is typical of semi-enclosed embayments with sufficient depth for vertical shear layers to develop. For example, in Port Phillip Bay, Black et al. (1993) observed that wind was highly correlated with vertical shear in the deepest part of the bay, with near-bed flows often directed approximately opposite surface flows.

Thus far the discussion has dealt with vertical circulation. It is recognised that this is dominated by surface wind stress except during high river discharge ($> 60\ m^3\ s^{-1}$), and that river-induced stratification plays an important role. However, Poverty Bay also exhibits a persistent horizontal anticyclonic gyre in the mid-water-column during (offshore-wind-driven) classic estuarine-type vertical circulation. The following paragraphs summarise the mechanisms responsible for the time-averaged anticyclonic gyre and in doing so meet specific thesis aim 5. Since the gyre-forcing process involves an interaction between hydrodynamic forces and the bathymetry, specific thesis aim 1 is also partially addressed.

It was demonstrated in Chapter 7 that wind stress is the dominant forcing mechanism in Poverty Bay, and this is the primary driver of the observed time-averaged anticyclonic circulation. This occurs because the prevailing offshore winds blow from slightly north of northwest, which is not directly through the cross-shore axis of Poverty Bay, but more from the port to Young Nicks Head. This tends to create stronger seaward currents along the shallow southwest coast, forcing more water out past Young Nicks Head than past Tuaheni Point. Additionally, the depth-variation in Poverty Bay contributes to the horizontal circulation; shoreward-directed bottom-return-flows tend to move onshore in the

deeper north-eastern half of the bay to replace water pushed offshore at the surface. When a flat-bottomed representation of Poverty Bay was simulated in Chapter 7, horizontal circulation broke down, indicating the importance of the depth variation. Glorioso and Davies (1995) demonstrated that a bay with variable depths was more prone to horizontal circulation than one with a flat bottom. Glorioso and Davies (1995) found that in an idealised bay with a flat bottom, surface wind stress induced a two-layer vertical circulation with surface flow in the wind direction and opposing bottom-return-flow, i.e. upwelling or downwelling. On introduction of a deep central channel in the bay, horizontal circulation was induced as bottom-return-flows concentrated in the channel, while wind-induced surface flows concentrated in the shallow margins. Hunter and Hearn (1987) explain that for wind-driven flows in closed or partially enclosed basins: in shallower water the dominant force balance is between surface wind stress and bottom friction, yielding a current in the direction of the wind. In deeper water, the dominant force balance is between the horizontal pressure gradient (induced by the surface slope) and bottom friction, yielding a current flowing in opposition to the wind. Horizontal circulation in a wind-driven bay is therefore controlled by the interaction between wind direction and the bathymetry.

This study has identified a different forcing mechanism for the time-averaged anticyclonic gyre (specific thesis aim 5) than that presented by Black et al. (1997). Model simulations by Black et al. (1997) suggested that 'circulation in the bay below the surface in the mid-water column was dominated by rotating eddies that responded to currents passing the entrance on the continental-shelf. The anticyclonic eddy was more pronounced, driving a net anticyclonic circulation in the bay'. Based on measured shelf-currents, the simulations of this study (Chapter 7) have shown that shelf-current velocities were approximately 5 times over-predicted by Black et al. (1997), (who had no shelf-current data), and eddies therefore have a much lesser role in forcing Poverty Bay circulation than concluded in that study.

Hunter and Hearn (1987) show that for most natural topographies, the total circulation is dominated by the horizontal circulation, and that low bottom roughness is particularly conducive to horizontal circulation. Poverty Bay has

low bottom roughness and exhibits substantial horizontal circulation, although vertical circulation is often well developed also. The time-averaged (anticyclonic) horizontal current speed in the bay was ~0.04 m s^{-1} and assuming an approximate median flow path through the time-averaged gyre centre of 15 km, this gives an approximate time of 5 days for a water particle to traverse the bay in the horizontal circulation.

Freshwater mixing typically reduces surface salinities to < 34.5 psu in Poverty Bay, particularly in the river plumes. The prevailing horizontal gyre in combination with time-averaged upwelling in the vertical dimension causes a high salinity surface slug of ~34.6 psu to form in central and inner Poverty Bay, between the two rivers. This is close to the background marine salinity of 34.8-35.0 psu. The model demonstrated this situation to arise under the prevailing offshore wind conditions as upwelling marine water was brought inshore. The prevalent anticyclonic horizontal flow favoured onshore transport along the northern side of the bay, and the marine water surfaced near the centre of the anticyclonic gyre and in the inner bay. The Waipaoa River discharge and offshore horizontal flow hindered the surfacing of marine water along the southern side of the bay. The anticyclonic gyre was usually disturbed by onshore wind events. Horizontal circulation was complex and did not settle into a consistent pattern during onshore wind periods, which tend to be of short duration and usually exhibit some directional swing while remaining generally onshore.

The following discussion summarises the role of shelf-current forcing in Poverty Bay (specific thesis aim 2) and addresses the important bathymetric controls on eddy formation in the bay (specific thesis aim 1). Measured continental-shelf-currents commonly reached 0.15 m s^{-1} with a maximum of 0.36 m s^{-1} and although relatively unimportant in the inner reaches of Poverty Bay modelling showed they influenced circulation in the outer bay at depths greater than ~18 m (Chapter 7). As shown in Chapter 2, shelf-currents of these magnitudes are capable of inducing eddies in a coastal embayment flanked by an abrupt headland (eg. Figure 8-4), and will induce a gyre in the centre of a smooth embayment on flow deceleration (eg. Figure 8-5 & Figure 8-6). Topographically generated coastal eddies are associated with upwelling near the eddy centre and

downwelling at the extremities (Deleersnijder et al., 1992; Lee et al., 1999b), and have also been shown to enhance bay to shelf advection of river plumes (Lin et al., 1994). They are therefore important mechanisms for exchange between coastal embayments and the adjacent continental-shelf, in embayments with wide shelf exposure. These eddies differ from the quadrupole of transient eddies commonly observed at various stages of the tide adjacent to a narrow tidal inlet, where the inlet/shelf waters are separated by shallow tidal deltas and the eddies play little role in exchange between the water bodies (Ridderinkhof, 1989). The most critical parameters governing eddy formation inside exposed coastal embayments are shelf-current speed and the dimensions of the headlands flanking the bay (Chapter 2), although other bathymetric features (such as a point reef or depth disparities) become important if the headlands are not abrupt and do not project out into the continental-shelf flow. Therefore, aside from its wide and deep entrance that allow free exchange between the bay and shelf, the key bathymetric features controlling Poverty Bay's interaction with the continental-shelf are the headlands. These principles are applicable to other coastal embayments, since they are often constrained by some form of hard substrate headland. In Poverty Bay, the preferred position for eddy formation was inside Tuaheni Point (Figure 8-7). Tuaheni Point and its associated underwater reef project abruptly onto the continental-shelf, and when shelf-currents flow southward with sufficient velocity, this causes flow separation and creates a wake inside the bay in which cyclonic eddies form. Conversely, Young Nicks Head has more evenly contoured reef that does not cause flow separation and provides little shelter for wake or eddy formation. Geometrical asymmetry is common in natural environments and it can be expected that one flanking headland will often dominate recirculation in coastal embayments, such as Nan Wan Bay where disparate headland shapes help control tide-driven eddy formation in one half of the bay (Lee et al., 1999a). In areas where shelf-currents are strong, then topographically generated eddies can consume the bay and dominate circulation, such as Nan Wan Bay (Lee et al., 1999b) and Yin-Yang Bay (Lin et al., 1994). This present study shows that shelf-current-driven eddies have a minor effect on circulation in Poverty Bay, but act to complicate flow in the outer bay. This makes circulation in the outer bay the most difficult to numerically model. Circulation here experiences eddy effects and shelf-current intrusion, while also

responding to the wind and river-driven processes that dominate in the inner bay. The balance varies in time depending on the relative magnitude of the shelf-currents compared with inner bay hydrodynamics.

8.3 IMPLICATIONS FOR OUTFALL EFFLUENT, LOBSTER RECRUITMENT AND AQUACULTURE DEVELOPMENTS

In the long term, time-averaged circulation in Poverty Bay is important to sedimentation in the port environs, the dispersal of sewage released from the submarine outfall, the advection of water-borne lobster larvae (*pueruli*) to recruitment areas inside the bay, and potential future aquaculture developments.

Sedimentation in the port and its approach channel was addressed during the Port Gisborne AEE investigation (Stephens et al., 1997). This study supports those results; the prevailing anticyclonic circulation will tend to transport sediment from the old spoil ground site (Figure 1-5) back into the dredged channel in time. The ports proximity to the Turanganui River and its exposure to wave action also influence sedimentation, and these processes were addressed in the initial AEE investigation and are beyond the scope of this thesis.

Sewage discharged into Poverty Bay is buoyant on account of its high freshwater content and rises directly to the surface, entraining seawater to form a buoyant surface plume (Stephens and Black, 1998). Therefore, surface water movement controls its dispersal and under the time-averaged circulation pattern, sewage can be expected to exit the bay past Tuaheni Point during offshore winds, or to flow alongshore toward the Waipaoa River and Young Nicks Head during calm wind conditions. This is a favourable outcome for beach users, but possibly results in some contamination on the rocky foreshore adjacent to Tuaheni Point. Sewage mixed into the upper 5 m of the water column is also likely to be carried along the eastern rocky-reef shoreline in the time-averaged seaward return-flow, providing a possible health hazard in this area. Episodic southerly and easterly wind events will bring sewage effluent onshore, particularly in the afternoon when the sea-breeze often occurs. At typical transport velocities of approximately 0.1 m s^{-1} the sewage would take around 5 hours to reach the beach, but the wind-wave chop

associated with onshore winds tends to mix and disperse the plume (Stephens and Black, 1998). However, *Faecal coliform* and *enterococci* counts are still highest in the margins of the bay during onshore winds (Pickett, 1999). The mean salinity patterns during the simulation period (Chapter 7, Figure 7-34) show that freshwater introduced at the surface tends to accumulate in the northeast corner of the bay on mixing downward through the water column. Combined with the proximity of the sewage outfall, contamination from the Turanganui River via broken sewer pipes (Pickett, 1999) and high recreational usage, this corner of the bay provides the greatest health hazard.

Rock lobster are a valuable domestic and export resource in the Gisborne region. The wharves of Port Gisborne are an important recruitment area for juvenile rock lobster (*pueruli*), but the mechanisms of their transport to the area remain unknown. Uncertainty exists as to whether lobster larvae actively seek recruitment habitat or happen upon it by chance (Jeffs, 1999), but it is known that in the onshore moving *puerulus* phase they often swim actively at night and seek shelter during the day (Booth and Phillips, 1994). Night swimming *pueruli* have been observed at the surface but also lower in the water column (Booth and Phillips, 1994). The prevailing offshore wind climate in the Gisborne region reduces the chances of settlement in the port area by surface swimming *pueruli*, but tends to induce shoreward flow past the port entrance in the lower water column. The commonly observed anticyclonic circulation and the seaward return flow in shallow water along the inner northeast edge, are conducive to lobster settlement along the port side of the bay if they travel below the surface layer.

Local Gisborne iwi have expressed interest as to the feasibility of aquaculture farming in Poverty Bay. Aquaculture is an increasing worldwide trend as natural seafood supplies decrease in abundance. In New Zealand, aquaculture is undertaken in environments sheltered from wave action, such as the Marlborough Sounds, and the active Poverty Bay wave climate has so far precluded such developments. Future aquaculture in the bay would depend on installation of breakwaters to provide a sheltered environment or an improvement in aquaculture technology. However, if such developments were to occur they would depend on adequate nutrient supply, acceptable sedimentation loads and bacterial

contamination levels, which are circulation dependent. The active sandy beach along the northwest edge of the bay is obviously unsuitable due to high wave activity. The northeast coast experiences some sheltering from Tuaheni Point and is comprised of rocky reef that helps to dissipate wave energy. Under the prevailing circulation patterns the northeast side of Poverty Bay receives the highest influx of marine water, which generally contains the cleanest water with adequate nutrients for successful aquaculture. However, in Chapter 7 the model showed a time-averaged seaward return-flow in the upper 5 m along the inner northeast edge of the bay (Figure 7-34). Therefore the inner northeast edge of the bay receives a relatively high proportion of the Turanganui River plume and sewage contamination. Pending qualified investigation into the bacterial limits needed for safe aquaculture, any development may need to be located at least half way from the port toward Tuaheni Point. However, planned sewage treatment improvements in Gisborne city may facilitate aquaculture development closer to the port.

Conversely the southwest of the bay is affected by the Waipaoa River discharge, it receives relatively high freshwater inputs and episodic mud deluges. The impact on the seabed of the high Waipaoa River mud discharges was evident from the AEE investigation, where a muddy sediment tongue was observed in central Poverty Bay offshore from the Waipaoa River (Beamsley et al., 1997; Healy et al., 1997; Foster and Carter, 1997), with a correspondingly low seabed biodiversity (Cole et al., 1997). Successful aquaculture on the southwest side of the bay would need to be located sufficiently far from the Waipaoa River to avoid regular siltation and the possibility of episodic high sediment load flood events would need to be assessed. The Waipaoa River also has elevated bacterial counts although these are more restricted in extent than in the northeast of the bay (Pickett, 1999). Based on the circulation patterns identified in this thesis, the most suitable area for aquaculture is adjacent the Wherowhero Lagoon (Figure 1-2) which is sheltered from southerly swell wave activity by Young Nicks Head (Miller, 1981; Kensington, 1990) and has a broad shallow sand flat. Based on mean salinities from simulations in Chapter 7, this area is also infrequently affected by the Waipaoa plume and has low bacterial counts (Pickett, 1999). However, the area is likely to be vulnerable to episodic mud sedimentation due to

non-rotational large flood discharges, and the impact of these events would require careful prior investigation. This area is also likely to be subjected to regular sea waves (chop) generated by the prevailing northwest wind, perhaps requiring a light breakwater for shelter.

8.4 CONCLUSIONS

Based on the results of Chapters 2-7, this chapter has discussed hydrodynamic forcing and typical circulation patterns in Poverty Bay, drawing comparisons with other coastal embayment studies worldwide. The discussion has examined prominent bathymetric controls on circulation and hydrodynamic forcing by tides, waves, coastal-trapped-waves, continental-shelf-currents, river discharges and wind stress. Typical circulation patterns during offshore and onshore winds are demonstrated in Figure 8-1 and Figure 8-2 respectively, and typical plume-dominated circulation during high Waipaoa River discharge is illustrated in Figure 8-3. The mechanisms for eddy formation in an embayment with abrupt headlands are illustrated in Figure 8-4 and those in a smooth embayment illustrated by Figure 8-5 and Figure 8-6, while the favoured shelf-current induced circulation in Poverty Bay is illustrated in Figure 8-7. The implications of the newly discovered knowledge of Poverty Bay hydrodynamics have been discussed for outfall effluent dispersal, lobster recruitment and aquaculture developments. Based on this discussion and the results of preceding chapters, the following chapter presents conclusions to address the specific thesis aims.

8.5 FIGURES

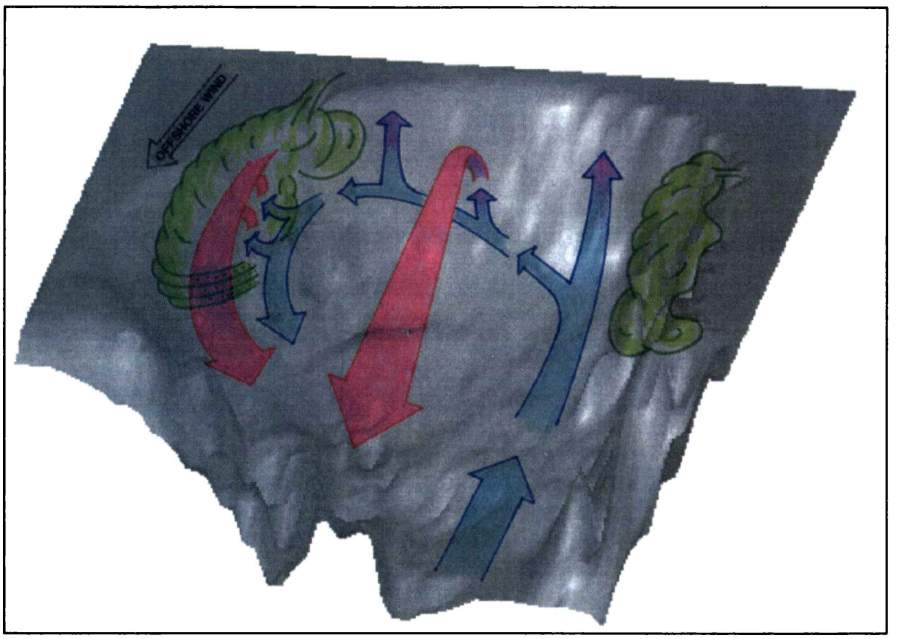

Figure 8-1. Three-dimensional shaded surface plot of Poverty Bay, showing typical circulation under *offshore* winds. Surface water migration is marked in red and bottom water migration in blue. River plumes are depicted in green.

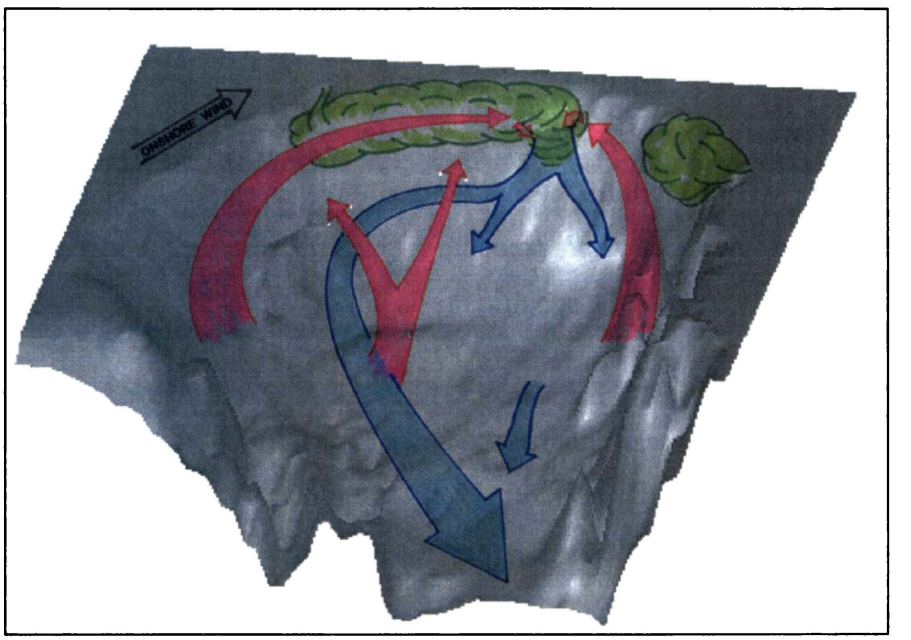

Figure 8-2. Three-dimensional shaded surface plot of Poverty Bay, showing typical circulation under *onshore* winds. Surface water migration is marked in red and bottom water migration in blue. River plumes are depicted in green.

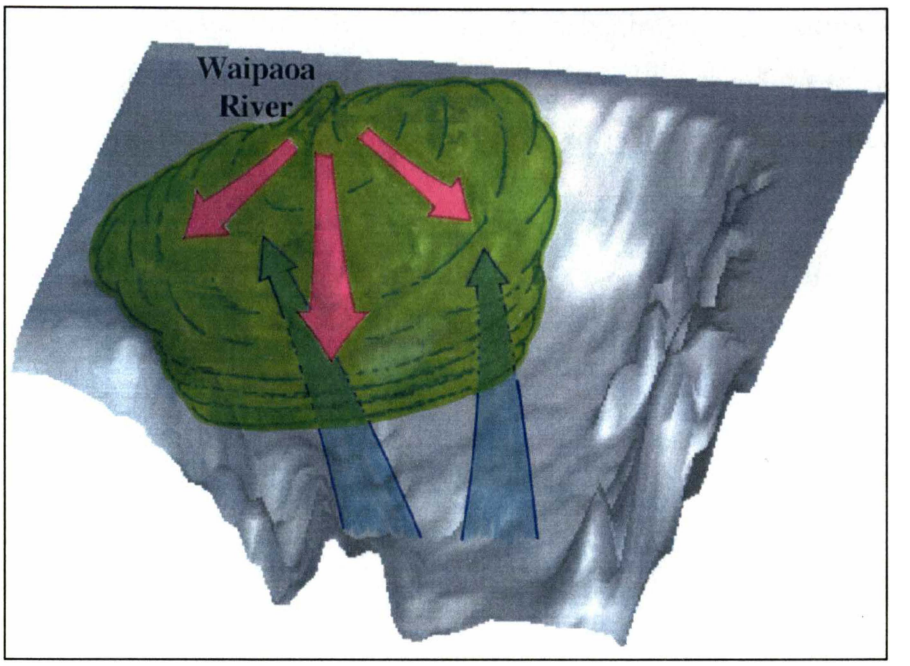

Figure 8-3. Three-dimensional shaded surface plot of Poverty Bay, showing typical circulation during high-discharge from the Waipaoa River. Surface water migration is marked in red and near-bed water migration in blue. The river plume is depicted in green.

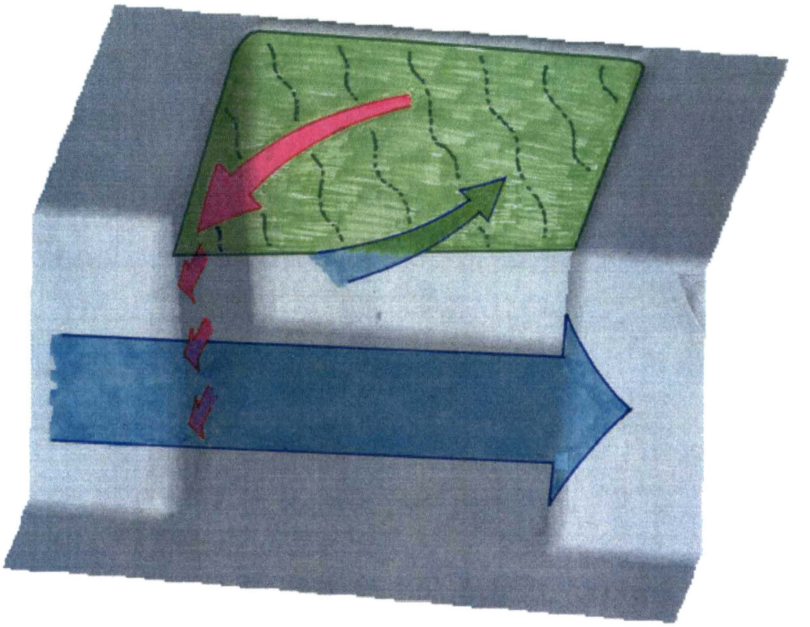

Figure 8-4. Three-dimensional shaded surface plot of a bluff-body embayment bathymetry (**Figure 7-42**a), depicting a steady-velocity continental-shelf-current turning into the embayment (blue arrows), embayment water entrained into the

shelf-current from behind the upstream headland (small red arrows), sea surface elevation in the embayment showing set-up against the downstream coast and set-down in the upstream headland lee due to horizontal shear entrainment (green), and surface return-flow (large red arrow).

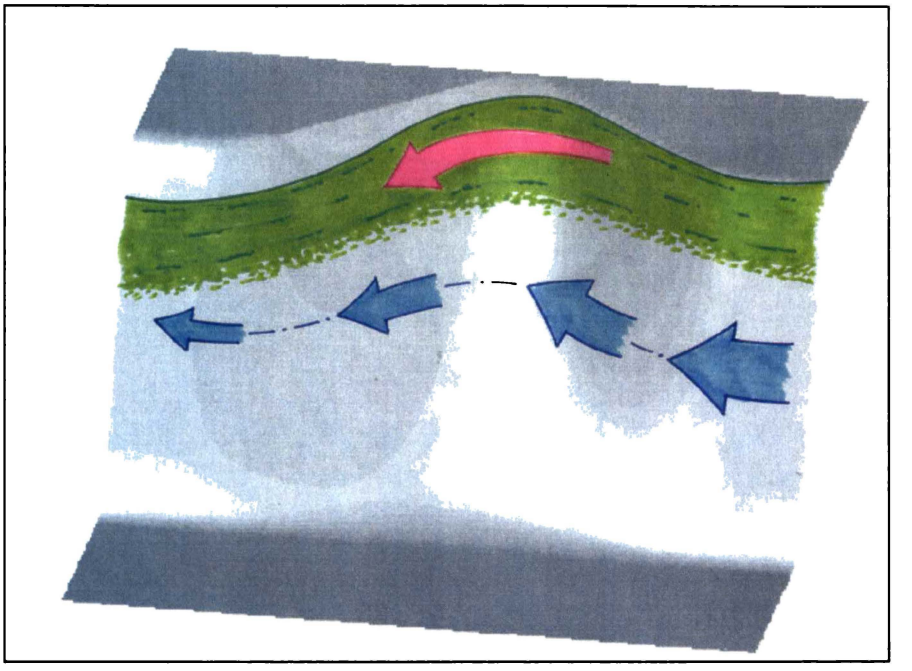

Figure 8-5. Three-dimensional shaded surface plot of a smooth embayment bathymetry (**Figure 7-41**), depicting an accelerating continental-shelf-current (blue arrows) sea surface elevation at the coast (green) and surface water flow in the smooth embayment (red arrow). No eddy forms in this situation.

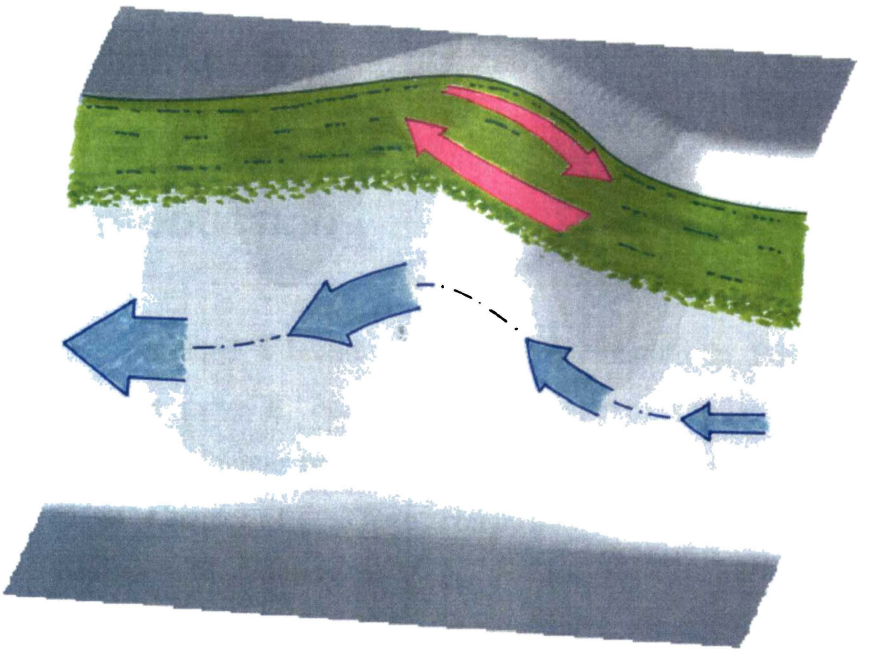

Figure 8-6. Three-dimensional shaded surface plot of a smooth embayment bathymetry (**Figure 7-41**), depicting a deccelerating continental-shelf-current (blue arrows) sea surface elevation at the coast (green) and surface water flow in the smooth embayment (red arrows). Eddy formation occurs due to favourable sea-surface pressure-gradients induced by the decelerating shelf-current.

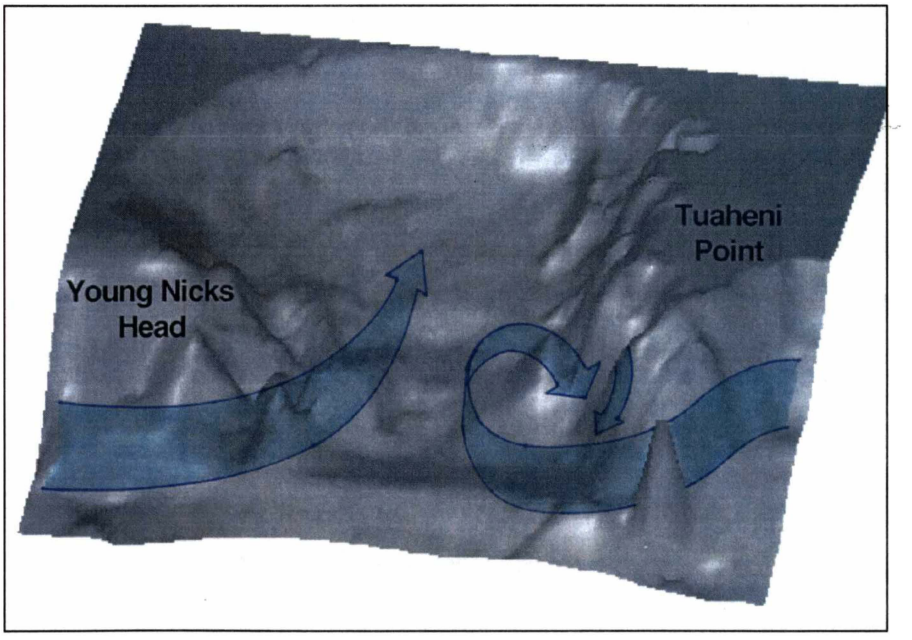

Figure 8-7. Three-dimensional shaded surface plot of Poverty Bay, depicting a south-westerly continental-shelf-current forming an eddy adjacent to Tuaheni Point, and a north-easterly shelf-current flowing into Poverty Bay.

9 – Conclusions

9.1 INTRODUCTION

Chapter 8 provided a broad summary of circulation in Poverty Bay and the processes that drive it, comparing the results to similar coastal embayment examples. This chapter provides conclusions to address the specific thesis aims outlined in Chapter 1. These conclusions describe the three-dimensional hydrodynamics of Poverty Bay in the context of its bathymetry, forcing parameters and typical circulation patterns.

9.2 SPECIFIC THESIS AIMS

9.2.1 Specific thesis aim 1 – the interplay between bathymetry and hydrodynamics

Eddy formation in a coastal embayment was investigated using two-dimensional simulations of simple bathymetries and shelf-currents, modelled on Poverty Bay, New Zealand. The enclosed geometry of an embayment creates recirculation-favourable pressure gradients in comparison to islands, reefs and headlands (eg. Figure 8-4). Consequently, recirculation occurs earlier, and an embayment eddy parameter E was developed to predict embayment recirculation. Recirculation is induced by a steady shelf-current when E is ~1 or greater. E is based on the island wake parameter P, but includes a correction factor $dP = 5.1\times10^5 \frac{L}{w}(\frac{h}{w})^2$ to allow for recirculation-favourable pressure gradients set up against the downstream coast of an embayment. These effects are least for wide embayments and greatest for narrow embayments. The change in propensity for eddy formation (dP) in a coastal embayment compared with that of an island can therefore be quantified in terms of two dimensionless length-scale ratios. The propensity for eddy formation increases with the ratio $\frac{L}{w}$ (embayment cross-shore length over

alongshore length), since this provides a geometric control on the size of the wake in which eddies form. The propensity for eddy formation is more sensitive to the second ratio $\frac{h}{w}$ (embayment depth over alongshore length), which represents the degree of frictional eddy damping within the embayment. As $\frac{h}{w}$ increases, frictional damping decreases within the embayment and eddies are more likely to form.

Simulation of simple bathymetries showed that the bathymetric features having largest influence on embayment circulation were the cross-shore seabed gradient and the shape of the headlands. Correct depth representation was more important for modelling circulation in the inner bay where headland effects were minor or non-existent, whereas the headlands influenced currents closer to the bay entrance, particularly in the lower water column. The cross-shore seabed gradient guided up- and downwelling currents, and thus provided an important control on the response of the mid and lower water column to surface-driven flow.

In smooth coastal embayments where headland effects are minor, the presence of a point reef has a strong influence on recirculation, facilitating earlier development and stronger growth of phase eddies. This can occur due to both increased friction and associated turbulence increasing horizontal eddy viscosity over the reef. At Poverty Bay, Tuaheni Point has a reef that projects onto the continental-shelf, providing an obstruction to shelf-currents. This creates a wake in its lee that is the preferred position for eddy formation (Figure 8-7). The physical presence of the Tuaheni Point headland and reef has more influence than increased frictional associated with the reef.

9.2.2 Specific thesis aim 2 – investigate continental-shelf-currents and their role in Poverty Bay

Continental-shelf-currents exhibited a strong non-tidal component (81% of variance) with relatively small tidal flows. During the field study non-tidal shelf-currents reached 0.32 m s^{-1} with a mean of 0.09 m s^{-1}, whereas tidal currents reached 0.12 m s^{-1} with a mean of 0.04 m s^{-1}.

Wavelet analyses showed that wind-forcing of continental-shelf-currents occurred throughout the field study period, at the majority of resolvable frequencies between 8 and 512 hours. This explains the large proportion of energy contained in the non-tidal shelf-current component.

Coastal-trapped-waves with amplitudes of 0.1 m and velocities 0.2 m s^{-1} also contributed to non-tidal shelf-current motion. Correlation and regression analyses showed that CTWs generated by wind-driven water flux through Cook Strait, could account for up to 40% of variance in Gisborne shelf-currents, at timescales of 2-20 day period. Simulated sea-levels showed 88% energy attenuation occurred as CTWs exited Cook Strait, but only 3% attenuation occurred as CTWs travelled up-coast from Riversdale, therefore a barotropic CTW generated by a Cook Strait flux had approximately 9% its original energy on reaching Gisborne. The small inner bay response to tidal forcing indicates that the response of Poverty Bay to coastal-trapped-waves is likely to be minimal, because there appears little phase lag between sea-level on the bay and shelf.

Continental-shelf-currents formed occasional eddies in the lee of Tuaheni Point with horizontal diameters of ~4 km and velocities up to 0.1 m s^{-1} (eg. Figure 8-7). Continental-shelf-currents contributed ~0.01 m s^{-1} to circulation in depths less than 18 m, small in comparison to those typically measured of 0.05-0.10 m s^{-1}. In depths greater than 18 m, shelf-currents intruded into the bay at speeds up to 0.05 m s^{-1}.

9.2.3 Specific thesis aim 3 – gather data of sufficient spatial coverage and quality to calibrate Model 3DD

Vessel-mounted ADP provided comprehensive spatial resolution of circulation in Poverty Bay. In combination with CTD measurements this provided a clear snapshot of three-dimensional circulation during the survey period. When combined with a continuous-recording current-meter deployment on the continental-shelf plus wind and river discharge measurements, these surveys provided data of sufficient spatial coverage and quality to calibrate a three-

dimensional numerical model. Measured velocities were typically 0.05-0.10 m s^{-1} inside the bay.

Model calibration involved the comparison of 60 simulations with measured data, during which the following parameter values were selected: A_H = 1 m^2 s^{-1}, K_H and K_Z = 0.005 m^2 s^{-1}, C'_M and C'_S were set to 12 and 5 respectively. Calibration also included appropriate adjustments to the wind speed and to river discharge timing and volume. The land-based measured wind speed was adjusted to an equivalent velocity over sea using the Hsu (1986) formula, but required a further 1.5 times multiplication factor to achieve realistic current-velocity predictions. The wind speed multiplication factor was required to account for the inadequacies of using land-based wind measurements in place of those over the sea and the inapplicability of the Wu (1982) wind drag coefficient C_d formula, used to calculate wind stress in the model. The measured Waipaoa River discharge was delayed by 15 hours and multiplied by 1.5 to account for the ~27 km distance between the gauging station and the bay. Following calibration the model generally predicted velocity and salinity patterns successfully, although occasional disruptions arose from inaccuracies in the body-force used to drive the model. Excessive horizontal salinity diffusion due to the mass conserving (Eulerian) advection/dispersion scheme created further inaccuracies. However, circulation was sufficiently well predicted to use the calibrated model for separation and analysis of the processes contributing to Poverty Bay hydrodynamics, namely shelf-currents, wind and river discharge. Simulations showed that wind-stress and river-discharge dominated circulation and accurate simulations of the inner bay could be undertaken without requiring continental-shelf-current data.

9.2.4 Specific thesis aim 4 – investigate the balance between wind and river-induced hydrodynamics

Under most conditions, the wind was the most important contributor to circulation with a response time of 1 hour for the upper and lower layers and ~5 hours in the mid-water column. Field measurements identified an up/down-welling response to cross-shore directed winds with speed $\geq$ 4 m s^{-1}, while the calibrated numerical model demonstrated a more subtle surface and near-bed current response to winds exceeding 2 m s^{-1} (i.e. a near-continuous response). The long-term wind-record

suggested that offshore winds prevail 77% of the time, and these have been shown to drive a time-averaged upwelling vertical circulation and an anticyclonic mid-water gyre (eg. Figure 8-1). The time-averaged vertical circulation is characterised by the offshore flow of buoyant surface water and onshore flow of dense marine water. A time-averaged horizontal anticyclonic gyre exists in the mid-water column as water flows in past Tuaheni Point, circles the bay and flows out past Young Nicks Head. The time-averaged surface salinity/density pattern is characterised by fresher plume water extending offshore in the vicinity of the two rivers, and a high salinity/density area in the central and inner bay between the river plumes. In the mid-water column, freshwater tends to accumulate in the northeast corner of the bay near the port, trapped by the anticyclonic horizontal circulation.

Variability to the typical circulation occurred during times of onshore wind stress, approximately 23% of the time (eg. Figure 8-2). Simulations suggested that once Waipaoa River discharge is greater than 60 $m^3 s^{-1}$ it can begin to dominate wind-induced circulation, but this occurs only 11% of the time. Conversely, winds of speed less than 5 $m s^{-1}$ may have little effect once the Waipaoa River discharge has reached this level.

Although wind stress dominated circulation during low-discharge periods, river discharge stratified the water column, with a surface-mixed layer incorporating substantial freshwater commonly of ~2 m depth, but varying between 1-10 m. During the study period salinities were typically < 34.5 psu in the surface layer compared with 34.8-35.0 psu in marine water, although surface salinities of ~32 psu were observed following the 74 $m^3 s^{-1}$ (peak) fresh on 19 September 1998. Freshwater-induced stratification served to reduce vertical mixing, enhance shear, and facilitate faster horizontal velocities, thus creating higher sensitivity to wind-driven processes.

The prevailing wind created circulation similar to the Waipaoa River discharge; therefore both processes contributed to the prevailing anticyclonic horizontal circulation in the bay (Figure 8-1).

9.2.5 Specific thesis aim 5- re-investigate the mechanisms responsible for the observed time-averaged anticyclonic horizontal gyre

Poverty Bay exhibits a single anticyclonic time-averaged gyre in the mid-water column of ~0.04 m s^{-1} (eg. Figure 8-1). This results primarily from the interaction between the prevailing north-northwest winds and the bathymetry. The prevailing wind direction is offset to the cross-shore axis of the bay and tends to push more surface water toward the southern side and out past Young Nicks Head (time-averaged cross-shore surface velocity 0.10 m s^{-1}) than past Tuaheni Point (time-averaged cross-shore surface velocity 0.03 m s^{-1}). Additionally, the bay is deeper in the northern entrance and simulations in Chapter 7 showed this to be the preferred channel for bottom-return-flows, with a mean shoreward flow of ~0.05 m s^{-1} (eg. Figure 8-1). The horizontal circulation is therefore interdependent with vertical circulation and their magnitudes are approximately similar. Anticyclonic circulation is also contributed by earth rotational forces (Coriolis) acting on the Waipaoa River plume, and this mechanism will be most important during high-discharge conditions (> 60 m^3 s^{-1}).

Freshwater mixing typically reduces surface salinities to < 34.5 psu in Poverty Bay, particularly in the river plumes. The prevailing horizontal gyre in combination with time-averaged upwelling in the vertical dimension often causes a high salinity surface slug of > 34.6 psu to form in central and inner Poverty Bay, between the two rivers.

9.3 IMPLICATIONS FOR OTHER COASTAL EMBAYMENTS

Although the complexity of the interaction between shelf-currents, wind stress, river discharge, temperature inputs and bathymetry are unique to Poverty Bay, many aspects of this thesis are applicable to other bays. The following thesis findings can be applied to other embayments in a qualitative sense.

The bathymetric characteristics of the bay entrance determine the interaction with any continental-shelf-current. Whereas narrow-necked embayments may be

subject to tidal jetting, embayments with a wide entrance allow smooth transition of sea-level changes between the bay and shelf, with little phase lag and minimal associated currents. Their interaction is instead influenced by the degree of bathymetric projection into the passing shelf-current and the horizontal embayment dimensions, which control the formation of eddies that advect shelf water into the bay. Nan Wan Bay (Lee et al., 1999b) and Yin-Yang Bay (Lin et al., 1994) are examples of embayments that experience strong internal eddy formation caused by adjacent headlands projecting into the shelf-current, whereas Jervis Bay (Holloway et al., 1992) is a contrary example. The likelihood of eddy formation also increases with shelf-current velocity, and the embayment eddy parameter E provides a tool that accounts for both bathymetric and velocity constraints when predicting embayment eddies.

Where freshwater discharges are minimal, temperature can dominate stratification (eg. Jervis Bay, (Holloway et al., 1992)). Significant freshwater inputs into an embayment serve to density-stratify the bay, and force circulation via both barotropic and baroclinic pressure gradients. In Poverty Bay the Waipaoa River exerts dominance over wind-induced circulation above ~60 $m^3 s^{-1}$. This equates to a discharge of 0.5% of the bay volume per day, that through diffusion and salt-water entrainment into the plume would affect ~30% of the bay. Embayments with similar freshwater discharge to total volume ratios are expected to also show strong river-induced circulation.

Surficial forcing via wind-stress is present to some degree in all coastal embayments. Higher bed-friction in shallow embayments favours horizontal over vertical wind-forced circulation (Kjerfve et al., 1992). In a deeper embayment such as Poverty Bay, it has been shown that vertical circulation is readily established by wind stress, and this is interdependent with horizontal circulation. The predominantly wind-driven anticyclonic gyre in Poverty Bay is an example of depth-disparity leading to horizontal wind-driven circulation, supporting previous research that currents flow with the wind direction in shallow water and bottom-return-flows occur in deeper sections. For determining coherence between wind and current data sets, wavelet analysis is a far more effective tool than traditional spectral analysis, because of the time-variant nature of the wind-current

relationship, and the hydrodynamic complexity where significant horizontal and vertical wind-driven circulation both occur.

Bibliography

Agnew, R. and Smith, E. T. 1973: Coastal disturbances affecting the North Island of New Zealand. *In:* First Australian Conference on Coastal Engineering, Sydney, Pp. 197-205.

Baisch, S. and Bokelmann, G. H. R. 1999: Spectral analysis with incomplete time series: an example from seismology. *Computers and Geosciences 25*: 729-738.

Beamsley, B., Healy, T. R. and Black, K. P. 1998: Supplementary Report: Proposed inshore sand spoil Ground sedimentological investigation. University Of Waikato, Hamilton, Pp. 50.

Beamsley, B. J., Stephens, S. A. and Healy, T. R. 1997: Geotechnical investigation of Port environs and dredge spoil dump grounds relating to the Port Gisborne Expansion. The University of Waikato, Hamilton, Pp. 137.

Beer, T. 1983: Environmental Oceanography: an introduction to the behaviour of coastal waters, Pergamon Press, New York. 262 p.

Bell, R. G. 1985: Coastal current data from Aanderaa current meter deployments 1982-1985. National Institute of Water and Atmospheric Research, Hamilton, New Zealand.

Black, K., Rosenberg, M., Symonds, G., Pattiaratchi, C. and Nielsen, P. 1996: Measurements of the wave, current and sea level dynamics of an exposed coastal site. *In:* Pattiaratchi, C. *ed.* Coastal and Estuarine Studies, Vol. 1 American Geophysical Union, Washington DC, pp. 29-56.

Black, K. P. 1983: Sediment transport and tidal inlet hydraulics. Unpublished PhD thesis, The University of Waikato, Hamilton. 331 p.

Black, K. P. 1987: A numerical sediment transport model for application to natural estuaries, harbours and rivers. *In:* Noye, J. *ed.* Numerical modelling applications to marine systems, Vol. Elsevier, North Holland, pp. 77-105.

Black, K. P. 1989: Numerical simulation of steady and unsteady meso-scale eddies. *In:* 9th Australasian Conference on Coastal and Ocean Engineering, Adelaide, Pp. 204-208.

Black, K. P. 1995: The hydrodynamic model 3DD and support software. Department of Earth Sciences, The University of Waikato, Hamilton, Pp. 53.

Black, K. P., Bell, R. G., Oldman, J. W., Carter, G. S. and Hume, T. M. 2000: Features of 3-dimensional barotropic and baroclinic circulation in the Hauraki Gulf, New Zealand. *New Zealand Journal of Marine and Freshwater Research 34*: 1-28.

Black, K. P. and de Lange, W. P. 1995: Numerical modelling of physical marine processes. Lecture notes: graduate course 0772.544. The University of Waikato, Hamilton, Pp. 74.

Black, K. P. and Gay, S. L. 1987: Eddy formation in unsteady flows. *Journal of Geophysical Research 92(C9)*: 9514-9522.

Black, K. P. and Gay, S. L. 1991: Reef-scale numerical hydrodynamic modelling developed to investigate crown-of-thorns starfish outbreaks. *In:* Bradbury, R. *ed.* Acanthaster and the Coral Reef: A Theoretical Perspective, Vol. Springer-Verlag, pp. 120-150.

Black, K. P., Gorman, R. M., Stephens, S. A., Beamsley, B. J., Healy, T. R., Bell, R. G. and Oldman, J. W. 1997: Numerical modelling for the Port Gisborne expansion. The University of Waikato and National Institute of Water and Atmospheric Research, Hamilton, Pp. 303.

Black, K. P., Hatton, D. and Rosenberg, M. 1993: Locally and externally-driven dynamics of a large semi-enclosed bay in southern Australia. *Journal of Coastal Research 9(2)*: 509-538.

Black, K. P. and Hatton, D. N. 1992: Hydrodynamic and Sediment Dynamic Measurements in Eastern Bass Strait. Volume 4: Two and three-dimensional numerical hydrodynamic and dispersal models. Victorian Institute of Marine Sciences, Melbourne, Pp. 66.

Black, K. P., Healy, T. R. and Hunter, M. 1989: Sediment dynamics in the lower section of a mixed sand and shell-lagged tidal estuary. *Journal of Coastal Research 5(3)*: 503-521.

Booth, J. D. and Phillips, B. F. 1994: Early life history of spiny lobster. *Crustaceana 66(3)*: 271-291.

Brodie, J. W. 1960: Coastal surface currents around New Zealand. *New Zealand Journal of Geology and Geophysics 3(2)*: 235-252.

Buchwald, V. T. and Adams, J. K. 1968: The propagation of continental shelf waves. *Proceedings of the Royal Society 305(A)*: 235-250.

Buchwald, V. T. and Kachoyan, B. J. 1987: Shelf waves generated by a coastal flux. *Australian Journal of Marine and Freshwater Research 38(3)*: 429-437.

Burling, M. C., Ivey, G. N. and Pattiaratchi, C. B. 1999: Convectively driven exchange in a shallow coastal embayment. *Continental Shelf Research 19(12)*: 1599-1616.

Burrage, D. M., Black, K. P. and Steinberg, C. R. 1995: Long-term sea-level variations in the central Great Barrier Reef. *Continental Shelf Research 15(8)*: 981-1014.

Cahill, M. L., Middleton, J. H. and Stanton, B. R. 1991: Coastal-trapped waves on the west coast of South Island, New Zealand. *Journal of Physical Oceanography 21*: 541-557.

Chatfield, C. 1980: The analysis of time series: an introduction, Chapman and Hall, London. 268 p.

Chiswell, R. J. and Roemmich, D. 1998: The East Cape current and two eddies: a mechanism for larval retention. *New Zealand Journal of Marine and Freshwater Research 32(3)*: 385-397.

Chiswell, S. M. 2000: The Wairarapa Coastal Current. *New Zealand Journal of Marine and Freshwater Research 34(2)*: 303-315.

Clark, A. J. and van Gorder, S. 1986: A method for estimating wind-driven frictional, time-dependent, stratified shelf and slope water flow. *Journal of Physical Oceanography 16*: 1013-1037.

Cole, R. C., Dobbie, N. J., Healy, T. R., Hull, P. J., Purdue, S. R. and Stephens, S. A. 1997: Assessment of impacts on fauna and flora of areas affected by the expansion of Port Gisborne Ltd. The University of Waikato, Hamilton, Pp. 110.

Csanady, G. T. 1997: On the theories that underlie our understanding of continental shelf circulation. *Journal of Oceanography 53*: 207-229.

D'Adamo, N., Mills, D. A. and Wilkinson, D. L. 1997: Exchange processes in Cockburn Sound - a seasonally stratified embayment off southwest Australia. *In:* Pacific Ports and Coasts '97, Vol. 2. Centre for Advanced Engineering, Christchurch, Pp. 667-674.

Davies, A. G., Soulsby, R. L. and King, H. L. 1988: A numerical model of the combined wave and current bottom boundary layer. *Journal of Geophysical Research 93(C1)*: 491-508.

de Lange, W. P. 1983: Tsunami hazard: an investigation into potential tsunami hazard of the Bay of Plenty region using numerical models. Unpublished MSc thesis, The University of Waikato, Hamilton. 250 p.

de Lange, W. P. and Healy, T. R. 1986: New Zealand tsunamis 1840-1982. *New Zealand Journal of Geology and Geophysics 29*: 115-134.

Deleersnijder, E., Norro, A. and Wolanski, E. 1992: A three-dimensional model of the water circulation around an island in shallow water. *Continental Shelf Research 12(7/8)*: 891-906.

Denhem, R. N., Bannister, R. W., Guthrie, K. M. and Crook, F. G. 1984: Surveys of the East Auckland and East Cape currents, New Zealand. *Australian Journal of Marine and Freshwater Research 35*: 491-504.

Denniss, T. and Middleton, J. H. 1994: Effects of viscosity and bottom friction on recirculating flows. *Journal of Geophysical Research 99(C5)*: 10183-10192.

Denniss, T., Middleton, J. H. and Manasseh, R. 1995: Recirculation in the lee of complicated headlands: A case study of Bass Point. *Journal of Geophysical Research 100(C8)*: 16087-16101.

Dera, J. 1992: Marine physics, Elsevier, Amsterdam. 516 p.

Ferentinos, G. and Collins, M. 1980: Effects of shoreline irregularities on a rectilinear tidal current and their significance in sedimentation processes. *Journal of Sedimentary Petrology 50*: 1081-1094.

Foreman, M. G. G. 1978: Manual for tidal currents analysis and prediction. Institute of Ocean Sciences, Patricia Bay, Victoria, British Columbia, Canada, Pp. 70.

Foster, G. and Carter, L. 1997: Mud sedimentation on the continental shelf at an accretionary margin - Poverty Bay, New Zealand. *New Zealand Journal of Geology and Geophysics 40*: 157-173.

Furukawa, K. and Wolanski, E. 1998: Shallow water frictional effects in island wakes. *Estuarine, Coastal, and Shelf Science 31*: 231-253.

Galperin, B. and Mellor, G. L. 1990: A time dependent, three dimensional model of the Delaware Bay and river system. Part 1: Description of the model and tidal analysis. *Estuarine, Coastal and Shelf Science 31*: 1307-1317.

Garvine, R. W. 1987: Estuary plumes and fronts in shelf waters: A layer model. *Journal of Physical Oceanography 17(11)*: 1877-1896.

Gerrard, S. 1989: New Zealand North Island East Coast: Cape Runaway to Table Cape, NZ55. Hydrographic Office of the Royal New Zealand Navy, Auckland.

Gill, A. E. 1982: Atmosphere-ocean dynamics, Academic Press, San Diego. 662 p.

Gilmour, A., E. 1987: A preliminary rotary spectral analysis of inertial currents off the west coast of New Zealand. *New Zealand Journal of Marine and Freshwater Research 21(2)*: 353-357.

Gisborne District Council 1994: Waipaoa River at Kanakanaia - monthly suspended sediment yields. Gisborne District Council, Gisborne, Pp. 2.

Gisborne Harbour Board 1984: The east coast timber port of the 1980's. Port Gisborne Ltd., Gisborne, Pp. 6.

Glorioso, P. D. and Davies, A. M. 1995: The influence of eddy viscosity formulation, bottom topography, and wind wave effects upon the circulation of shallow bays. *Journal of Physical Oceanography 25*: 1243-1264.

Golden Software 1996: Surfer. Golden Software Inc., Colorado.

Goring, D. G. 1995: Short level variations in sea level (2-15 days) in the New Zealand region. *New Zealand Journal of Marine and Freshwater Research 29*: 69-82.

Goring, D. G. and Bell, R. G. 1999: El Nino and decadal effects on sea-level variability in northern New Zealand: a wavelet analysis. *New Zealand Journal of Marine and Freshwater Research 33*: 587-598.

Gorman, R. M., Stephens, S. A., Beamsley, B. J., Black, K. P., Bryan, K. and Healy, T. R. 1997: Field data collection programme for the Port Gisborne expansion. The University of Waikato and National Institute of Water and Atmospheric Research, Hamilton, Pp. 143.

Hamon, B. V. 1962: The spectrums of sea level at Sydney, Coff's Harbour and Lord Howe Island. *Journal of Geophysical Research 67(13)*: 5147-5155.

Hamon, B. V. 1976: Generation of shelf waves on the East Australian Coast by wind stress. *Memoires Societe Royale des Sciences de Liege 6*: 359-367.

Harms, S. and Winant, C. D. 1994: Synthetic Subsurface Pressure derived from bottom pressure and tide gauge observations. *Atmospheric and Oceanic Technology 11*: 1625-1636.

Hawkey, W. N. 1984: New Zealand Topographical Map: NZMS 260, Y18, Gisborne. Department of Lands and Survey, New Zealand, Wellington.

Healy, T. R., Stephens, S. A., Immenga, D., Mathew, J., Beamsley, B. J. and Black, K. P. 1997: Side-Scan sonar investigation of sedimentation relating to the Port Gisborne expansion. The University of Waikato, Hamilton, Pp. 34.

Heath, R. A. 1978: Atmospherically induced water motions off the west coast of New Zealand. *New Zealand Journal of Marine and Freshwater Research 12(4)*: 381-390.

Heath, R. A. 1980: Eastwards oceanic flow past northern New Zealand. *New Zealand Journal of Marine and Freshwater Research 14(2)*: 169-182.

Heath, R. A. 1985: A review of the physical oceanography of the seas around New Zealand-1982. *New Zealand Journal of Marine and Freshwater Research 19*: 79-124.

Hessell, J. W. D. 1980: The climate and weather of the Gisborne region. *New Zealand meteorological service miscellaneous publication 115(8)*: 29.

Holloway, P. E., Symonds, G. and Nunes Vaz, R. 1992: Observations of circulation and exchange processes in Jervis Bay, New South Wales. *Australian Journal of Marine and Freshwater Research 43*: 1487-1515.

Hsu, S. A. 1986: Correction of land-based wind data for offshore applications: A further evaluation. *Journal of Physical Oceanography 16(2)*: 390-394.

Hunter, J. R. and Hearn, C. J. 1987: Lateral and vertical variations in the wind-driven circulation in long, shallow lakes. *Journal of Geophysical Research 92(C12)*: 13106-13114.

Imasato, N. 1983: What is tide induced Residual Current? *Journal of Physical Oceanography 13*: 1307-1317.

Ivey, G. N. and Patterson, J. C. 1984: A model of the vertical mixing in Lake Erie in summer. *Limnology and Oceanography 29(3)*: 553-563.

Jeffs, A. 1999a: Super-swimmers or lazy lobsters. *In:* New Zealand Marine Sciences Society Conference, Wellington.

Jeffs, A. 1999b: Vertical migration of lobster. December e-mail, National Institute of Water and Atmospheric Research, Auckland.

Jenkins, G. M. and Watts, D. G. 1968: Spectral analysis and its applications, Holden-day, San Francisco. 525 p.

Keen, T. R. and Glenn, S. M. 1999: Shallow water currents during Hurricane Andrew. *Journal of Geophysical Research 104(C10)*: 23443-43458.

Kensington, G. L. 1990: Port developments and dredge spoil dispersion in northern Poverty Bay. Unpublished MSc thesis, The University of Waikato, Hamilton. 235 p.

Kjerfve, B., Seim, H. E., Blumberg, A. F. and Wright, L. D. 1992: Modelling of the residual circulation in Broken Bay and the Lower Hawkesbury River, NSW. *Australian Journal of Marine and Freshwater Research 43*: 1339-1357.

Klinck, J. M. 1996: Circulation near submarine canyons: a modelling study. *Journal of Geophysical Research 101(C1)*: 1211-1223.

Kohl, C. 1989: New Zealand North Island Poverty Bay and approaches to Gisborne, NZ 5613. Hydrographic Office of the Royal New Zealand Navy, Auckland.

Komar, P. D. 1998: Beach processes and sedimentation, Prentice-Hall, New Jersey. 544 p.

Laing, A. K. and Brenstrum, E. 1996: Scatterometer observations of low-level wind jets over New Zealand coastal waters. *Weather and Forecasting 11(4)*: 458-475.

Laing, A. K., Revell, M. J. and Brenstrum, E. 1997: ERS scatterometer observations of airflow around mountainous islands. *In:* Proceedings of the 3rd ERS Symposium on Space at the Service of our Environment, Florence, Italy, Pp. 1579-1584.

Large, W. G. and Pond, S. 1981: Open ocean momentum flux measurements in moderate to strong winds. *Journal of Physical Oceanography 11*: 324-337.

Lee, H.-J., Chao, S.-Y. and Fan, K.-L. 1999a: Flood-ebb disparity of tidally induced recirculation eddies in a semi-enclosed basin: Nan Wan Bay. *Continental Shelf Research 19(7)*: 871-890.

Lee, H. J., Chao, S. Y., Fan, K. L. and Kuo, T. Y. 1999b: Tide-induced eddies and upwelling in a semi-enclosed basin: Nan Wan. *Estuarine, Coastal and Shelf Science 49*: 775-787.

Leendertse, J. J. and Liu, S. K. 1975: Modelling of three-dimensional flows in estuaries. *In:* 2nd Annual Symposium on Modelling Techniques. Waterways, Harbours and Coastal Engineering (ASCE), Pp. 625-642.

Lin, C.-T., Fan, K.-L. and Chao, S.-Y. 1994: Small-scale plumes from a semi-enclosed basin: Yin-Yang Bay. *Terrestrial, Atmospheric and Oceanic Sciences 5(1)*: 91-107.

Liu, J. T., Zarillo, G. A. and Surak, C. R. 1997: The influence of river discharge on hydrodynamics and mixing in a subtropical lagoon. *Journal of Coastal Research 13(4)*: 1016-1034.

McClimans, T. A. 1988: Estuarine fronts and river plumes. *In:* Dronkers, J. and van Leussen, W. *ed.* Physical processes in estuaries, Vol. Springer-Verlag, Berlin, Heidelberg, pp. 55-69.

Middleton, J. F. and Black, K. P. 1994: The low frequency circulation in and around Bass Strait: a numerical study. *Continental Shelf Research 14(13/14)*: 1495-1521.

Middleton, J. H., Griffin, D. A. and Moore, A. M. 1993: Oceanic circulation and turbulence in the coastal zone. *Continental Shelf Research 13(2/3)*: 143-168.

Miller, K. R. 1981: Surficial sediments and sediment transport in Poverty Bay. Unpublished MSc thesis, The University of Waikato, Hamilton. 179 p.

Ministry of Works and Development 1979: East coast project - Gisborne Harbour development. Ministry of Works and Development, Pp. 46.

National Institute of Water and Atmospheric Research 1997: Cover page. *Water and Atmosphere 5(2).*

New Zealand Meteorological Service 1980: Summaries of climatological observations to 1980. *New Zealand Meteorological Service Miscellaneous Publication 177*, Pp.172.

Pattiaratchi, C., James, A. and Collins, M. 1987: Island wakes and headland eddies: a comparison between remotely sensed data and laboratory experiments. *Journal of Geophysical Research 92(C1)*: 783-794.

Perenne, N., Verron, J., Renouard, D., Boyer, D. L. and Zhang, X. 1997: Rectified barotropic flow over a submarine canyon. *Journal of Physical Oceanography 27*: 1868-1893.

Perrels, P. A. J. and Karelse, M. 1982: A two-dimensional laterally averaged model for salt intrusion in estuaries. Delft Hydraulics Laboratory, Pp. 483-535.

Pickard, G. L. and Emery, W. J. 1990: Descriptive physical oceanography: an Introduction, Pergamon Press, New York. 320 p.

Pickett, V. 1999: Submarine sewer outfall, Poverty Bay; coastal permits and resource consent applications; assessment of environmental effects report. Opus International Consultants Limited Environmental, Hamilton, Pp. 62 plus appendices.

Pond, S. and Pickard, G. L. 1983: Introductory dynamical oceanography, Pergamon Press, New York. 329 p.

Prandle, D. and Matthews, J. 1990: The dynamics of nearshore surface currents generated by tides, wind and horizontal density gradients. *Continental Shelf Research 10(7)*: 665-681.

Reid, S. 1996: Pressure gradients and winds in Cook Strait. *Weather and Forecasting 11*: 476-488.

Ridderinkhof, H. 1989: Tidal and residual flows in the Western Dutch Wadden Sea III: vorticity balances. *Netherlands Journal of Sea Research 24(1)*: 9-26.

Schwarz, M. A. 1997: Factors influencing storm surge variability on the New Zealand coast. Diploma in Applied Science (Meteorology) thesis, Victoria University, Wellington. 94 p.

Shirtcliffe, T. G. L., Moore, M. I., Cole, A. G., Viner, A. B., Baldwin, R. and Chapman, B. 1990: Dynamics of the Cape Farewell upwelling plume, New Zealand. *New Zealand Journal of Marine and Freshwater Research 24(4)*: 555-568.

Signell, R. P., Beardsley, R. C., Graber, H. C. and Capotondi, A. 1990: Effect of wave-current interaction on wind-driven circulation in narrow, shallow embayments. *Journal of Geophysical Research 95(C6)*: 2671-9678.

Signell, R. P. and Geyer, W. R. 1991: Transient eddy formation around headlands. *Journal of Geophysical Research 96(C2)*: 2561-2575.

Sinclair, M. R. 1993: A diagnostic study of the extratropical precipitation resulting from tropical cyclone Bola. *Monthly Weather Review 121(10)*: 2690-2707.

Singleton, P., Trotter, C., Widdowson, J., Brenstrum, E. and Brown, L. 1989: Cyclone Bola DSIR extension information. Department of Scientific and Industrial Research, Wellington, Pp. 5.

Smith, R. K. 1975: Sedimentation in Poverty Bay - a study of sediment sources. Ministry of Works and Development, Water and Soil Division, Napier District.

Smith, R. K. 1988: Poverty Bay, New Zealand: a case of coastal accretion 1886-1975. *New Zealand Journal of Marine and Freshwater Research 22(1)*: 135-141.

Sontek 1997: SonTek Acoustic Doppler Profiler (ADP) Principles of Operation: SonTek ADP Introductory Documentation, Software Version 4.4. Sontek Inc., San Diego.

Stanton, B. R. 1995: Sea level variability on the West Coast of New Zealand. *Journal of Physical Oceanography 25(6)*: 1265-1272.

Stephens, S. A. and Black, K. P. 1998: Gisborne district council sewer outfall, field investigation. The University of Waikato, Hamilton, Pp. 49.

Stephens, S. A., Black, K. P., Bell , R. G. and Healy, T. R. in prep: A search for coastal trapped waves on the east coast of the North Island, New Zealand. *New Zealand Journal of Marine and Freshwater Research.*

Stephens, S. A., Black, K. P., Healy, T. R. and Tahata, B. 1999: Circulation in Poverty Bay New Zealand: a verification of numerical modelling predictions. *In:* Coasts and Ports '99: Challenges and Directions for the New Century, Vol. 2. National Committee on Coastal and Ocean Engineering, Institution of Engineers, Australia, Perth, Pp. 639-643.

Stephens, S. A., Healy, T. R., Black, K. P., Beamsley, B. J. and Gorman, R. M. 1997: Overview summary for the Port Gisborne expansion. The University of Waikato, Hamilton, Pp. 29.

The Open University 1989: Ocean Circulation, Pergamon Press, Oxford. 238 p.

Tipler, P. A. 1982: Physics, Worth, New York. 1062 p.

Torrence, C. and Compo, G. P. 1998: A practical guide to wavelet analysis. *Bulletin of the American Meteorological Society 79(1)*: 61-78.

Turnpenny, B., Healy, T. R., Black, K. P. and Tahata, B. 1998: Port Gisborne Limited proposed capital dredging and maintenance dredging: description and assessment of effects. Turnpenny Associates Ltd., Gisborne, Pp. 67.

van Alphen, J. S. L. J., de Ruijter, W. P. M. and Borst, J. C. 1988: Outflow and three-dimensional spreading of Rhine River water in the Netherlands coastal zone. *In:* Dronkers, J. and van Leussen, W. *ed.* Physical processes in estuaries, Vol. Springer-Verlag, Berlin, Heidelberg, pp. 70-92.

Visser, A. W. 1996: Shear dispersion in a wind and density driven plume. *In:* Aubrey, D. G. and Friedrichs, C. T. *ed.* Buoyancy effects on coastal and estuarine dynamics, Vol. American Geophysical Union, Washington DC, pp. 359.

Wang, J., Mysak, L. A. and Ingram, G. 1994: A three-dimensional numerical simulation of Hudson Bay summer ocean circulation: topographical gyres, separations, and coastal jets. *Journal of Physical Oceanography 24(*2496-2514.

Wang, X. H. and Symonds, G. 1999: Coastal embayment circulation due to atmospheric cooling. *Journal of Geophysical Research 104(C12)*: 29801-29816.

Williams, H. C. 1966: The Gisborne submarine sewer outfall. *New Zealand Engineering 21*: 110-120.

Wolanski, E., Asaeda, T., Tanaka, A. and Deleersnijder, E. 1996: 3-dimensional island wakes in the field, laboratory experiments and numerical models. *Continental Shelf Research 16(11)*: 1437-1452.

Wolanski, E., Imberger, J. and Heron, M. L. 1984: Island wakes in shallow coastal waters. *Journal of Geophysical Research 89(C6)*: 10553-10569.

Wright, D. G., Greenberg, D. A. and Majaess, F. G. 1987: The influence of bays on adjusted sea level over adjacent shelves with application to the Labrador Shelf. *Journal of Geophysical Research 92(C13)*: 14610-14620.

Wu, J. 1982: Wind stress coefficients over sea surface from breeze to hurricane. *Journal of Geophysical Research C87*: 9704-9706.

Young, I. R., Black, K. P. and Heron, M. L. 1994: Circulation in the Ribbon Reef region of the Great Barrier Reef. *Continental Shelf Research 14(2/3)*: 117-142.

Appendix 1 – CTD contours, 2 February 1997

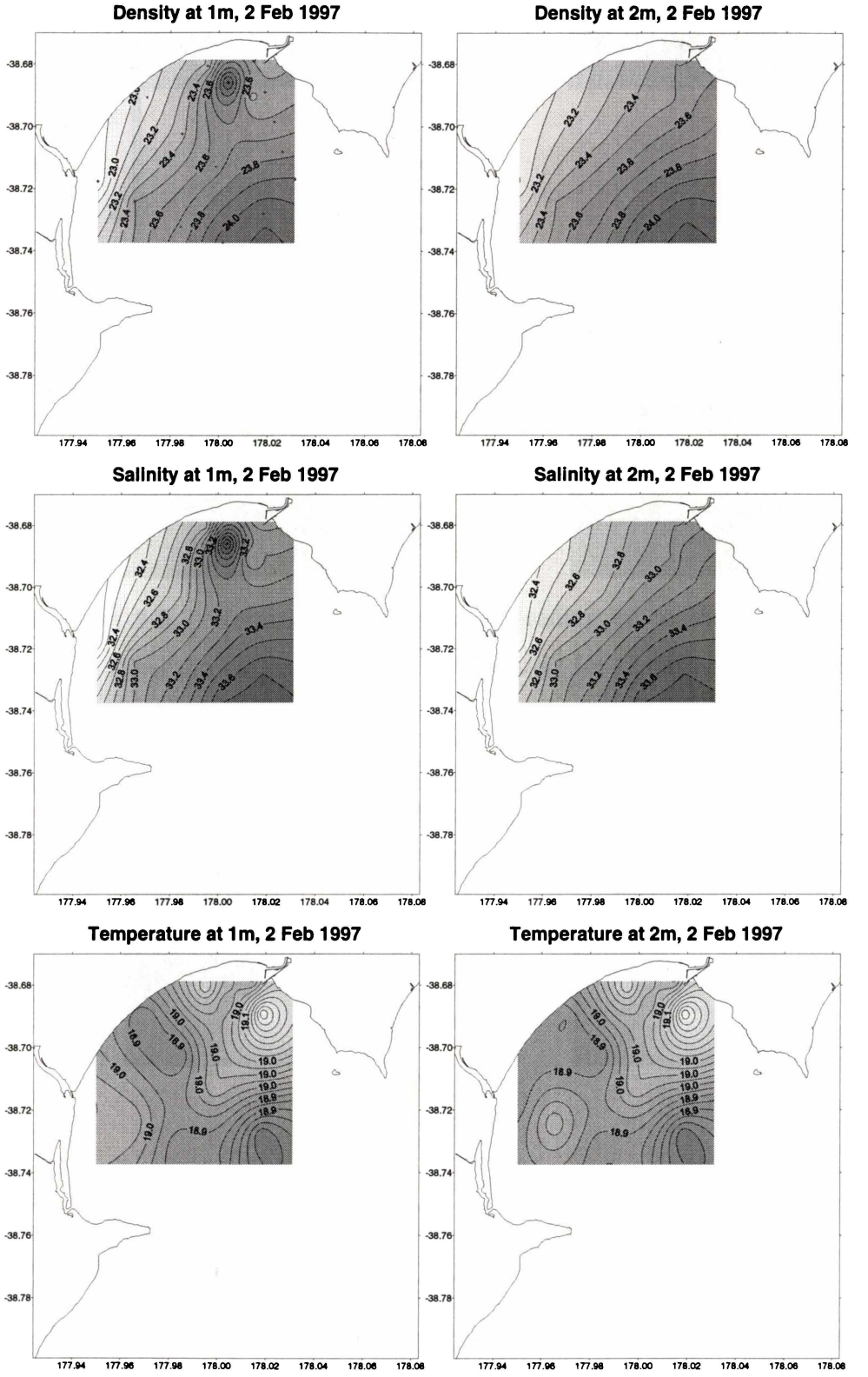

Figure A-9-1. Density (top), salinity (middle) and temperature (lower) at 1 m (left) and 2 m (right) depth in Poverty Bay, 2 February 1997.

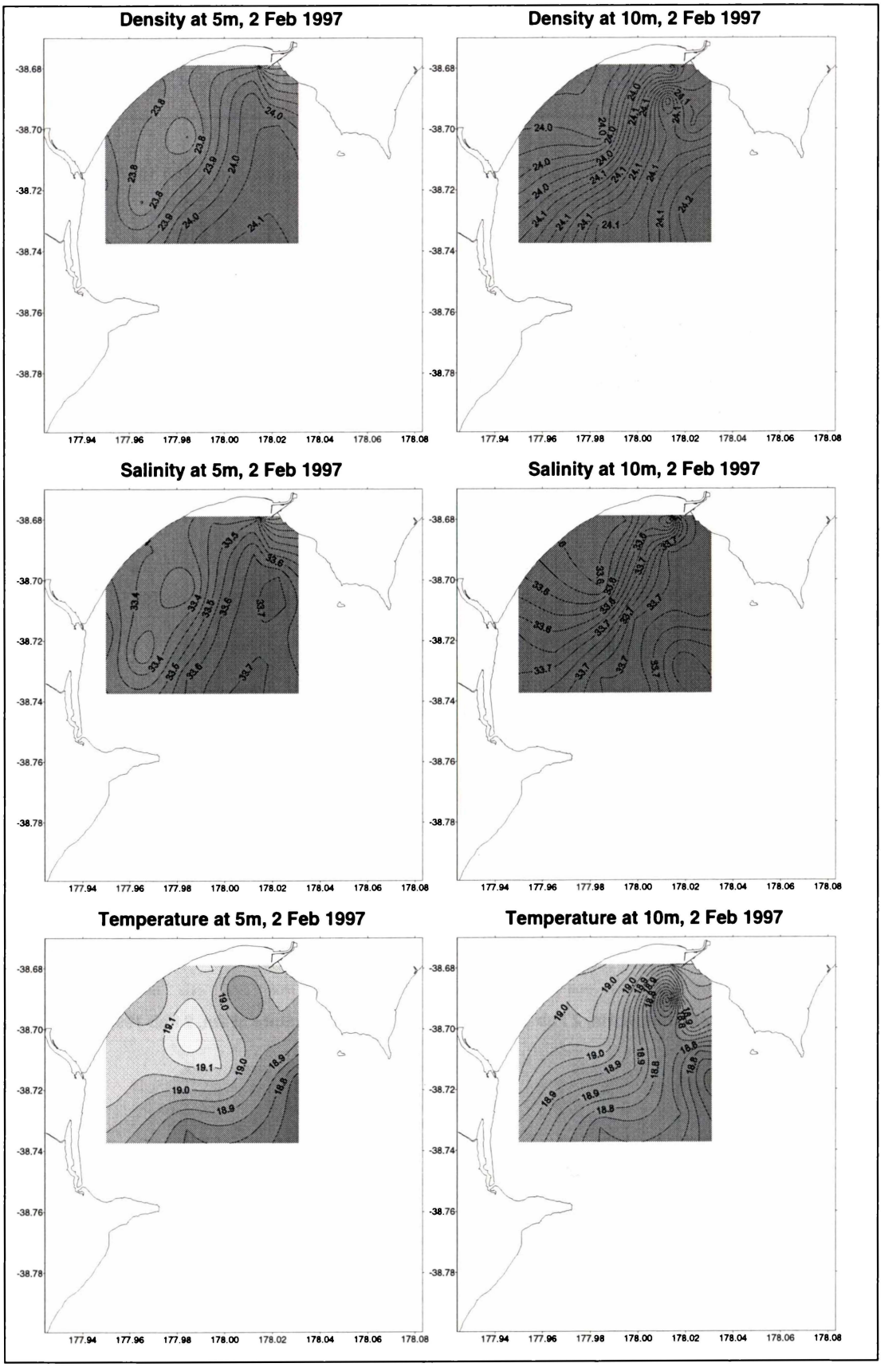

Figure A-9-2. Density (top), salinity (middle) and temperature (lower) at 5 m (left) and 10 m (right) depth in Poverty Bay, 2 February 1997.

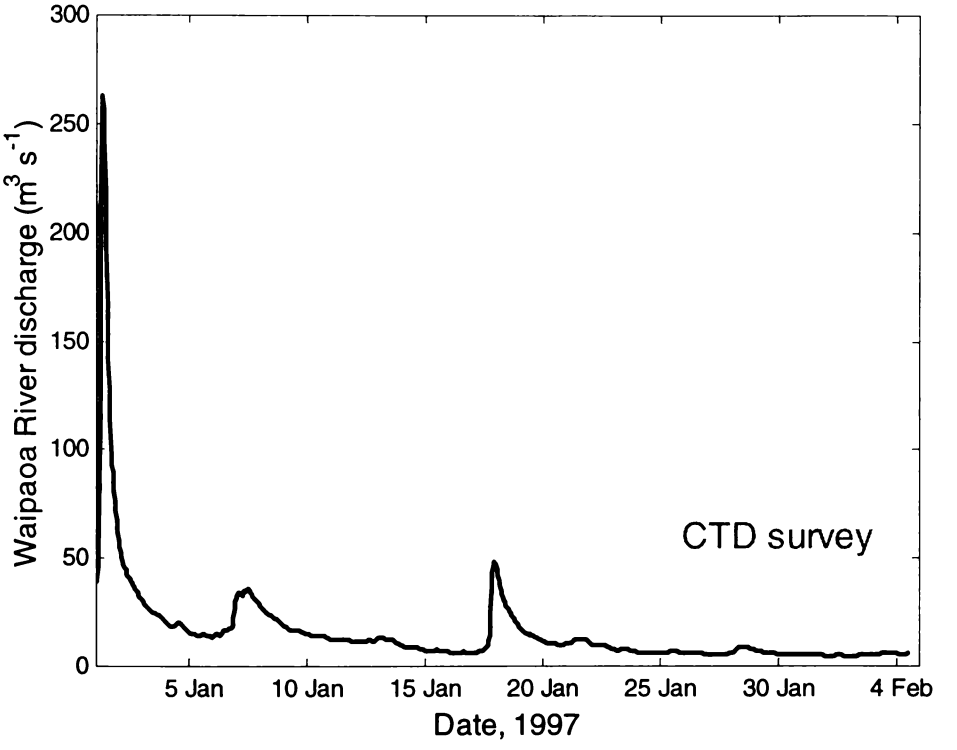

Figure A-9-3. Waipaoa River discharge leading up to the 2 February CTD survey. River discharges were less than 10 $m^3 s^{-1}$ for 12 days prior to the survey.

Appendix 2 – Model 3DD three-dimensional equations and constants

9.4 LIST OF VARIABLES

u velocity in the x direction (m s^{-1})

v velocity in the y direction (m s^{-1})

w velocity in the z direction, positive upward (m s^{-1})

t time (s)

dx size in the x-direction of an averaging region (m)

dy size in the y-direction of an averaging region (m)

dz size in the z-direction of an averaging region (m)

A_H horizontal eddy viscosity coefficient (m^2 s^{-1})

f Coriolis parameter (s^{-1})

N_Z vertical eddy viscosity coefficient (m^2 s^{-1})

P pressure (hPa)

ρ fluid density (kg m^{-3})

h water depth (m)

z vertical distance above seabed (m)

P_{atm} atmospheric pressure (hPa)

g gravitational constant (9.81 m^2 s^{-1})

T temperature (°C)

S salinity (psu)

K_H horizontal eddy diffusivity coefficient (m^2 s^{-1})

K_Z vertical eddy diffusivity coefficient (m^2 s^{-1})

τ^s_x wind stress in the x direction (kg m^{-1} s^{-2})

τ^s_y wind stress in the y direction (kg m^{-1} s^{-2})

ς sea-level (m)

γ wind drag coefficient

ρ_a density of air (kg m^{-3})

W wind speed (m s^{-1})

W_x wind speed in x direction (m s^{-1})

W_y wind speed in y direction (m s^{-1})

τ^b_x bottom stress in the x direction at seabed (kg m^{-1} s^{-2})

τ^b_y bottom stress in the y direction at seabed (kg m^{-1} s^{-2})

u_h bottom current in x direction (m s^{-1})

v_h bottom current in y direction (m s^{-1})

C Chezy's C ($m^{1/2}$ s^{-1})

z_0 frictional roughness length (m)

l_m mixing length (m)

N_0 vertical eddy viscosity coefficient in homogenous water bodies (m^2 s^{-1})

R_i gradient Richardson number

C' Vertical eddy viscosity constant

9.5 GENERAL DESCRIPTION

Model 3DD (Black, 1995) is a 3-dimensional circulation, advection/dispersion and heat transfer model, for application to vertically-stratified or homogeneous ocean, continental-shelf and shallow water environments. An explicit finite difference (Eulerian) solution is used to solve the momentum and continuity equations for velocity and sea-level, while the temperature and salinity advection/dispersion equations are solved using either Eulerian or Lagrangian particle techniques, Eulerian chosen for this study.

Model 3DD has several features that were not used in this study, such as Boussinesq approximation and friction formulations for wave refraction modelling and solar heating, temperature exchange. Only model equations relevant to the present study are included in this Appendix, further information on Model 3DD can be found in Black (1995)

9.6 MODEL GRID

A staggered finite difference grid is utilised similar to that applied by (Leendertse and Liu, 1975) which places the v and u components on "north" and "east" walls respectively. *w* is located in the centre of the "top" wall. The sea-level replaces *w* in the top layer. The solution is found by time stepping with an explicit scheme.

9.7 MODEL EQUATIONS

3DD (Black, 1995) is a layered 3-dimensional hydrodynamic and transport/dispersion model which incorporates the vertically-averaged model hydrodynamic Model 2DD (Black, 1983). The 3-dimensional equations are,

$$\frac{\partial u}{\partial t}+\frac{u\partial u}{\partial x}+\frac{v\partial u}{\partial y}+\frac{w\partial u}{\partial z}-fv=-\frac{g\partial \varsigma}{\partial x}-\frac{1\partial P}{\rho\partial x}+A_H\left(\frac{\partial^2 u}{\partial x^2}+\frac{\partial^2 u}{\partial y^2}\right)+\frac{\partial}{\partial z}\left(N_z\frac{\partial u}{\partial z}\right) \quad \text{(A2.1)}$$

$$\frac{\partial v}{\partial t}+\frac{u\partial v}{\partial x}+\frac{v\partial v}{\partial y}+\frac{w\partial v}{\partial z}+fu=-\frac{g\partial \varsigma}{\partial y}-\frac{1\partial P}{\rho\partial y}+A_H\left(\frac{\partial^2 v}{\partial x^2}+\frac{\partial^2 v}{\partial y^2}\right)+\frac{\partial}{\partial z}\left(N_z\frac{\partial v}{\partial z}\right) \quad \text{(A2.2)}$$

$$w=-\frac{\partial}{\partial x}\int_{-h}^{z} u\,dz-\frac{\partial}{\partial y}\int_{-h}^{z} v\,dz \quad \text{(A2.3)}$$

t is the time, u, v are velocities in the x, y directions respectively, w the vertical velocity in the z direction (positive upward) at the top of each layer, h the depth, g the gravitational acceleration, ζ the sea-level above a horizontal datum, f the Coriolis parameter, P the pressure, ρ the density of water, A_H the horizontal eddy viscosity coefficient, and N_Z the vertical eddy viscosity coefficient.

The pressure at depth z is

$$P=P_{atm}+g\int_{z}^{o}\rho\,dz \quad \text{(A2.4)}$$

where P_{atm} is the atmospheric pressure. The conservation equation for salinity may be written as

$$\frac{\partial S}{\partial t}+\frac{u\partial S}{\partial x}+\frac{v\partial S}{\partial y}+\frac{w\partial S}{\partial z}=\frac{\partial}{\partial z}\left(K_z\frac{\partial S}{\partial z}\right)+K_H\left(\frac{\partial^2 S}{\partial x^2}+\frac{\partial^2 S}{\partial y^2}\right) \quad \text{(A2.5)}$$

where S is salinity, and K_H, K_Z are the horizontal and vertical coefficients of eddy diffusivity.

Using the temperature and salinity, the density is computed according to an equation of state of the form,

$$\rho = \rho(T,S,z) \tag{A2.6}$$

that is,

$$\begin{aligned} T_K &= T + 2.7 \\ \rho &= 1000(1 - 3.7\times10^{-6}T_K^2 + 8.13\times10^{-4}S) \end{aligned} \tag{A2.7}$$

Surface boundary conditions at $z = 0$ are

$$\begin{aligned} &\rho N_z \tfrac{\partial u}{\partial z} = \tau_x^s \\ &\rho N_z \tfrac{\partial v}{\partial z} = \tau_y^s \\ &\tfrac{\partial \varsigma}{\partial t} + u\tfrac{\partial \varsigma}{\partial x} + v\tfrac{\partial \varsigma}{\partial y} = w^s \end{aligned} \tag{A2.8}$$

where τ_x^s, τ_y^s denote the components of wind stress and

$$\begin{aligned} \tau_x^s &= \frac{\rho_a}{\rho}\gamma\,|W|\;W_x \\ \tau_y^s &= \frac{\rho_a}{\rho}\gamma\,|W|\;W_y \end{aligned} \tag{A2.9}$$

ρ is the water density, W the wind speed at 10 m above sea-level with W_x and W_y its x and y components, $\gamma$is the wind drag coefficient, ρ_a the density of air.

At the seabed, $z = -h$, we have

$$\begin{aligned} &\rho N_z \tfrac{\partial u}{\partial z} = \tau_x^h \\ &\rho N_z \tfrac{\partial v}{\partial z} = \tau_y^h \end{aligned} \tag{A2.10}$$

where τ_x^h, τ_y^h denotes the components of bottom stress. Applying a quadratic law at the seabed,

$$\tau_x^h = g u_h (u_h^2 + v_h^2)^{1/2} / C^2$$
$$\tau_y^h = g v_h (u_h^2 + v_h^2)^{1/2} / C^2 \qquad \text{(A2.11)}$$

with u_h, v_h being the bottom currents and C is Chezy's C. For a logarithmic profile,

$$C = 18 \log_{10}(0.37 h/z_0) \qquad \text{(A2.12)}$$

where z_0 is the roughness length ($z_0 = H^2/2L$, where H, L are bedform height and width).

Also,

$$\frac{\partial S}{\partial z} = 0$$
$$\frac{\partial T}{\partial z} = 0 \qquad \text{(A2.13)}$$
$$w_h = -u_h \frac{\partial h}{\partial x} - v_h \frac{\partial h}{\partial y}$$

to ensure no transport of mass, salinity or temperature through the bed.

For vertical eddy viscosity and diffusivity, a parabolic mixing length and Richardson number parameterisation was adopted. Thus,

$$l_m = \kappa z(1 - z/h)$$
$$N_o = l_m^2 \left[\left(\frac{\partial u}{\partial z} \right)^2 + \left(\frac{\partial v}{\partial z} \right)^2 \right]^{1/2} \qquad \text{(A2.14)}$$

where l_m is the mixing length $\kappa = 0.4$, z the distance from the bed, h is the water depth and u and v the orthogonal velocities. In this formula, the eddy viscosity in homogeneous water bodies N_O is parabolic in z and goes to zero at the top and bottom boundaries. The reduction in eddy viscosity across a density interface is parameterised using a gradient Richardson Number (R_i) formulation,

$$R_i = g\left(\frac{\partial \rho}{\partial z}\right) / \rho\left(\frac{\partial u}{\partial z}\right)^2 \qquad \text{(A2.15)}$$

where ρ is the density and g the gravitational acceleration.

The reduced eddy viscosity in the presence of density stratification N_z is,

$$N_z = N_o e^{-C'R_i} \qquad \text{(A2.16)}$$

where the constant C' is taken to be $C' = 4$ for eddy viscosity and $C' = 12$ for eddy diffusivity calculations (Perrels and Karelse, 1982).

Appendix 3 – Matlab™ function for body-force calculation

```
function [Fx,Fy] = BodyFrce(u,v,Wx,Wy,Z,h,timestep,z0,latitude,rot)
% Calculate a body-force surrogate for pressure gradient in 2D using the pressure-gradient, local-acceleration, wind-stress and bed-friction terms
% Usage [Fx,Fy] = BodyFrce(u,v,Wx,Wy,Z,h,timestep,z0,latitude,rot);
% Inputs:   u           Current U velocity time-series (m/s)
%           v           Current V velocity time-series (m/s)
%           Wx          Wind X velocity time-series (m/s) - should be in true vectors convention
%           Wy          Wind Y velocity time-series (m/s) - should be in true vectors convention
%           Z           Sea-level time-series above datum (m)
%           h           Average water depth (m)
%           timestep    Time step between u,v,Wx,Wy data (s)
%           z0          roughness length for Chezy's C (m)
%           latitudeLatitude in decimal degrees
%           rot         +ve degrees clockwise to rotate u,v,Wx,Wy data (default = zero)
% Outputs:
%           Fx          Body-force in x direction
%           Fy          Body-force in y direction

% Scott Stephens, Coastal Marine Group, The University of Waikato, 29/08/00

if nargin == 10
 [u,v] = rotdata2(u,v,rot,1,1,0,0);
 [Wx,Wy] = rotdata2(Wx,Wy,rot,1,1,0,0);
end

% Add datum to depths
h = Z + h;
```

```
DEFF = 0.50 % Should be set as in model

% Local acceleration - third order approximation
Ula = zeros(size(u)); Vla = zeros(size(v));
Ula(2) = (u(3) - u(1)) ./ (2.*timestep) - (u(3) - 3.*u(2) + 3.*u(1) - u(1)) ./
(6.*timestep);
Vla(2) = (v(3) - v(1)) ./ (2.*timestep) - (v(3) - 3.*v(2) + 3.*v(1) - v(1)) ./
(6.*timestep);
for i = 3:size(u,1)-1
  Ula(i) = (u(i+1) - u(i-1)) ./ (2.*timestep) - (u(i+1) - 3.*u(i) + 3.*u(i-1) - u(i-2)) ./
(6.*timestep);
  Vla(i) = (v(i+1) - v(i-1)) ./ (2.*timestep) - (v(i+1) - 3.*v(i) + 3.*v(i-1) - v(i-2)) ./
(6.*timestep);
end
Ula(size(u,1)) = (u(size(u,1)) - u(size(u,1)-1)) ./ (2.*timestep) - (u(size(u,1)) -
3.*u(size(u,1)) + 3.*u(size(u,1)-1) - u(size(u,1)-2)) ./ (6.*timestep);
Vla(size(u,1)) = (v(size(u,1)) - v(size(u,1)-1)) ./ (2.*timestep) - (v(size(u,1)) -
3.*v(size(u,1)) + 3.*v(size(u,1)-1) - v(size(u,1)-2)) ./ (6.*timestep);

% Local acceleration
%Ula = zeros(size(u)); Vla = zeros(size(v));
%for ii = 2:size(u,1)
%   Ula(ii) = (u(ii) - u(ii-1))/timestep;
%   Vla(ii) = (v(ii) - v(ii-1))/timestep;
%end

% Local acceleration
%Ula = zeros(size(u)); Vla = zeros(size(v));
%for ii = 1:size(u,1)-1
%   Ula(ii) = (u(ii+1) - u(ii))/timestep;
%   Vla(ii) = (v(ii+1) - v(ii))/timestep;
%end

% Bed friction acceleration
```

```
C = 18*log10(0.37 .* (h + DEFF) ./ z0); % Chezy's C
Ubf = 9.81 .* u .* sqrt(u.^2 + v.^2) ./ (C.^2 .* (h + DEFF));
Vbf = 9.81 .* v .* sqrt(u.^2 + v.^2) ./ (C.^2 .* (h + DEFF));

% Wind stress
W = sqrt(Wx.^2 + Wy.^2); % Calculate wind magnitude from vectors

% Calculate gamma for wind stress calculation after Large and Pond (1981)
gamma = ones(size(W));
%is=find(W < 11); gamma(is) = gamma(is) .* 0.0012;
%il=find(W >= 11); gamma(il) = gamma(il) .* (0.49+0.065.*W(il))./1000;

% Calculate gamma according to 3DD method
gamma = gamma .* (0.8+0.065.*W)./1000;
pa=1.29;                    % Density of air (Tipler, Physics)
ps = 1025;                  % Density of seawater

% Wind stress acceleration

Wu = pa .* gamma .* Wx .* W ./ (ps .* (h + DEFF));
Wv = pa .* gamma .* Wy .* W ./ (ps .* (h + DEFF));

% Coriolis acceleration

lat = latitude * pi/180;
f = 2 * 0.00007292 * sin(lat)
fV = f .* v;
fU = f .* u;

% Calculate body-force

choice = input('Enter 1 to disclude wind-induced acceleration from body-force ');
if choice ~= 1
  Fx = -Ula + Wu - Ubf + fV; % Body force in X direction
```

```
  Fy = -Vla + Wv - Vbf - fU; % Body force in Y direction
else
  Fx = -Ula - Ubf + fV; % Body force in X direction
  Fy = -Vla - Vbf - fU; % Body force in Y direction
end
```